Simulation of Growing Cell Sheets

Inaugural-Dissertation

zur

Erlangung des Doktorgrades

der Mathematisch-Naturwissenschaftlichen Fakultät

der Universität zu Köln

vorgelegt von

Raphael Hornung

aus Zweibrücken

Köln

2019

Berichterstatter: Dr. habil. Jens Elgeti

Prof. Dr. Tobias Bollenbach

Tag der mündlichen Prüfung: 27. September 2019

Zusammenfassung

In der Natur gibt es viele Beispiele für Zellwachstum in Schichten: Bakterienfilme bevölkern fast jede freie Fläche, Haut, Schleimhäute und Drüsengewebe bestehen aus Lagen von Epithelzellen, Pflanzenzellen bilden Blätter und Blüten aus. Sowohl in Bakterien als auch in Körperzellen wird Wachstum durch eine Kombination von biochemischen und mechanischen Signalen reguliert welche oft noch nicht vollständig verstanden sind. Man vermutet, dass diese Einflüsse auf das Wachstum der mikroskopischen Zelle durch Selbstregulation zu dem makroskopisch beobachteten Verhalten des Gewebes oder der Bakerienkolonie führen. Zum Beispiel wird die Ausbildung von Darmzotten während der embryonalen Entwicklung auf die Reaktion der Zellen auf lokalen Druck und die Konzentration von Wachstumsfaktoren zurückgeführt. Ein anderes Beispiel bilden Bakterien deren Wachstumsverhalten sich der Konzentration einer Vielzahl diffusiver Substanzen wie Nährstoffen, Antibiotika oder Autoinducern anpasst.

In dieser Arbeit untersuchen wir anhand von zwei Beispielen mit Hilfe einer vereinheitlichten Simulationsmethode wie lokale Wachstumsregulation die Morphologie einer Schicht von Zellen determiniert. Zuerst befassen wir uns mit der Faltenbildung einer zweidimensionalen Gewebsmembran, welche in einem dreidimensionalen, dissipativen Medium eingebettet ist und deren lokale Wachstumsrate eine mechanische Rückkoppelung aufweist. Hierbei erfolgt das Wachstum gemäß der Theorie des homöostatischen Drucks, die eine Wachstumrate k_g animmt welche ausschließlich von der Differenz $\delta p = p_h - p$ zwischen lokalem Druck p und einem Gewebeparameter p_h, dem homöostatischen Druck, abhängt. Die Wachstumsrate verschwindet am homöostatischen Druck und ist in dessen Umgebung durch eine lineare Entwicklung $k_g = \xi \delta p + \mathcal{O}\left(\delta p^2\right)$ gegeben; hiermit bestimmt die Druckempfindlichkeit ξ die Zeitskala des Wachstums. Das Simulationsverfahren besteht aus einer Kombination der *two particle growth* Methode (Abk. 2PG-Methode), implementiert von Nils Podewitz, und dem *moving least-squares meshless membrane* Modell (Abk. MMM-Modell). Membranparameter wie Biegesteifigkeit κ, homöostatische Oberflächenspannung $\gamma_h = -p_h d$ (d bezeichnet die Membrandicke), Druckempfindlichkeit ξ und Flächen-Kompressibilität χ_a werden in der Simulation gemessen. Durch analytische Untersuchung des MMM-Potentials (1) zeigen wir, dass dessen Stresskomponenten in Ebenenrichtung vernachlässigbar klein sind gegenüber entsprechenden 2PG-Komponenten und (2) finden wir eine Näherungsformel für dessen Biegesteifigkeit, die mit unseren Messungen übereinstimmt. Als Ergebnis erhalten wir damit eine Membran mit wohl definierter Biegesteifigkeit und mechanisch kontrolliertem Wachstum.

Bei einer zu Beginn im flachen Zustand unter periodischen Randbedingungen equilibrierten Membran beobachten wir bei hinreichend großem homöostatischem Druck Buckling. Insbesondere ist die charakteristische Wellenlänge λ der Faltungsmuster viel kleiner als die System-umfassende Wellenlänge $\lambda = L$ welche von der klassischen Euler-Instabilitätsanalyse vorhergesagt wird. Zur Beschreibung der Faltungsdynamik aufgrund druckabhängigen Wachstums entwickeln wir ein vereinfachtes Kontinuumsmodell basierend auf den Föppl-von Kármán-Gleichungen. Unser Modell ergibt, dass die am stärksten anwachsende Wellenlänge anfangs nahe der homöostatischen Wellenlänge $\lambda_h = 2\pi\sqrt{2\kappa/|\gamma_h|}$ liegt und mit der Zeit größer wird, begleitet von einer Entspannung des Oberflächenstresses. Unsere Theorie reproduziert die in Simulationen beobachtete Faltungsdynamik quantitativ und weist darauf hin, dass die Zeitskalen von Gewebewachstum τ_g und Membran-Deformation τ_{ampl} eine entscheidende Rolle spielen für die Auswahl der vorherrschenden Wellenlänge. Für $\tau_{ampl} \ll \tau_g$ wächst das

Gewebe sehr viel langsamer als sich die Membran verformt, die Verformung der Membran erfolgt fast quasistatisch und die Biegung tritt nahe klassischem Euler-Buckling bei $\lambda = L$ auf. Sind jedoch τ_g und τ_{ampl} von vergleichbarer Größenordnung verkleinert sich die Wellenlänge, im Limes langsamer elastischer Relaxation $\tau_{ampl} \gg \tau_g$ wird schließlich die homöostatische Wellenlänge λ_h asymptotisch stabil. Die Abhängigkeit von Zeitskalen bedeutet insbesondere, dass die vorherrschende Wellenlänge von Reibungsparametern wie zum Beispiel dem Reibungskoeffizient ν mit dem dissipativen Medium oder der intrazellulären Reibungskonstante γ_c abhängt.

Jenseits kleiner Amplituden bildet die Membran Ausstülpungen deren Querschnitt einem "Ω" ähneln. Der horizontale Abstand zwischen Falten ändert sich dabei kaum. Damit können die Vorhersagen für die dominante Wellenlänge λ aus unserem Kontinuumsmodell auch jenseits kleiner Amplituden verwendet werden. Vor dem Hintergrund der Morphogenese von Geweben bietet unser Modell eine Alternative zur *differential growth* Hypothese, welche annimmt, dass die dominante Mode im gefalteten Gewebe durch verschiedene Wachstumsraten in benachbarten Gewebeschichten zustande kommt.

Ein zweites Forschungsprojekt widmet sich dem Wachstum einlagig geschichteter Bakterienkolonien des Stamms *Corynebacterium glutamicum* in mikrofluidischen Experimenten. In einem ersten Schritt ermitteln wir die Abhängigkeit des Bakterienwachstums von der Nährstoffkonzentration. Dazu messen wir das stationäre Flußprofil von Bakterien in einem breiten Kanal abhängig von der gefütterten Konzentration g eines limitierenden Nährstoffes. Die Flußmessungen erfolgen mit particle image velocimetry (Abk. PIV) und ermöglichen es uns die lokale Wachstumsrate zu berechnen. Die einfache Geometrie des Wachstumskanals erlaubt uns den Vergleich des Flußprofils mit der Vorhersage eines eindimensionalen Reaktions-Diffusions-Modells für Nährstofftransport, -aufnahme und -umwandlung in Biomasse. Unser analytisches Modell nimmt eine bakterielle Wachstumsrate k_g proportional zur konzentrationsabhängigen Nährstoffaufnahmerate an, $k_g \propto U(g)$. Eine Anpassung unseres Modells an die Experimentaldaten mittels der Methode der kleinsten Fehlerquadrate erlaubt uns die Ermittlung der Form der Aufnahmefunktion $U(g)$ sowie der maximalen Wachstumsrate k_{max} und der Längenskala l_g des Abfalls der Nährstoffkonzentration innerhalb der Kolonie. Wir finden eine gute Übereinstimmung mit der häufig angenommenen Monod-Kinetik $U(g) \propto g/\big(g_{1/2} + g\big)$ mit Konzentrationsskala $g_{1/2} = 13 - 20\,\mu\text{M}$, maximaler Wachstumsrate von etwa $k_{max} = 0.2 - 0.26\,\text{h}^{-1}$ und Abfallslängenskala um $l_g = 3.8 - 4.2\,\mu\text{m}$. Da der Wert für l_g etwa $2 - 3$ Bakterienlängen entspricht, deutet dies insbesondere darauf hin, dass Nährstoffgradienten bereits bei kleinen Kolonien auftreten und daher für die Interpretation der Wachstumsmuster in Betracht gezogen werden müssen.

Im nächsten Schritt benutzen wir die gemessenen Parameter für ein 2PG-Setup welches um die Reaktions-Diffusions-Dynamik erweitert wurde. Unser Simulationsverfahren ermöglicht es uns das Wachstumsverhalten in komplexeren mikrofluidischen Kammergeometrien vorherzusagen sowie elastische Wechselwirkungen zu berücksichtigen. Der Vergleich der Kolonieausbreitung zwischen Experiment und Simulation in einer Kammer mit engen Zuflüssen zeigt eine gute Übereinstimmung von Kolonieform und -ausbreitung für Kolonien größer als etwa $500\,\mu\text{m}^2$. Abweichungen treten für kleine Nährstoffkonzentrationen auf während bei mittleren Konzentrationen Experiment und Simulation übereinstimmen für Koloniegrößen bis hinunter zu nur wenigen Zellen. Desweiteren berücksichtigen wir den Effekt verminderter Diffusion durch die Zellwände der Bakterien. Unsere Ergebnisse weisen darauf hin, dass Bakterien nur ein schwaches Hindernis für Nährstoffdiffusion darstellen, da wir die beste Übereinstimmung

mit effektiven Diffusionskonstanten der gleichen Größenordnung wie die der freien Diffusionskonstante erhalten. Die gute Übereinstimmung unseres Modells legt nahe, dass bereits für eine Kolonie von nur wenigen tausend Bakterien eine vergröberte Beschreibung mit Hilfe eines Reaktions-Diffusions-Modells gute quantitative Vorhersagen des Koloniewachstums ergibt. Unsere Simulationsmethode sagt Kolonieausbreitung und Nährstoffgradienten innerhalb der Kammern voraus und hilft hiermit bei Design und Interpretation von mikrofluidischen Wachstumsexperimenten. Besonders die Messungen von Flußprofilen in einem einfachen Wachstumskanal stellt eine leicht zugängliche Möglichkeit dar um die Nährstoffabhängigkeit bakteriellen Wachstums zu ermitteln.

Abstract

Cells grow in sheets in various systems in nature: bacterial films occupy almost every free surface, epithelial cells comprise skin, mucous membranes or glandular tissue, plant cells form leaves and petals. Both in bacteria and body cells, growth is regulated by a combination of biochemical and mechanical cues which are often not understood completely. The response of microscopic cell growth to these various cues is assumed to determine macroscopic behavior of the tissue or cell colony in a self-organized manner. For example, evolution of gut folds during embryonic development is attributed to the reaction of cells to local pressure and growth factor concentration, furthermore, growth behavior of bacterial colonies adapts to the concentration of a variety of diffusing agents such as nutrients, antibiotics or autoinducers.

In this work, we study two examples of how local growth regulation mechanisms determine the morphology of cell sheets within an unified simulation framework. First, we investigate wrinkling of a two-dimensional tissue membrane embedded in a dissipative, three-dimensional medium with a local growth rate subject to mechanical feedback. Growth follows the homeostatic pressure theory which assumes a growth rate k_g solely dependent on the difference $\delta p = p_h - p$ of local pressure p and a tissue-inherent pressure scale, the homeostatic pressure p_h. It is assumed that growth stops at $p = p_h$ and the growth rate close to p_h follows from a linear expansion to $k_g = \xi \delta p + \mathcal{O}\left(\delta p^2\right)$; the pressure-sensitivity constant ξ determines hereby the growth timescale. The simulation technique consists of a combination of the *two particle growth* simulation framework (abbreviated 2PG-framework) implemented by N. Podewitz and the *moving least-squares meshless membrane* model (abbreviated MMM-model). Membrane parameters such as bending rigidity κ, homeostatic surface tension $\gamma_h = -p_h d$ (d denotes the membrane thickness), pressure-sensitivity ξ and area compressibility χ_a are measured in simulations. Furthermore, a detailed analysis of the MMM-potential (1) shows that its in-plane stress contributions are negligible compared to the 2PG-stresses and (2) provides analytic estimates for the bending rigidity which agree with our measurements. Thus, we obtain a membrane with a well-defined bending rigidity and growth with mechanical feedback.

Starting from a flat, equilibrated, membrane in periodic boundary conditions, we observe buckling for sufficiently large homeostatic pressure. In particular, the characteristic wavelength λ is much smaller than the system-spanning wavelength $\lambda = L$ predicted by classical Euler buckling. To describe the wrinkling dynamics with stress-dependent growth, we develop a simplified continuum model based on the Föppl-von Kármán equations. Our model predicts that the strongest amplified wavelength is initially close to the homeostatic wavelength $\lambda_h = 2\pi\sqrt{2\kappa/|\gamma_h|}$ and increases over time, paralleled by a relaxation of compressive surface stress. Our model quantitatively reproduces the wrinkling dynamics in simulations and suggests that the timescales of tissue growth τ_g and membrane deformation τ_{ampl} play a crucial role for the selection of the dominant wavelength. For $\tau_{ampl} \ll \tau_g$ the tissue grows much slower than the membrane deforms, membrane deformation is almost quasi-static and buckling occurs close to classical Euler buckling at $\lambda = L$. However, if τ_{ampl} and τ_g are of comparable scale, the wavelength decreases and in the limit $\tau_{ampl} \gg \tau_g$ the homeostatic wavelength λ_h becomes asymptotically stable. In particular, this suggests that the dominant wavelength can be steered by changing frictional parameters such as the friction constant ν with the dissipative medium or the intracell friction constant γ_c.

Beyond small amplitudes, the membrane forms bulges whose cross-sections resemble the letter "Ω". Interestingly, the horizontal distance between folds does hardly change. Therefore, the predictions for the dominant wavelength λ apply beyond small amplitudes. In the

context of tissue morphogenesis, our model provides an alternative to the *differential growth* hypothesis which assumes that the wrinkling mode is selected due to different growth rates in adjacent tissue layers.

A second research project analyses the growth of monolayered bacterial colonies of the stem *Corynebacterium glutamicum* in microfluidic devices. In a first step, we estimate the nutrient dependency of growth. To do so, we measure the steady state flow pattern of bacteria in a wide channel dependent on the fed concentration g of a single limiting nutrient. Flow measurements via particle image velocimetry (abbreviated PIV) allow us to infer the local growth rate. The simple geometry of the growth channel enables us to compare the flow profile with the prediction of an one-dimensional reaction-diffusion model for nutrient transport, uptake and conversion into biomass. Our analytic model assumes a bacterial growth rate k_g proportional to the concentration-dependent nutrient uptake rate of bacteria $k_g \propto U(g)$. With a least squares minimization fit of measured flow velocity versus the prediction by our model, we infer the shape of the function $U(g)$ as well as maximum growth rate k_{max} and the decay lengthscale l_g of nutrient concentration inside the colony. We find a good agreement for commonly assumed Monod-kinetic uptake $U(g) \propto g/\big(g_{1/2} + g\big)$ with concentration scale around $g_{1/2} = 13 - 20\,\mu\mathrm{M}$, maximum growth rate around $k_{max} = 0.2 - 0.26\,\mathrm{h}^{-1}$ and a decay length scale of $l_g = 3.8 - 4.2\,\mu\mathrm{m}$. In particular, the estimate for l_g corresponds to roughly $2-3$ bacterial lengths which suggests that nutrient gradients occur already for small colonies and have to be taken into account for the interpretation of growth patterns.

In the next step, we feed the measured model parameters into a 2PG setup, adapted to simulate the reaction-diffusion dynamics of nutrient uptake and growth. Our simulation model allows us to predict growth in more complex microfluidic chamber geometries as well as inclusion of elastic interactions. Comparison of colony spreading between experiment and simulation in a chamber with narrow inlets yields a good agreement of colony shape and area for colonies larger than approximately $500\,\mu\mathrm{m}^2$. Deviations occur for small nutrient concentration, whereas medium nutrient concentrations agree down to colony sizes of a few bacteria. Moreover, we included the effect of hindered diffusion through cell walls. Our findings suggest that bacteria represent only a weak obstacle for nutrient diffusion as we get best agreement for effective diffusion constants very similar to the free diffusion constant. The good overall agreement with our model suggests that already for a colony of only a few thousand bacteria a coarse-grained reaction-diffusion model description yields good quantitative predictions of colony growth. Our simulation framework predicts colony spreading and nutrient gradients inside the growth chamber aiding in design and interpretation of microfluidic growth experiments. In particular, measurement of flow profiles in a simple growth channel experiment provides an easy way to estimate the nutrient dependency of bacterial growth.

Contents

Zusammenfassung 3
Abstract 7
Notations and Conventions 13
Abbreviations 14
Nomenclature 15

Chapter 1. Introduction 17
Structure of this Thesis 20

Chapter 2. General Properties of Growth Regulation 21
2.1. Growth Kinetics - Biochemical and Mechanic Regulation 22
2.1.1. Growth Regulation by Pressure 22
2.1.2. Transport of Biochemical Agents 24
2.1.3. Growth Regulation by Biochemical Agents 26
2.2. Patterning Models for Tissue Morphogenesis 32

Chapter 3. Simulation Framework and Tissue Model 37
3.1. The Two Particle Growth Simulation Method 37
3.2. Integration of Equations of Motion 40
3.3. The Meshless Membrane Model 42
3.3.1. Definition and Resulting Force 42
3.3.2. Forces in the Nearly Flat State 44
3.3.3. Curvature Moduli: Bending Rigidity and Saddle-Splay Modulus 48
3.3.4. Isotropic Compressibility Dependence on Weight Function 55
3.3.5. Adaptations to Algorithm 57
3.4. Measurement of Growing Membrane Parameters 58
3.4.1. Surface Tension Measurements and Virial Stress 59
3.4.2. Homeostatic Surface Tension 60
3.4.3. Growth Pressure Sensitivity Constant 62
3.4.4. Area Compressibility 64
3.4.5. Bending Rigidity 66
3.5. Reaction-Diffusion Model of Limiting Nutrient 70

Chapter 4. Growth of 2D-Manifolds in 3D 73
4.1. Buckling of Thin, Planar Membranes 74
4.1.1. Energy Contributions 74
4.1.2. Buckling Instabilities 76
4.1.3. Buckling Dynamics in Small Angle Limit 78
4.2. Buckling with Stress-Dependent Growth 81

4.3. Simulations of Growing Membranes 88
4.3.1. Small Amplitude Buckling 89
4.3.2. Shapes with Overlap 94
4.4. Summary 99

Chapter 5. Nutrient Limited Growth of Bacterial Microcolonies 101
5.1. Bacterial Growth Model - Theory and Simulation 102
5.1.1. Nutrient Uptake and Biomass Conversion 102
5.1.2. Pressure and Growth Channel Deformation 104
5.1.3. Choice of Simulation Units and Parameters 105
5.2. Growth Channel Experiments with *Corynebacterium glutamicum* 108
5.2.1. Selection for further Evaluation 108
5.2.2. Measurement of Flow Fields 111
5.2.3. Quantitative Match between Analytic Model and Experiments 114
5.2.4. Fit Procedure 117
5.2.5. Streaming Instabilities 119
5.3. Prediction of Colony Shape Dynamics in Two Dimensions 123
5.4. Summary 126

Chapter 6. Conclusion and Outlook 129

Appendix A. Meshless Membrane Model - Force Calculation 133

Appendix B. Multibody Potentials and Stress Calculations with Spatial Resolution 135

Appendix C. Differential Geometric Framework 139
C.1. Membranes as Smooth Surfaces 139
C.2. Inner and Outer Geometry of a Surface 140
C.3. The Monge-Representation 143
C.4. The Theorem of Gauss-Bonnet 144

Appendix D. Deformation of Elastic Substrate 149
D.1. Deformation by Single Plane Wave 151
D.2. Deformation by Arbitrary Wavepattern 152
D.3. Energy of Deformed Support 154

Appendix E. Buckling Dynamics in Small Angle Limit
Phase Angle Dynamics - Fluctuation Spectra - Hydrodynamic Interactions 157
E.1. Phase Angle Dynamics and Spontaneous Curvature 157
E.2. Amplitude and Phase Angle Fluctuations in the Planar State 158
E.3. Growing Membrane with Hydrodynamic Interactions at Low Reynolds Numbers 160

Appendix F. Simulations of Growing Membranes 165
All Simulation and Theory Data 165

Appendix G. Growth Channel Experiments 171
All Velocity Profile Data 171

Appendix H. Growth Chamber Experiments 181
All Colony Spreading Data 181

Appendix I. Standard Simulation Parameters 185

Bibliography 187

List of Figures 195

List of Tables 201

Erklärung der Selbständigkeit 203

Lebenslauf 205

Notations and Conventions

Throughout this work, scalars are typeset in plain style, vectors in bold style and tensors in bold style with a bar on top. For example,

σ denotes the Poisson ratio,
$\boldsymbol{k}$ a wavevector and
$\overline{\boldsymbol{\sigma}}$ the stress tensor.

The sign convention for stress and surface tension is such that a negative sign corresponds to a *compressed state* and a positive sign to a *tensile state.* Pressure has the *opposite* sign of stress.

In plots which have not been adopted from other publications, error bars correspond to the standard deviation (abbreviated STDEV) of the data set, if not stated otherwise explicitly. We denote with angle brackets $\langle X \rangle$ the average value of the observable X. For n measurements $\{X_i\}_{i=1}^{n}$ of X, mean $\langle X \rangle$ and standard deviation $\sigma(X)$ of X are given by

$$\langle X \rangle = \frac{1}{n}\sum_{i}^{n} X_i,$$

$$\sigma(X) = \sqrt{\left\langle (X - \langle X \rangle)^2 \right\rangle} = \sqrt{\langle X^2 \rangle - \langle X \rangle^2}.$$

The “$\otimes$” symbol is used to denote an operation which assigns two vectors $\boldsymbol{a}, \boldsymbol{b}$ a tensor $\boldsymbol{a} \otimes \boldsymbol{b}$ defined via

$$\boldsymbol{a} \otimes \boldsymbol{b} = \begin{pmatrix} a_1b_1 & a_1b_2 & a_1b_3 \\ a_2b_1 & a_2b_2 & a_2b_3 \\ a_3b_1 & a_3b_2 & a_3b_3 \end{pmatrix}.$$

Dots above symbols denote total time derivatives, e.g. the total derivative of particle number N with respect to time reads

$$\dot{N} = \frac{dN}{dt}.$$

Partial derivatives are sometimes abbreviated according to following examples

$$\frac{\partial f}{\partial x} = \partial_x f \qquad \frac{\partial^2 f}{\partial x \partial y} = \partial_{xy}^2 f.$$

Numbers of equations, figures and tables follow the rules (i)-(ii) where the counter is reset to one (i) every section or (ii) every chapter. The section number is omitted for equations which appear in the introduction of every chapter.

(i) Equation number format

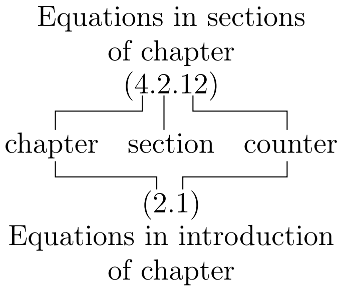
Equations in sections
of chapter
(4.2.12)
chapter
section
counter
(2.1)
Equations in introduction
of chapter

(ii) Figure/Table number format

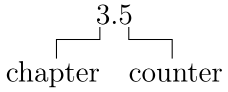
3.5
chapter
counter

Abbreviations

2PG	two particle growth (model), see p. 3
MMM	moving least-squares meshless membrane (model), see p. 3
PIV	particle image velocimetry, see p. 4
STDEV	standard deviation, see p. 13
PDMS	polydimethylsiloxane, see p. 25
IBM	individual based model, see p. 29
LALI	local activation and long-range inhibition, see p. 33
DPP	decapentaplegic, see p. 36
DPD	dissipative particle dynamics, see p. 37
BD	brownian dynamics, see p. 38
VV	velocity verlet, see p. 40
FFT	discrete fast fourier transform, see p. 68
FFTW	“Fastest Fourier Transform in the West”, a C-library for discrete Fourier transforms, see p. 68 and ref. [1]
PCA	protocatechuic acid, see p. 102
CGXII	CGXII growth medium, see p. 108 and ref. [2]
NMT	normalized median test, see p. 113
CFD	central force decomposition, see p. 136

Nomenclature

N	cell number
L;A;V	length/area/volume
m	mass
$\boldsymbol{j}$	cell flux
$\varrho; \widehat{\varrho}; \varrho_m; \varrho_h; \varrho_{sf}$	number/projected number/mass/homeostatic/stress-free density
$k_g; k_{max}$	growth rate/maximum growth rate
ξ	growth rate pressure sensitivity
$p; p_h$	pressure/homeostatic press., compressive pressure has **positive** sign
$\gamma; \gamma_h; \gamma_\infty$	surface tension/homeostatic surf. tens./asymptotic surf. tens., compressive surface tension has **negative** sign
Γ	cumulative time-integral of surface tension
$\overline{\boldsymbol{\sigma}}$	stress tensor $\overline{\boldsymbol{\sigma}} = (\sigma_{ij})$, compressive stress components have **negative** sign
$\overline{\boldsymbol{u}}$	deformation tensor $\overline{\boldsymbol{u}} = (u_{ij})$
$E; \widehat{E}$	Young's/elastic substrate modulus
χ_a	area compressibility
κ_x	bulk compressibility in ensemble with x constant
K_x	bulk modulus in ensemble with x constant
σ	Poisson ratio
ν	friction constant of dissipative medium
λ_p	membrane permeability
η	viscosity of embedding medium
$a; a_{opt}$	harmonic confinement potential strength/optimal harm. conf. pot. strength
$\kappa; \widehat{\kappa}$	bending rigidity/saddle-splay modulus
$C_0; C_1; C_2; H; G$	spontaneous/first main/second main/mean/Gaussian curvature
$\overline{\boldsymbol{g}}$	first fundamental form (metric tensor)
h	membrane elevation in Monge-representation
$h_{\boldsymbol{k}}; r_{\boldsymbol{k}}; \varphi_{\boldsymbol{k}}$	membrane elevation Fourier component/comp. amplitude/comp. phase
d	in chapter 4: membrane thickness/in chapter 5: growth chamber inlet width
$k; k_h; k_\infty$	wavenumber/homeostatic wvn./asymptotic wvn.
$k_{min}; k_{min}^{\widehat{E}}$	minimal energy wavenumber for free membrane/membrane with linear elastic substrate
$\gamma^c; \gamma^{c,\widehat{E}}$	critical buckling surface tension for free membrane/membrane with linear elastic substrate
$\tau_g; \tau_{ampl}$	growth/deformation amplitude increase timescale
$\Theta'; \Theta''$	first/second growth-buckling-ratio
$g; \widehat{g}; \bar{g}; g_{1/2}$	nutrient concentration/dimensionless nutr. conc./nutr. conc. unit conversion factor/half-maximum nutr. conc.
u	nutrient uptake function (dependent on concentration g)

u_∞	maximum nutrient uptake rate
ϵ	nutrient to biomass conversion efficiency
l_g	nutrient decay length
$D_{bulk}; D_{free}$	nutrient diffusion constant in- and outside of bacterial colony
Pe	Péclet number
Re	Reynolds number
k_bT	boltzmann constant times absolute temperature
$\boldsymbol{r}_g$	weighted center of mass
$\overline{\boldsymbol{a}}$	gyration tensor
α_{pl}	aplanarity
k_α	MMM-potential strength
r_{pp}	pair-potential cutoff radius
r_{mp}	MMM-potential cutoff radius
d_c	size threshold for cell division
r_c	distance at which new particles are placed after division
r_0	growth force length constant
B	growth force strength
$f_0; f_1$	repulsive/attractive force constant
$\gamma_b; \gamma_t; \gamma_c$	background/intercell/intracell friction constant

CHAPTER 1

Introduction

The ability to grow and reproduce is one property defining life and distinguishes living from dead matter [3, 4]. Already early nature philosophers contemplated about growth, e.g. Aristotle in his work *Περὶ ζῴων γενέσεως* (*On the Generation of Animals* [5]) about the development of chicken embryos in the egg. Invention of the microscope lead to the discovery that all organisms are made of cells which grow and divide. Robert Koch discovered that microorganisms of roughly the same size as cells are the cause of infectious diseases [6], underlining the medical importance of microbiology. Roughly half a century later, Alexander Fleming described with penicillin the first antibiotic attacking the growth mechanism of bacteria [7]. Today, the study of growth is a multidisciplinary endeavor at the interface between biology and related biosciences: biophysics, biochemistry, bioengineering, bioinformatics to name just a few. Dependent on scientific background, chosen field and personal motivation, scientists may strive for very different goals and with varying approaches. “Classical” biologists may investigate functional properties, such as which evolutionary benefit an organisms achieves by growing in a certain form. A physician may study microbioma to discover new agents blocking multiplication of infectious microorganisms or to understand how misregulation of tissue growth gives rise to cancer. A bioengineer may see in a microorganism a producer of proteins, enzymes, drugs (e.g. insulin), or food (dairy industry) and wants to optimize bacterial growth to achieve a better ratio between feeding medium input and amount of produced output. All these objects of study have in common that they are subject to the laws of physics. The physicist thus contributes to these questions by applying his knowledge about physical laws of nature to aid in the development of models of the underlying physical process. The key challenge is often to reduce the many degrees of freedom of extremely complex living systems to a minimum set of variables necessary to describe experimental observations accurately. Growing systems represent a form of active matter as cells grow and divide under constant energy supply and are thus permanently out of thermodynamic equilibrium. An early pioneer advocating for physical modeling of growth phenomena was D’Arcy Wentworth Thompson with his work *On Growth and Form*, first published in 1917 [8]. Thompson was startled how life forms develop highly ordered patterns such as hexagonal cells in plant tissues or bee hives, the twisted and evenly ridged antlers of goats or the various shapes of spiral seashells (see fig. 1.1 a)-b)). Hundred years later, the question of morphogenesis (from Greek, “creation of the shape”), i.e. how the regulation of growth leads to the particular pattern or structure of a tissue or organ, remains a topic of current research. Recent studies investigate, for example, the formation of complicated structures such as brain folds [9], ordered patterns of hair or feather follicles [10], or the fractal, self-similar structures of bacteria growing on agar plates [11, 12] (see fig. 1.1 c)-f)). From a medical perspective, understanding growth mechanisms comprises a key topic in the treatment of ailments related to disturbed growth regulation such as cancer.

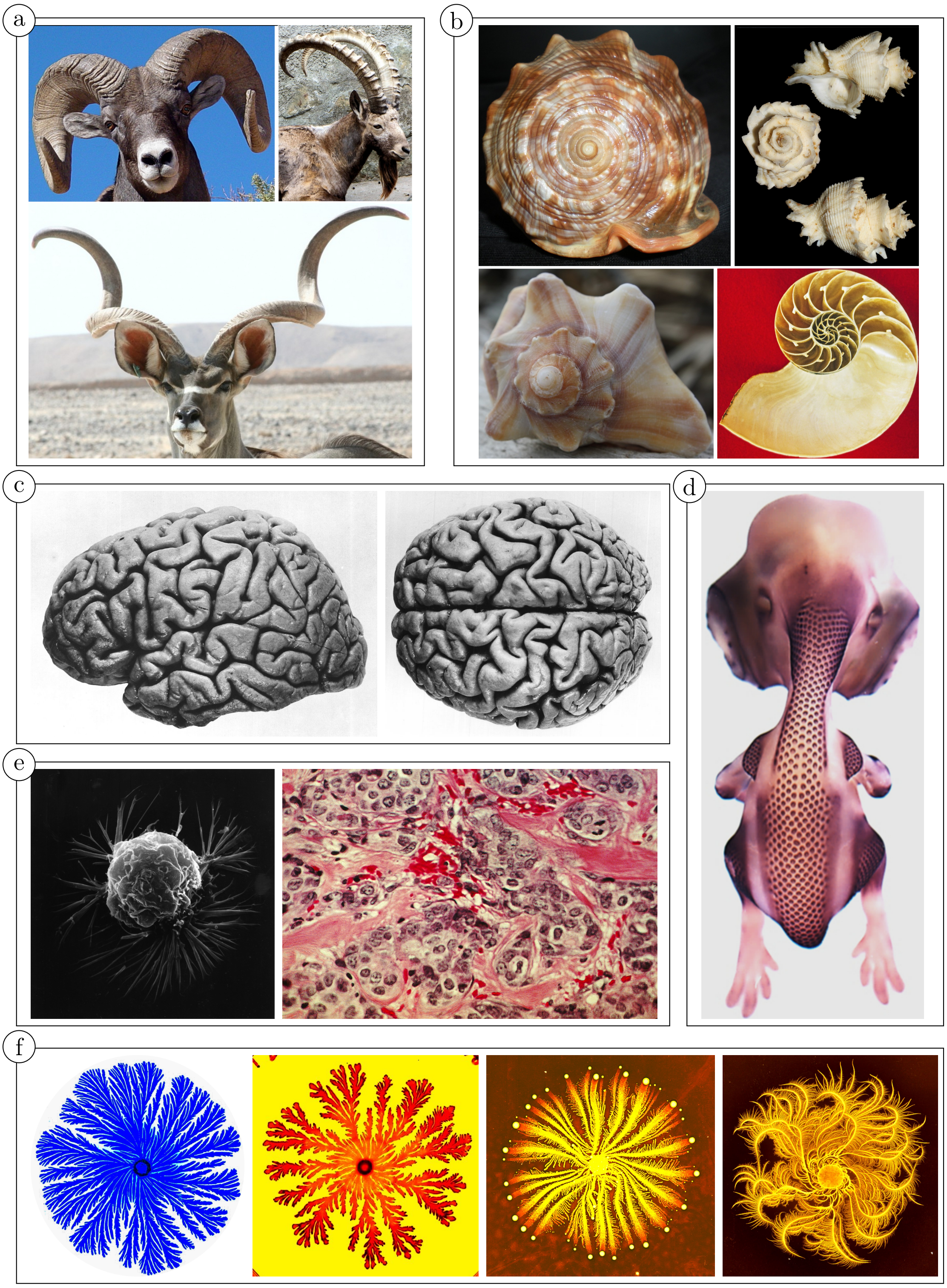
a
b
c
d
e
f

FIGURE 1.1. (previous page) **a)** Horns of sheep, goats or antelopes grow in various curves, with or without twist, with smooth or ridged surface. **b)** Spiral seashells occur with different spiral radii, smooth surfaces, with even or irregular ridges. Images from a)-b) have been released to public domain on `pxhere.com`. **c)** Brain of an adult human with typical folding pattern [13]. **d)** View of a chicken embryo from the back. The purple speckles are regions of feather follicle formation which appear in an almost defect-free grid. Photo courtesy of The Roslin Institute Chicken Embryology group (RICE), The Roslin Institute, The University of Edinburgh [14]. Published under Creative Commons license. **e)** (left) A single breast cancer cell [15]. (right) Histological slide of cancerous breast tissue. Clusters of cancer cells (blueish-purple) invade healthy connective tissue (red and pink) [16]. Photographs have been published and made public domain by the National Cancer Institute, US Department of Health and Human Services. **f)** Colonies of bacteria of the genus *Paenibacillus* grow on agar plates in various forms and shapes. Photographs by Eshel Ben-Jacob, Tel-Aviv University, published under Creative Commons license [17].

Of the many biological systems which offer interesting growth phenomena to study, we focus in this work on systems of a particular geometry: cells growing in thin sheets. In nature, this category already contains a broad variety of systems such as epithelial tissues forming human gut folds, the wings of the common fruit fly, sea shells or the various forms of plant leaves to name just a few. Furthermore, in experiments, the growth of microorganisms like bacteria or fungi is often confined to a thin layer to ease observation. As the detailed growth mechanisms are often unknown, different hypotheses have to be verified by comparison of their results with experimental evidence. The regulation mechanisms studied in this work can be grouped in two classes:

Biochemical factors such as the availability of nutrients or growth factors are of major importance for growth regulation in all living beings, ranging from colonies of microorganisms to tissues of multicellular organisms. For example, if we think of a bacterial colony or a cancer metastasis in a host tissue which need nutrients to grow and multiply, its fate depends on questions like: *How much nutrients does a cell need to survive? What is the relation between nutrient uptake and growth rate? How are nutrients transported to/in the colony or the tumor? How do the cells react to a deficit of nutrients? How does it compete with other microorganisms or the host tissue?* Investigation of these questions involves several fields of physics; hydrodynamics governs nutrient transport, statistical mechanics and thermodynamics nutrient metabolism.

Mechanical interactions between cells are thought to regulate growth in various manners. For example, epithelial cell sheets grow stress-dependent [18, 19], undergo apoptosis (programmed cell death, from ancient Greek "falling off") if their adhesion to neighbors is disrupted [20], and control elastic parameters like the spontaneous curvature [21] to structurize morphogenesis. Other examples include plant cells which react to external forces such as gravity or wind, the latter leading to the formation of stress wood in tress [22, 23]. Combinations of these mechanical influences are thought to play a crucial role, for example, in embryonic morphogenesis of the drosophila larvae [24, 25], the mammalian intestine [26, 27], human brain foldings [9] as well as in the ability of a cancer metastasis to invade the host tissue [19, 28]. If we think of a morphogenetic process, e.g. tissue folding during brain development, questions of importance are, for example: *What are the elastic parameters, like the bending rigidity, of the tissue sheet? Is growth itself pressure dependent, and if so, how? How* *does growth activity influence buckling dynamics?* Model construction for these phenomena starts from classical elasticity theory, extended by terms to describe growth activity. Often, a coupling of biochemical factors and mechanical interactions needs to be taken into account for a proper description. For example, diffusing growth factors are mandatory for epithelial growth, which in turn generates and depends on mechanical forces. Signaling molecules induce the generation of mechanical forces that rearrange tissues in development. In bacterial colonies, quorum sensing, i.e. the perception of the density of bacteria via the release of special messengers (so-called autoinducers), coordinates release of extracellular polymeric substances which in turn “glues” the bacteria together, changing the viscosity of the colony.

Structure of this Thesis

In this work, we explore two specific examples for growth regulation and pattern formation of thin cell sheets within one unified simulation framework. First, we investigate how mechanical feedback on growth results in buckling patterns of growing membranes. Second, we study how growth is regulated by nutrient limitation in microfluidic experiments of growing bacterial colonies of the species *Corynebacterium glutamicum*. The first project comprises a theoretical study employing simulations and analytical methods whereas the latter project aims for a quantitatively exact description of experimental observations.

We outline the content of this work in the following. In chapter 2, we embed the modeling and simulation approaches used in both projects into the broader context of current research. We recapitulate general properties of growth regulation and patterning mechanisms and discuss representative state-of-the-art models to illustrate general theoretical concepts.

The simulation framework this work is based on, its parameters and properties as known from the literature, is introduced in chapter 3. Our simulation consists of a coarse-grained particle-based technique where a particle may be interpreted as a single cell or a small patch of tissue, dependent on the context. The simulation follows a minimalistic approach where we only incorporate the relevant degrees of freedom in a simple manner.

In chapter 4, we analyze the buckling of monolayered tissues embedded in a dissipative medium. We demonstrate how pressure dependent growth leads to buckling with a characteristic wavenumber k much larger than the system-spanning mode $k = 2\pi/L$, where L denotes the system size. This behavior deviates from the classical quasi-static Euler instability which predicts buckling at the system-spanning mode $k = 2\pi/L$. We show that explicit buckling dynamics need to be considered to understand this phenomenon. In particular, the timescales of growth and membrane deformation play a crucial role in wavenumber determination.

Chapter 5 investigates the role of nutrient feedback on the growth of bacteria of the species *C. glutamicum*. We develop a simple reaction-diffusion-type model of nutrient dynamics which we incorporate in the simulations. Model and simulations are then compared with microfluidic experiments of growing bacteria in limiting nutrient conditions. In this way, we develop a standard protocol to estimate growth parameters in microfluidic devices. Moreover, we can show that nutrient gradients occur already for bacterial colonies of only a few thousand individuals and need to be considered in experiment design and interpretation. We achieve quantitative match between colony spreading in simulation and experiment, demonstrating that our coarse-grained model is precise enough to yield accurate predictions.

These steps bring together novel aspects of growth regulation into one framework. In chapter 6, we conclude our work by summarizing what we found, and providing an outlook of what is to come.

CHAPTER 2

General Properties of Growth Regulation

A common feature of all growth models is that they define a measure for the "amount of biomass", e.g. the number N of individuals. This number may increase or decrease over time, measured by the growth rate k_g. Biological systems have the property that, on average, every individual itself is able to grow and reproduce itself to produce offspring. The growth rate k_g is therefore often defined per individual. With this definition, the net change rate $\frac{dN}{dt}$ of the entire population reads:

$$\frac{dN}{dt} = k_g N. \tag{2.1}$$

In presence of constant environmental conditions, ecosystems on all scales tend to approach a state where the number of individuals fluctuates around a constant mean value. From a modeling perspective, the key task is to identify the functional dependence of the growth rate k_g on environmental variables which leads to the growth regulation maintaining the observed state. In the simplest case, k_g is a positive constant, not subject to any regulation mechanism, which leads to exponential increase of the population $N \propto \exp(k_g t)$ with time. Unregulated exponential growth occurs seldom in nature on long timescales, as the optimal conditions necessary for a constant growth rate can only be maintained for a limited number of individuals. Hence, a simple regulatory mechanism is the finite resource input into the habitat which can only sustain a finite number of resource consumers. We describe this limitation by a capacity variable K. If the number of individuals N exceeds K, starvation and death decrease N until it is again below K. An adapted growth equation which takes into account a finite habitat capacity K is referred to as *logistic equation*

$$\frac{dN}{dt} = r\left(1 - \frac{N}{K}\right) N, \tag{2.2}$$

with a growth rate dependent on the current number of individuals

$$k_g = r\left(1 - \frac{N}{K}\right), \tag{2.3}$$

with the maximum growth rate r. The analytic solution for any positive initial number $N_0 = N(t = 0)$ is given by

$$N(t) = \frac{K N_0 e^{rt}}{K + N_0 \left(e^{rt} - 1\right)}. \tag{2.4}$$

For small $N \ll K$ growth is still exponential $N \propto \exp(rt)$. As soon as N and K are of comparable magnitude, the total number of individuals starts to saturate and converges asymptotically to $N \overset{t\to\infty}{\longrightarrow} K$. The convergence towards $N = K$ is independent of the initial number N_0, for $N > K$ the growth rate is negative, i.e. individuals are dying or leaving the population until N drops below K. Even though very simple, the logistic growth model has been used successfully to describe population dynamics for a variety of species, e.g. yeast [29], African elephants [30] or Peruvian anchovies [31]; models based on logistic growth are still in use [32].

2.1. Growth Kinetics - Biochemical and Mechanic Regulation

On the scale of bacterial colonies or cell tissues, cell growth reacts to local mechanical or biochemical stimuli such as the pressure or the concentration of nutrients, growth factors, messenger substances or toxins (for example antibiotics in case of bacteria). Some of these stimuli play also a role in intercell communication pathways such as, for example, quorum sensing in bacteria [33] or mechanotransduction in tissues [34, 35]. Quorum sensing denotes the ability of bacteria to sense the local population density via the expression of special messengers, so-called autoinducers. Mechanotransduction in tissue cells defines the transformation of mechanical signals, received via the cytoskeleton, into biochemical messages. The carrier medium for both nutrient and signal transport is often the aqueous medium the cells reside in. The response to a multitude of stimuli, all transferred via the aqueous medium simultaneously, renders the understanding of cell growth extremely difficult as cross-correlations between different pathways can never be ruled out. Owing to this complexity, the exact dependence of cell growth on biochemical and mechanical cues remains so far not understood as a whole. Therefore, physical models of growth often focus on a single influence on cell growth, e.g. the concentration of a limiting nutrient. In the following, some state of the art models are reviewed, either dependent on concentration of biochemical agents or external pressure. To model growth phenomena with spatial resolution, it is often useful to turn to a continuum description. In this case, growth enters the continuity equation as a source term

$$\frac{\partial \varrho}{\partial t} = k_g \varrho - \nabla \boldsymbol{j}, \tag{2.1.1}$$

where ϱ denotes the cell density, $\boldsymbol{j} = \varrho \boldsymbol{v}$ the cell flux with the flow field $\boldsymbol{v}$ and k_g the growth rate as before. The continuity equation (2.1.1) is the continuum equivalent to eq. (2.1).

2.1.1. Growth Regulation by Pressure. An example for pressure dependent mechanical regulation is the *homeostatic pressure model* [28]. Under constant biochemical conditions, the net growth rate depends only on the pressure p. The model introduces the homeostatic pressure p_h as the pressure at which division and apoptosis balance such that the growth rate is zero. Linear expansion of the growth rate around the homeostatic state reads

$$k_g = \xi \left(p_h - p\right) + \mathcal{O}\left(\left(p_h - p\right)^2\right), \tag{2.1.2}$$

with ξ being a tissue dependent pressure sensitivity parameter. For $p < p_h$, the growth rate k_g is positive and the tissue grows, whereas for $p > p_h$ apoptosis dominates such that $k_g < 0$ and the tissue shrinks. The assumption of tissue density linearly dependent on pressure, $\varrho \propto p + p_0$, leads to an equivalent form of eq. (2.1.2)

$$k_g = \widehat{\xi} \left(\varrho_h - \varrho\right) + \mathcal{O}\left(\left(\varrho_h - \varrho\right)^2\right), \tag{2.1.3}$$

in terms of the homeostatic density ϱ_h. In the competition of two tissues for the same finite volume, the key question is whether a faster growing tissue or a tissue with a larger homeostatic pressure will win? Remarkably, with a homeostatic pressure growth law as eq. 2.1.2, the tissue with the higher homeostatic pressure always wins the competition [28],

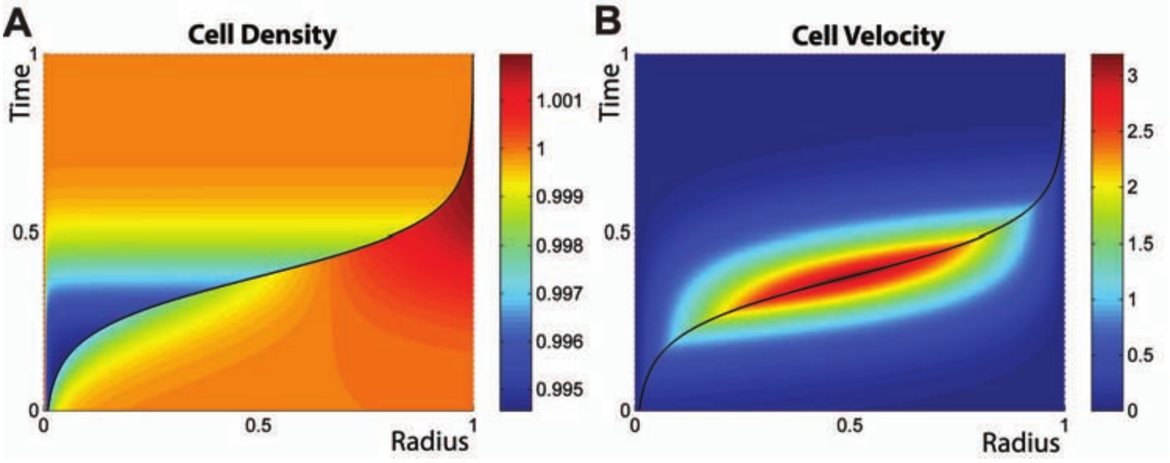

FIGURE 2.1. Kymograph of a competition simulation between two tissues with different homeostatic pressure in spherical geometry. Initially, a tissue with larger homeostatic pressure occupies a small sphere inside a continuum of the other tissue. The black line depicts the sphere radius as a function of time, the color scale density (A) and velocity (B) during growth. From [28].

independent of the initial distribution of the two tissues or their growth timescales. This can be understood easily with a simple thought experiment: Imagine a single cell of the tissue type l with large homeostatic pressure p_h^l inside a tissue of type s with a smaller homeostatic pressure $p_h^s < p_h^l$. Independent of the initial configuration, the s-tissue evolves towards its homeostatic state characterized by zero net growth and a pressure equal the homeostatic pressure p_h^s. However, the single cell of type l can then always grow at the expense of tissue s because for $p = p_h^s < p_h^l$ its growth rate is positive. Thus, over time the l-tissue takes over the whole compartment. Hence, in case of tumor growth, a single mutated tumor cell may give rise to a macroscopic tumor if its homeostatic pressure is larger than the homeostatic pressure of the surrounding healthy tissue. Numerical analysis of a continuum model of this case for a spherical tumor which grows inside a compartment filled with healthy tissue indeed shows that the tumor will take over the whole available space [28] (see fig. 2.1). Furthermore, tumor size over time exhibits a sigmoidal relationship which has also been found in experiments [36].

In the context of simulation techniques, the *two particle growth model* (abbreviated 2PG-model) is an example for a simulation framework which incorporates pressure dependent growth [37] (see section 3.1). A combination of the 2PG-technique with experiments of tumor spheroids grown in an embedding substrate successfully explains their growth behavior under pressure [19]. The experiments show that tumor spheroids grow slower under the influence of a moderate external pressure and, in particular, that this pressure dependent growth is *reversible*: as soon as external pressure is released, the spheroids grow to the same size as the unpressurized control group. Remarkably, a comparison of tumor spheroid growth with a two-rate growth model, which assumes a bulk growth rate k_b in the center and a larger growth rate $k_b + \delta k_s$ in a thin surface layer, suggests that the net bulk growth rate k_b is *negative*, i.e. more cells are dying than dividing. The stability of the dying core is maintained by a constant flux of cells from the boundary layer to the center. This finding leads to the question whether such a steady state, where a positive growth rate at the surface compensates a negative growth rate in the center, is also possible for a freely growing tissue spheroid? A simulation study suggests that this is indeed possible in case of a negative homeostatic pressure, i.e. a tissue that is under tension in its homeostatic state [38]. At first glance, a freely growing tissue with negative homeostatic pressure seems to be unstable, since the growth rate is negative for zero external pressure. However, simulations show that cells at the free boundary of the tissue can still maintain positive growth rates, even though the bulk homeostatic pressure is negative. Cells at the surface of the tissue need less deformation energy to grow, due to the free boundary, than cells in the bulk tissue. In a certain window of simulation parameters, the larger surface growth is able to compensate for the net loss of cells in the bulk tissue and results in the aforementioned steady state at a well-defined spheroid radius. Comparison of net bulk growth rates in simulations with experimental measurements for five different cell lines suggests that at least four of them possess a negative homeostatic pressure [38]. It remains an open question which evolutionary advantage comes with a negative homeostatic pressure for a tissue, apart from a natural control of compartment size.

2.1.2. Transport of Biochemical Agents. Any biochemical active molecule (such as nutrient, toxin or messenger molecules) needs to be transported to the cell before it can take effect. Transport of biochemical molecules occurs mostly by advection and diffusion in the aqueous medium. The pressure gradients in biological systems are often small compared to the compression modulus of water such that the water flow $\boldsymbol{v}_w$ can be assumed to be incompressible, i.e. $\nabla \boldsymbol{v}_w = 0$. The dynamics of the water flow is described by the Navier-Stokes equations; Studies of fluid flow in biological systems encompass, for example, flows of nutrients in the deep sea [39], transport in the bloodstream [40] or experiments in microfluidic devices [41, 42]. The transport dynamics of the concentration c of a biochemical agent follow by consideration of local mass conservation

$$\frac{\partial c}{\partial t} = -\nabla \boldsymbol{j}_c + P - U, \tag{2.1.4}$$

with the local flux $\boldsymbol{j}_c$ and the rates of production P and uptake U by the cells. The flux $\boldsymbol{j}_c$ consists of an advective term and a diffusive term with diffusion constant D

$$\boldsymbol{j}_c = c\boldsymbol{v}_w - D\nabla c. \tag{2.1.5}$$

Often, either the advective or the diffusive contribution of transport dominates. For a given lengthscale L, the timescales to cross this distance by advection or diffusion are

$$t_{adv} = \frac{L}{|\boldsymbol{v}_w|}, \qquad t_{\mathit{diff}} = \frac{L^2}{D}; \tag{2.1.6}$$

the smaller the timescale the larger the contribution. The fraction $t_{\mathit{diff}}/t_{adv}$ defines the dimensionless Péclet number:

$$Pe = \frac{L\,|\boldsymbol{v}_w|}{D}. \tag{2.1.7}$$

For $Pe \ll 1$ transport is mostly diffusive, for $Pe \gg 1$ mostly advective. Hence, diffusion always dominates on lengthscales $L \ll D/|\boldsymbol{v}_w|$ and advection on large lengthscales. For molecules diffusing from an external source into a cell aggregate where they are consumed, the ratio between uptake and diffusion constant determines the diffusion limitation lengthscale l_c. The lengthscale l_c estimates on which distance the concentration decays inside the aggregate.

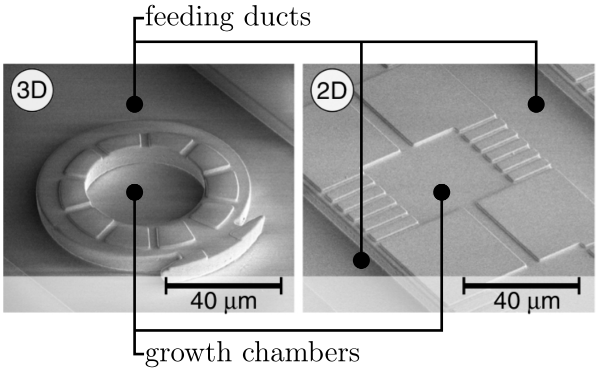

FIGURE 2.2. Microscopic images of two growth chamber geometries with surrounding feeding ducts. Colonies of microorganisms grow inside the chambers, continuous flow in the feeding ducts ensures a constant chemical environment. In the left chamber geometry cells grow in multiple layers whereas the right chamber confines the cells into a quasi-two-dimensional monolayer which eases observation. From [45] (annotations of growth chambers and feeding ducts have been added).

For example, in one dimension with linear uptake $U = u_0 c$, eq. (2.1.4) has exponentially decaying solutions:

$$c(x) \propto \exp(\pm x/l_c) \text{ with } l_c = \sqrt{D/u_0}. \tag{2.1.8}$$

In the case of nutrient molecules, l_c determines up to which size of the cell aggregate purely diffusive transport is sufficient to supply every cell with nutrients. For example, since carcinoma cells die without constant nutrient supply, the size of non-vascularized carcinoma is constrained to 1-2 mm owing to diffusion limited nutrient transport [43, 44]. In general, a large diffusion constant of a nutrient molecule is beneficial for the growth of larger aggregates or colonies. We conclude this section with a few examples for transport in biological systems and corresponding estimates of the Péclet number.

Microfluidic Experiments. Analysis of the transport dynamics of biochemical compounds is of major importance for the design of microfluidic experiments. In these experiments, growth and behavior of microorganisms are observed in chambers with typical dimensions in the range of a few 10 µm (see fig. 2.2). Dependent on the chamber geometry, cells grow in several layers or are confined to a quasi-two-dimensional monolayer which eases distinction of different cells. The chambers are supplied via feeding ducts with a controlled flow of a nutrient solution. The walls of chambers and ducts consist typically of polydimethylsiloxane (abbreviated PDMS) glued on top of a transparent glass plate, for details of fabrication see e.g. [46, 47]. A microfluidic chip consists of an array of many growth chambers connected by one or more feeding ducts. Growth dynamics is observed typically via an optical microscope which moves periodically along the chip and scans chamber per chamber. Microfluidic cultivation experiments have the advantage that they are easy to parallelize and allow the observation of microbial behavior in a controlled chemical environment, determined by the fed nutrient solution [45]. Often, it is desirable to design chamber and duct dimensions such that nutrient transport is mostly advective in the ducts. Advective transport via a laminar flow ensures that (1) no large concentration gradient builds up due to nutrient consumption along the stream and (2) waste products do not accumulate. However, large flow velocities inside the growth chambers are often undesirable as microorganisms may be flushed out of the chamber. Thus, ducts and chambers are often connected via very narrow and flat channels to suppress propagation of the laminar flow into the chamber. A numerical study suggests Péclet numbers

around $Pe < 0.1$ in the growth chambers and $Pe \approx 10$ in the feeding ducts for a chamber-duct geometry similar to the ones depicted in fig. 2.2 [41].
Volvox carteri. The multicellular green algae *Volvox carteri* consists of flagellated cells which form a spherical-shell-shaped body. The cells generate a flow field in the vicinity of the sphere via beating of their flagella. Measurements estimate the Péclet numbers of this flow field to be around $Pe \approx 100 - 300$ [48], thus, nutrient transport is almost entirely advective. Theoretical arguments indicate that advective transport is necessary for spherical-shell-shaped organisms such as *V. carteri* to grow above a certain size [48]. The diffusive nutrient flux I_d into the spherical shell grows linear with the sphere radius, i.e. $I_d = 4\pi D R c_\infty$; c_∞ denotes the concentration far from the colony. However, if the nutrient demand per shell area β is constant, the total nutrient demand $I_m = 4\pi R^2 \beta$ grows quadratically with radius. Thus, purely diffusive transport leads to a bottleneck radius $R_b = Dc_\infty/\beta$ up to which the organism can grow [48]. However, with advective contributions as generated by *V. carteri*, the nutrient absorption flux scales quadratically in R; sufficient to overcome the bottleneck radius [48].
Blood Sugar. In animals, nutrient transport can be divided into two stages: advective transport in the blood and diffusion from the vessels to the individual cells. For example, consider transport of glucose from the intestine via the bloodstream to the limbs: The lengthscale is $L \approx 1m$ for an adult human, flow velocities in arteria are typically on the order of $10\,\mathrm{cm\,s^{-1}}$[49], the diffusion constant of glucose is on the order of $500\,\mu\mathrm{m}^2/\mathrm{s}$, hence $Pe \approx 2 \cdot 10^8$. After passage through the blood vessel walls into the interstitial fluid, velocity drops to almost zero $\boldsymbol{v}_w \approx \mathbf{0}$ and hence $Pe \approx 0$, transport is mostly diffusive.

2.1.3. Growth Regulation by Biochemical Agents.

Models for two biochemical agents which regulate growth are presented in the following: nutrients and antibiotics.

Nutrients. Models which describe the nutrient dependency of cell growth often share the common assumption that the growth rate can be written as a function of the local nutrient concentration $k = k(c)$. Hereby, the nutrient concentration c is assumed to be the limiting reactant of the biochemical reaction network which sustains growth. Furthermore, it is assumed that uptake and replenishment of internal stores happen on a timescale much shorter than the timescale of growth such that the growth rate depends effectively on the instantaneous concentration.

Dependent on the modeling approach, these basic assumptions are implemented in different ways. As a first example, we present a *cellular automata* model to qualitatively describe biofilm growth in presence of an external shear flow [50]. This system resembles growing biofilms in the river bed of a slowly flowing river. Space is divided into a rectangular grid of lattice sites which are either free or occupied by cells. The nutrient concentration is assumed to be constant at free sites which have at least a distance d_B to the next occupied site, transport in all other sites is purely diffusive. The boundary layer thickness d_B models the transition from advective to diffusive transport in a boundary layer of the biofilm. Note that the boundary layer thickness can be interpreted as an offset to subtract from the diffusion limitation length scale l_c, as diffusive transport dominates in the perimeter of the biofilm. The configuration is updated according to a set of stochastic rules. Every cell divides with a probability

$$P_d = \frac{c}{c + \bar{c}}, \tag{2.1.9}$$

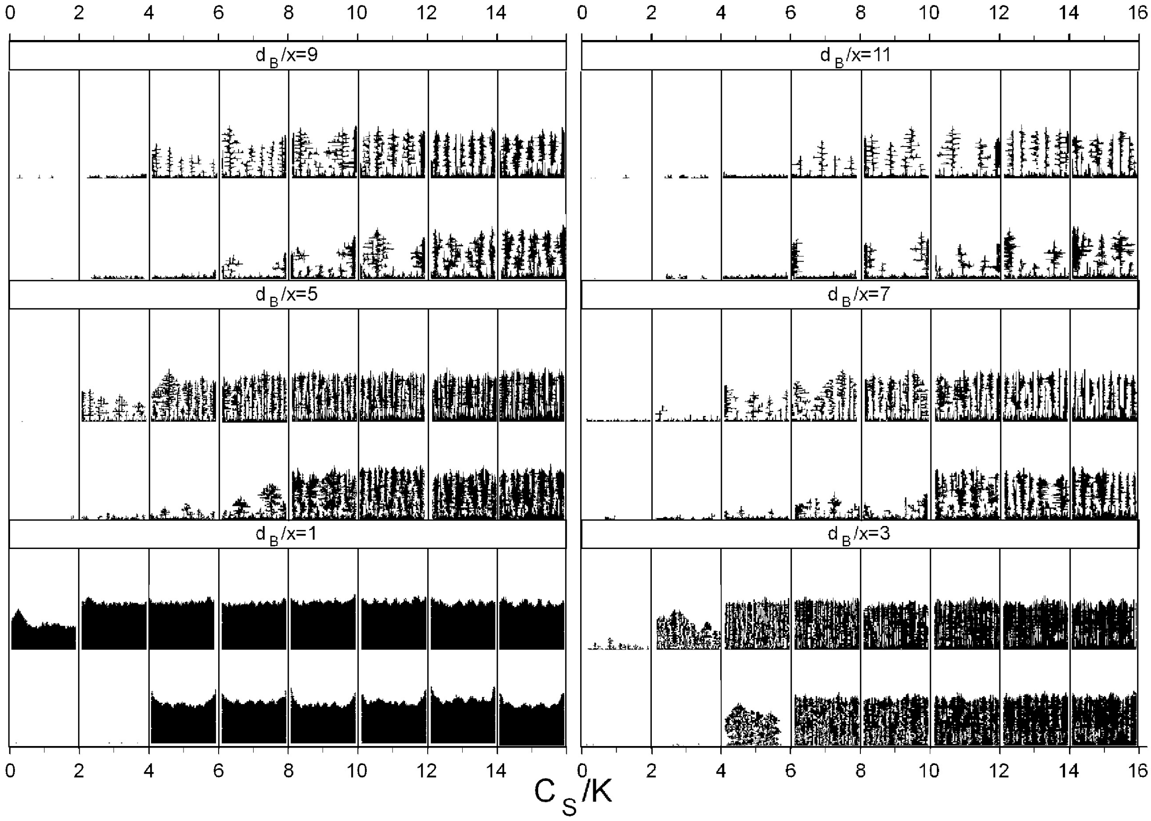

FIGURE 2.3. Various morphologies of biofilm growth from a cellular automata model [50]. In every row, the nutrient substrate concentration c_s increases from left to right, d_B denotes the diffusive boundary layer thickness. From [50].

dependent on the local nutrient concentration c and a parameter $\bar{c}$. Daughter cells are either placed in a free neighbor site or push the neighbor cell away which has the smallest distance to the nearest biomass/liquid interface. Cells at the biomass/liquid interface are subject to erosion and are removed with probability $P_e = 1/(1 + \sigma/\tau)$, the ratio σ/τ describes the ratio of cohesion versus shear forces. Although quite minimalistic, the model results in a variety of biofilm morphologies ranging from dense and compact films with a smooth interface for small boundary thickness d_B, to branched, dentritic shapes for large d_B (see fig. 2.3).

The transition from a smooth biofilm interface to branched configurations is a well-known observation in experiments and is subject of many theoretical studies. Dependent on experimental conditions, such as growth medium and bacterial stem, different mechanisms are thought to be responsible for the branching transition.

For *Bacillus subtilis* grown on agar plates, a combination of nutrient-limitation and motility comprises a possible mechanism to explain the observed branching [51]. Experimental observations suggest that the flagellated bacterium moves on agar plates in a random-walk like fashion. The motility depends on the local nutrient concentration c and bacterial density ϱ; bacteria become non-motile if either c or ϱ are too low. Spreading of bacteria due to

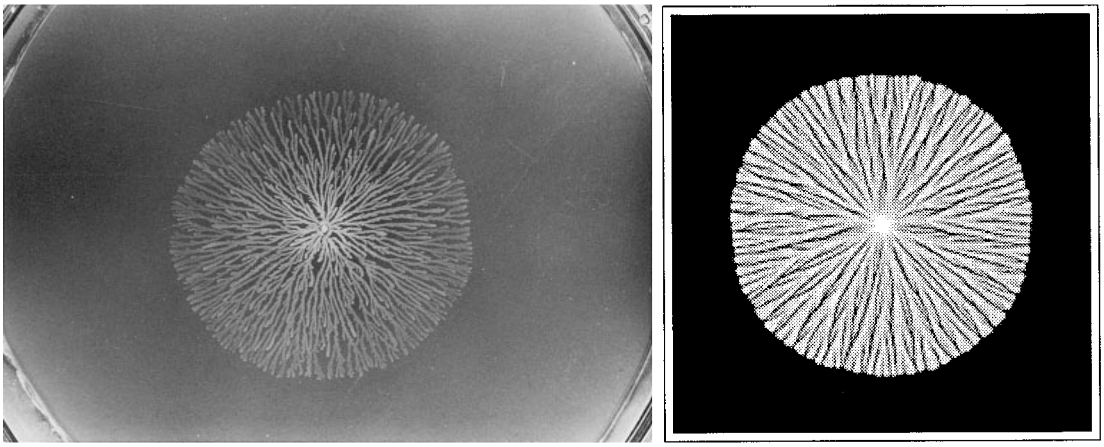

FIGURE 2.4. Densely branched morphology in an experiment with *Bacillus subtillis* grown on agarose (left) and in a reaction-diffusion simulation (right). From [51].

growth and motility can be modeled, for example, by a *reaction-diffusion* system [51]:

$$\begin{aligned}\frac{\partial c}{\partial t} &= D_n \Delta c - U(c,\varrho)\,,\\ \frac{\partial \varrho}{\partial t} &= \nabla\left(D_b\left(c,\varrho\right)\nabla\varrho\right) + \epsilon U(c,\varrho)\,,\end{aligned} \tag{2.1.10}$$

with D_n the diffusion constant of nutrients, D_b the diffusion constant of the random-walk like motility of bacteria and the nutrient uptake function U. The parameter ϵ can be thought of as a conversion efficiency from nutrients into biomass. Both D_b and U are functions of c and ϱ:

$$D_b = \sigma c \varrho, \quad \sigma = \sigma_0\left(1+\delta\right), \quad U = u_\infty \varrho c. \tag{2.1.11}$$

The parameters σ_0 and u_∞ are constants which define the magnitudes of motility and uptake, whereas δ is a random number independently chosen for every timestep and lattice side of the numerical discretization. The random number δ is added to introduce some form of stochasticity into the pattern formation. It is chosen from a triangular distribution supported by $[-\rho,\rho]$ with $0 \leq \rho \leq 1$. Comparison of numerical solutions with saturating uptake $U \propto c/(c+\bar{c})$ yield qualitatively similar results. The two-dimensional solution of the model exhibits a good qualitative agreement with shapes observed in experiments such as disc-like and densely-branched morphologies (see fig. 2.4). The transition from dense, but separate branches to a confluent disc occurs for high initial nutrient concentrations c_0 or large motility D_b. For small nutrient availability and low motility, non-circular patterns are observed and screening effects become visible: individual branches stop growth and do not reach the outer boundary anymore due to competition for nutrients with neighboring branches. Numerical solution of the one-dimensional version of model eqns. (2.1.10) allows for traveling wave solutions of the form $\varrho = \varrho(x - vt)$ with a velocity v close to the radial growth velocity of the branches observed in two dimensions. Approximation with the analytically solvable model

$$\frac{\partial \varrho}{\partial t} = \frac{\partial}{\partial x}\left(\sigma_0 c_0 \varrho \frac{\partial \varrho}{\partial x}\right) + c_0\varrho\left(1 - \frac{\varrho}{\epsilon c_0}\right) \tag{2.1.12}$$

which has traveling wave solutions with velocity

$$v = \frac{1}{\sqrt{2}} c_0^{3/2} \sigma_0^{1/2} \left(\frac{\epsilon}{D_n} \right)^{3/4} \qquad (2.1.13)$$

yields a good match with the wave velocities measured with the full model. Note the similarity of the production term in eq. (2.1.12) with the logistic growth rate in eq. (2.2). Model equation 2.1.12 with constant diffusion yields the *Fisher-Kolmogorov*-model, a continuous version of the logistic growth law. Above models include several assumptions often encountered in nutrient dependent growth models.

Growth proportional to nutrient uptake. The proportionality of the growth rate to the nutrient uptake assumes that all nutrients are directly available for growth activity. This implies that cells need only a negligible amount of nutrients for all other tasks of cell maintenance. Experimental evidence indicates that this is a good approximation for some bacterial stems like *Escherichia Coli* [52], whereas other stems require a portion of energy for cell maintenance [53]. Furthermore, it is often assumed that bacteria can survive without nutrients on typical experiment timescales. In contrast, tissue cells die quickly without nutrients such that their growth rate may even be negative for $c \approx 0$.

Monod-like kinetics. Both models use the Monod-kinetic growth rate of the form $k_g \propto c/(c + \bar{c})$. Owing to its simplicity, the Monod-relation between substrate concentration and growth rate enjoys an immense popularity and widespread use since its publication [52]. It can be motivated by consideration of Michaelis-Menten kinetics for a set of reactions with one limiting step which yields Monod-like expressions between substrate and product concentration in the steady state. However, this interpretation is usually too simple to describe the biochemical reactions which sustain growth such that Monod-kinetics may be viewed as a more phenomenological approach: under nutrient limitation growth is approximately proportional to substrate concentration and saturates in nutrient abundance.

Limitations of reaction-diffusion models occur in the implementation of elastic interactions and discrete stochastic events. For example, in the model eqns. (2.1.10) stochastic variations of motility are added in an *ad hoc* fashion. To overcome this caveats, *individual-based models* (abbreviated IBMs, sometimes also referred to as *autonomeous agent models*) were developed at the end of the 1990s [54]. In these models, the individual cells are explicitly modeled, often as rigid elastic bodies, whereas the nutrient solution is still represented by a continuous diffusion equation. For example, in ref. [12] an IBM is used to investigate the role of mechanical interactions in the branching transition. Here, every cell is represented by an extending rod of diameter d with spherical caps (see fig. 2.5). Nutrient diffusion and uptake are modeled by a reaction-diffusion system as in eq. (2.1.10), with a Monod-function for the uptake $U \propto u_\infty c/(c + \bar{c})$. The cells grow by elongation of the rod axis at a rate $v_{div} U(c)$ and split in half to yield two new cells at some critical length l_{div}. Elastic interaction between overlapping rods is modeled with a force $F = E d^{1/2} h^{3/2}$ where h denotes the overlap and the parameter E is proportional to the elastic modulus of the cells. This form of the force originates from Hertzian contact theory of elastic bodies [55]. Bacterial dynamics is assumed to be overdamped as a result of the background substrate friction force density $\boldsymbol{f}_b = -\mu \varrho \boldsymbol{v}$, with the cell velocity $\boldsymbol{v}$. Simulations exhibit a distinct branching (see fig. 2.5); The transition occurs if the dimensionless parameter

$$\beta = \frac{u_\infty \varrho_{cp} l_{div}}{c_0 v_{div}}, \qquad (2.1.14)$$

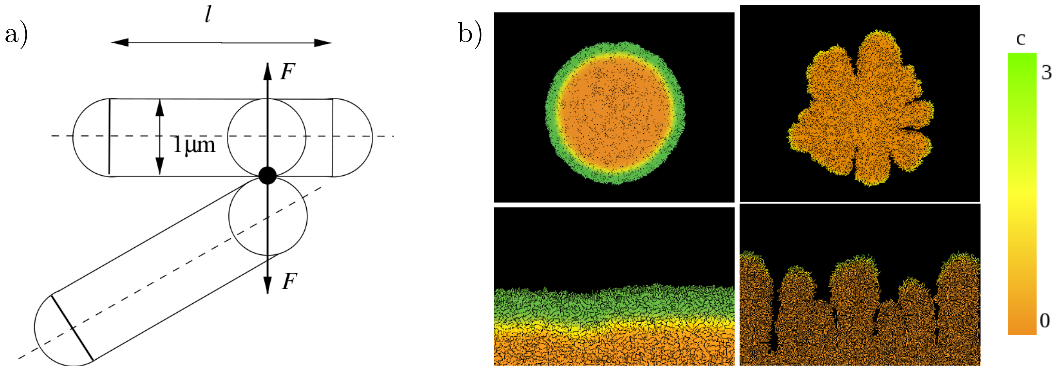

FIGURE 2.5. **a)** In the individual-based model of ref. [12], bacteria are represented as cylinders with spherical caps. During growth, the length l of the cylinder axis extends up to a threshold l_{div} at which the cell is divided into two daughter cells. The repulsive force F between different cells follows from the Hertzian contact theory of two touching spheres. **b)** Spreading of a cell colony starting from an uniform distribution along one axis (bottom panels) or from a single cell (top panels). Colorscale indicates level of nutrient concentration. In both configurations a branching instability occurs (right panels). From [12].

is close to unity. The parameter ϱ_{cp} denotes the close-packing density of the bacteria, c_0 the fed nutrient concentration which is kept constant in large distance to the colony. In contrast to the model eqns. 2.1.10, where branching occurs due to an interplay of nutrient diffusion and diffusive bacterial motility, here, the branching occurs only due to the growing rods mechanically pushing each other. Notably, the branching transition occurs *independently* of the nutrient diffusion constant. Furthermore, analysis of traveling wave solutions of model eqns. (2.1.10) without active bacterial motility suggests that no wavefront moving with constant velocity exists in the incompressible limit. However, both in experiments as well as in the simulation results of ref. [12], linear colony growth is observed which suggests that finite compressibility has to be taken into account. Moreover, analytical investigation of the traveling wave velocity of colony expansion due to purely mechanical interactions result in the estimate

$$v \approx \sqrt{\frac{EU(c_0)\, v_{div}}{\mu \varrho_{cp} l_{div}}}\,(1-\beta)^{3/4}\,, \tag{2.1.15}$$

which is again independent of the nutrient diffusion constant and exhibits a good agreement with simulations [12].

Antibiotics. Antibiotic drugs are since their discovery an important pillar of medical treatment. The spreading of antibiotic resistance has been labeled a serious threat by the world health organization [56]. Thus, understanding the mechanisms of action of antibiotics and the mutation pathways which lead to resistance is of pivotal importance. In the following, two examples of physical models are briefly introduced to illustrate insights into these questions from the physics perspective.

The first study suggests that the dose-response relationship of a major class of antibiotics cannot be viewed separately from nutrient availability, in fact, antibiotic efficacy is largely dependent on nutrient composition [57]. This dependence implies that clinical tests as well as

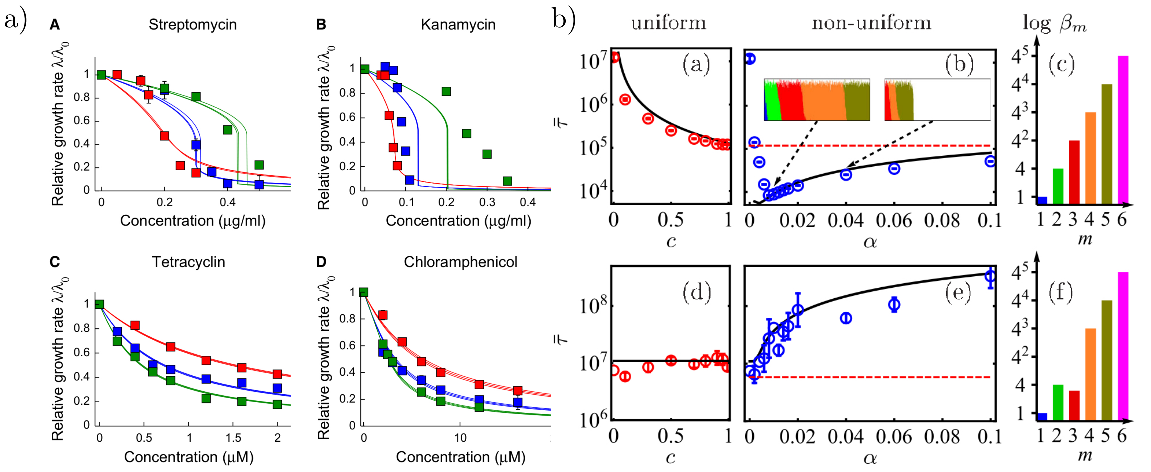

FIGURE 2.6. **a)** Growth rate of *Escherichia Coli* in presence of various concentration levels of four different ribosome-targeting antibiotics, relative to drug-free growth rate. Squares show measurements, lines fit with reaction kinetic model. Colors correspond to different growth media, with drug-free growth rate increasing in the order red-blue-green. Note the difference in efficacy between irreversible binding (A and B) and reversible binding antibiotics (C and D), dependent on the drug-free growth rate. From [57]. **b)** Dependent on the mutational pathway m which leads to increasing resistance β_m, (c) monotonic increasing resistance or (f) pathway with a fitness valley, the mean time $\bar{\tau}$ to result in the maximal resistant mutation is either shorter (monotonic increasing resistance) or longer (fitness valley) if a spatial drug gradient of the form $c(x) = \exp(\alpha x) - 1$ is present ((b) and (e)), compared to an uniform drug distribution ((a) and (d)). From [58].

physical models have to carefully consider the pair of nutrient substrate and antibiotic they investigate. Antibiotics diminish the growth of bacterial populations via various pathways, e.g. by destroying the cell membrane, impairing enzymes or perturbing the protein synthesis [59]. The coupling between antibiotic efficacy and nutrient composition arises indirectly via their involvement in protein synthesis. A major class of antibiotics targets the *ribosomes*, cell organelles which translate genetic information into proteins, to disrupt the protein synthesis and stop growth. These substances block ribosome activity by directly binding to them, the degree of reversibility varies among substances. The number of ribosomes per cell is in turn positively correlated with the growth rate which itself depends on the nutrient medium composition [60]. The correlation between growth rate and ribosome concentration can be understood intuitively: the faster a cell grows, the more protein factories are necessary to provide the cell's building blocks. Reference [57] establishes the link between growth rate and antibiotics by combination of mechanistic antibiotic-ribosome reaction kinetics and empirical relations between growth rate and ribosome concentration. This results in a comparably simple growth model which consists of a few reaction equations for the concentration of nutrients, antibiotics and ribosomes. Nevertheless, the model successfully captures the relationship between relative growth rate reduction and antibiotic concentration for various nutrient-antibiotic pairs (see fig. 2.6). Furthermore, it predicts that reversible ribosome-targeting antibiotics suppress better fast-growing infections whereas slow-growing infections should be treated with irreversible binding antibiotics.

As a second example, we take a look at the role of drug gradients for the evolution of resistances [58]. The response of cells to concentration gradients differs strongly for nutrients and antibiotics due to the occurrence of *resistance*. Drug gradients in tissues or cell aggregates arise, as in case of nutrients, due to diffusive limitation of transport. Nutrient gradients directly translate to gradients in growth rate. In contrast, a much more complex response to drug gradients has been found if mutations lead to resistance [58]. Drug resistances can arise due to random mutations of cells in a population. Whenever a single cell mutates to a more resistant strain, it has a growth advantage in presence of the drug and its offspring may take over the population. In this manner, presence of drugs benefits subsequent mutations which lead to increasing drug resistance. Due to its randomness, a mutation may also be neutral or decrease the resistance of the cell. In this case, a cell may first mutate into an intermediate, less resistant strain, before it acquires more resistant traits. Reference [58] analyses these "fitness valleys" in the context of drug gradients within a discrete reaction-diffusion framework. Cells populate a set of L microhabitats with different drug concentrations and are allowed to diffuse between habitats. Every habitat has a finite capacity K to which cell growth couples in a logistic manner as in eq. (2.2). Furthermore, cell growth decreases with increasing drug concentration until growth stops. Cells acquire resistance by moving stochastically between M different genotypes with varying resistance. Increasing resistance is defined as smaller decrease in growth rate in presence of the drug. Two different mutational pathways have been analyzed in presence of a drug gradient: a set of continuously increasing resistant mutants and another set of mutations with a fitness valley. Even though the model is quite minimalistic, the findings suggest a complex interplay between drug resistance pathways and drug gradients: whereas drug gradients accelerated the evolution to the maximum resistant genotype in the case of the continuously increasing mutational pathway, the opposite was true for the pathway in which cells have to pass through a fitness valley (see fig. 2.6).

2.2. Patterning Models for Tissue Morphogenesis

Biochemical and mechanical regulation mechanisms of growth play an important role in all aspects of self-organized tissue morphogenesis which determine tissue shape, size and patterning. Owing to the manifold mechanisms which regulate growth, morphogenetic models may be constructed from a vast toolbox of physical mechanisms. Often, these mechanisms are coupled and structures evolve due to the interplay of mechanic and biochemical cues. To elucidate tissue patterning mechanisms, models based on biochemical agents and mechanical interactions are introduced.

Morphogens. A special class of messenger molecules, so-called morphogens, is known to direct growth pattern formation in developing tissues. Morphogens control cell behavior via the regulation of the expression of specific genes which results in a characteristic dose-response relationship: Cells which receive low levels of morphogens behave differently from cells which receive high levels. Examples where morphogens are thought to play a role include the digit/non-digit patterning during limb formation; Dependent on the local morphogen level, cells either form bones or undergo apoptosis [61]. Another example are periodic color patterns of animals such as the zebra fish [61]. Morphogen transport in tissues is diffusive, thus, patterns and shapes arise in a very similar fashion as in the reaction-diffusion models

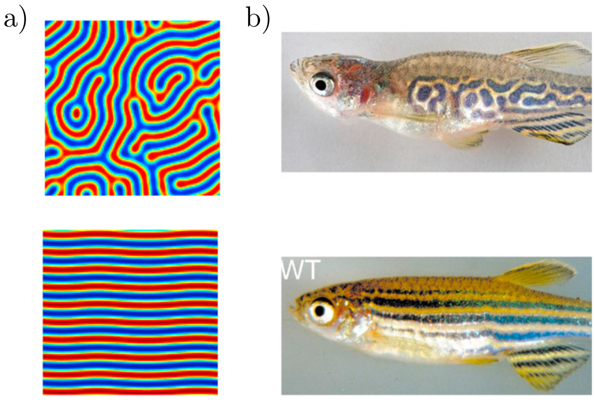

FIGURE 2.7. **a)** Turing patterns generated with the Swift-Hohenberg model. Top image shows labyrinth patterns which evolve with the isotropic model. Bottom image shows orientated patterns which occur if the symmetry is broken, e.g. by anisotropic diffusion. **b)** Zebrafish specimen, top the *choker* mutant with labyrinthine stripes in contrast to the orientated stripes of the wild type (bottom). From [61].

for nutrient dependent growth given in the previous section. The idea of morphogenetic structuring through reaction-diffusion systems was pioneered by Alan Turing in 1952 [62], the arising patterns are also referred to as *Turing patterns.* Morphogens are often modeled in a reaction-diffusion approach, the model principle can be summarized as local activation and long-range inhibition (abbreviated LALI). To illustrate the LALI-principle, we investigate the linear reaction-diffusion system [63]

$$\begin{aligned} \partial_t c_a &= D_a \partial_{xx} c_a + \alpha_a c_a - \beta_a c_i, \\ \partial_t c_i &= D_i \partial_{xx} c_i - \alpha_i c_i + \beta_i c_a \end{aligned} \tag{2.2.1}$$

of an activator concentration c_a and an inhibitor concentration c_i, all constants are positive. The activator facilitates production of both activator and inhibitor, whereas the inhibitor leads to decay of both substances. The system eqns. (2.2.1) exhibits an instability towards a spatially oscillating steady-state with wavenumber

$$k = \sqrt{\frac{1}{2}\left(\frac{\alpha_i}{D_i} - \frac{\alpha_a}{D_a}\right)}. \tag{2.2.2}$$

Note that the constants α_a/D_a and α_i/D_i are the squares of the substances diffusion limitation lengthscale, introduced in section 2.1.2. A necessary condition for the instability to occur is $\alpha_i/D_i > \alpha_a/D_a$, thus, the inhibitor has to decay on a *longer* length scale than the activator. Of course, the model equations 2.2.1 are only a simplified description of activator-inhibitor dynamics which lead to patterning and have to be refined by further knowledge about the detailed morphogen signaling pathways. However, since these pathways are in detail often not known, phenomenological models to study the principles of patterning mechanisms are of interest as well. For two-dimensional stripe pattern generation, the *Swift-Hohenberg equation*

$$\partial_t \Phi(x, y, t) = a\Phi - ab\left(1 + 2l^2\Delta + l^4\Delta\Delta\right)\Phi - d\Phi^3, \tag{2.2.3}$$

comprises a minimal qualitative model to understand stripe formation in a variety of contexts [61, 63]. It is motivated by general aspects of periodic pattern phenomenology [61]. Dependent on the sign of the parameter $r = a/3d$ the steady-state is either uniform ($r < 0$) or evolves periodic, labyrinth-like patterns ($r > 0$) with a typical lengthscale l (see fig. 2.7). The labyrinth patterns can be understood as a superposition of many randomly orientated stripes. To orient the stripes in a certain direction, the symmetry of the isotropic Swift-Hohenberg equation has to be broken. Reference [61] shows that either a gradient in Φ-production (by adding a source term $P(x)$), a gradient in the parameters or introduction of anisotropy leads to a stable orientation of the stripes. Furthermore, the hereby demonstrated orientation mechanisms where consistently reproduced in several, more complicated patterning models [61]. In conclusion, the Swift-Hohenberg equation appeals through its simplicity and a certain generality, as mechanisms of more complicated models can be mapped onto it [61].

Elastic Instabilities. Regular patterns in elastic materials can also be created by induction of elastic instabilities through mechanical stress. Historically, elastic instabilities have been studied in the context of large structures, such as buildings, bridges or ships, where they are in general undesirable. Today, they are induced on purpose in technical applications, for example to yield patterning of thin polymer films [64]. In the context of morphogenesis, a proposed mechanism which leads to regular structured instabilities is the *mismatch stress* or *differential growth* hypothesis [65]. This hypothesis is based on the observation that many biological structures consist of multiple layers with distinct properties, e.g. monolayered epithelial cell sheets on top of stroma tissue or gray and white matter in the brain. A lateral differential in the growth rates of two adjacent layers results in a residual mismatch stress which deforms the tissue. An illustrative example of this principle are bimetallic strip thermometers: If two strips of metals with different thermal expansion coefficients are welded together, the strip deforms upon heating due to the length difference between the two strips. We elucidate this mechanism with a simple model: a thin, growing membrane, bonded on one side to a passive linear elastic substrate (see fig. 2.8). The critical surface tension at which the first finite wavenumber becomes unstable is

$$\gamma^{c,\widehat{E}} = -3\left(\frac{1}{4}\kappa\widehat{E}^2\right)^{\frac{1}{3}}, \tag{2.2.4}$$

where κ denotes the bending rigidity of the membrane and $\widehat{E}$ an effective elastic modulus of the linear elastic substrate. The effective modulus $\widehat{E}$ is equal to the Young's modulus E of the substrate times a constant depending on the Poisson ratio σ of the material. For $\sigma = 1/2$, i.e. a volume conserving material, it is $\widehat{E} = E/3$. The first unstable wavemode at $\gamma = \gamma^{c,\widehat{E}}$ is given by

$$k^{\widehat{E}}_{min} = \left(\frac{\widehat{E}}{2\kappa}\right)^{\frac{1}{3}}. \tag{2.2.5}$$

For stronger compressive stress $|\gamma| > |\gamma^{c,\widehat{E}}|$ the minimum energy wavemode shifts towards

$$k^{\widehat{E}}_{min} = \sqrt{\frac{2\,|\gamma|}{3\kappa}}\cos\left(\frac{\pi}{3} - \frac{1}{3}\arccos\left(\sqrt{\frac{27\kappa\widehat{E}^2}{8\,|\gamma|^3}}\right)\right) \tag{2.2.6}$$

with arccos(. . .) evaluated in the interval $[0, \pi]$. Note that critical buckling stress and wavenumber do not depend on the system size L which is an effect of the elastic substrate. Without elastic substrate, buckling occurs first at a critical stress $\gamma^c = \kappa\,(2\pi/L)^2$ for which the largest wavemode $k_{min} = 2\pi/L$ becomes unstable. In the limit of strong compression $\gamma \to -\infty$, minimum energy wavenumbers with and without elastic substrate scale both as $k \sim \sqrt{|\gamma|\,/(2\kappa)}$. From eqns. (2.2.4)-(2.2.6) it follows that the buckling wavenumber increases with increasing magnitude $|\gamma|$ of the surface tension and decreases with increasing κ or $\widehat{E}$.

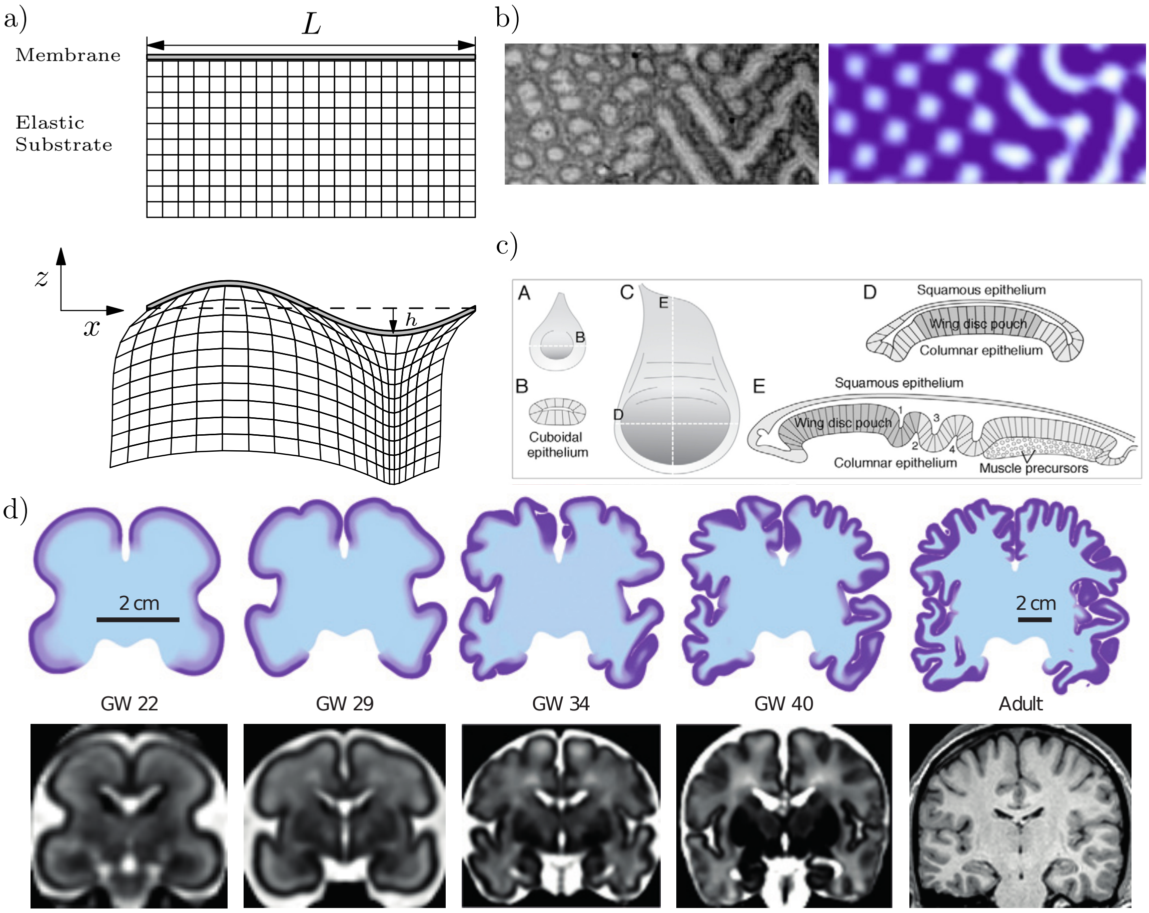
a)
L
Membrane
Elastic Substrate
z
x
h
b)
c)
A
B
B
Cuboidal epithelium
C
E
D
D
Squamous epithelium
Wing disc pouch
Columnar epithelium
E
Squamous epithelium
Wing disc pouch
1
2
3
4
Columnar epithelium
Muscle precursors
d)
2 cm
2 cm
GW 22
GW 29
GW 34
GW 40
Adult

FIGURE 2.8. **a)** A thin growing membrane bonded on top of an elastic substrate. **b)** Transition from a dot-like to a herring-bone buckling pattern *in vivo* (left, chicken gut) and *in silico* (right). Simulations suggest that this transition is caused by an increase in surface tension from left to right [26]. From [26] **c)** Development of *Drosophila melanogaster* wingdisc during second (A-B) and third (C-E) larval stage. The shape of the wing is thought to be modulated by spontaneous curvature changes of the epithelial cell sheets. From [25]. **d)** Development of human brain folding, in simulation (top) and experiment (bottom). In the simulation model, tangential growth rate of brain matter increases from blue to purple. From [9].

Models based on the differential growth mechanism are used, for example, to describe the folding patterns in the gut [26, 27] or the brain [9] (see fig. 2.8). Whereas the mechanism, in principle, stays the same, models are refined to take into account specifics of the biological system. For example, in case of gut tissue [26], it is assumed that diffusing growth factors cause anisotropic growth in the lateral direction. In ref. [26] this is implemented heuristically by a growth term dependent on the local curvature, such that convex folds grow faster than concave ones.

The elastic energies related to bending, surface expansion and substrate deformation couple to different parameters of the wavepattern. Compressive stress $\gamma < 0$ favors larger surface area, the bending rigidity κ smaller curvature and the elastic substrate smaller deformation amplitude and slope. In tissues, the surface tension γ corresponds to the active growth stress which is exerted by the cells. The parameters κ and $\widehat{E}$ depend on the elasticity of cells and extracellular matrix which is determined by e.g. fibroblast activity. Thus, cell layers may achieve patterns with a characteristic wavelength by regulation of growth and/or elastic parameters of the tissue. In particular, apart from the differential growth model, tissues may also direct morphogenesis by imposing a spatial profile on elastic parameters. For example, spatial changes in bending rigidity are proposed as a morphogenetic mechanism, e.g. in seashells [66]. Here, the spatial pattern of the bending rigidity translates to the observed pattern of the membrane under compression, as softer regions buckle stronger than stiffer regions. Another example in this category are mechanisms based on local changes in the *spontaneous curvature* C_0 of a membrane. The spontaneous curvature C_0 defines a preferred local curvature radius. A free sheet of material with constant spontaneous curvature C_0 achieves its energetic minimum in a spherical conformation with radius $R = 1/C_0$. As epithelial tissues are inherently *polar*, with an apical and a basal side, they can change their shape through active apical constriction [21]. In a coarse-grained description, this can be interpreted as a local change of spontaneous curvature. In case of the drosophila wing disc formation, it has been found that the morphogen DPP is involved in local shape changes of the epithelial sheet, which, in turn, control the global shape of the wing [25]. Another example for spontaneous curvature directed morphogenesis is the invagination formed during gastrulation stage of embryonic development [67]. In contrast to the differential growth mechanism, changes in spontaneous curvature or bending rigidity do not require a layered tissue structure.

CHAPTER 3

Simulation Framework and Tissue Model

The simulation algorithm used in this work is based on the *two particle growth* model (abbreviated 2PG-model) mentioned in section 2.1.1. The implementation builds up on the parallelized C-code developed by Nils Podewitz during his doctorate studies [68]. It adapts the standard *dissipative particle dynamics* technique (abbreviated DPD-technique, see e.g. [69]) to model tissue growth in the framework of the homeostatic growth theory [28]. An extensive discussion of the 2PG-technique together with parameter measurements can be found in refs. [37, 68]; It has been used e.g. to study fluidization of tissues due to cell-turnover [70], the pressure dependency of tumor growth [19], cell motility [71], alignment of cell division during cell migration [72] and tensile homeostatic states [38].

We extend the original implementation by (1) a module to confine the cells on a semi-flexible membrane and (2) a module to include the reaction-diffusion dynamics of a limiting nutrient. We use the *moving least-squares meshless membrane* method (abbreviated MMM-method) to constrain the cells in a monolayer with defined bending rigidity [73, 74]. The MMM-method achieves a membrane configuration via a multibody potential energy which favors a locally flat arrangement of particles. To model nutrient transport and uptake, we solve a continuum reaction-diffusion equation for the nutrient concentration by means of a finite-difference discretization. The reaction-diffusion equation is solved in parallel to the particle-based cell dynamics. Cell multiplication dynamics is coupled with the local nutrient concentration to achieve a well-defined concentration-dependent growth rate.

3.1. The Two Particle Growth Simulation Method

The preexisting simulation framework is particle-based and favors a minimalistic approach to model cell growth and the interactions between cells. Every cell consists of two particles and the particle-particle interactions are divided into intercell interactions (between particles of different cells) and intracell interactions (between the two particles of one cell). Intracell forces determine the growth mechanism of the cell whereas intercell forces define adhesion and repulsion with the surrounding cells. Intra- and intercell forces, denoted $\boldsymbol{F}^{intra}$ and $\boldsymbol{F}^{inter}$, are based on the DPD-technique [69] which defines conservative, dissipative and random forces between the particles. All pairwise forces act along the direction of the connecting unit vector

$$\widehat{\boldsymbol{r}}_{ij} = \frac{\boldsymbol{r}_i - \boldsymbol{r}_j}{|\boldsymbol{r}_i - \boldsymbol{r}_j|} \tag{3.1.1}$$

of the particles at positions $\boldsymbol{r}_i$ and $\boldsymbol{r}_j$. This leads to conservation of linear momentum in the DPD-framework which is important to investigate e.g. hydrodynamic interactions. Furthermore, dissipative and random forces satisfy the fluctuation-dissipation theorem and preserve a preset temperature $k_b T$ in the system. Apart from the DPD-interactions, a weak background friction with the embedding medium of the particles is added. This friction takes

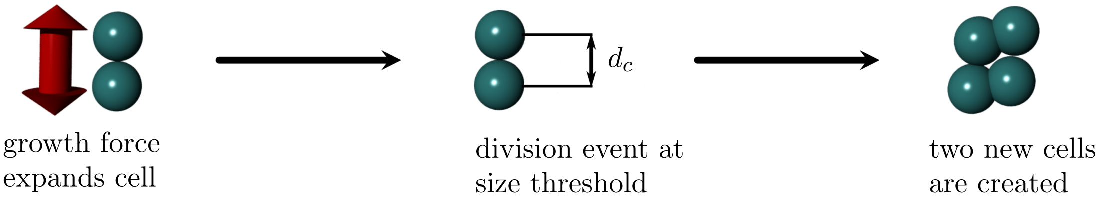
d_c
growth force expands cell
division event at size threshold
two new cells are created

FIGURE 3.1. The cell division is sampled in the steps depicted above. Every cell consists of two point particles which repel each other with the growth force F_g, eq. (3.1.3). When the length of the particle-particle distance has reached a predefined size threshold d_c, a division event takes place: Two new daughter cells are placed randomly in close vicinity to the mother cell. Appeared similarly in [75].

the form of a Brownian dynamics (abbreviated BD) dissipative-random force pair $\boldsymbol{F}^b$ [76]. Thus, the net force $\boldsymbol{F}_i$ on particle i reads

$$\boldsymbol{F}_i = \boldsymbol{F}_i^{intra} + \boldsymbol{F}_i^{inter} + \boldsymbol{F}_i^b. \tag{3.1.2}$$

All forces are cut off at a cutoff radius r_{pp}. We briefly discuss all force contributions.

Intracell Forces. The intracell forces consist of a purely repulsive growth force $\boldsymbol{F}^g$ and a dissipative-random force pair $\boldsymbol{F}^d$ and $\boldsymbol{F}^r$. For a particle i we denote with i^* the index of the other particle of the same cell. The growth force on particle i reads

$$\boldsymbol{F}_{ii^*}^g = \frac{B}{\left(r_{ii^*} + r_0\right)^2} \widehat{\boldsymbol{r}}_{ii^*}, \tag{3.1.3}$$

with the cellular pressure coefficient r_0 and the growth strength B. The repulsive growth force increases the distance r_{ii^*} between the two cell particles (see fig. 3.1). At a distance threshold $r_{ii^*} = d_c$ a division event is sampled upon which two new particles are created within distance r_c at random positions. These four particles form then the two new cells. Furthermore, to model cell death, cells are randomly removed with a constant rate k_a. Dissipative and random forces take the DPD-form

$$\boldsymbol{F}_{ii^*}^d = \gamma w^d(r_{ii^*}) \left((\boldsymbol{v}_i - \boldsymbol{v}_{i^*}) \cdot \widehat{\boldsymbol{r}}_{ii^*} \right) \widehat{\boldsymbol{r}}_{ii^*} \quad \text{and} \quad \boldsymbol{F}_{ii^*}^r = \eta w^r(r_{ii^*})\, \zeta_{ii^*} \widehat{\boldsymbol{r}}_{ii^*}, \tag{3.1.4}$$

where $\boldsymbol{v}_i = \frac{d}{dt}\boldsymbol{r}_i$ denotes particle velocity, γ, η respective force strengths, w^d, w^r respective weight functions and ζ_{ii^*} a symmetric Gaussian random variable with zero mean and unit variance. Dissipative and random forces are related to each other to fulfill the fluctuation-dissipation theorem [77], namely

$$w^d(r_{ii^*}) = \left(w^r(r_{ii^*})\right)^2 \quad \text{and} \quad \eta^2 = 2\gamma k_b T. \tag{3.1.5}$$

For the intracell interaction we use uniform weighting with cutoff,

$$w^d = w^r = \Theta(r_{pp} - r_{ii^*}), \tag{3.1.6}$$

where $\Theta(r)$ denotes the Heaviside step function.

Intercell Forces. Intercell forces consist of pairwise volume exclusion forces $\boldsymbol{F}^v$ and adhesion forces $\boldsymbol{F}^a$. For a pair i, j of particles inside cutoff range, with $j \neq i^*$, these read

$$\boldsymbol{F}_{ij}^v = f_0 \left(\left(\frac{r_{pp}}{r_{ij}} \right)^5 - 1 \right) \quad \text{and} \quad \boldsymbol{F}_{ij}^a = -f_1 \widehat{\boldsymbol{r}}_{ij}, \tag{3.1.7}$$

TABLE 3.1. Standard simulation parameters for the 2PG model [68].

Parameter	Value [sim. units]	Description
dt_{dpd}	10^{-3}	DPD-integration timestep
B	50	Growth force constants, see eq. (3.1.3)
r_0	1	
r_{pp}	1	Cutoff radius of all pair-potentials
d_c	0.8	Size threshold for cell division
r_c	10^{-5}	Distance at which new particles are placed after division
k_a	0.01	Apoptosis rate
k_bT	0.1	Noise temperature (both DPD- and BD-noise)
γ_t	50	Intercell friction constant
γ_c	100	Intracell friction constant
γ_b	0.1	Background friction constant
f_0	2.39566	Repulsive force constant
f_1	7.5	Attractive force constant

where f_0 and f_1 denote repulsive and adhesive intercell force constants. Dissipative and random intercell forces take equivalent forms to the respective intracell forces eqns. (3.1.4); for a pair i, j replace i^* by $j \neq i^*$ in eqns. (3.1.4). Furthermore, we employ different weight functions, namely

$$w^d(r) = (w^r(r))^2 = \left(1 - \frac{r}{r_{pp}}\right)^2. \tag{3.1.8}$$

Background Friction. The background friction forces $\boldsymbol{F}^b$ consist of a BD dissipative-random force pair $\boldsymbol{F}^{bd}$ and $\boldsymbol{F}^{br}$

$$\boldsymbol{F}_i^{bd} = -\gamma_b \boldsymbol{v}_i \quad \text{and} \quad \boldsymbol{F}_i^{br} = \eta_b \boldsymbol{\zeta}, \tag{3.1.9}$$

where γ_b, η_b denote the respective force strengths and $\boldsymbol{\zeta}$ a vector whose components are independent, Gaussian distributed random numbers with zero mean and unit variance. Furthermore, it is $\eta_b^2 = 2\gamma_b k_b T$ to fulfill the fluctuation-dissipation theorem. Standard simulation parameters are given in table 3.1. Throughout this work, starred parameter values refer to ratios with respect to the standard parameter set, i.e. $B^* = B/B_{std}$ with B_{std} from table 3.1. We continue with some observations on frictional timescales and elastic behavior of the model tissue.

Inertia and Frictional Timescales. The growth processes we aim to describe happen on timescales of at least hours (e.g. bacteria) or even days or weeks (e.g. tissues). Thus, inertia effects do not play a role in observed dynamics. Hence, simulation parameters should be chosen such that frictional timescales are much shorter than other observed timescales. In the 2PG-technique we identify three frictional effects: intracell friction, shear friction and background friction with their respective intensities γ_c, γ_t and γ_b. In the systems studied in this work, the relevant dynamics are dominated by background friction. This requires that the frictional relaxation time $1/\gamma_b$ is much shorter than other relevant time scales, as for example the characteristic time of growth $1/\langle|k_g|\rangle$ or advective timescales $L/\langle|v|\rangle$, hereby, $\langle|k_g|\rangle$ denotes the average growth rate magnitude, L a typical system lengthscale and $\langle|v|\rangle$

the average velocity. Thus, parameters have to be chosen such that

$$\gamma_b \gg \frac{\langle|v|\rangle}{L} \qquad \text{and} \qquad \gamma_b \gg \langle|k|\rangle\,, \tag{3.1.10}$$

to ensure sufficiently fast relaxation of velocities.

Compressibility and Elastic Response. Next, we take a look at an elastic quantity, the *compressibility* κ_x, to investigate the elastic response of the model tissue. The ratio

$$\kappa_x = -\frac{1}{V}\left(\frac{\partial V}{\partial p}\right)_x, \tag{3.1.11}$$

denotes the compressibility of the system, its inverse $K_x = 1/\kappa_x$ the compression (or bulk) modulus. The index x indicates variables kept constant during the volume change, e.g. temperature T or number of particles N. For our actively growing system, the timescale on which a volume change is applied affects the pressure response. For example, assume we let the tissue equilibrate to the homeostatic state $p = p_h$ in a cylinder with a movable piston. Now, we move the piston slowly in either direction, much slower than the cell-turnover timescale $1/(k_d + k_a)$. As the tissue equilibrates towards the homeostatic state on the cell-turnover timescale, pressure remains in good approximation constant $p = p_h$ during movement of the piston. Thus, on timescales $t \gg 1/(k_d + k_a)$ the compressibility modulus K vanishes. On the other end of the scale, on timescales much shorter than the cell-turnover timescale (but longer than acoustic scales), the cell number remains constant and we probe the elastic response of the tissue material. If we move the piston a small distance Δl we expect a linear behavior in the pressure change $\Delta p = -E\Delta l/l = -E\Delta V/3V$, such that $K = E/3$; E denotes the Young's modulus. In simulations, the elastic response is governed by the cell-cell interaction and the growth force, thus, we expect the bulk modulus to scale roughly as $K \sim f_0/l^2$ or $K \sim B/l^4$; l denotes a length scale to obtain the correct units. In particular, if the external pressure on the tissue is bounded, we can approximate the incompressible limit by increasing the bulk modulus until $K \gg p_{ext}$. Both limits correspond to the remarkable property that the pressure difference $p_h - p$ follows the dynamics of a Maxwell model:

$$\left(1 + \frac{\zeta}{E}\frac{d}{dt}\right)(p_h - p) = \zeta \nabla \cdot \boldsymbol{v}, \tag{3.1.12}$$

with a volume viscosity $\zeta \propto 1/(k_d + k_a)$ [70].

3.2. Integration of Equations of Motion

With the definitions of the forces $\{\boldsymbol{F}_i\}$ exerted on the particles, their dynamic follows the Newtonian equations of motion

$$m\frac{d^2}{dt^2}\boldsymbol{r}_i = \boldsymbol{F}_i = \boldsymbol{F}_i^r + \boldsymbol{F}_i^d\left(\{\boldsymbol{r}_j\}, \{\boldsymbol{v}_j\}\right) + \boldsymbol{F}_i^c\left(\{\boldsymbol{r}_j\}\right), \tag{3.2.1}$$

where m denotes the particle mass and the terms on the right-hand side random, dissipative and conservative forces. We set $m = 1$ for all particles in our simulations. To integrate the set of N differential equations 3.2.1 for the N particles, Runge-Kutta-type integration schemes such as the leapfrog scheme or the velocity-Verlet scheme (abbreviated VV-scheme) have been devised [69, 76]. In the context of integration of many-particle systems, consistency, stability and correct resolution of physical quantities (e.g. conservation laws, correlation functions) are often more important than the approximation order of the integrator. The integrator used in this work is based on the second order accuracy VV-scheme to propagate

TABLE 3.2. Iteration steps of a) VV-algorithm and b) DPD-VV-algorithm to propagate given particle data $\{\boldsymbol{r}_i, \boldsymbol{v}_i, \boldsymbol{F}_i\}|_t$ at time t to time $t + dt$.

a)	VV-scheme
1.	Overwrite current velocities with velocities at half timestep: $\boldsymbol{v}_i(t) \leftarrow \boldsymbol{v}_i\big(t + \frac{1}{2}dt\big) = \boldsymbol{v}_i(t) + \frac{1}{2m}\boldsymbol{F}_i(t)\,dt$
2.	Overwrite current positions with positions at full timestep: $\boldsymbol{r}_i(t) \leftarrow \boldsymbol{r}_i(t + dt) = \boldsymbol{r}_i(t) + \boldsymbol{v}_i\big(t + \frac{1}{2}dt\big)\,dt$
3.	Overwrite current forces with forces at full timestep: $\boldsymbol{F}_i(t) \leftarrow \boldsymbol{F}_i(t + dt) = \boldsymbol{F}_i(t + dt, \{\boldsymbol{r}_i(t + dt)\})$
4.	Overwrite half-step velocities with velocities at full timestep: $\boldsymbol{v}_i\big(t + \frac{1}{2}dt\big) \leftarrow \boldsymbol{v}_i(t + dt) = \boldsymbol{v}_i\big(t + \frac{1}{2}dt\big) + \frac{1}{2m}\boldsymbol{F}_i(t + dt)\,dt$

b)	DPD-VV-scheme
1.	Overwrite current velocities with velocities at half timestep: $\boldsymbol{v}_i(t) \leftarrow \boldsymbol{v}_i\big(t + \frac{1}{2}dt\big) = \boldsymbol{v}_i(t) + \frac{1}{2m}\Big(\boldsymbol{F}_i^c(t)\,dt + \boldsymbol{F}_i^d(t)\,dt + \boldsymbol{F}_i^r(t)\,\sqrt{dt}\Big)$
2.	Overwrite current positions with positions at full timestep: $\boldsymbol{r}_i(t) \leftarrow \boldsymbol{r}_i(t + dt) = \boldsymbol{r}_i(t) + \boldsymbol{v}_i\big(t + \frac{1}{2}dt\big)\,dt$
3.	Overwrite current forces with forces at full timestep: $\boldsymbol{F}_i^{c,r}(t) \leftarrow \boldsymbol{F}_i^{c,r}(t + dt) = \boldsymbol{F}_i^{c,r}(t + dt, \{\boldsymbol{r}_i(t + dt)\})$ $\boldsymbol{F}_i^d(t) \leftarrow \boldsymbol{F}_i^d(t + dt) = \boldsymbol{F}_i^d\big(t + dt, \big\{\boldsymbol{r}_i(t + dt)\,, \boldsymbol{v}_i\big(t + \frac{1}{2}dt\big)\big\}\big)$
4.	Overwrite half-step velocities with velocities at full timestep: (a) $\boldsymbol{v}_i\big(t + \frac{1}{2}dt\big) \leftarrow \boldsymbol{v}_i(t + dt) = \boldsymbol{v}_i\big(t + \frac{1}{2}dt\big) + \frac{1}{2m}\Big(\boldsymbol{F}_i^c(t + dt)\,dt + \boldsymbol{F}_i^r(t + dt)\,\sqrt{dt}\Big)$ (b) $\boldsymbol{v}_i(t + dt) \leftarrow \boldsymbol{v}_i(t + dt) + \boldsymbol{F}_i^d(t + dt)\,dt$
5.	Overwrite dissipative forces with values estimated from velocities at full timestep: $\boldsymbol{F}_i^d(t + dt)\,dt \leftarrow \boldsymbol{F}_i^d(t + dt, \{\boldsymbol{r}_i(t + dt)\,, \boldsymbol{v}_i(t + dt)\})$
6.	End of iteration if velocities and dissipative forces are accurate enough. If not, go to step 4.(b).

the particle properties $\{\boldsymbol{r}_i, \boldsymbol{v}_i, \boldsymbol{F}_i\}|_t$ at time t to time $t+dt$. The steps of the VV-algorithm are summarized in table 3.2. Note that in the third step of the VV-scheme the forces are assumed to be conservative as they only depend on the particle positions. As the 2PG-method is based on the DPD-method which contains forces dependent on velocities, the VV-scheme has to be modified to account for consistency between forces and velocities. We employ the so-called DPD-VV-scheme which divides the force calculation along conservative forces $\boldsymbol{F}_i^c$, random forces $\boldsymbol{F}_i^r$ and velocity dependent dissipative forces $\boldsymbol{F}_i^d$ [78, 79]. The steps of the DPD-VV-scheme are given in table 3.2. Note that in the third step a first guess of the dissipative forces is calculated using the velocities at half timestep. In step 4(b), the velocities at full timestep are calculated with this first guess of the dissipative forces. In the last step, dissipative forces are then reevaluated with the velocity at full timestep. To ensure consistency between velocities and dissipative forces, steps 4(b) and 5 may me repeated until a self-consistency criterion is fulfilled. A possible criterion is for example the convergence of the instantaneous temperature to its limiting value [79]. We assume that one sweep through steps 4(b) and (5) is enough to ensure a sufficient degree of consistency to achieve a good trade-off between accuracy and efficiency [79].

3.3. The Meshless Membrane Model

A variety of different approaches exist to simulate semi-flexible membranes. The approaches can be divided into descriptions based on a mesh of triangulated surfaces [80] and meshless methods (see e.g. [73, 81, 82]). To facilitate coupling to the 2PG-model, we choose the MMM-method, which results in a flexible, monolayered membrane with well-defined bending rigidity and zero spontaneous curvature. The MMM-method can be added directly onto any existing, particle-based molecular dynamics simulation. In contrast, triangulated surface models require a careful redefinition of all physical properties of a system (e.g. stress dependent growth in our context) on the triangle mesh. However, this extra effort also ensures control of the model properties such that material constants, for example the bending rigidity, are input parameters. In the MMM-framework, the bending rigidity has to be measured separately as it has not been related analytically to the input parameters. Furthermore, so far it is not clear how much the MMM-model affects the "non-membrane" properties such as the growth dynamics which mainly takes place in the in-plane dimensions. To elucidate these issues, we investigate the MMM-model with analytic methods.

3.3.1. Definition and Resulting Force. The MMM-model is based on a dimensionless, geometrical quantity of a set of N points $\{\boldsymbol{r}_j\}_{j=1}^{N}$, the *aplanarity* α_{pl} [73]. Simply spoken, the aplanarity describes the deviation of the point positions $\boldsymbol{r}_j$ from a mathematical plane. It varies between zero and one, zero corresponds to all points lying on a plane and one to a point cloud which (1) is symmetric with respect to three rectangular axes and (2) has the same extend along all these axes (for example points uniformly distributed on a sphere or a cube). In particular, α_{pl} vanishes for a set of less than four points. The aplanarity is defined with respect to a center particle which interacts with all other particles. To avoid ambiguities, we write the position of the center particle always at the first argument position, for example, if particle i is the center particle the corresponding aplanarity reads

$$\alpha_{pl}\Big(\boldsymbol{r}_i, \{\boldsymbol{r}_j\}_{j\neq i}\Big)\,. \tag{3.3.1}$$

The MMM-potential U_α of a set of points $\{\boldsymbol{r}_j\}_{j=1}^{N}$ is defined as the sum of the aplanarities of all points:

$$U_\alpha = k_\alpha \sum_{i=1}^{N} \alpha_{pl}\Big(\boldsymbol{r}_i, \{\boldsymbol{r}_j\}_{j\neq i}\Big)\,. \tag{3.3.2}$$

The proportionality constant k_α determines the strength of the potential. Measurements of the bending rigidity κ in refs. [73, 74] for a Brownian dynamics simulation show that it is directly proportional to k_α over a wide parameter range. The individual aplanarity of every particle i is defined with respect to the weighted point cloud which contains all particles within a distance smaller than a cutoff radius r_{mp}. The interaction decreases smoothly depending on the distance to $\boldsymbol{r}_i$. This smooth decay is controlled by the weight function

$$w(r) = \begin{cases} \exp\left(\dfrac{\left(\frac{r}{r_{ga}}\right)^2}{\left(\frac{r}{r_{mp}}\right)^n - 1}\right) & (r < r_{mp}) \\ 0 & (r \geq r_{mp}) \end{cases}\,, \tag{3.3.3}$$

with the parameters $n = 12$ and $r_{ga} = r_{mp}/2$ [73]. In principle, one can choose any other weight function. However, a smooth decay towards $r = r_{mp}$ is desirable as the potential is not differentiable for a set of four particles with one having exactly the distance $r = r_{mp}$ to all others. Furthermore, the weight function affects elastic parameters such as bending rigidity or isotropic compressibility (see sections 3.3.3-3.3.4). We define the weighted center of mass with respect to particle i

$$\boldsymbol{r}_g\Big(\boldsymbol{r}_i, \{\boldsymbol{r}_j\}_{j\neq i}\Big) = \frac{\sum_{j=1}^{N} \boldsymbol{r}_j w\left(r_{ij}\right)}{\sum_{j=1}^{N} w\left(r_{ij}\right)}, \tag{3.3.4}$$

with $r_{ij} = |\boldsymbol{r}_i - \boldsymbol{r}_j|$. With the components of the center of mass $\boldsymbol{r}_g = (x_g, y_g, z_g)$ we define the components of the gyration tensor $\overline{\boldsymbol{a}} = (a_{\alpha\beta})$ via

$$a_{\alpha\beta}\Big(\boldsymbol{r}_i, \{\boldsymbol{r}_j\}_{j\neq i}\Big) = \sum_{j=1}^{N} \left(\alpha_j - \alpha_g\right)\left(\beta_j - \beta_g\right) w\left(r_{ij}\right), \qquad \alpha, \beta \in \{x, y, z\}\,. \tag{3.3.5}$$

We see directly that the gyration tensor is symmetric $a_{\alpha\beta} = a_{\beta\alpha}$ and therefore possesses an orthogonal basis of eigenvectors with real-valued eigenvalues $\lambda_1, \lambda_2, \lambda_3$. The gyration tensor describes the extension of the point cloud in the directions given by the eigenvectors, a small eigenvalue corresponds to a “thin” extension in this direction and vice versa. The aplanarity is defined via the invariants of the gyration tensor, trace, determinant and the sum of the three principal minors:

$$\alpha_{pl}\Big(\boldsymbol{r}_i, \{\boldsymbol{r}_j\}_{j\neq i}\Big) = 9\frac{\det\left(\overline{\boldsymbol{a}}\right)}{\operatorname{tr}\left(\overline{\boldsymbol{a}}\right)\operatorname{sm}\left(\overline{\boldsymbol{a}}\right)} = 9\frac{\lambda_x\lambda_y\lambda_z}{\left(\lambda_x + \lambda_y + \lambda_z\right)\left(\lambda_x\lambda_y + \lambda_y\lambda_z + \lambda_x\lambda_z\right)}, \tag{3.3.6}$$

with

$$\begin{aligned} \operatorname{tr}\left(\overline{\boldsymbol{a}}\right) &= a_{xx} + a_{yy} + a_{zz} = \lambda_x + \lambda_y + \lambda_z, \\ \det\left(\overline{\boldsymbol{a}}\right) &= a_{xx}a_{yy}a_{zz} - a_{xx}a_{yz}^2 - a_{zz}a_{xy}^2 - a_{yy}a_{xz}^2 + 2a_{xy}a_{yz}a_{xz} = \lambda_x\lambda_y\lambda_z, \\ \operatorname{sm}\left(\overline{\boldsymbol{a}}\right) &= a_{xx}a_{yy} + a_{yy}a_{zz} + a_{zz}a_{xx} - a_{xy}^2 - a_{yz}^2 - a_{xz}^2 = \lambda_x\lambda_y + \lambda_y\lambda_z + \lambda_x\lambda_z. \end{aligned} \tag{3.3.7}$$

Note as $2\operatorname{sm}\left(\overline{\boldsymbol{a}}\right) = \operatorname{tr}\left(\overline{\boldsymbol{a}}\right)^2 - \operatorname{tr}\left(\overline{\boldsymbol{a}}^2\right)$ holds, the aplanarity may be expressed in terms of determinants and traces of $\overline{\boldsymbol{a}}$ and $\overline{\boldsymbol{a}}^2$. The force on particle k in direction $\rho \in \{x, y, z\}$ is given by

$$\boldsymbol{F}_k \cdot \boldsymbol{e}_\rho = -\frac{\partial}{\partial \rho_k} k_\alpha \sum_{i=1}^{N} \alpha_{pl}\Big(\boldsymbol{r}_i, \{\boldsymbol{r}_j\}_{j\neq i}\Big), \tag{3.3.8}$$

where $\frac{\partial}{\partial \rho_k}$ denotes the derivative with respect to coordinate ρ of particle k. The calculations to get an analytical expression for the MMM-force are lengthy but straightforward. Since the aplanarity eq. (3.3.6) is a fraction of two third-order polynomials in the gyration tensor components $a_{\alpha\beta}$, chain and product rule reduce the calculation of the forces eq. (3.3.8) ultimately to derivatives of the gyration tensor components

$$\frac{\partial}{\partial \rho_k} a_{\alpha\beta}\Big(\boldsymbol{r}_i, \{\boldsymbol{r}_j\}_{j\neq i}\Big)\,. \tag{3.3.9}$$

In appendix A, the derivatives 3.3.9 for the case $k = i$ are calculated, one obtains

$$\begin{aligned}\frac{\partial}{\partial\rho_i} a_{\alpha\beta}\Big(\boldsymbol{r}_i, \{\boldsymbol{r}_j\}_{j\neq i}\Big) =& \,\delta_{\rho\alpha}\left(\beta_i - \beta_g\right) + \delta_{\rho\beta}\left(\alpha_i - \alpha_g\right) \\ &+ \sum_{j\neq i}\left(\alpha_j - \alpha_g\right)\left(\beta_j - \beta_g\right)\frac{w'\left(r_{ij}\right)}{r_{ij}}\left(\rho_i - \rho_j\right) .\end{aligned} \tag{3.3.10}$$

Analogously, one can show for the case $k \neq i$

$$\begin{aligned}\frac{\partial}{\partial\rho_k} a_{\alpha\beta}\Big(\boldsymbol{r}_i, \{\boldsymbol{r}_j\}_{j\neq i}\Big) =& \,\delta_{\rho\alpha}\left(\beta_k - \beta_g\right) w\left(r_{ki}\right) + \delta_{\rho\beta}\left(\alpha_k - \alpha_g\right) w\left(r_{ki}\right) \\ &+ \left(\alpha_k - \alpha_g\right)\left(\beta_k - \beta_g\right)\frac{w'\left(r_{ki}\right)}{r_{ki}}\left(\rho_k - \rho_i\right) .\end{aligned} \tag{3.3.11}$$

3.3.2. Forces in the Nearly Flat State. We take a look at the force contributions in a planar, almost flat configuration. We first investigate how the forces scale with the membrane thickness d. For this purpose, we define the coordinate system such that the membrane lies in the xy-plane. In simulations, d corresponds to the lateral extend of the point cloud. We denote by F_z and F_{xy} typical MMM-force magnitudes in lateral and in-plane direction. To analyze how F_z and F_{xy} scale with d, we collect the leading order terms in the expression for the force $F_{k\rho} = \partial_{\rho_k}\alpha_{pl}$, eq. (3.3.8), in the limit of small membrane thickness $d \to 0$ and fixed in-plane extend. We set $\boldsymbol{r}_g$ into the origin of our coordinate system. For small membrane thickness $d \ll 1$, the eigenvalues λ_x, λ_y of the gyration tensor in in-plane direction are much larger than the eigenvalue in lateral direction $\lambda_z \ll \lambda_x, \lambda_y$. Furthermore, the major contribution to the particle-distances r_{ij} arises from the in-plane extend of the point cloud, which we keep constant. Thus, the terms $w\left(r_{ij}\right)$ and $w'\left(r_{ij}\right)$ do not affect the scaling. With the expression $\lambda_\alpha = \sum_j \alpha_j^2 w\left(r_{ij}\right)$ for the eigenvalues we can directly calculate the leading order terms and their derivatives along the coordinate of an arbitrary particle:

$$\begin{aligned}\lambda_{x,y} &= \mathcal{O}\left(1\right), & \partial_z\lambda_{x,y} &= \mathcal{O}\left(d\right), & \partial_x\lambda_{x,y} &= \mathcal{O}\left(1\right), & \partial_y\lambda_{x,y} &= \mathcal{O}\left(1\right), \\ \lambda_z &= \mathcal{O}\left(d^2\right), & \partial_z\lambda_z &= \mathcal{O}\left(d\right), & \partial_x\lambda_z &= \mathcal{O}\left(d^2\right), & \partial_y\lambda_z &= \mathcal{O}\left(d^2\right) .\end{aligned} \tag{3.3.12}$$

Insertion of these terms in $\partial_{\rho_k}\alpha_{pl}$ results in a quadratic scaling of the in-plane forces F_{xy}

$$F_{xy} = \mathcal{O}\left(d^2\right) , \tag{3.3.13}$$

and linear scaling of the normal forces F_z:

$$F_z = \mathcal{O}\left(d\right) . \tag{3.3.14}$$

Hence, the in-plane forces decay much faster than the lateral forces. Above scaling argument does not include cancellation of force contributions from different aplanarity terms. Therefore, above scaling laws provide an upper bound for the sum of absolute values of the force contributions of all particles $\sum_i |F_i|$. In simulations, particle order is isotropic on lengthscales much larger than the excluded volume radius. Thus, we expect in-plane force contributions to cancel out to a large degree, effectively scaling with an even higher exponent in d. In conclusion, we expect the MMM-in-plane forces to be negligible compared to the in-plane forces of the 2PG-module.

Next, we investigate how the MMM-potential keeps particles in the membrane and what happens if two different membrane folds “touch”. To do so, we analyze the interaction energy of a single particle at position $\boldsymbol{r}_p = (0, 0, z_p)$ with a flat membrane in the xy-plane under

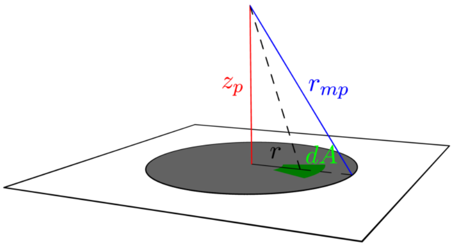

FIGURE 3.2. A single particle at $\boldsymbol{r} = z_p \boldsymbol{e}_z$ interacts with all particles on the membrane inside the cutoff radius r_{mp} (dark gray circle). A membrane patch dA (green), with radial distance r to the particle's base point on the membrane, interacts with it if $z_p^2 + r^2 \leq r_{mp}^2$.

the assumption that the membrane thickness is much smaller than the membrane-particle distance, i.e. $d \ll z_p$ (see fig. 3.2). The single particle can either be a particle which tries to escape the membrane or a particle which belongs to another membrane. The quantities which determine the interaction of the particle with the membrane are its distance z_p to the membrane, the maximal interaction range r_{mp} and the number density ϱ of particles in the membrane. The lengthscale $l_p = 1/\sqrt{\varrho}$ estimates the average particle-particle distance for an uniform distribution of particles on the membrane. To simplify the calculations, we assume an uniform weight function with cutoff $w\,(r) = \Theta(r_{mp} - r)$. We first calculate the interaction energy of a membrane patch dA at the position $\boldsymbol{r}_{patch} = r\boldsymbol{e}_r = r\,(\cos\varphi, \sin\varphi)$ for $r^2 \leq r_{mp}^2 - z_p^2$ with the particle. The number density is given by

$$\varrho(\boldsymbol{r}) = \varrho\delta(z) + \delta(\boldsymbol{r} - \boldsymbol{r}_p)\,. \tag{3.3.15}$$

The continuum equivalent of the discrete center of mass definition eq. (3.3.4) reads:

$$\boldsymbol{r}_g(\boldsymbol{r}) = \frac{\int_{\mathbb{R}^3} \boldsymbol{r}' w\,(|\boldsymbol{r}' - \boldsymbol{r}|)\,\varrho(\boldsymbol{r}')\,dV'}{\int_{\mathbb{R}^3} w\,(|\boldsymbol{r}' - \boldsymbol{r}|)\,\varrho(\boldsymbol{r}')\,dV'}, \tag{3.3.16}$$

with $\boldsymbol{r}$ taken from the set of particle positions such that $\varrho(\boldsymbol{r}) \neq 0$. The center of mass vectors for particle and patch are given by

$$\boldsymbol{r}_g(\boldsymbol{r}_p) = \frac{z_p \boldsymbol{e}_z}{\pi\left(r_{mp}^2 - z_p^2\right)\varrho + 1}, \quad \boldsymbol{r}_g(\boldsymbol{r}_{patch}) = \frac{\pi r_{mp}^2 \varrho r \boldsymbol{e}_r + z_p \boldsymbol{e}_z}{\pi r_{mp}^2 \varrho + 1}. \tag{3.3.17}$$

Next, we determine the diagonal components of the gyration tensor

$$a_{\alpha\alpha}(\boldsymbol{r}) = \int_{\mathbb{R}^3} (\alpha - \alpha_g(\boldsymbol{r}))^2\, w\left(\left|\boldsymbol{r}' - \boldsymbol{r}\right|\right)\varrho\left(\boldsymbol{r}'\right)dV' \tag{3.3.18}$$

for the particle to

$$\begin{aligned} a_{xx} &= a_{yy} = \frac{1}{4}\pi\left(r_{mp}^2 - z_p^2\right)^2 \varrho, \\ a_{zz} &= z_g(\boldsymbol{r}_p)^2\,\pi\left(r_{mp}^2 - z_p^2\right)\varrho + (z_p - z_g(\boldsymbol{r}_p)^2)^2 = z_p^2\left(1 - \frac{1}{\pi\left(r_{mp}^2 - z_p^2\right)\varrho + 1}\right). \end{aligned} \tag{3.3.19}$$

Due to the azimuthal symmetry with respect to the z-axis, all non-diagonal entries of the gyration tensor vanish, a_{xx}, a_{yy}, a_{zz} are directly the eigenvalues of the gyration tensor. Note that while a_{xx} and a_{yy} diverge for $\varrho \to \infty$, it is $a_{zz} < z_p^2$ and a_{zz} converges against z_p^2, which may seem counter-intuitive at first glance. Since $z_g(\boldsymbol{r}_p) = \mathcal{O}(1/\varrho)$, the membrane contributions to a_{zz} scale as $z_g(\boldsymbol{r}_p)^2\varrho = \mathcal{O}(1/\varrho)$ and vanish for $\varrho \to \infty$; only the contribution of the single particle remains. The aplanarity of the membrane patch at $\boldsymbol{r}_{patch} = r(\cos\varphi, \sin\varphi)$ can not depend on the azimuthal angle φ due to the radial symmetry, hence, we set $\varphi = 0$ to ease the gyration tensor calculations. The calculation of the components of the gyration tensor yields:

$$\begin{aligned}
a_{xx} &= \frac{1}{4}\pi\varrho\left(r_{mp}^4 + \frac{4r^2r_{mp}^2}{1+\pi r_{mp}^2\varrho}\right), & a_{xy} &= z_p r\left(\frac{1}{\pi\varrho r_{mp}^2} - 1\right), \\
a_{yy} &= \frac{1}{4}\pi\varrho r_{mp}^4, & a_{zz} &= z_p^2\left(1 - \frac{1}{\pi r_{mp}^2\varrho + 1}\right),
\end{aligned} \tag{3.3.20}$$

all other components vanish. Insertion into the aplanarity definition, eq. (3.3.6), yields the aplanarity contribution α_{pl} of particle and membrane patch:

$$\begin{aligned}
\alpha_{pl}^{particle} &= \frac{24z_p^2}{\pi\varrho\left(z_p^2 - r_{mp}^2\right)^2 + 7z_p^2 + r_{mp}^2} - \frac{6z_p^2}{\pi\varrho\left(z_p^2 - r_{mp}^2\right)^2 + z_p^2 + r_{mp}^2}, \\
\alpha_{pl}^{patch} &= \frac{18z_p^2r_{mp}^2\left(\pi r_{mp}^2\varrho + 1\right)}{\left(2z_p^2 + 2r^2 + \pi r_{mp}^4\varrho + r_{mp}^2\right)\left(8z_p^2 + 4r^2 + \pi r_{mp}^4\varrho + r_{mp}^2\right)}.
\end{aligned} \tag{3.3.21}$$

The remaining calculations are simple: First, we collect all interaction energies by integration over the membrane area the particle interacts with, i.e. the circle with radius $\sqrt{r_{mp}^2 - d^2}$ around $r = 0$. Second, we add the single aplanarity term of the particle. Hence, the total MMM-potential energy is given by

$$U_\alpha/k_\alpha = 2\pi\varrho\int_0^{\sqrt{r_{mp}^2-d^2}} r\alpha_{pl}^{patch}(r)\,dr + \alpha_{pl}^{particle}, \tag{3.3.22}$$

with the MMM-potential strength k_α. Note that due to $\alpha_{pl}^{patch} \sim 1/\varrho$ for $\varrho \to \infty$ the total energy U_α does not vanish in this limit. In rescaled parameters $\tilde{z}_p = z_p/r_{mp}$, $\tilde{l}_p = l_p/r_{mp}$ above integral reads

$$\begin{aligned}
U_\alpha\left(\tilde{z}_p, \tilde{l}_p\right)/k_\alpha = &\frac{24\tilde{z}_p^2\tilde{l}_p^2}{\pi\left(\tilde{z}_p^2 - 1\right)^2 + 7\tilde{z}_p^2\tilde{l}_p^2 + \tilde{l}_p^2} - \frac{6\tilde{z}_p^2\tilde{l}_p^2}{\pi\left(\tilde{z}_p^2 - 1\right)^2 + \tilde{z}_p^2\tilde{l}_p^2 + \tilde{l}_p^2} \\
&- \frac{9\tilde{z}_p^2\pi\left(\pi + \tilde{l}_p^2\right)}{\tilde{l}_p^2\left(\pi + \tilde{l}_p^2\right) - 4\tilde{z}_p^2\tilde{l}_p^2}\log\left[\frac{\left(\pi + 3\tilde{l}_p^2\right)\left(\pi + \tilde{l}_p^2 + 8\tilde{z}_p^2\tilde{l}_p^2\right)}{\left(\pi + \tilde{l}_p^2 + 2\tilde{z}_p^2\tilde{l}_p^2\right)\left(\pi + 5\tilde{l}_p^2 + 4\tilde{z}_p^2\tilde{l}_p^2\right)}\right].
\end{aligned} \tag{3.3.23}$$

Figure 3.3 shows plots of $U_\alpha(\tilde{z}_p, \tilde{l}_p)/k_\alpha$. We take a look at the series expansions of U_α for $\tilde{z}_p = 0$ and $\tilde{z}_p = 1$ to investigate how particles are kept in the membrane and how a membrane interacts with particles which intrude from the outside. The corresponding expansions to

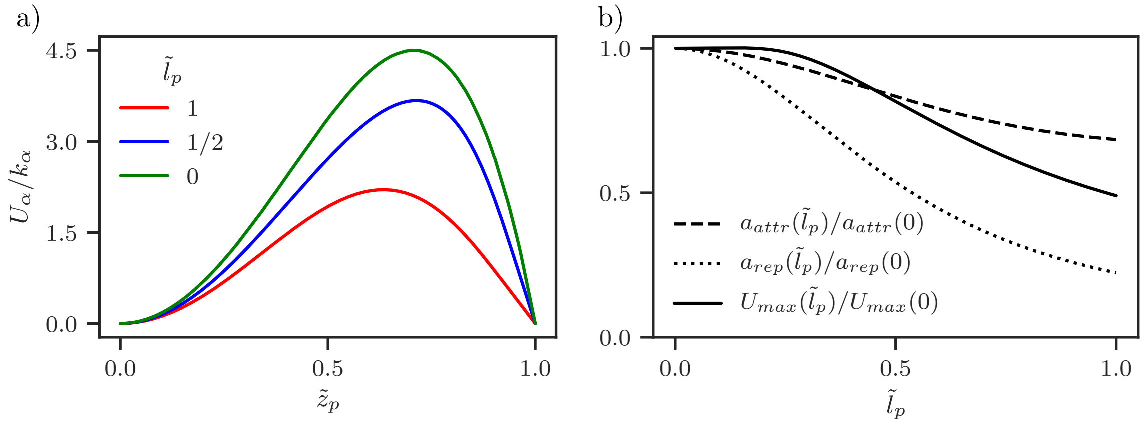

FIGURE 3.3. **a)** Plot of the MMM-potential energy $U_\alpha(\tilde{z}_p, \tilde{l}_p)$, eq. (3.3.23), of the particle-membrane system for rescaled particle-particle distances $\tilde{l}_p = l_p/r_{mp} = 0, 1/2$ and 1. The curve for $\tilde{l}_p = 0$ corresponds to the limit of infinite density $\varrho \to \infty$. **b)** Strengths of harmonic attraction a_{attr}, linear repulsion a_{rep} (see eqns. (3.3.24)) and the height U_{max} of the potential hill, dependent on average particle-particle distance $\tilde{l}_p = l_p/r_{mp}$.

lowest order are given by

$$\begin{aligned} U_\alpha\left(\tilde{z}_p, \tilde{l}_p\right)/k_\alpha &= a_{attr}\tilde{z}_p^2 + \mathcal{O}\left(\tilde{z}_p^4\right) \quad \text{with} \quad a_{attr} &&= \frac{18\tilde{l}_p^2}{\pi + \tilde{l}_p^2} - \frac{9\pi}{\tilde{l}_p^2}\log\left(\frac{\pi + 3\tilde{l}_p^2}{\pi + 5\tilde{l}_p^2}\right), \\ U_\alpha\left(\tilde{z}_p - 1, \tilde{l}_p\right)/k_\alpha &= a_{rep}\tilde{z}_p + \mathcal{O}\left(\tilde{z}_p^2\right) \quad \text{with} \quad a_{rep} &&= -\frac{36\pi\left(\tilde{l}_p^2 + \pi\right)}{\left(3\tilde{l}_p^2 + \pi\right)\left(9\tilde{l}_p^2 + \pi\right)} - \frac{9}{4}, \end{aligned} \tag{3.3.24}$$

the prefactors a_{attr} and a_{rep} are depicted in fig. 3.3. Hence, the MMM-potential acts as a *harmonic* potential for particles inside the membrane, whereas particles outside the membrane are *repelled*. In between these two extremes lies a "potential hill" of finite height U_{max} (see fig. 3.3), defining both the depth of the potential well trapping the membrane particles, as well as the separation energy scale of two touching membranes. To estimate U_{max}, it is convenient to perform the limit of infinite membrane density (or zero particle-particle distance, $\tilde{l}_p \to 0$) which provides an upper bound for U_{max} (see fig. 3.3). In the limit $\tilde{l}_p \to 0$ the potential energy U_α converges pointwise against

$$U_\alpha(\tilde{z}_p)/k_\alpha \overset{\tilde{l}_p \to 0}{\longrightarrow} U_\alpha^\infty/k_\alpha = 18\tilde{z}_p^2\left(1 - \tilde{z}_p^2\right), \quad \tilde{z}_p \le 1 \tag{3.3.25}$$

such that the potential depth is given by

$$U_{max} = \frac{9}{2}k_\alpha. \tag{3.3.26}$$

Note, however, that pointwise convergence of a sequence of functions $\{f_n\}$ against a function f does *not* imply that the derivatives $f_n', f_n'' \ldots$ converge against the corresponding derivatives of f. Indeed, the derivatives of U_α at $\tilde{z}_p = 1$ do not converge against the corresponding derivatives of U_α^∞, e.g.

$$U'_\alpha(1) = a_{rep} \overset{\tilde{l}_p \to 0}{\longrightarrow} -\frac{153}{4} \neq U_\alpha^{\infty\prime}(1) = -36 = -\frac{144}{4}. \tag{3.3.27}$$

However, as $\tilde{z}_p = 1$ is the sole point where this is the case, U_α^∞ still yields a good approximation of U_α for $\tilde{l}_p \ll 1$ apart from a small environment around $\tilde{z}_p = 1$.

In conclusion, the equations (3.3.24)-(3.3.26) capture the characteristics of the MMM-potential interaction with particles outside the membrane: short-range harmonic attraction, long-range repulsion which result in a membrane binding energy around $U_{max} = 9/2k_\alpha$.

3.3.3. Curvature Moduli: Bending Rigidity and Saddle-Splay Modulus. To get analytical insight into the curvature moduli of the MMM-potential, bending rigidity κ and saddle-splay modulus $\widehat{\kappa}$, we compare the total energy U_α of the MMM-potential with the Helfrich-Canham energy

$$E_{bend} = \int_S \frac{\kappa}{2} H^2 + \frac{\widehat{\kappa}}{2} G dA, \tag{3.3.28}$$

for a given surface S (see also section 4.1 for a brief discussion of the Helfrich-Canham energy and appendix C for the differential geometric framework). Ideally, the energies U_α and E_{bend} should be identical up to an additive constant E_0, i.e. $U_\alpha = E_{bend} + E_0$. For a flat plane $S \equiv 0$ both U_α and E_{bend} vanish such that $E_0 = 0$, hence, MMM-potential and the Helfrich-Canham energy have the same "zero-point". We have to derive two independent equations in order to determine the two moduli κ and $\widehat{\kappa}$. Thus, we have to calculate U_α for at least two, preferably simple, surfaces S, for example a sphere and a cylinder surface. For a sphere of radius R, mean and Gaussian curvature are $H = 2/R$ and $G = 1/R^2$, hence

$$E_{bend}^{sphere} = \int_S \frac{\kappa}{2} H^2 + \frac{\widehat{\kappa}}{2} G dA = \int_S \frac{\kappa}{2}\left(\frac{2}{R}\right)^2 + \frac{\widehat{\kappa}}{2}\frac{1}{R^2} dA = 4\pi\left(2\kappa + \frac{\widehat{\kappa}}{2}\right). \tag{3.3.29}$$

Note that the total curvature energy is independent of the sphere radius. For a cylinder surface of radius R and length L it is $H = 1/R$ and $G = 0$, hence

$$E_{bend}^{cyl} = \int_C \frac{\kappa}{2} H^2 dA = \int_C \frac{\kappa}{2}\left(\frac{1}{R}\right)^2 dA = \pi \frac{L}{R}\kappa. \tag{3.3.30}$$

To be consistent, the corresponding expressions U_α^{sphere} and U_α^{cyl} for the MMM-potential energy have to have the same dependency on the surface parameters R and L as E_{bend}^{sphere} and E_{bend}^{cyl}, i.e. ideally $U_\alpha^{sphere} = \text{const.}$ and $U_\alpha^{cyl} \propto L/R$.

We start with the calculation of U_α^{sphere} to check whether this is the case. As in the previous section, we denote with ϱ the homogeneous particle density on the surface and with r_{mp} the MMM-interaction range. In a first step, we assume an uniform weight function with cutoff $w = \Theta(r_{mp} - r)$, estimates for a non-uniform weight function follow afterwards. We investigate the MMM-energy of a small membrane patch dA on the sphere as depicted in fig. 3.4. The coordinate system is chosen such that the membrane patch lies on the pole of the sphere at $x = y = 0, z = R$, or $\theta = 0, r = R$ in spherical coordinates. The center of mass vector $\boldsymbol{r}_g$ is then parallel to $\boldsymbol{e}_z$ due to the azimuthal symmetry. The membrane patch interacts with all particles within a distance of r_{mp}, these are located on a spherical

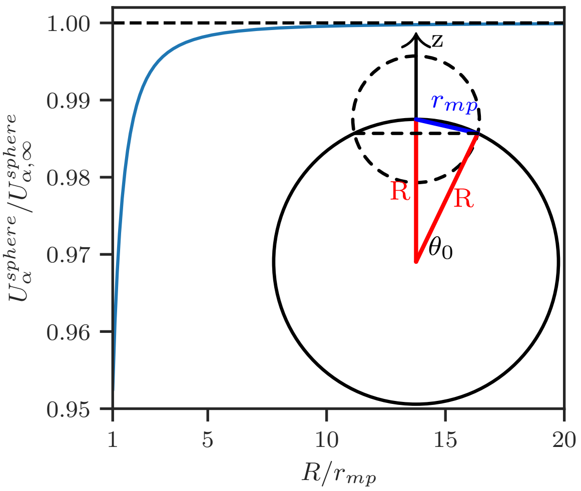

FIGURE 3.4. **Inset**: A small membrane patch dA at the pole of the sphere with radius R interacts with all particles in the spherical cap S_{cap} inside the cut-off radius r_{mp}. The angle θ_0 defines the spherical cap S_{cap} in spherical coordinates. Application of the cosine theorem on the highlighted triangle yields $r_{mp}^2 = 2R^2\left(1-\cos\theta_0\right)$, hence $\theta_0 = \arccos\left(1 - r_{mp}^2/2R^2\right)$.
Graph: The rescaled MMM-potential energy $U_\alpha^{sphere}/U_{\alpha,\infty}^{sphere}$ (see eqns. (3.3.34) and (3.3.35)) of the whole sphere as a function of the radii fraction R/r_{mp} in the range $R/r_{mp} > 1$. Note the rapid convergence, for $R/r_{mp} = 1$ it is $U_\alpha^{sphere}/U_{\alpha,\infty}^{sphere} \approx 0.95$.

cap S_{cap} with opening angle $\theta_0 = \arccos\left(1 - r_{mp}^2/2R^2\right)$, as depicted in fig. 3.4. Hence, the z-coordinate of the center of mass is given by

$$z_g = \frac{\int_{S_{cap}} z dA}{\int_{S_{cap}} dA} = \frac{2\pi R^2 \int_0^{\theta_0} \sin\theta R \cos\theta d\theta}{2\pi R^2 \int_0^{\theta_0} \sin\theta d\theta} = R - \frac{r_{mp}^2}{4R}. \tag{3.3.31}$$

The non-vanishing components of the gyration tensor $\overline{\boldsymbol{a}}$ follow to

$$\begin{aligned} a_{xx} = a_{yy} &= \frac{\pi\varrho\left(6R^2 r_{mp}^4 - r_{mp}^6\right)}{24R^2}, \\ a_{zz} &= \frac{\pi r_{mp}^6 \varrho}{48R^2}, \end{aligned} \tag{3.3.32}$$

insertion into eq. (3.3.6) leads to the aplanarity α_{pl}

$$\alpha_{pl} = 1 + \frac{1}{2}\left(\frac{r_{mp}}{R}\right)^2 + \frac{8}{\left(\frac{r_{mp}}{R}\right)^2 - 8}, \tag{3.3.33}$$

of the membrane patch dA. To get the total MMM-potential energy U_α^{sphere}, we have to integrate $k_\alpha \varrho \alpha_{pl}$ over the complete sphere which yields

$$U_\alpha^{sphere} = 4\pi R^2 \varrho k_\alpha \left(1 + \frac{1}{2}\left(\frac{r_{mp}}{R}\right)^2 + \frac{8}{\left(\frac{r_{mp}}{R}\right)^2 - 8}\right). \tag{3.3.34}$$

Unfortunately, unlike the continuum theory expression E_{bend}^{sphere}, the MMM-potential energy *depends* on the sphere radius (see fig. 3.4). However, in the limit $R \to \infty$, U_α^{sphere} converges asymptotically against the constant $U_{\alpha,\infty}^{sphere}$

$$U_\alpha^{sphere} \overset{R\to\infty}{\longrightarrow} U_{\alpha,\infty}^{sphere} = \frac{3}{2}\pi k_\alpha \varrho r_{mp}^2. \tag{3.3.35}$$

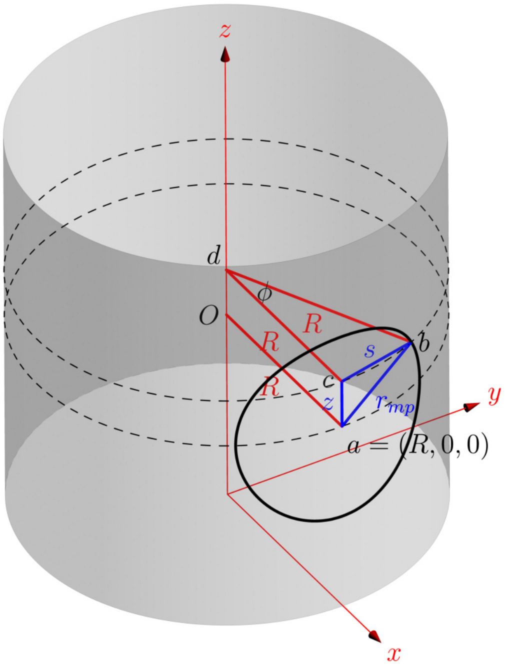

FIGURE 3.5. To calculate the integral (3.3.41) over the cylinder cap (solid black line depicts perimeter) cut out by the sphere with radius r_{mp} around the particle on the cylinder surface at point a, we need to find an expression for the angle $\phi(z) = \measuredangle cdb$. To do so, we start in the sphere center point a and construct a line of length $z \leq r_{mp}$ parallel to the cylinder axis $\boldsymbol{e}_z$ to reach the point c. Next, we define the point b as the intersection point of the cylinder surface at height z and the sphere surface and draw the connection line $[ab]$. The line $[ab]$ has the length r_{mp} as it is connecting the center point a with a point on the sphere's surface. The triangle $\triangle abc$ has a right angle in point c since $[ac] \parallel \boldsymbol{e}_z$ by construction and the points b and c have the same z-coordinate, also by construction. Hence, the length of the chord $s = [bc]$ obeys $r_{mp}^2 = z^2 + s^2$. Furthermore, application of the cosine theorem on the triangle $\triangle bcd$ yields $s^2 = 2R^2(1 - \cos\phi)$. Elimination of s^2 from the latter equation and rearrangement leads to the result (3.3.42).

We interpret this behavior in the sense that the MMM-potential only provides "proper" curvature moduli for curvatures much smaller than $1/r_{mp}$. In this case, equating eqns. 3.3.35 and 3.3.29 leads to the relation

$$2\kappa + \frac{\widehat{\kappa}}{2} = \frac{3}{8} k_\alpha \varrho r_{mp}^2. \tag{3.3.36}$$

We use the fact that the MMM-potential only provides proper curvature moduli in the limit $R \to \infty$ to ease the calculations for the cylinder: It is not necessary to calculate the MMM-potential energy U_α^{cyl} for finite R, we just need to know its asymptotic behavior in the limit $R \to \infty$. As in the case for the sphere, we need to calculate the aplanarity α_{pl} of a particle on the cylinder surface with particle density ϱ which interacts with all particles in interaction range r_{mp} (see fig. 3.5). The integral of the MMM-potential energy over the whole cylinder surface follows then by multiplication of α_{pl} with the total number of particles $2\pi RL\varrho$ and k_α as α_{pl} cannot depend on the position on the cylinder due to the symmetries of the configuration. Hence, it is $U_\alpha^{cyl} = k_\alpha \cdot 2\pi RL\varrho \cdot \alpha_{pl}$ and we expect that U_α^{cyl} converges asymptotically against E_{bend}^{cyl}, eq. (3.3.30), for $R \to \infty$:

$$U_\alpha^{cyl} = 2\pi RL\varrho k_\alpha \alpha_{pl} \overset{R\to\infty}{\longrightarrow} E_{bend}^{cyl} = \pi \frac{L}{R}\kappa. \tag{3.3.37}$$

Therefore, α_{pl} has to scale asymptotically as $\alpha_{pl} \overset{R\to\infty}{\longrightarrow} c/R^2$ with a prefactor $c > 0$ with the unit of an area. Insertion of $\alpha_{pl} = c/R^2$ into eq. (3.3.37) and rearrangement leads to

$$\kappa = 2k_\alpha \varrho c. \tag{3.3.38}$$

Hence, we only need to estimate the proportionality factor c to determine κ. To do so, we calculate the aplanarity of a particle on the cylinder surface up to order $1/R^2$. We use cylindrical coordinates with the z-axis parallel to the cylinder axis and the x-axis pointing on the particle on the cylinder surface (see fig. 3.5). The particle has the coordinates $\boldsymbol{r}_p = (R, 0, 0)$ and the center of mass components y_g and z_g vanish in these coordinates. We assume again uniform weighting with cutoff $w = \Theta(r_{mp} - r)$. The sphere of radius r_{mp} around the particle cuts out a curved cylinder cap C_{cap} over which we have to take the integrals to calculate x_g and the gyration tensor entries $a_{\alpha\beta}$. Due to symmetry, its non-diagonal components vanish, as in the case for the sphere, such that $\lambda_\alpha = a_{\alpha\alpha}$ for $\alpha = x, y, z$. In the limit $R \to \infty$, the cylinder surface becomes flatter and flatter and the cylinder cap C_{cap} converges against a flat circle C_{circ} with center $\boldsymbol{r}_p$ and radius r_{mp} in the yz-plane. Hence, the gyration tensor entries a_{yy} and a_{zz} converge both against

$$a_{\alpha\alpha} = \int\limits_{C_{cap}} \alpha^2 \varrho \, dA \overset{R\to\infty}{\longrightarrow} \int\limits_{C_{circ}} \alpha^2 \varrho \, dA = \frac{1}{4}\pi\varrho r_{mp}^4, \text{ for } \alpha = y, z. \tag{3.3.39}$$

Therefore, the aplanarity α_{pl} of the particle behaves asymptotically

$$\alpha_{pl} = 9\frac{\lambda_x\lambda_y\lambda_z}{(\lambda_x+\lambda_y+\lambda_z)(\lambda_x\lambda_y+\lambda_y\lambda_z+\lambda_x\lambda_z)} \overset{R\to\infty}{\longrightarrow} 9\frac{\lambda_x\lambda_y^2}{2\lambda_y\lambda_y^2} = 9\frac{\lambda_x}{2\lambda_y}, \tag{3.3.40}$$

We see that the aplanarity α_{pl} is proportional to λ_x for $R \to \infty$, hence, λ_x has to behave asymptotically as $\lambda_x \overset{R\to\infty}{\longrightarrow} \tilde{c}/R^2$ for a prefactor $\tilde{c} > 0$ with the unit of squared area. To determine $\tilde{c}$, we need to estimate $\lambda_x = \varrho \int_{C_{cap}} (x - x_g)^2 \, dA$ up to terms of order $1/R^2$. First, we note that the integral over the area of the cylinder cap reads in our cylindrical coordinates

$$\int\limits_{C_{cap}} dA = R \int\limits_{-r_{mp}}^{r_{mp}} dz \int\limits_{-\phi(z)}^{\phi(z)} d\varphi, \tag{3.3.41}$$

where the range $\pm\phi(z)$ in the azimuthal angle φ is z-dependent. Second, from fig. 3.5, we derive the expression for the azimuthal angle range

$$\phi(z) = \arccos\left(1 - \frac{r_{mp}^2 - z^2}{2R^2}\right) = \left(\frac{{r_{mp}}^2 - z^2}{R^2}\right)^{1/2} + \frac{1}{24}\left(\frac{{r_{mp}}^2 - z^2}{R^2}\right)^{3/2} + \mathcal{O}\left(\frac{1}{R^5}\right), \tag{3.3.42}$$

by elementary trigonometry. We start with the estimate of x_g up to lowest order in $1/R$. We get the prefactor of this lowest order term by series expansion of the integrands of the integrals we have to estimate for x_g. To lowest order, the integrals $\int_{C_{cap}} dA$ and $\int_{C_{cap}} x dA$

are given by

$$\begin{aligned}\int\limits_{C_{cap}} dA &= \pi r_{mp}^2 \left(1 + \frac{1}{32}\left(\frac{r_{mp}}{R}\right)^2\right) + \mathcal{O}\left(\frac{1}{R^4}\right),\\ \int\limits_{C_{cap}} x dA &= \pi r_{mp}^2 R \left(1 - \frac{3}{32}\left(\frac{r_{mp}}{R}\right)^2\right) + \mathcal{O}\left(\frac{1}{R^3}\right).\end{aligned} \tag{3.3.43}$$

Hence

$$x_g = R\frac{1 - \frac{3}{32}\left(\frac{r_{mp}}{R}\right)^2 + \mathcal{O}\left(\frac{1}{R^4}\right)}{1 + \frac{1}{32}\left(\frac{r_{mp}}{R}\right)^2 + \mathcal{O}\left(\frac{1}{R^4}\right)} = R - \frac{1}{8}\frac{r_{mp}^2}{R} + \mathcal{O}\left(\frac{1}{R^3}\right). \tag{3.3.44}$$

Next, we investigate how the approximation error ϵ of an approximation $\widehat{x}_g = x_g - \epsilon$ for x_g propagates in the estimation of the gyration tensor component a_{xx}:

$$\begin{aligned}a_{xx}/\varrho = \int_{C_{cap}} (x - x_g)^2 \, dA &= \int_{C_{cap}} (x - \widehat{x}_g - \epsilon)^2 \, dA,\\ &= \int_{C_{cap}} (x - \widehat{x}_g)^2 \, dA - 2\epsilon \int_{C_{cap}} (x - \widehat{x}_g) \, dA + \epsilon^2 A_{C_{cap}},\\ &= \int_{C_{cap}} (x - \widehat{x}_g)^2 \, dA - 2\epsilon \int_{C_{cap}} (x - x_g + \epsilon) \, dA + \epsilon^2 A_{C_{cap}},\\ &= \int_{C_{cap}} (x - \widehat{x}_g)^2 \, dA - 2\epsilon \underbrace{\int_{C_{cap}} (x - x_g) \, dA}_{=0} - \epsilon^2 A_{C_{cap}},\\ &= \int_{C_{cap}} (x - \widehat{x}_g)^2 \, dA - \epsilon^2 A_{C_{cap}},\end{aligned} \tag{3.3.45}$$

where $A_{C_{cap}}$ denotes the total area of the cylinder cap. Thus, if we use expression (3.3.44) to calculate $a_{xx} = \lambda_x$ we introduce an error of the order $\epsilon^2 = \mathcal{O}\left(1/R^6\right)$. Hence, as we need to estimate λ_x up to order $1/R^2$, the approximation order in eq. (3.3.44) is sufficient. Insertion of x_g into the definition $\lambda_x = \varrho \int_{C_{cap}} (x - x_g)^2 \, dA$ and collecting lowest order terms yields for λ_x the result

$$\lambda_x = \frac{\pi}{64}\frac{r_{mp}^6}{R^2}\varrho + \mathcal{O}\left(\frac{1}{R^4}\right), \tag{3.3.46}$$

which scales with $1/R^2$, as expected. We read off the prefactor $\tilde{c} = \pi r_{mp}^6 \varrho/64$ and by insertion of $\lambda_x = \tilde{c}/R^2$ and λ_y from eq. (3.3.39) into eq. (3.3.40) we obtain

$$\alpha_{pl} = \frac{9}{32}\left(\frac{r_{mp}}{R}\right)^2, \tag{3.3.47}$$

and by insertion of $c = 9r_{mp}^2/32$ into eq. (3.3.38) we finally arrive at

$$\kappa = \frac{9}{16}k_\alpha r_{mp}^2 \varrho. \tag{3.3.48}$$

With this results for κ, we determine the saddle-splay modulus by means of relation eq. (3.3.36) to

$$\widehat{\kappa} = -\frac{3}{2} k_\alpha r_{mp}^2 \varrho. \tag{3.3.49}$$

Both curvature moduli are proportional to the number of particles $\pi r_{mp}^2 \varrho$ inside one cutoff range. Note that the negative sign of $\widehat{\kappa}$ indicates that “saddles”, i.e. principal curvatures having different signs, are unfavorable. Since above expression for κ ($\widehat{\kappa}$) has been derived by assuming an uniform weight function with cutoff $w = \Theta(r_{mp} - r)$ it provides an upper(lower) bound for κ ($\widehat{\kappa}$) compared to non-uniform weighting $w \leq \Theta(r_{mp} - r)$.

In the following, we investigate the bending rigidity κ for the non-uniform weight function in eq. (3.3.3) which we use in simulations. We expect that the asymptotic scaling argument we used for the calculation with uniform weighting is suitable for non-uniform weighting as well. In particular, we expect the bending rigidity again to scale as $\kappa \propto k_\alpha r_{mp}^2 \varrho$, only the proportionality constant may depend on the choice of the weighting. The exact value of the proportionality constant is important for comparison with measurements of the bending rigidity in simulations, see section 3.4.5.

We start from eq. (3.3.40), derived for the cylinder geometry, and estimate the prefactor c in the relation $\alpha_{pl} = c/R^2$. To calculate λ_y with the weight function eq.(3.3.3) in the limit $R \to \infty$, we insert the weight function into the integrand in eq. (3.3.39) which results in

$$\lambda_y \overset{R\to\infty}{\longrightarrow} \varrho \int\limits_{C_{circ}} y^2 w\left(r\right) dA = \varrho \pi r_{mp}^4 \int_0^1 u^3 w\left(u\right) du \approx \varrho \pi r_{mp}^4 \cdot 0.02449, \tag{3.3.50}$$

with the substitution $u = r/r_{mp}$. For the weight function eq. (3.3.3), the integral cannot be calculated analytically such that we resort on numerical evaluation. To estimate the remaining eigenvalue $\lambda_x = \varrho \int_{C_{cap}} \left(x - x_g\right)^2 w\left(|\boldsymbol{r}_p - \boldsymbol{r}|\right) dA$, we first calculate the center of mass position x_g. Our previous result for uniform weighting, eq. (3.3.44), implies that x_g behaves asymptotically as

$$x_g = R - c_1 \frac{r_{mp}^2}{R} + \mathcal{O}\left(\frac{1}{R^3}\right), \tag{3.3.51}$$

for a dimensionless constant $c_1 > 0$ which we estimate in the following. To apply the definition of x_g, eq. (3.3.16), we have to calculate the distance $|\boldsymbol{r}_p - \boldsymbol{r}|$ of the particle at position $\boldsymbol{r}_p$ with an arbitrary particle inside the interaction range. In our cylindrical coordinate system it is $\boldsymbol{r}_p = (R, 0, 0)$ and $\boldsymbol{r} = (R\cos\varphi, R\sin\varphi, z)$, hence

$$|\boldsymbol{r}_p - \boldsymbol{r}| = \sqrt{2R^2\left(1 - \cos\varphi\right) + z^2}. \tag{3.3.52}$$

We introduce the rescaled variables $\eta = z/r_{mp}$ and $\zeta = R/r_{mp}$ and rewrite $w\left(|\boldsymbol{r}_p - \boldsymbol{r}|\right)$ with eqns. (3.3.3) and (3.3.52) as

$$w\left(\eta, \varphi, \zeta\right) = \exp\left(\frac{4\left(2\zeta^2\left(1 - \cos\varphi\right) + \eta^2\right)}{\left(2\zeta^2\left(1 - \cos\varphi\right) + \eta^2\right)^6 - 1}\right). \tag{3.3.53}$$

The integration range $\phi(z)$ in φ, eq. (3.3.42), yields rewritten

$$\phi(\eta, \zeta) = \arccos\left(1 - \frac{1}{2}\frac{1 - \eta^2}{\zeta^2}\right). \tag{3.3.54}$$

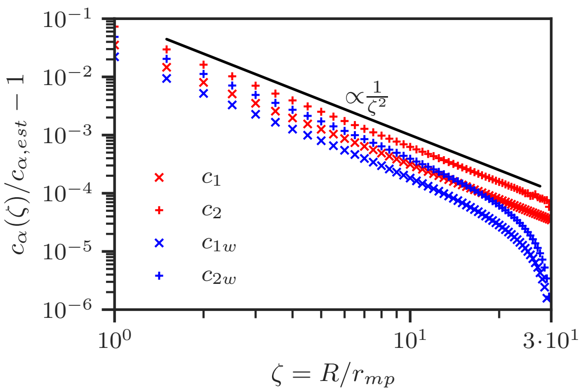

FIGURE 3.6. Relative deviation of the estimates for the constants c_α ($\alpha = 1, 2$ for uniform, $\alpha = 1w, 2w$ for non-uniform weight) via numerical calculation of eqns. (3.3.56),(3.3.59) for varying $\zeta = R/r_{mp}$ from the final estimate $c_{\alpha,est}$ used for the bending rigidity estimation. Red curves show the case of uniform weighting with cutoff, blue curves correspond to the non-uniform weight function eq. (3.3.53). For uniform weighting, we set $c_{1,est} = 1/8, c_{2,est} = \pi/64$ from the analytical results eqns. (3.3.44),(3.3.46), for non-uniform weighting we set $c_{\alpha w,est} = c_{\alpha w}(\zeta = 30)$, see eqns. (3.3.57) and (3.3.60).

We could estimate the constant c_1 in eq. (3.3.51) by a series expansion of $w(\eta, \phi, \zeta)$ and $\phi(\eta, \zeta)$ in the integrands occurring in the definition of x_g, eq. (3.3.16), as we did in the case of uniform weighting. However, it is easier to start from what we already know about the asymptotic behavior of x_g. Equating eq. (3.3.51) with the definition of x_g eq. (3.3.16) leads to the equation

$$\begin{aligned} x_g = \frac{\int_{C_{cap}} x w\left(|\boldsymbol{r}_p - \boldsymbol{r}|\right) dA}{\int_{C_{cap}} w\left(|\boldsymbol{r}_p - \boldsymbol{r}|\right) dA} &= \frac{r_{mp} R \int_{-1}^{+1} \int_{-\phi(\eta,\zeta)}^{+\phi(\eta,\zeta)} R \cos\varphi \, w\left(\eta, \varphi, \zeta\right) d\varphi d\eta}{r_{mp} R \int_{-1}^{+1} \int_{-\phi(\eta,\zeta)}^{+\phi(\eta,\zeta)} w\left(\eta, \varphi, \zeta\right) d\varphi d\eta} \\ &= R - c_1 \frac{r_{mp}^2}{R} + \mathcal{O}\left(\frac{1}{R^3}\right), \end{aligned} \tag{3.3.55}$$

which we rearrange to

$$\zeta^2 \frac{\int_{-1}^{+1} \int_{-\phi(\eta,\zeta)}^{+\phi(\eta,\zeta)} \left(1 - \cos\varphi\right) w\left(\eta, \varphi, \zeta\right) d\varphi d\eta}{\int_{-1}^{+1} \int_{-\phi(\eta,\zeta)}^{+\phi(\eta,\zeta)} w\left(\eta, \varphi, \zeta\right) d\varphi d\eta} = c_1 + \mathcal{O}\left(\frac{1}{\zeta^2}\right). \tag{3.3.56}$$

The left-hand side of this equation can be evaluated numerically as a function of $\zeta = R/r_{mp}$ and converges against the desired constant c_1 for $\zeta \to \infty$. The charm in the evaluation of c_1 in this way is that we can easily exchange the weight function with any other function we want to evaluate the bending rigidity for. With w as in eq. (3.3.53), numerical estimation for $\zeta \gg 1$ leads to

$$c_1 \approx 0.05199879. \tag{3.3.57}$$

Numerical convergence of eq. (3.3.56) is rather rapid, with estimates for $\zeta = 1$ and $\zeta = 30$ differing by less than 10% (see fig. 3.6). We derive an expression which converges against the eigenvalue λ_x in the same fashion. From eq. (3.3.46) follows that λ_x behaves asymptotically as $\lambda_x = c_2 \varrho r_{mp}^6 / R^2 + \mathcal{O}(1/R^4)$ for a constant $c_2 > 0$, hence

$$\lambda_x = \varrho r_{mp} R \int_{-1}^{+1} \int_{-\phi(\eta,\zeta)}^{+\phi(\eta,\zeta)} \left(R\cos\varphi - R + c_1 \frac{r_{mp}^2}{R} \right)^2 w\left(\eta, \varphi, \zeta\right) d\varphi d\eta = c_2 \varrho \frac{r_{mp}^6}{R^2} + \mathcal{O}\left(\frac{1}{R^4}\right), \tag{3.3.58}$$

where we already inserted x_g up to order $1/R$. Rearrangement of terms yields

$$\zeta^5 \int_{-1}^{+1} \int_{-\phi(\eta,\zeta)}^{+\phi(\eta,\zeta)} \left(\cos\varphi - 1 + c_1 \frac{1}{\zeta^2} \right)^2 w\left(\eta, \varphi, \zeta\right) d\varphi d\eta = c_2 + \mathcal{O}\left(\frac{1}{\zeta^2}\right) \tag{3.3.59}$$

Insertion of c_1 from above and numerical evaluation of the limit $\zeta \gg 1$ of the left hand side yields

$$c_2 \approx 0.00315362565, \tag{3.3.60}$$

and hence $\lambda_x \approx 0.00315 \varrho r_{mp}^6 / R^2$. Together with λ_y from eq. (3.3.50), insertion into eqns. (3.3.40) and (3.3.38) yields the estimate

$$\kappa \approx 0.368 k_\alpha \varrho r_{mp}^2, \tag{3.3.61}$$

for the MMM-bending rigidity with weight function eq. (3.3.3). For the numerical evaluation of eqns. (3.3.50),(3.3.56) and (3.3.59) we rely on the routine `NIntegrate[]` of the computer algebra system MATHEMATICA [83]. The bending rigidity in eq. (3.3.61) amounts to approximately 60% of the bending rigidity with uniform weighting, eq. (3.3.48). In section 3.4.5 measurements of the bending rigidity in simulations are compared with the estimate eq. (3.3.61) from continuum theory. Differences may arise due to the finite temperature as well as the non-uniform particle density in simulations; both have not been accounted for in the presented continuum approach.

In conclusion, we derived exact expressions for bending rigidity eq. (3.3.48) and saddle-splay modulus eq. (3.3.49) for uniform weighting and an estimate eq. (3.3.61) of the bending rigidity for the non-uniform weight function eq. (3.3.3). Our approach allows approximation of these curvature moduli for any other weight function.

3.3.4. Isotropic Compressibility Dependence on Weight Function.

We take a look at the isotropic *compressibility* of the MMM-potential and especially its dependence on the choice of the weight function. The isotropic compressibility determines how the system volume changes upon an isotropic pressure change and is defined for an isothermic system as

$$\kappa_T = -\frac{1}{V}\left(\frac{\partial V}{\partial p}\right)_T = \frac{1}{V}\left(\frac{\partial^2 F}{\partial V^2}\right)_T^{-1}. \tag{3.3.62}$$

Its inverse $K_T = 1/\kappa_T = -V\left(\frac{\partial p}{\partial V}\right)_T$ is referred to as *compressibility modulus.* To connect the MMM-potential with the compressibility, we introduce the virial stress tensor $\overline{\boldsymbol{\sigma}}_V$. Let U be the potential energy of our system, such that $\boldsymbol{F}_i = -\nabla_i U$ is the resulting force on particle i. The virial stress can then be expressed through the positions $\{\boldsymbol{r}_i\}$ and forces $\{\boldsymbol{F}_i\}$ on the particles [76]:

$$\overline{\boldsymbol{\sigma}}_V = -\frac{1}{V}\sum_i \boldsymbol{r}_i \otimes \nabla_i U, \tag{3.3.63}$$

where V denotes the system volume. Only internal stresses, generated by forces between the particles, enter in the calculation of the virial stress. The net pressure p the system exerts on its surroundings is then given by $p = -\operatorname{tr}\left(\overline{\boldsymbol{\sigma}}_V\right)/3$ or

$$p = -\frac{1}{3}\sum_{\alpha}\sigma^V_{\alpha\alpha} = -\frac{1}{3V}\sum_{\alpha}\sum_{i}\alpha_i\partial_{\alpha_i}U = -\frac{1}{3V}\sum_{i}\boldsymbol{r}_i\cdot\nabla_i U. \tag{3.3.64}$$

To analyze the compressibility, we investigate the work $\delta W = pdV$ necessary for an isotropic volume change by a factor $a \in \mathbb{R}$. We choose the coordinate system such that the gyration tensor is diagonal. From the definitions of center of mass , eq. (3.3.4), and gyration tensor, eq. (3.3.5), we see that for a rescaling of all particle positions $\boldsymbol{r}_i \to a\boldsymbol{r}_i$ the quantities behave as

$$\begin{aligned}
\boldsymbol{r}_g(\{\boldsymbol{r}_i\}) = \frac{\sum_{j=1}^N \boldsymbol{r}_j w\left(r_{ij}\right)}{\sum_{j=1}^N w\left(r_{ij}\right)} &\longrightarrow \boldsymbol{r}_g(\{a\boldsymbol{r}_i\}) = a\frac{\sum_{j=1}^N \boldsymbol{r}_j w\left(ar_{ij}\right)}{\sum_{j=1}^N w\left(ar_{ij}\right)} \\
\lambda_\alpha(\{\boldsymbol{r}_i\}) = \sum_{j=1}^N\left(\alpha - \alpha_g(\{\boldsymbol{r}_i\})\right)^2 w\left(r_{ij}\right) &\longrightarrow \lambda_\alpha(\{a\boldsymbol{r}_i\}) = \sum_{j=1}^N\left(a\alpha - \alpha_g(\{a\boldsymbol{r}_i\})\right)^2 w\left(ar_{ij}\right)
\end{aligned} \tag{3.3.65}$$

for $\alpha = x, y, z$. For a weight function which is homogeneous of degree $n \in \mathbb{R}$, i.e. for which $w\left(ar\right) = a^n w\left(r\right)$ we see that $\boldsymbol{r}_g(\{a\boldsymbol{r}_i\}) = a\boldsymbol{r}_g(\{\boldsymbol{r}_i\})$ and $\lambda_\alpha(\{a\boldsymbol{r}_i\}) = a^{n+2}\lambda_\alpha(\{\boldsymbol{r}_i\})$. By insertion of the gyration tensor eigenvalues in the aplanarity definition, eq. (3.3.6), we see that the factors a^{n+2} in denominator and nominator cancel and the aplanarity does not change:

$$\alpha_{pl}(\{a\boldsymbol{r}_i\}) = \alpha_{pl}(\{\boldsymbol{r}_i\})\,. \tag{3.3.66}$$

Hence, the total MMM-potential energy is constant. Since the MMM-potential energy is constant during volume expansion, the corresponding work $\delta W = pdV$ has to vanish, i.e. the net pressure p has to be zero. We can derive the same result by using the *Euler homogeneity relation*

$$n\Phi(\boldsymbol{r}) = \boldsymbol{r}\cdot\nabla\Phi(\boldsymbol{r})\,, \tag{3.3.67}$$

for any homogeneous function Φ of degree $n \in \mathbb{R}$. If the MMM-potential energy U stays constant during volume expansion $\boldsymbol{r}_i \to a\boldsymbol{r}_i$, it is a homogeneous function of degree $n = 0$ and by comparision of eqns. (3.3.67) and (3.3.64) we see again that $p \equiv 0$.

Hence, for any homogeneous weight function w, net pressure vanishes $p \equiv 0$ as well as the compressibility modulus K_T. From a practical point of view, the MMM-potential should influence non-membrane properties (i.e. all properties not directly related to the bending rigidity) as little as possible. In one dimension, the family of homogeneous functions of degree n is given by $w\left(r\right) = w\left(1\right)r^n$ with $w\left(1\right) \in \mathbb{R}$. We expect that, the closer the weight function resembles one member of this family, the smaller will be the MMM-potential contribution to net pressure and compressibility modulus K_T. A simple example is constant weighting with cutoff $w = \Theta(r_{mp} - r)$; Non-zero contributions to the net pressure only arise if particles cross the interaction range r_{mp}.

3.3.5. Adaptations to Algorithm. In the context of periodic boundary conditions and parallelization, adaptations to the simulation algorithm are necessary.

Periodic Boundary Conditions. To calculate the MMM-force on a particle i we have to add all force contributions from particles j inside the interaction range, i.e. all particles with $r_{ij} \leq r_{mp}$. In simulations, a common construct is the Verlet-list V_i which stores the indices of all particles j which interact with particle i. Note that for the MMM-potential the particle i itself also yields a force contribution such that $i \in V_i$. The MMM-force $F_{i\rho}$ on particle i in direction $\rho \in \{x, y, z\}$ reads then

$$F_{i\rho} = k_\alpha \sum_{j \in V_i} \frac{\partial}{\partial \rho_i} \alpha_{pl}\Big(\boldsymbol{r}_j, \{\boldsymbol{r}_k\}_{k \neq j}\Big) \,, \tag{3.3.68}$$

where $\alpha_{pl}\Big(\boldsymbol{r}_j, \{\boldsymbol{r}_k\}_{k \neq j}\Big)$ denotes the aplanarity with center particle j; the partial derivatives follow from eqns. (3.3.10) and (3.3.11). In the pre-existing simulation framework, reflective, bouncing-back and periodic boundary conditions are implemented at the faces of the simulation box [68]. Reflective and bouncing-back boundary conditions can be directly applied to the MMM-potential as implemented in ref. [68]. For periodic boundary conditions, it is necessary to rewrite the particle positions in terms of distance vectors to the center particle:

$$\alpha_{pl}\Big(\boldsymbol{r}_j, \{\boldsymbol{r}_k\}_{k \neq j}\Big) = \alpha_{pl}\Big(\boldsymbol{r}_j, \{\boldsymbol{r}_j + \boldsymbol{r}_{kj}\}_{k \neq j}\Big) \,, \tag{3.3.69}$$

as for every particle j the distance vectors $\boldsymbol{r}_{kj}$ are well-defined, whereas the absolute positions are not. In this work, we apply the minimal image convention [76], i.e.

$$\rho_{kj} = \rho_k - \rho_j - L_\rho \,\mathrm{nint}\left(\frac{\rho_k - \rho_j}{L_\rho}\right), \qquad \rho \in \{x, y, z\} \,, \tag{3.3.70}$$

for a simulation box volume $V_b = \prod_\rho [0, L_\rho]$, nint() denotes the nearest-integer function. Expression of the the aplanarities in terms of distance vectors also resolves ambiguities which arise in the calculation of the virial stress [84].

Parallelization. In the pre-existing simulation algorithm, the force calculation is parallelized along the loop over all particles. In the former model, all forces are pairwise such that the force calculation can be performed by a pseudo-routine `calcForce(i,j)` which receives the indices i, j of the particle pair as arguments. Thus, for N particles the update of the array `Force[]`, which contains the current forces, is accomplished by the pseudocode

```
BEGIN PARALLEL LOOP
for $i \in \{0, 1, \dots N\}$ do
  for $j \in V_i$ do
    Force[i] += calcForce(i,j)
  end for
end for
END PARALLEL LOOP
```

The inner loop calculates the net force on particle i. In the pre-existing simulation, the parallelization of the force loop is done by splitting up the index set $\{0, 1, \dots N\}$ of the particles into chunks which are distributed among the threads. To split the workload along net force calculations for chunks of particle indices is not suitable for the MMM-potential as it involves many redundant calculations. The calculation of the net force on particle i

involves calculation of all MMM-related quantities for the particles $j \in V_i$, which are also necessary to calculate the forces of all particles $\{k : \exists j \in V_i \text{ with } k \in V_j\}$ which interact with the particles in the Verlet-list V_i of particle i. To avoid this redundancy, the MMM-force calculation is performed by looping over all force contribution calculations of particle i to the particles $j \in V_i$. From eq. (3.3.68) we see that this force contribution is given by the term $k_\alpha \frac{\partial}{\partial \rho_j} \alpha_{pl}\Big(\boldsymbol{r}_i, \{\boldsymbol{r}_k\}_{k \neq i}\Big)$. We denote with `calcMMMForceContrib(i,j)` the pseudo-function which receives the indices of a particle pair i, j (i being the center particle) and returns the force contribution on particle j. Note that `calcMMMForceContrib(i,j)` is, in general, not symmetric

$$\texttt{calcMMMForceContrib(i,j)} \neq \texttt{calcMMMForceContrib(j,i)} \tag{3.3.71}$$

and that every particle contributes to its own force (the case $j = i$ occurs as well). For n_p parallel processors with individual ids $pid \in \{0, 1, \dots n_p\}$, the pseudo-code for the MMM-force calculation reads

```
BEGIN PARALLEL LOOP
for $i \in \{0, 1, \dots N\}$ do
   for $j \in V_i$ do
      storeForce[pid][j] += calcMMMForceContrib(i,j)
   end for
end for
END PARALLEL LOOP
for $pid \in \{0, 1, \dots n_p\}$ do
   for $i \in \{0, 1, \dots N\}$ do
      Force[i] += storeForce[pid][i]
   end for
end for
```

Again, the outermost loop over the set of particle indices is distributed among the processors. Note that in the inner loop of the parallel block the force of particle j is incremented. As a consequence, the force contributions are stored in an intermediate array `storeForce[][]`, separately for every processor, to avoid that two processors access the same memory address at the same time. After the parallel loop, the force contributions are added up to the total force by a single processor.

3.4. Measurement of Growing Membrane Parameters

We present *in silico* measurements for homeostatic pressure γ_h, growth rate pressure sensitivity ξ, area compressibility χ_a, homeostatic density ϱ_h as well as the bending rigidity κ. Measurements are performed for different simulation parameter values, starred simulation parameters refer to values relative to the standard parameter set (table I.1 in appendix I), e.g. $B^* = B/B_{std}$. Unless explicitly stated otherwise, all simulation parameters equal their standard values. Tables I.2 and I.3 show an overview of all measurement results.

3.4.1. Surface Tension Measurements and Virial Stress. To begin, we take a look at surface tension measurements which are required for all parameter measurements. The surface tension is related to the profile of the stress tensor along the membrane thickness d

$$\gamma = \int_{-d/2}^{d/2} \left(\sigma_{\|}(z) - \sigma_{\perp}(z)\right) \, dz \tag{3.4.1}$$

where $\sigma_{\|}$ and $\sigma_{\perp}$ denote the local stress components in in-plane and normal direction of the membrane [85]. These components are calculated from the stress tensor $\overline{\boldsymbol{\sigma}}$ via multiplication with the unit vectors $\boldsymbol{e}_{\|}$, $\boldsymbol{e}_{\perp}$ in the corresponding directions, hereby we interpret the stress tensor as a bilinear form:

$$\sigma_{\|} = \boldsymbol{e}_{\|} \cdot \left(\overline{\boldsymbol{\sigma}} \boldsymbol{e}_{\|}\right), \qquad \sigma_{\perp} = \boldsymbol{e}_{\perp} \cdot \left(\overline{\boldsymbol{\sigma}} \boldsymbol{e}_{\perp}\right). \tag{3.4.2}$$

For a monolayered membrane, the stress tensor is approximately constant in lateral direction, thus $\gamma = d\left(\sigma_{\|} - \sigma_{\perp}\right)$. The surface tension calculation consists of two steps: first we have to estimate the stress tensor and second project it onto normal and in-plane directions of the membrane. We first analyze the projection problem. To calculate the projections 3.4.2 for a given stress tensor field $\overline{\boldsymbol{\sigma}}(\boldsymbol{x})$, normal and in-plane directions have to be calculated at every point on the membrane with time, since they do not stay constant during the folding process. Numerical estimation of the local surface normal can be done, for example, by diagonalization of the local gyration tensor which we already calculate in the MMM-force routines. However, together with the necessary consistency checks of the surface normal field to guarantee proper orientation and removal of spurious vectors, this is a numerical expensive task to be done at every point in membrane-space-time. To avoid the normal field calculation, we note the similarity of the surface tension with the isotropic net pressure:

$$p = -\frac{1}{3} \operatorname{tr}\left(\overline{\boldsymbol{\sigma}}\right) = -\frac{1}{3}\left(2\sigma_{\|} + \sigma_{\perp}\right), \tag{3.4.3}$$

where we assume isotropic stress in the in-plane direction. The pair-potentials in the simulation mainly contribute to the in-plane stress component $\sigma_{\|}$, since their forces are directed along the particle bonds in the membrane. Therefore, the main contribution to the normal stress $\sigma_{\perp}$ arises from the MMM-potential. The force scaling arguments in section 3.3.2 estimate the lateral MMM-forces F_z to scale as $F_z \sim d$, thus $\sigma_{\perp} \sim F_z d \sim d^2$. Therefore, we expect that the lateral MMM-stress is small compared to the stress of the in-plane pairwise potentials. We neglect the normal component compared to the in-plane stress $\sigma_{\perp} \ll \sigma_{\|}$ and approximate the surface tension with the local stress tensor via

$$\gamma(\boldsymbol{x}) \approx \sigma_{\|} d \approx -\frac{3}{2} p\left(\boldsymbol{x}\right) d = \frac{d}{2} \operatorname{tr} \overline{\boldsymbol{\sigma}}(\boldsymbol{x}). \tag{3.4.4}$$

Above relation eases the calculation of the surface tension tremendously as the trace of the stress tensor is invariant under rotations of the coordinate system, hence, we can choose at every point $\boldsymbol{x}$ the convenient Cartesian coordinate system

$$\gamma\left(\boldsymbol{x}\right) = \frac{d}{2} \sum_{i \in \{x,y,z\}} \sigma_{ii}(\boldsymbol{x}). \tag{3.4.5}$$

With above approximation we completely avoid the estimation of the surface normal field and instead calculate γ in the Cartesian lab coordinate system.

Next, we take a look at the task of measuring the stress tensor. We already touched the subject of stress calculation briefly in section 3.3.4 where we took a look at the net pressure contribution of the MMM-potential. The stress tensor can be separated into two contributions $\overline{\boldsymbol{\sigma}} = \overline{\boldsymbol{\sigma}}_{kin} + \overline{\boldsymbol{\sigma}}_{pot}$ related to momentum transport and force contributions [76, 86]. The virial stress tensor contributions are given by

$$\begin{aligned} \overline{\boldsymbol{\sigma}}_{kin} V &= \sum_i m \boldsymbol{v}_i \otimes \boldsymbol{v}_i \\ \overline{\boldsymbol{\sigma}}_{pot} V &= \sum_i \boldsymbol{r}_i \otimes \boldsymbol{F}_i \end{aligned} \tag{3.4.6}$$

where $\boldsymbol{r}_i$, $\boldsymbol{v}_i$ and $\boldsymbol{F}_i$ denote position, velocity and net force of particle i and V the system volume. With the formulas 3.4.6 and 3.4.5 we can directly calculate the "virial" surface tension from the virial stress. In the context of our membrane the total system volume V has to be replaced by the total membrane area A. As the virial stress tensor corresponds to the average of the local stress over the total system volume, the hereby determined surface tension is the spatial average of the local surface tension. Unfortunately, measurement of the stress tensor with spatial resolution comprises, in case of a multibody potential such as the MMM potential, a much harder problem (see appendix B). Therefore, we limit the surface tension evaluation to the spatially averaged "virial" surface tension.

3.4.2. Homeostatic Surface Tension. We define the homeostatic surface tension γ_h as the equilibrium surface tension of a flat, quadratic patch of membrane. To measure surface tension, we use eq. (3.4.6) where we replace system volume V with the membrane area A

$$A = \int_0^L \int_0^L \sqrt{1 + |\nabla h(x,y)|^2}\, dx dy. \tag{3.4.7}$$

The membrane area is calculated by numerical evaluation of above integral. To do so, we discretize the height profile $h(x,y)$ on a quadratic lattice with grid constant $r_{pp}/2$. At every point $(x_i, y_j) = (i r_{pp}/2, j r_{pp}/2)$ the approximated height z_{ij} is calculated as the weighted average $z_{ij} = \sum_\alpha z_\alpha w\left(|x_i - x_\alpha|, |y_i - y_\alpha|\right) / \sum_\alpha w\left(|x_i - x_\alpha|, |y_i - y_\alpha|\right)$ over all particles α in the cell (i,j) and its four nearest neighbors. We use a linear weight function $w\left(|x_i - x_\alpha|, |y_i - y_\alpha|\right) = \left(1 - \frac{4}{3}|x_i - x_\alpha|/r_{pp}\right)\left(1 - \frac{4}{3}|y_i - y_\alpha|/r_{pp}\right)$. The gradient ∇h is estimated by a three-point stencil in each direction of the discretized height profile $h(x_i, y_j)$. We expect the homeostatic surface tension γ_h to behave similar to its three-dimensional pendant, the homeostatic pressure p_h. Previous measurements of the homeostatic pressure found that p_h [68]

(1) decreases linearly with the adhesion strength $p_h \propto (f_1^* - 1)$,
(2) increases linearly with the growth force strength $p_h \propto (B^* - 1)$,
(3) is rather independent of the cell death rate k_a,
(4) increases with the compressibility $\kappa_T = 1/f_0$ for constant excluded volume radius (i.e. constant f_1/f_0).

Note that a negative homeostatic pressure, corresponding to a *tensile* homeostatic state, is possible as well [38]. Since the bending rigidity introduced by the MMM-potential does not tamper directly with the growth dynamics taking place in the in-plane direction, we expect that the sign of above relations 1.-4. stays the same for our membrane system. In particular, that the homeostatic surface tension is increasingly compressive with increasing growth pressure constant B^*. However, for the membrane system, measurements in the homeostatic state are not as easy to perform as for the three-dimensional analog, as we must avoid membrane buckling. For γ_h above the buckling threshold, we need to add a lateral

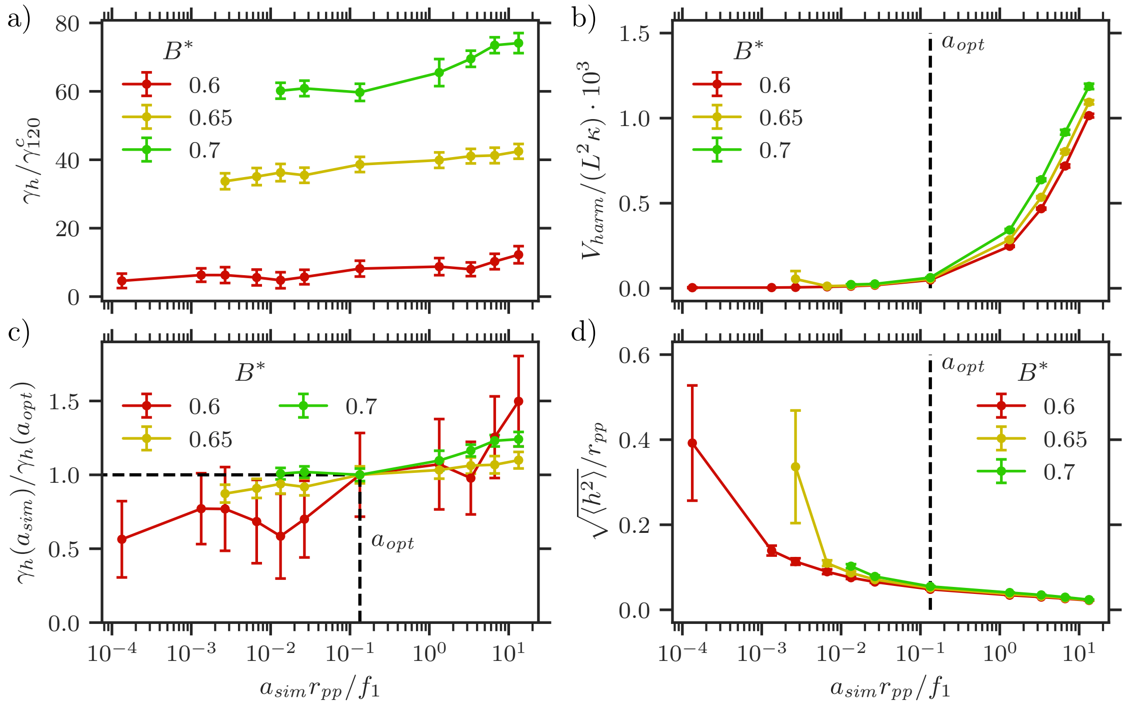

FIGURE 3.7. **a)** Homeostatic surface tension measurement for three different growth strengths B dependent on the applied harmonic confinement strength a_{sim}, measured with a medium system size of $L = 90r_{pp}$. The confinement strength a_{sim} has the unit force/length and is given in the units of attractive force constant over cutoff radius f_1/r_{pp}. The surface tension is given in units of the critical buckling surface tension $\gamma_{120}^c = \kappa(2\pi/L)^2$ for a medium system size $L = 120r_{pp}$. Note the shift to larger compressive tensions with increasing confinement strength. **b)** Energy per area V_{harm}/L^2 of the harmonic potential as a function of confinement strength, given in units of $10^{-3}\kappa$, κ denotes the bending rigidity. **c)** Fraction of surface tension measured at confinement strength a over measurement at chosen optimal confinement strength a_{opt}. Strongest deviations occur for the smallest growth strength $B^* = 0.6$. **d)** Square root of the second central moment $\langle h^2 \rangle$ as a measure of flatness of the membrane as a function of confinement strength. A value of $a_{sim} \approx 0.1 f_1/r_{pp}$ provides a good compromise in minimizing both V_{harm} and $\langle h^2 \rangle$. Error bars in a)-d) correspond to STDEV.

confinement to keep the membrane flat during the equilibration process. We expect that the lateral degree of freedom is sensible to any confinement as it consists only of a thin layer of particles. Therefore, instead of a hard confinement, we add a soft harmonic potential which contributes the energy

$$V_{harm} = \frac{a}{2}\int_A h^2 dA = \frac{a}{2}L^2\frac{1}{L^2}\int_A h^2 dA = \frac{a}{2}L^2\left\langle h^2 \right\rangle, \tag{3.4.8}$$

to the membrane and study the dependence of the equilibrium surface tension on the potential strength a (see fig. 3.7). In the context of our particle-based simulation, note that applying

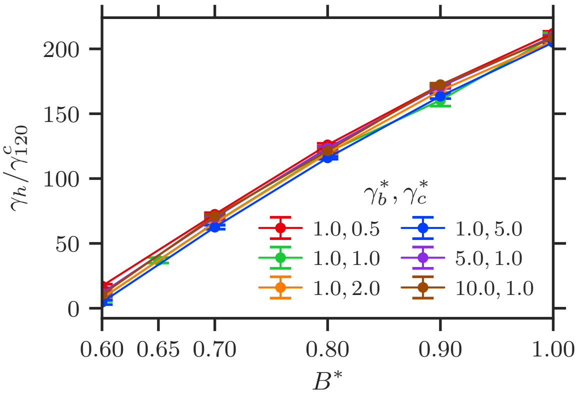

FIGURE 3.8. Surface tension measurements with optimal confinement strength a_{opt} dependent on growth strength B^*. Every line corresponds to one pair γ^*_b, γ^*_c of background and intracell friction (see legend). The apoptosis rate k_a is adjusted such that $\gamma^*_c k^*_a = 1$ for the different values of γ^*_c (see also section 4.3). We recover a linear relationship as in ref. [68]. Error bars correspond to STDEV.

a harmonic force $\boldsymbol{F} = -a_{sim}\boldsymbol{z}$ on every particle corresponds to a continuum energy density $f_{harm} = a_{sim}\varrho z^2/2$ with the particle density ϱ. Since the density ϱ in our simulations is typically spatially constant, we translate via $a = a_{sim}\varrho$ the simulation force strength a_{sim} to the continuum parameter a in eq. (3.4.8). The harmonic potential adds a net energy penalty on the lateral deflection h which is directly proportional to the average squared deflection $\langle h^2 \rangle$. To define the optimal value a_{opt} for the potential strength, we demand that the harmonic potential is strong enough to keep the membrane system flat, but still so weak that it does not tamper too much with the lateral degree of freedom. The homeostatic surface tension is then defined at this optimal confinement strength. As a measure of flatness we compare $\sqrt{\langle h^2 \rangle}$ with the cell-diameter on the order of the cutoff radius r_{pp}. Furthermore, we measure the total energy V_{harm} stored in the harmonic energy and demand it to be as small as possible. Hereby, particles buckling out of plane receive a "gentle punch" into the flat state, gentle enough that the general energy landscape of the membrane system is changed as little as possible by the harmonic potential. From the results summarized in fig. 3.7 we see that a value of a_{opt} around $a_{sim} \approx 0.1 f_1/r_{pp}$ is a good trade-off between both requirements. Comparison of the surface tensions γ reveal that for increasing a the surface tension shifts towards negative values, corresponding to an increase in compressive stress. Hence, the confinement of the lateral dimension leads to a compression in the in-plane direction. The ratio $\gamma(a)/\gamma(a_{opt})$ varies strongest for the smallest growth strength $B^* = 0.6$, for larger B^* the ratio takes values larger than 120% only for strong confinements $a \gg 0.1 f_1/r_{pp}$. Figure 3.8 depicts measurements for growth pressure constants in the range $B^* = 0.6 - 1.0$. We recover a linear relationship as for the three-dimensional tissue.

3.4.3. Growth Pressure Sensitivity Constant. Corresponding to the general growth law eq. (2.1.2), the homeostatic growth rate law for the membrane system reads

$$k_g = \xi\left(\gamma - \gamma_h\right) \tag{3.4.9}$$

To access the pressure sensitivity constant ξ in above growth law, we need to measure the surface tension γ for a fixed growth rate k_g or vice versa. To do so, we develop a method to prescribe a fixed growth rate for a growing, flat membrane. We impose a harmonic confinement with $a_{sim} = a_{opt}$, as in the homeostatic surface tension measurements. For a flat membrane it is $A = L^2$ and by virtue of eq. (3.4.9) follows

$$\gamma = \gamma_h + \frac{k_g}{\xi} = \gamma_h + \frac{\partial_t A}{\xi A} = \gamma_h + \frac{2\partial_t L}{\xi L}. \tag{3.4.10}$$

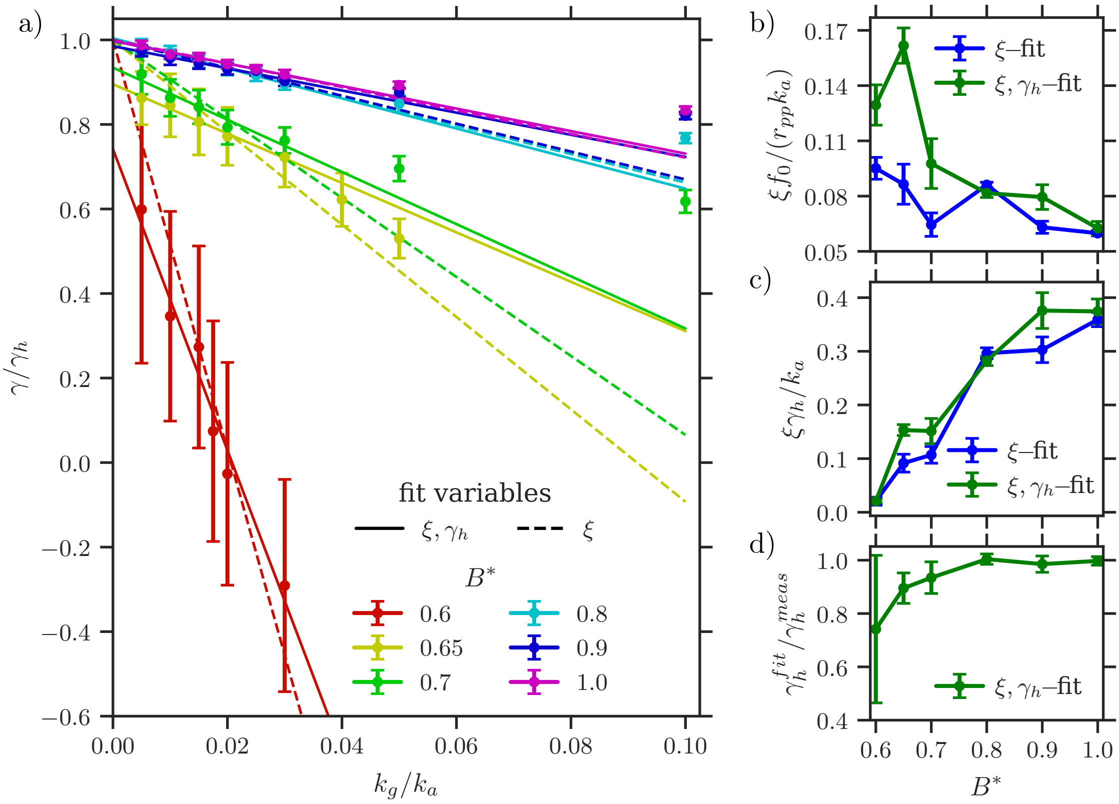

FIGURE 3.9. **a)** Growth rate k_g as a function of the measured equilibrium surface tension γ for growth strength parameters in the range $B^* = 0.6 - 1.0$. The growth rate is given in units of the fixed apoptosis rate k_a, surface tension in units of the homeostatic surface tension γ_h. Error bars refer to STDEV. Continuous lines depict linear fits of eq. (3.4.9) with both ξ and γ_h as free parameters, dashed lines linear fits with only ξ free and γ_h fixed to the previously measured value. **b)** Fit results for growth parameter ξ from both fitting methods, green with ξ, γ_h free and blue with only ξ as free parameter. **c)** As b) but results for inverse growth time scale $\xi\gamma_h$. **d)** Ratio of the homeostatic surface tension result from the fit over previously measured value. Error bars in b)-d) refer to square root of diagonal elements of the covariance matrix from least-squares minimization. The method `least_squares()` of the python package SciPy was used to solve the minimization problem [87].

This allows us to directly impose the growth rate by a constant rescaling of the box size L. For constant growth rate $k_g = 2\partial_t \log L$ it is

$$L(t) = L(0)\exp\left(\frac{k_g t}{2}\right). \tag{3.4.11}$$

In simulations, we directly set the box size to its value according to the exponential growth law eq. (3.4.11) and measure the resulting surface tension γ. The hereby implemented "constant-growth-module" is similar to an approach described in ref. [88] to achieve a constant-pressure-ensemble via rescaling of the system size. Figure 3.9 depicts an overview of the measured surface tensions γ for different prescribed values of the growth rate k_g. The measurements start from a flat, equilibrated membrane of size $L = 90 r_{pp}$ which grows at least up to a size of $L = 150 r_{pp}$. During membrane growth, the total number of cells N is monitored to ensure that the overall density ϱ stays constant. To estimate ξ, linear fits of relation eq. (3.4.10) are performed, one with the homeostatic surface tension γ_h fixed to their previous measured values and another with both γ_h and ξ as free parameters. For growth rates $k_g/k_a < 0.03$ the surface tension increases linearly with the growth rate, larger growth rates exhibit a non-linear increase. Therefore, the linear fits are constrained to growth rates $k_g/k_a \leq 0.03$. For $B^* \geq 0.7$ and $k_g/k_a > 0.03$ the surface tension γ is larger than the extrapolation of the linear fit. Thus, for fixed surface tension, the growth rate is *larger* than the value predicted by the linear extrapolation. For $B^* < 0.7$ the non-linear behavior is difficult to quantify due to large fluctuations in γ, as indicated by the large error bars. Whereas both fits lead to similar results for larger growth strength values $B^* \geq 0.8$, the spread in the two estimates increases towards the smallest growth strength $B^* = 0.6$. This difference can be attributed to the differences in the estimates for the homeostatic surface tension γ_h; the fitted value γ_h^{fit} is up to %25 smaller than the previously measured value γ_h^{meas}. It remains a difficult task to pin point the correct values for γ_h and ξ for growth strengths $B^* < 0.7$ due to the large fluctuations in the surface tension during measurements. Therefore, we have to be careful to draw conclusions about the scaling of ξ with B^*. For $B^* \geq 0.8$, ξ seems to be fairly constant around $\xi \approx 0.08 f_0 / r_{pp}^2 k_a$, for $B^* < 0.8$ the estimates from both fits fall in the range $\xi \approx 0.06 - 0.16 f_0 / r_{pp}^2 k_a$. Surprisingly, the prediction for the inverse growth time scale $\xi \gamma_h$ are consistent for both fits and show a clear increase with increasing B^*. The growth timescales for $B^* = 0.6 - 1.0$ cover roughly one order of magnitude, with $1/(\xi\gamma_h) \approx 2 - 50 k_a^{-1}$.

In conclusion, we can say that the ξ-measurements with the constant-growth module become more reliable for increasing B^*. For values B^* close to the switch from tension to compression around $B^* = 0.6$, the large signal to noise ratio of the surface tension measurements of around $\gamma_h / \Delta\gamma_h \approx 1$ makes precise measurements of both γ_h and ξ a difficult task. This imprecision results in a uncertainty factor of around two for the ξ measurements, whereas the errors in the inverse growth timescale $\xi\gamma_h$ luckily seem to cancel.

3.4.4. Area Compressibility. Surface tension is build up due to compression or expansion of the area the cells can occupy. For constant cell number, the area per cell is inversely proportional to the number density ϱ. We denote with ϱ_h the homeostatic density at which the surface tension equals the homeostatic value $\gamma = \gamma_h$. We expect the surface tension to scale linearly in the difference $\delta\varrho = \varrho_h - \varrho$ for small enough $\delta\varrho$. Thus, we relate surface tension γ and density ϱ via

$$\gamma - \gamma_h = \chi_a^{-1} \left(\varrho_h - \varrho \right). \tag{3.4.12}$$

where $\chi_a > 0$ denotes an effective compressive modulus, the *area compressibility*. To estimate χ_a, we use the surface tension measurements of the constant-growth module from the previous section. We expect that the linear relation (3.4.12) between surface tension γ and density ϱ holds if the system size growth rate k_g of the constant-growth module is small enough. Density measurements during system growth allow us then to measure the area compressibility χ_a as the proportionality factor between γ and ϱ. Figure 3.10 depicts the resulting $\gamma - \varrho$-plots. The surface tension scales indeed linearly with the density close to the homeostatic surface tension, whereas for too large deviations from γ_h the relation becomes non-linear. Deviations from linear behavior occur roughly at growth rates $k_g/k_a > 0.03$, as for the $k_g - \gamma$ scaling in the previous section. The fits of eq. (3.4.12) are performed in the linear range, i.e. for $k_g/k_a \leq$

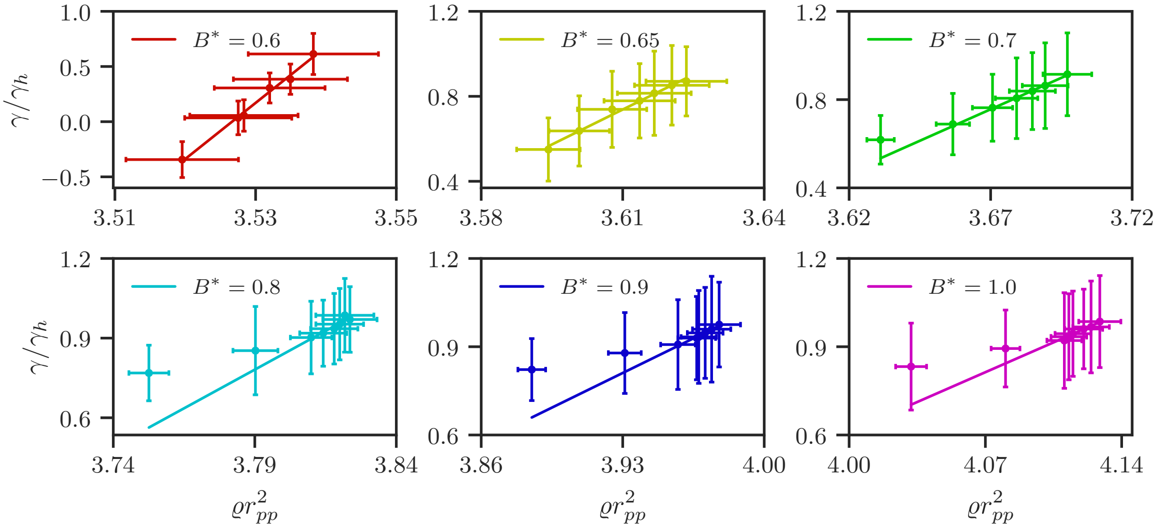

FIGURE 3.10. Surface tension γ versus particle density ϱ for growth strengths in the range $B^* = 0.6 - 1.0$. Error bars refer to STDEV. Continuous lines depict linear fits of relation eq. (3.4.12) with the method `least_squares()` of the python package SciPy [87].

FIGURE 3.11. Fit results for area compressibility χ_a (left axis, blue) and homeostatic density (right axis, red). Error bars refer to square root of diagonal entries of covariance matrix of least-squares fit (depicted in fig 3.10) with the method `least_squares()` of the python package SciPy [87].

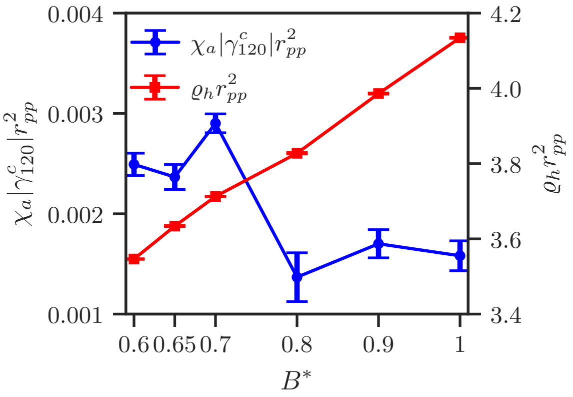

0.03. The non-linear behavior yields larger stresses as compared with the extrapolation of the linear fits of eq. (3.4.12). Thus, the hereby estimated value for the area compressibility is most likely too small. Figure 3.11 shows the fit result for area compressibility χ_a and the corresponding homeostatic density ϱ_h, dependent on growth strength parameter B^*. The homeostatic density exhibits a stable linear behavior. The estimated area compressibility χ_a is approximately constant $\chi_a \approx 0.0025\,|\gamma_{120}^c|\,r_{pp}^2$ for $B^* <= 0.7$ (γ_{120}^c denotes the critical buckling pressure for membrane size $L = 120r_{pp}$) and drops to $\chi_a \approx 0.0015\,|\gamma_{120}^c|\,r_{pp}^2$ for $B^* > 0.7$.

3.4.5. Bending Rigidity. In section 3.3.3 we derived an analytical prediction of the bending rigidity eq. (3.3.61)

$$\kappa \approx 0.368 k_\alpha r_{mp}^2 \varrho, \tag{3.4.13}$$

for the MMM-model with strength k_α, cutoff radius r_{mp}, particle density ϱ and weight function

$$w\left(r\right) = \exp\left(\frac{4\left(\frac{r}{r_{mp}}\right)^2}{\left(\frac{r}{r_{mp}}\right)^{12} - 1}\right). \tag{3.4.14}$$

In the analytic derivation of eq. (3.3.61), neither thermal noise, growth activity nor the non-homogeneous spatial particle distribution are taken into account. To investigate whether these phenomena lead to deviations, we compare measurements of κ in simulations with the analytical prediction of eq. (3.3.61). Theoretical studies of the effect of thermal fluctuations on the bending rigidity propose an effective rigidity κ_{th} of the form

$$\kappa_{th} = \kappa\left(1 - \alpha\frac{\delta A}{A}\right), \tag{3.4.15}$$

where κ denotes the bending rigidity without thermal fluctuations, A the equilibrium area at $k_bT = 0$, δA the average excess area created by thermal fluctuations and α a dimensionless factor [89, 90, 91]. To lowest order in k_bT, the analysis estimates $\delta A/A$ to

$$\frac{\delta A}{A} = \frac{k_bT}{8\pi\kappa}\log N, \tag{3.4.16}$$

where N denotes the number of molecules in the membrane. Remarkably, theoretical estimates of the exact value of the prefactor α result in contradicting signs. Values ranging from $\alpha = -1$ to $\alpha = 3$ are reported [89, 90, 91], leaving the question open whether thermal fluctuations lead to *softening* ($\alpha > 0$) or *stiffening* ($\alpha < 0$) of a membrane. As all mentioned studies agree on the functional dependence of the effective bending rigidity, eqns. (3.4.16) and (3.4.15), we estimate the order of magnitude of the correction term for the simulations performed in this work. With $k_bT = 0.1$ and $N = 10^4 - 10^5$ it is

$$\left|\frac{\kappa_{th} - \kappa}{\alpha}\right| = \frac{k_bT}{8\pi}\log N \approx 0.037 - 0.046, \tag{3.4.17}$$

in simulation units. In comparison, with $k_\alpha = 10$, $r_{mp} = 1.5$ and $\varrho = 3.5 - 4$, eq. (3.3.61) predicts $\kappa \approx 29 - 33$, thus, thermal fluctuations are largely negligible. Considering growth activity, it is known that division and apoptosis cause tissue fluidization leading to viscoelastic behavior [70]. In the context of growing membranes, these findings apply to the in-plane dynamics. The impact of growth activity on the fluctuation spectrum of a surface is a subject of current research, see e.g. refs. [92, 93].

In simulations, the bending rigidity is accessible by analysis of the thermal fluctuation spectrum. The fluctuation spectrum with a harmonic confinement according to eq. (3.4.8) and without elastic substrate reads

$$\left\langle\left|h_{\boldsymbol{k}}\right|^2\right\rangle = \frac{k_bT}{\kappa k^4 + \gamma k^2 + a}, \tag{3.4.18}$$

as a function of the wavenumber k (see appendix E.2). Above expression for the fluctuation spectrum is strictly only correct for passive membranes in thermal equilibrium. However, since our growth activity mainly affects cell dynamics in the in-plane direction, we are in

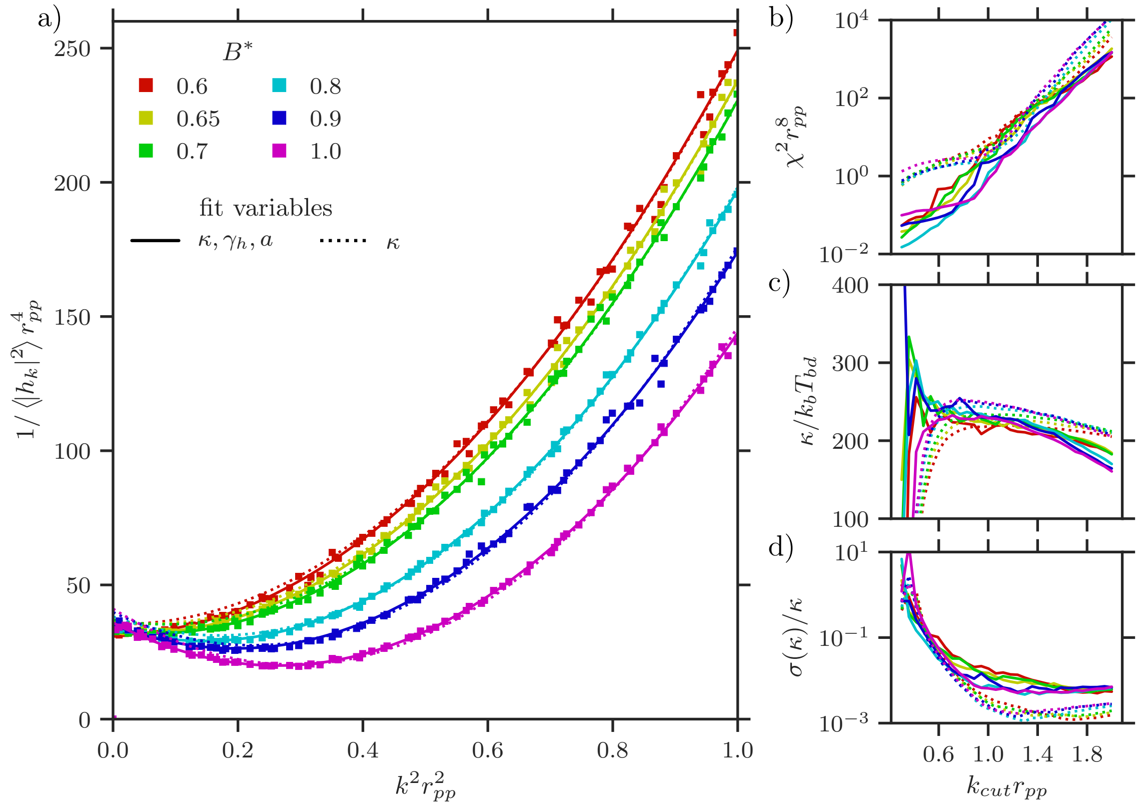

FIGURE 3.12. **a)** Inverse fluctuation spectra as a function of squared wavenumber k^2 for growth strength B^* in the range $B^* = 0.6 - 1.0$ (see legend). Continuous lines depict fits with all three parameters κ, γ_h, a free, dotted lines with only κ free and γ_h and $a = a_{opt}\varrho$ from separate measurements. The wavenumber cutoff for both fits is $k_{cut} = 1 r_{pp}$. **b)** Squared residue for inverse fluctuation spectra fits as a function of the wavenumber cutoff k_{cut}. Color code corresponds to growth strength parameter B^* as in a). Continuous lines correspond to three parameter fit with κ, γ_h, a free, dotted lines to one parameter fit with only κ free. **c)** Fit results for bending rigidity κ corresponding to b). **d)** Standard deviation of fitted value for bending rigidity $\sigma(\kappa)$ divided by κ; corresponding to b). The standard deviation $\sigma(\kappa)$ is calculated as square root of diagonal entries of covariance matrix of the least squares minimization.

good spirit that it holds also in our case. Another concern arises about the isotropy of the noise as implemented in the DPD simulation technique. DPD-noise with temperature $k_b T_{dpd}$ results in random forces along the line connecting interacting particles, hence, these forces are aligned mostly along the in-plane direction. In contrast, the Brownian background noise is isotropic. Hence, in the lateral direction the noise is mostly Brownian with a small DPD-contribution as the particle-particle connectors are not perfectly aligned in-plane. Thus, the effective lateral noise temperature $k_b T_e$ may be noticeably larger than the preset Brownian dynamics temperature $k_b T_{bd}$.

As the reciprocal fluctuation spectrum is a polynomial in k^2, a parabolic fit of $1/|h_{\boldsymbol{k}}|^2$ versus k^2 is typically used to estimate κ (see ref. [73], for a comparison with respect to other methods see ref. [74]). Note that the fitting range of the independent variable k determines the in-plane lengthscales of the considered fluctuations. From the calculations in section 3.3.3 we have already learned that the MMM-potential provides a "proper" bending rigidity only for curvature radii R much larger than the used cutoff radius $R \gg r_{mp}$. Hence, we cannot expect fluctuations on the length scale of r_{mp} to follow eq. (3.4.18). Furthermore, in simulations, the particle density ϱ determines down to which lengthscale the membrane is discretized by the particles. The discrete FFT of a set of N equidistant data points covers all wavevectors in the range $k \in [2\pi/L, N\pi/L]$ corresponding to the largest wavelength $\lambda = L$ spanning the whole system and the smallest wavelength $\lambda = 2L/N$, fitting on two equidistant intervals of size L/N. We expect especially for large wavenumbers deviations of the fluctuation spectrum measured in simulations from the analytic expression, eq. (3.4.18), due to decreasing number of particles fitting onto one wavelength. Therefore, the fits of the inverse fluctuation spectrum are done with different upper wavenumber cutoff k_{cut} to observe the changes in the fitted values for κ, γ and a. In simulations, a medium sized system of size $L = 90r_{pp}$ in homeostatic equilibrium is used to measure the Fourier coefficients $h_{\boldsymbol{k}}$ by discrete Fourier transformation of the same grid $z_{ij} = h(x_i, y_j)$ used for the area measurements (see section 3.4.2). The fast Fourier transform algorithm package FFTW is employed to numerically perform the Fourier transformation [1]. The same harmonic potential strength $a_{sim} = a_{opt}$ as in the measurements of γ_h and ξ is used to enforce the flat state during measurements. As the fluctuation spectrum only depends on the magnitude $k = |\boldsymbol{k}|$ of the wavevector, an average over all amplitudes with the same magnitude is performed. This average is defined via

$$\left\langle |h_k|^2 \right\rangle = \frac{\sum_{|\boldsymbol{k}|=k} |h_{\boldsymbol{k}}|^2}{\sum_{|\boldsymbol{k}|=k} 1}. \tag{3.4.19}$$

We perform a time average over a time window of $t = 50k_a^{-1}$ time units where k_a denotes the apoptosis rate. Noise temperatures are chosen to $k_bT_{dpd} = k_bT_{bd} = 0.1$ in simulation units. We measure the spectra for the same growth strength parameters in the range $B^* = 0.6 - 1$ as in the previous measurements of γ_h, ξ and χ_a. Figure 3.12 shows the resulting inverse fluctuation spectra as a function of k^2. Two fits of the inverse fluctuation spectra are performed, one with only κ as a free parameter and $\gamma_h, a = a_{opt}\varrho$ from previous measurements, another with all parameters κ, γ_h and a free. The comparison of both fits enables us to judge the error in the results due to uncertainties in the previous measurements of γ_h. The method `least_squares()` of the python package SciPy is used for the fits [87]. A comparison of measured and fitted inverse spectra for wavenumber cutoff $k_{cut} = 1r_{pp}$ is depicted in fig. 3.12. As expected, the three parameter fit leads to the smaller squared residual $\chi^2 = \sum_i \left(y\left(x_i\right) - y_{\mathrm{fit}}\left(x_i\right)\right)^2$. However, the estimated bending rigidities mostly agree in the wavenumber cutoff range $0.6 < k_{cut}r_{pp} < 2$, hereby, the one parameter fit yields slightly larger results. In the range $1 < k_{cut}r_{pp} < 2$ the squared residual increases by several orders of magnitude as the measured spectrum starts to deviate from the analytic expression eq. (3.4.18). We denote by $\sigma(\kappa)$ the standard deviation of the fit result for κ, defined by the square root of the diagonal entries of the covariance matrix of the corresponding least-squares minimization problem. We quantify with the fraction $\sigma(\kappa)/\kappa$ the relative uncertainty in the fitted κ. For $k_{cut} < 0.6$, the uncertainty parameter becomes of order $\sigma(\kappa)/\kappa \sim 1$ for both fits. Thus, from the measurements of χ^2 and $\sigma(\kappa)/\kappa$, we deem a cutoff in the range $0.6 < k_{cut}r_{pp} < 1.0$ to

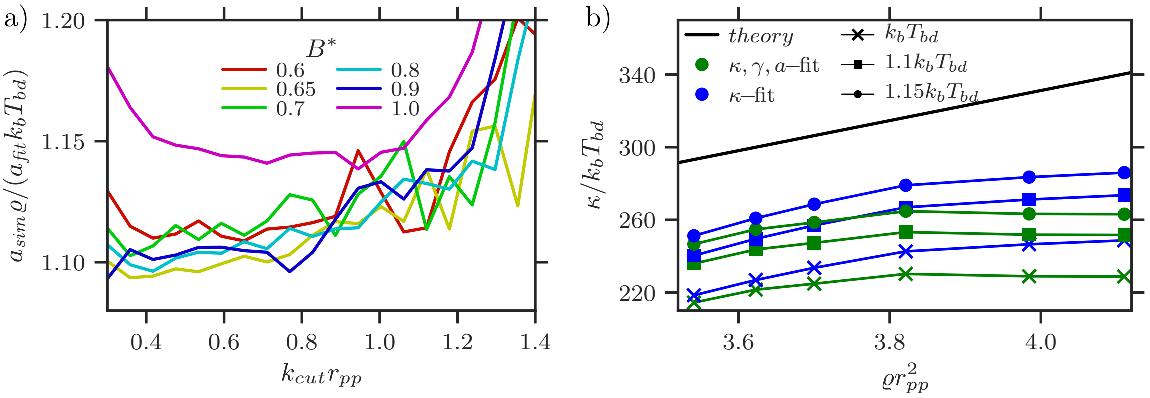

FIGURE 3.13. **a)** Actual confinement strength $a = a_{sim}\varrho$ divided by fit result for confinement strength a_{fit} from the three parameter fit as a function of wavenumber cutoff k_{cut}. Given in units of the prescribed Brownian dynamics temperature $k_bT_{bd} = 0.1$. As of eq. (3.4.20), this ratio determines the effective temperature k_bT_e. Different curves correspond to growth strengths in the range $B^* = 0.6 - 1$ (see legend). **b)** Bending rigidity as a function of particle density ϱ. Continuous black line depicts analytical approximation eq. (3.3.61). Colors green and blue correspond to results from three or one parameter fit for wavenumber cutoff $k_{cut} = 1/r_{pp}$. Cross symbols correspond to temperature k_bT_{bd}, squares and circles to temperatures $1.1k_bT_{bd}$ and $1.15k_bT_{bd}$.

yield the most accurate results. Figure 3.13 depicts the bending rigidity, in units of k_bT_{bd}, measured at $k_{cut} = 1.0r_{pp}$ as a function of the particle density. The analytical prediction, eq. (3.3.61), is roughly $35\% - 40\%$ larger than the measured values. However, these measurements may be biased due to the effective noise temperature in lateral direction being larger than k_bT_{bd}. We denote this effective noise temperature with k_bT_e. To estimate k_bT_e, we note that our polynomial fit results in an estimate of confinement strength a divided by the effective temperature, i.e. the quantity $a_{fit} = a/k_bT_e$. Thus, with the exact value a_{sim} of our simulation force strength and the relation $a = a_{sim}\varrho$ between simulation force strength and confinement strength (see section 3.4.2), we write

$$k_bT_e = \frac{a}{a_{fit}} = \frac{a_{sim}\varrho}{a_{fit}}, \tag{3.4.20}$$

which allows calculation of the effective temperature k_bT_e (see fig. (3.13)). Hereby, we obtain values for the temperature fraction k_bT_e/k_bT_{bd} around $k_bT_e/k_bT_{bd} \approx 1.1 - 1.15$. Within this range of k_bT_e the analytical result, eq. (3.3.61), is only $\approx 20\%$ larger than the measured bending rigidities (see fig. (3.13) b)). We can only speculate what is the reason for the remaining deviation. One possibility is given by the discretization error made when comparing continuum theory with particle-based simulations. With a typical particle density in simulations of $\varrho \approx 4$, there are only a few dozen particles inside cutoff range $r_{mp} = 1.5$ and their local order may not be negligible. A possibility to improve the analytic results in this regard would be to take the pair distribution function $g(r)$ into account.

3.5. Reaction-Diffusion Model of Limiting Nutrient

We implement the reaction-diffusion dynamics of a limiting nutrient with concentration g in a similar manner as the individual-based models (abbreviated IBMs) introduced in section 2.1.3. Reaction-diffusion dynamics is modeled by a continuum reaction-diffusion equation which we solve with a finite-difference method. The growth force parameters of the 2PG-module are then adjusted according to the local nutrient concentration to couple growth with nutrient availability. We denote with ϱ the number density of cells and assume nutrient uptake is proportional to density times a concentration-dependent uptake function $U(g)$. The uptake function is chosen dependent on the uptake characteristics of the cells, see section 5.2.3. Thus, the concentration g follows the dynamic equation

$$\frac{\partial g}{\partial t} = \nabla \cdot (D \nabla g) - \varrho U(g), \tag{3.5.1}$$

with the diffusion constant D. We integrate the nutrient dynamic eq. (3.5.1) on a cubic lattice $\boldsymbol{r}_{i,j,k} = (x_i, y_j, z_j) = (ih, jh, kh)$ with grid constant h. To do so, we employ a forward-time, central-space finite-difference scheme which accounts for spatially varying diffusion constants:

$$\begin{aligned}\frac{g^{n+1}_{i,j,k} - g^n_{i,j,k}}{\Delta t} = \frac{1}{h^2} &\big(D^n_{i+1/2,j,k}\left(g^n_{i+1,j,k} - g^n_{i,j,k}\right) + D^n_{i-1/2,j,k}\left(g^n_{i-1,j,k} - g^n_{i,j,k}\right) \\ &+D^n_{i,j+1/2,k}\left(g^n_{i,j+1,k} - g^n_{i,j,k}\right) + D^n_{i,j-1/2,k}\left(g^n_{i,j-1,k} - g^n_{i,j,k}\right) \\ &+D^n_{i,j,k+1/2}\left(g^n_{i,j,k+1} - g^n_{i,j,k}\right) + D^n_{i,j,k-1/2}\left(g^n_{i,j,k-1} - g^n_{i,j,k}\right)\big) - \varrho^n_{i,j,k} U\left(g^n_{i,j,k}\right),\end{aligned} \tag{3.5.2}$$

where $\bullet^n_{i,j,k}$ denotes the value of the respective quantity at grid point $\boldsymbol{r}_{i,j,k} = (ih, jh, kh)$ and time $t^n = n\Delta t$ [94]. The cell density $\varrho^n_{i,j,k}$ is calculated by summing up all cells which have their center of mass in lattice side (i, j, k) at time t^n and subsequent division by the lattice volume h^3. This scheme is stable and consistent if $D^n_{i,j,k}\Delta t/h^2 \leq 1/4$ for all $(t^n, \boldsymbol{r}_{i,j,k})$ in the domain of computation. It ensures a continuous solution for g even though D may change non-continuously[94].

We assume that the resulting cell growth rate k_g is proportional to the local nutrient uptake $k_g = \epsilon U(g)$. The proportionality constant ϵ determines the efficiency of nutrient to biomass conversion. Thus, the continuity equation of the cell density ϱ is given by

$$\frac{\partial \varrho}{\partial t} = -\nabla \cdot (\varrho \boldsymbol{v}) + \epsilon U(g). \tag{3.5.3}$$

To achieve a nutrient dependent growth rate in the 2PG-model, we need to couple the concentration g to the parameters of the growth force. We begin with the observation that the growth force parameter B determines the scale $p_{int} \sim B/[l_c^4]$ of the internal cell pressure; l_c denotes a typical cell-lengthscale. Thus, if the external pressure is bounded, we may increase B until $p_{int} \gg p_{ext}$ such that external pressure has only a minuscule influence on the growth process. Furthermore, for a friction-dominated system, the intracell distance r follows approximately the dynamic equation

$$F_g(r) = \frac{B}{(r_0 + r)^2} = -\widehat{\gamma}_c \frac{dr}{dt} \tag{3.5.4}$$

where $\widehat{\gamma}_c$ denotes an effective friction constant comprised of intracell friction γ_c and contributions from interactions with the surrounding cells. From above equation results the division time

$$\tau_{div} = \frac{\widehat{\gamma}_c}{B} \int_{r_c}^{d_c} (r + r_0)^2 \, dr, \tag{3.5.5}$$

which corresponds to the growth rate $k_g = \log 2/\tau_{div}$. The factor $\log 2$ occurs because a division event doubles the amount of cells. To tune the growth rate, we adjust the value of γ_c to change the value of the effective friction $\widehat{\gamma}_c$. For large enough γ_c, the intracell friction becomes the dominant friction contribution such that $\widehat{\gamma}_c \approx \gamma_c$. With the relation $k_g = \epsilon U(g) = \log 2/\tau_{div}$ and eq. (3.5.5) we obtain an expression for the growth force parameter B

$$\frac{B(g)}{\gamma_c} = \frac{\epsilon U(g)}{\log(2)} \int_{0}^{d_c} (r + r_0)^2 \, dr, \tag{3.5.6}$$

which we expect to result in the desired growth rate. With the discrete solution $g^n_{i,j,k}$ for the nutrient profile we assign every cell with center of mass inside lattice side of point $\boldsymbol{r}_{i,j,k}$ at time t^n a growth constant $B(g^n_{i,j,k})$ according to eq. (3.5.6). Note, however, that the coupling of local nutrient concentration and cell mass creation according to eq. (3.5.6) yields the desired growth rate $k_g = \epsilon U(g)$ only if growth force and intracell friction dominate the dynamics along the cell axis.

CHAPTER 4

Growth of 2D-Manifolds in 3D

We investigate the patterning of a freely growing, square membrane subject to periodic boundary conditions by means of our particle-based simulation. Starting from an initially flat configuration with edge length L, buckling patterns with a characteristic wavenumber evolve, see fig. 4.1. Remarkably, the observed wavenumbers k are much larger than the system-spanning mode $k = 2\pi/L$, which is predicted to be the first unstable mode in classical quasi-static Euler-instability analysis for periodic boundary conditions. To analyze this behavior, we briefly recapitulate the results of classical buckling theory upon which we develop a model which incorporates stress-dependent growth. For simplicity, we constrain our model in the Monge-representation, i.e. for membrane shapes which can be described by a lateral height profile $z = h(x, y)$. To validate our model, we compare analytical predictions with simulation results in the Monge-representation. Furthermore, we take a look at the dynamics of overlapping membrane shapes with our simulations. In particular, we investigate to what extend overlapping membrane shapes are determined by the anterior dynamics in the Monge-representation. In contrast to the differential growth hypothesis, which assumes

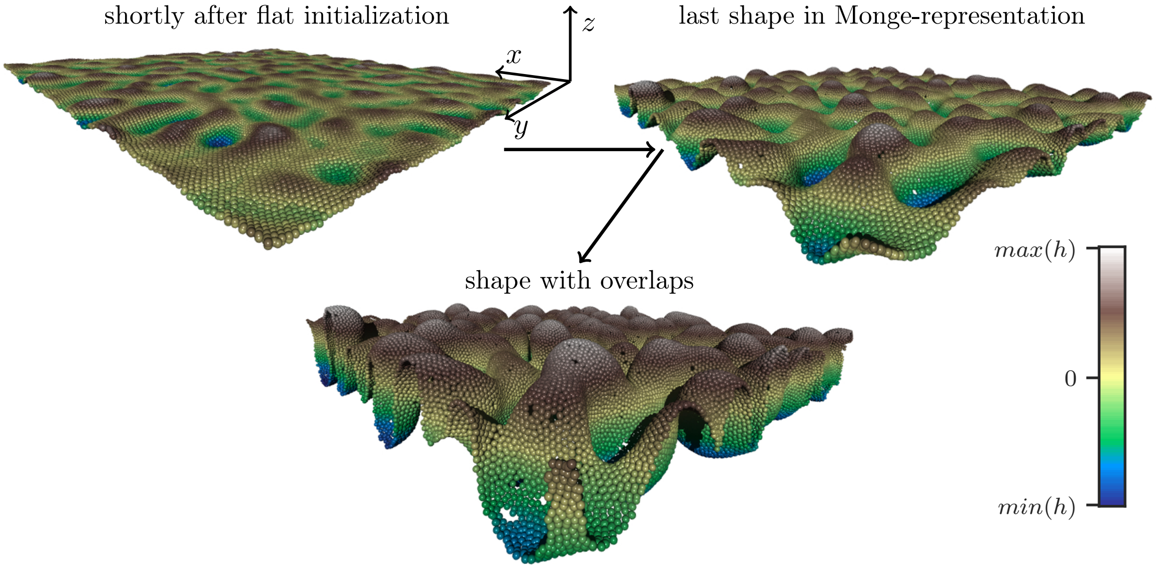
shortly after flat initialization
z
x
y
last shape in Monge-representation
shape with overlaps
$max(h)$
0
$min(h)$

FIGURE 4.1. Simulation of temporal evolution of wrinkling patterns of a square membrane which grows freely in z-direction, subject to periodic boundary conditions in x- and y-direction. Time evolution begins from top left and continues in clock-wise order. Color coding relative to minimal and maximal lateral height (see legend).

that wrinkling patterns are formed due to different lateral expansion rates of adjacent tissue layers (see section 2.2), our theory explains a patterning mechanism for a free monolayer without said differential.

4.1. Buckling of Thin, Planar Membranes

We briefly recapitulate the classical theory of buckling instabilities of thin, planar membranes. In particular, we derive the results for critical stress and buckling wavenumbers eqns. (2.2.4)-(2.2.6). An introduction into the necessary differential geometric concepts can be found in appendix C.

4.1.1. Energy Contributions. The energy contributions to understand buckling instabilities of a thin membrane S are *membrane bending energy* E_{bend} and *membrane surface energy* E_{surf}. For a planar membrane with linear elastic substrate, the *substrate deformation energy* E_{subs} contributes as well. The membrane bending energy E_{bend} is determined by mean curvature H, Gaussian curvature G and spontaneous curvature C_0 of S:

$$E_{bend} = \int_U \left(\frac{\kappa}{2} \left(H - C_0\right)^2 + \frac{\widehat{\kappa}}{2} G \right) \sqrt{\det \boldsymbol{\bar{g}}}\, dx dy. \tag{4.1.1}$$

The curvature moduli $\kappa, \widehat{\kappa}$ are called bending rigidity and saddle-splay modulus. The spontaneous curvature field C_0 prescribes a preferred mean curvature, such that the state of minimal energy is curved. The form eq. 4.1.1 of the bending energy is representation independent and results from collecting all rotational invariant terms in curvature up to quadratic order [95]. It is often referred to as *Helfrich-Canham* energy in honor of physicists Wolfgang Helfrich and Peter Canham [95, 96]. In the framework of linear elasticity, an illustrative derivation of the bending energy results by consideration of the strains along the membrane thickness of the bent membrane (see fig. 4.2). Bending a membrane in a curved shape extends the material

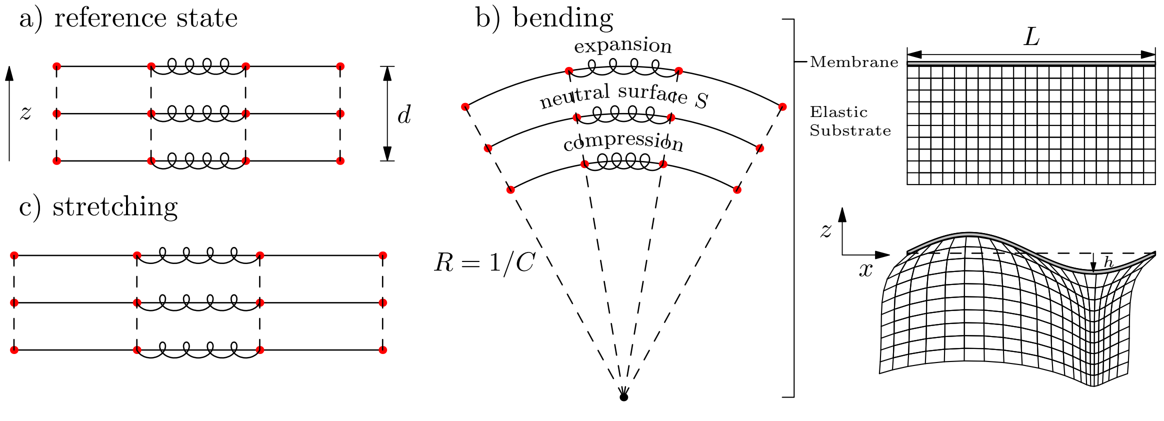

FIGURE 4.2. We define the flat, unstretched state a) as the stress-free reference state of the membrane. The deformational degrees of freedom are then b) bending and c) stretching/surface expansion, corresponding to the energies E_{bend} and E_{surf}. Additionally, the deformation of an attached elastic substrate yields an energy contribution E_{subs} (see appendix D). The illustrations a)-c) refer to a linear elastic membrane material for which the energetic contributions can be imagined to arise from extension/compression of tiny springs connecting the atoms.

layers on the convex side of the curvature and compresses the layers on the concave side. The layer in the mid between the two outer membrane surfaces remains free of compressive stress and is referred to as *neutral surface.* The surface S to describe membrane deformation commonly refers to the neutral surface of the thin membrane. The bending energy is the total elastic energy necessary to compress and expand the lateral membrane layers during bending. Explicit calculation for small buckling amplitudes leads then to a bending energy equivalent to eq. 4.1.1 [55]. The membrane surface energy E_{surf} is the energy necessary to change the total surface area of S. We denote the surface energy density per area with γ, the total energy equals then

$$E_{surf} = \int_U \gamma \sqrt{\det \overline{\boldsymbol{g}}}\, dxdy. \tag{4.1.2}$$

The surface energy per area γ is called *surface tension.* Intuitively, the surface tension is related to the in-plane stresses of the membrane (see fig 4.2): work has to be performed against the in-plane stresses to change the surface area. A thorough analysis of the stress contributions at an interface results in the expression [85]

$$\gamma = \int_{-d/2}^{d/2} \left(\sigma_{\parallel}(z) - \sigma_{\perp}(z)\right)\, dz, \tag{4.1.3}$$

where $\sigma_{\parallel}$ and $\sigma_{\perp}$ denote in-plane and normal components of the stress tensor and the integral has to be taken over the interface thickness d. To describe an elastic support, we assume for simplicity that membrane and support are tightly connected such that no tangential slip occurs. Hence, the substrate energy contribution E_{subs} is given by the net energy of an elastic half-space subject to the deformation $(0, 0, h\,(x, y))$ at its free surface. It is shown in appendix D that E_{subs} is given by

$$E_{subs} = \widehat{E} \sum_{\boldsymbol{k}} k\, |h_{\boldsymbol{k}}|^2\,, \tag{4.1.4}$$

with $h_{\boldsymbol{k}}$ the Fourier-transform of h (see appendix C.3) and the wavevector magnitude $k = |\boldsymbol{k}|$. Here, the effective transversal elasticity modulus $\widehat{E}$ is proportional to the Young modulus $\widehat{E} \propto E$ of the substrate material, the proportionality factor solely depends on the Poisson number σ. As shown in appendix D, imposing the lateral deflection h at the surface is not sufficient to pin-point the solutions of stress and strain in the substrate. Additionally, it is necessary to prescribe either tangential stress or strain in the direction perpendicular to the wavevector $\boldsymbol{k}$ of a mode $h_{\boldsymbol{k}}$. Under the assumption of vanishing tangential strain perpendicular to $\boldsymbol{k}$ and a volume conserving material, i.e. $\sigma = 1/2$, the effective modulus is $\widehat{E} = E/3$.

In analytical calculations, the energy contributions are commonly approximated by a series expansion in terms up to quadratic order in the deflections. Expansion of the Monge-representation (see appendix C.3) $z = h(x, y)$ around the flat state $h(\boldsymbol{x}) \equiv 0$ leads to the description of a *nearly planar membrane.* For a nearly planar membrane we allow only small deviations of the surface normal from the z-axis $\boldsymbol{n} \approx \boldsymbol{e}_z$. From eq. (C.3.2) we see that this condition corresponds to

$$|\nabla h|^2 \ll 1. \tag{4.1.5}$$

We keep only terms up to quadratic order in h and approximate the total energy E_{tot} of the membrane-substrate system with

$$E_{tot} = E_{bend} + E_{surf} + E_{subs} = \frac{1}{2}\int_U \kappa\left((\Delta h)^2 - 2C_0\Delta h\right) + \gamma\left|\nabla h\right|^2\, dxdy + \widehat{E}\sum_{\boldsymbol{k}} k\left|h_{\boldsymbol{k}}\right|^2 , \tag{4.1.6}$$

where we already omitted all terms which stay constant during deformation.

We conclude this section with a remark on fluid and solid degrees of freedom. Throughout this section we used terminology which is typically associated with fluids, such as surface tension, as well as solids, such as bending rigidity. Microscopically, a characterizing property of a fluid is that thermal energy is sufficient to switch the position of two fluid particles. This results in a vanishing shear modulus. In contrast, particles in a solid are bound in a more or less ordered state and work, exceeding thermal energy scales by many orders of magnitude, has to be performed to change position of particles. Membrane systems can exhibit both fluid and solid properties by an anisotropy of in-plane and lateral degrees of freedom. An example are lipid bilayers which consist of amphiphilic lipid molecules or soap bubbles consisting of water with dissolved soap molecules. Amphiphilic (Greek, "*loving on both sides*") lipid molecules are made of a hydrophobic "tail" and a hydrophilic "head". Thus, in aqueous solution, they favor a configuration where heads are bonded to heads and tails to tails such that they self-assemble into a lipid bilayer. These bonds are weak enough to be broken by thermal noise such that the in-plane configuration of molecules exhibits fluid behavior. However, lipid bilayers possess a finite bending rigidity, albeit small compared to solids. This is a result of the fact that we need to compress the inward facing tails of the lipid molecules during bending, as in figure 4.2. Here, we need to perform work against the electrostatic repulsion of the tails. Thus, the in-plane degrees of freedom exhibit fluid behavior, whereas the lateral compression during bending resembles the bending of a solid. As we will see in the next section, the in-plane and lateral degrees of freedom, corresponding to surface extension and bending, decouple for small deformations. This allows for a combined treatment of membranes with solid or fluid in-plane degrees of freedom as we just need to interpret the surface tension in a different manner. In case of a soap bubble, the surface tension corresponds to the surface tension of the soap-water-air interface. For solids, the surface tension can be expressed in terms of the elastic stresses, which leads to the classical *Föppl-von-Kármán* theory of bend plates [55].

4.1.2. Buckling Instabilities. We perform a stability analysis of the total energy E_{tot} of the nearly planar membrane. It is convenient to analyze the stability in Fourier-space. With the Fourier-transform as defined in appendix C.3, the total energy of eq. (4.1.6) becomes

$$\begin{aligned} E_{tot} = &\sum_{\boldsymbol{k}\neq\boldsymbol{0}} \frac{1}{2}\left(\kappa k^4 + \langle\gamma\rangle_x k^2 + \widehat{E}k\right)\left|h_{\boldsymbol{k}}\right|^2 + \kappa k^2\,\mathrm{Re}\left(C^*_{0,\boldsymbol{k}} h_{\boldsymbol{k}}\right) \\ &+\frac{1}{2}\sum_{\boldsymbol{k},\boldsymbol{k}'\neq\boldsymbol{0}} \left(k^2 + \boldsymbol{k}\boldsymbol{k}'\right)\mathrm{Re}\left(\gamma_{\boldsymbol{k}'} h_{\boldsymbol{k}} h^*_{\boldsymbol{k}+\boldsymbol{k}'}\right) , \end{aligned} \tag{4.1.7}$$

where we already omitted terms which do not depend on the deflection h such that $E_{tot} = 0$ in the flat state. Furthermore, we set $\langle h\rangle_x = 0$, i.e. the flat state coincides with the xy-plane. Note that the spatial average $\langle\gamma\rangle_x$ has been put into the first sum. Components $\gamma_{\boldsymbol{k}}$ correspond to spatial varying surface tension and lead to coupling of different wavemodes

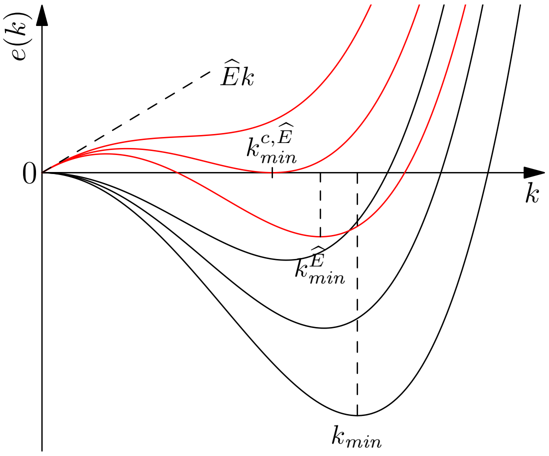

FIGURE 4.3. The sign of the polynomial $e\,(k)$ in eq. (4.1.8) determines the unstable modes for spatially constant surface tension and vanishing spontaneous curvature. Every mode $\boldsymbol{k}$ for which $e\,(k) < 0$ has lower energy than the flat state and becomes unstable. Without elastic substrate (black curves), the unstable modes lie between the two zero-crossings $k = 0$ and $k = \sqrt{-\langle\gamma\rangle_x/\kappa}$ of $e\,(k)$. With an elastic substrate (red curves), the linear term $\widehat{E}k$ increases the energy contribution of all modes k which contracts the interval of unstable modes. Compressive surface tension $\langle\gamma\rangle_x$ increases from left to right in both sets of curves.

owing to the term $h_{\boldsymbol{k}}h^*_{\boldsymbol{k}+\boldsymbol{k}'}$. For spatially constant surface tension $\gamma \equiv \langle\gamma\rangle_x$ the instable modes are determined by the summand of the first sum. As the energy of the flat state equals zero, a wavemode $\boldsymbol{k}$ becomes unstable if its energy contribution is negative. For infinitely small amplitudes, the term proportional to $|h_{\boldsymbol{k}}|^2$ can be neglected relative to the spontaneous curvature term which scales linearly with $h_{\boldsymbol{k}}$. Thus, all modes $\boldsymbol{k}$ for which $C_{0,\boldsymbol{k}} \neq 0$ are unstable and buckle. For finite amplitudes, the sign of the summand in the first term has to be discussed as a whole. In the case of vanishing spontaneous curvature $C_0 \equiv 0$, the sign of the summand solely depends on the polynomial

$$e\,(k) = \kappa k^4 + \langle\gamma\rangle_x k^2 + \widehat{E}k \tag{4.1.8}$$

in the first term (see fig. 4.3). Owing to $k \geq 0$, the polynomial $e\,(k)$ can only take negative values for compressive stress $\langle\gamma\rangle_x < 0$, as we would expect. The energy contributions lead to buckling in a characteristic wavemode range which can be understood intuitively. Without elastic substrate, energy has to be minimized with respect to surface tension and bending. The negative surface tension strives to increase the overall surface, therefore strongly undulating large wavemodes are excited which create a lot of surface. However, strongly undulating wavemodes are strongly curved as well, which is penalized by the curvature energy term. Thus, we expect that buckling occurs up to a maximal wavenumber up to which the gain in surface is larger than the penalty in curvature. Developing an intuitive understanding of the elastic substrate contribution is a bit more difficult. For a single wavemode excitation $h(\boldsymbol{x}) \propto \sin(\boldsymbol{kx})$, the substrate energy takes the form $E_{subs} \propto |h\nabla h|$ such that large amplitudes and large gradients are penalized. Wavemodes with small k need larger amplitude $|h|$ to create a given surface area, whereas modes with large k exhibit large gradients $|\nabla h|$; the optimum lying somewhere in the middle. In the following, we discuss the polynomial $e\,(k)$ to calculate the optimal wavemodes exactly. We first analyze the case without elastic substrate. In this case all modes between the two zero-crossings

$$0 < k < \sqrt{-\frac{\langle\gamma\rangle_x}{\kappa}}, \tag{4.1.9}$$

of $e\left(k\right)$ are unstable. Thus, an infinitely large membrane $L\to\infty$ buckles for any compressive stress $\left\langle \gamma\right\rangle_x < 0$, whereas for finite L the discretization of the wavemodes $\boldsymbol{k}\in 2\pi/L\,\mathbb{Z}^2$ yields a finite critical stress $\left\langle \gamma\right\rangle_x^c$. By equating the smallest wavenumber $k=2\pi/L$ with the positive zero-crossing of $e\left(k\right)$ we calculate $\left\langle \gamma\right\rangle_x^c$ to

$$\left\langle \gamma\right\rangle_x^c = -\kappa\left(\frac{2\pi}{L}\right)^2. \tag{4.1.10}$$

The buckling wavenumber $k=2\pi/L$ corresponds to a mode spanning the whole system as depicted in fig. 4.2. For larger compressive stresses $\left\langle \gamma\right\rangle_x < \left\langle \gamma\right\rangle_x^c$ all discrete wavemodes in the interval eq. 4.1.9 become unstable. The minimum of $e(k)$ at

$$k_{min} = \sqrt{\frac{\left|\left\langle \gamma\right\rangle_x\right|}{2\kappa}} \tag{4.1.11}$$

determines then the strongest buckling wavemode.

With an elastic substrate, the linear term $\widehat{E}k$ increases the energy contribution of all wavenumbers narrowing down the interval of instable modes (see fig. 4.3). In particular, modes in a neighborhood of $k=0$ become stable such that even in the limit $L\to\infty$ buckling occurs only above a finite critical surface tension $\left\langle \gamma\right\rangle_x^{c,\widehat{E}}$. As depicted in fig. 4.3, the polynomial $e\left(k\right)$ exhibits a local minimum $k_{min}^{\widehat{E}}$ for large enough compressive stress $\left\langle \gamma\right\rangle_x < 0$. Thus, buckling occurs when the local minimum reaches zero, i.e $e(k_{min}^{\widehat{E}})=0$. Solution of this equation and the extremal condition $e'(k_{min}^{\widehat{E}})=0$ yields the critical surface tension

$$\left\langle \gamma\right\rangle_x^{c,\widehat{E}} = -3\left(\frac{1}{4}\kappa\widehat{E}^2\right)^{\frac{1}{3}}, \tag{4.1.12}$$

at which the mode

$$k_{min}^{c,\widehat{E}} = \left(\frac{\widehat{E}}{2\kappa}\right)^{\frac{1}{3}}, \tag{4.1.13}$$

starts to buckle. The critical wavemode eq. (4.1.13) has been used to explain, for example, gut patterning [26]. For larger compressive surface tensions $\left\langle \gamma\right\rangle_x < \left\langle \gamma\right\rangle_x^{c,\widehat{E}}$, $e\left(k\right)$ exhibits two zero-crossings for $k>0$ which determine the interval of buckling modes. Strongest buckling occurs at the minimum energy mode located at

$$k_{min}^{\widehat{E}} = \sqrt{\frac{2\left|\left\langle \gamma\right\rangle_x\right|}{3\kappa}}\cos\left(\frac{\pi}{3}-\frac{1}{3}\arccos\left(\sqrt{\frac{27\kappa\widehat{E}^2}{8\left|\left\langle \gamma\right\rangle_x\right|^3}}\right)\right) < \sqrt{\frac{\left|\left\langle \gamma\right\rangle_x\right|}{2\kappa}} = k_{min}, \tag{4.1.14}$$

with arccos evaluated in the interval $[0,\pi]$. In particular, the minimal energy wavenumber with substrate is always smaller than the one without, i.e. $k_{min}^{\widehat{E}} < k_{min}$.

4.1.3. Buckling Dynamics in Small Angle Limit. We derive the equations of motion of the membrane deflection $h(\boldsymbol{x},t)$ in the limit of small angles $\measuredangle\left(\boldsymbol{n},\boldsymbol{e}_z\right)\approx 0$ which corresponds to $\left|\nabla h\right|^2 \ll 1$. These equations serve as the basis for a simple model of a membrane with stress dependent growth in section 4.2. The Lagrangian formalism enables a clean derivation of the equations of motion by interpretation of the energy in eq. (4.1.7) as the potential energy V of the configuration $h(\boldsymbol{x}, t)$ of the membrane system. We define amplitude $r_{\boldsymbol{k}}$ and modulus $\varphi_{\boldsymbol{k}}$ of the Fourier-coefficients

$$h_{\boldsymbol{k}} = r_{\boldsymbol{k}} \exp\left(i\varphi_{\boldsymbol{k}}\right), \tag{4.1.15}$$

as the generalized coordinates $\{q_i\} = \{r_{\boldsymbol{k}}, \varphi_{\boldsymbol{k}}\}$. Care has to be taken to identify the independent degrees of freedom. Due to $h_{\boldsymbol{k}} = h^*_{-\boldsymbol{k}}$ it is

$$r_{\boldsymbol{k}} = r_{-\boldsymbol{k}} \qquad \varphi_{\boldsymbol{k}} = -\varphi_{-\boldsymbol{k}}. \tag{4.1.16}$$

Thus, in eq. (4.1.15) the modes $\boldsymbol{k}$ and $-\boldsymbol{k}$ contain the same degrees of freedom. We define the $r_{\boldsymbol{k}}, \varphi_{\boldsymbol{k}}$ with wavevectors $\boldsymbol{k}$ in the "slitted" upper half-plane

$$\text{⬒} = \left\{ \boldsymbol{k} \in \frac{2\pi}{L}\mathbb{Z}^2 : k_y > 0 \vee (k_y = 0 \wedge k_x > 0) \right\} \tag{4.1.17}$$

as the independent degrees of freedom. We focus on the case of spatial constant surface tension and vanishing spontaneous curvature. As the initial state of the flat membrane is homogeneous, we expect that spatial gradients are negligible in the initial buckling dynamics. Furthermore, analytical solutions are easily to derive in this case as the total energy E_{tot}, eq. (4.1.7), decouples then in quadratic terms in the wavenumber amplitudes $r_{\boldsymbol{k}} = |h_{\boldsymbol{k}}|$. The equations of motion with non-vanishing spontaneous curvature can be found in appendix E. We denote with

$$\mathcal{L} = \mathcal{L}\left(\{q_i\}, \{\dot{q}_i\}, t\right) = \mathcal{T} - \mathcal{V} \tag{4.1.18}$$

the Lagrangian of the membrane system. The equations of motions are then given by

$$\frac{d}{dt}\frac{\partial \mathcal{L}}{\partial \dot{q}_i} - \frac{\partial \mathcal{L}}{\partial q_i} + \frac{\partial \mathcal{F}}{\partial \dot{q}} = 0, \tag{4.1.19}$$

where $\mathcal{F}$ denotes the Rayleigh dissipation function to include dissipative friction forces [97]. To apply the Lagrangian formalism, we define $\mathcal{V} = E_{tot}$ from eq. (4.1.7) as the potential energy of the system and rewrite $\mathcal{V}$ in the generalized coordinates $\{r_{\boldsymbol{k}}, \varphi_{\boldsymbol{k}}\}$

$$\mathcal{V} = \frac{1}{2}\sum_{\boldsymbol{k}} \widehat{e}\,(k)\, r_{\boldsymbol{k}}^2 + k^2 \left\langle\gamma\right\rangle_x r_{\boldsymbol{k}}^2 = \sum_{\boldsymbol{k}\in\text{⬒}} \widehat{e}\,(k)\, r_{\boldsymbol{k}}^2 + k^2 \left\langle\gamma\right\rangle_x r_{\boldsymbol{k}}^2 \tag{4.1.20}$$

with

$$\widehat{e}\,(k) = e\,(k) - \left\langle\gamma\right\rangle_x k^2 = \kappa k^4 + \widehat{E}k. \tag{4.1.21}$$

The total kinetic energy $\mathcal{T}$ is approximated via

$$\mathcal{T} = \frac{1}{2}\int_U \left(\frac{dh}{dt}\right)^2 \varrho_m \sqrt{\det \overline{\boldsymbol{g}}}\, dxdy = \frac{1}{2}\int_U \left(\frac{dh}{dt}\right)^2 \varrho_m\, dxdy + \mathcal{O}\left(|\nabla h|^2\right) \tag{4.1.22}$$

where we introduced the constant membrane mass density ϱ_m per area. Owing to

$$\dot{h} = \sum_{\boldsymbol{k}} \dot{h}_{\boldsymbol{k}} \exp\left(i\boldsymbol{k}\boldsymbol{x}\right) = \sum_{\boldsymbol{k}} \left(\dot{r}_{\boldsymbol{k}} + i r_{\boldsymbol{k}}\dot{\varphi}_{\boldsymbol{k}}\right) \exp\left(i\varphi_{\boldsymbol{k}}\right) \exp\left(i\boldsymbol{k}\boldsymbol{x}\right) \tag{4.1.23}$$

we follow

$$\mathcal{T} \approx \frac{1}{2}\int_U \left(\frac{dh}{dt}\right)^2 \varrho_m\, dxdy = \frac{1}{2}\varrho_m \sum_{\boldsymbol{k}} \frac{dh_{\boldsymbol{k}}}{dt}\frac{dh^*_{\boldsymbol{k}}}{dt} = \frac{\varrho_m}{2}\sum_{\boldsymbol{k}} \dot{r}_{\boldsymbol{k}}^2 + r_{\boldsymbol{k}}^2\dot{\varphi}_{\boldsymbol{k}}^2 = \varrho_m \sum_{\boldsymbol{k}\in\text{⬒}} \dot{r}_{\boldsymbol{k}}^2 + r_{\boldsymbol{k}}^2\dot{\varphi}_{\boldsymbol{k}}^2. \tag{4.1.24}$$

by virtue of the orthogonality relation eq. (C.3.11). Insertion of potential energy $\mathcal{V}$ eq. (4.1.20) and kinetic energy $\mathcal{T}$ eq. (4.1.22) into eq. (4.1.18) yields a quadratic Lagrangian in $\{r_{\boldsymbol{k}}, \dot{r}_{\boldsymbol{k}}\}$. For simplicity, we assume an uniform friction force density $\boldsymbol{F}_\nu = \nu \partial_t h \boldsymbol{e}_z$ as the dissipative response of the embedding medium. A dissipative response of this form is independent of the wavenumber k of membrane wavemodes. This corresponds, for example, to a permeable membrane in a Newtonian fluid [98] or a membrane embedded in a thin layer of tissue of thickness H in the limit of small wavenumbers $kH \ll 1$ [92]. In appendix E.3, more detailed calculations are performed for a impermeable membrane in a Newtonian fluid which result in qualitatively similar dynamics. To include an uniform background friction force density, we define the Rayleigh dissipation function as

$$\mathcal{F} = \frac{\nu}{2} \int_U \left(\frac{dh}{dt}\right)^2 \sqrt{\det \overline{\boldsymbol{g}}}\, dxdy \approx \frac{\nu}{2} \int_U \left(\frac{dh}{dt}\right)^2 dxdy = \frac{\nu}{2} \sum_{\boldsymbol{k}} \dot{r}_{\boldsymbol{k}}^2 + r_{\boldsymbol{k}}^2 \dot{\varphi}_{\boldsymbol{k}}^2 = \nu \sum_{\boldsymbol{k} \in \text{⬒}} \dot{r}_{\boldsymbol{k}}^2 + r_{\boldsymbol{k}}^2 \dot{\varphi}_{\boldsymbol{k}}^2 \tag{4.1.25}$$

The equations of motions (4.1.19) follow to

$$\varrho_m \ddot{r}_{\boldsymbol{k}} + \nu \dot{r}_{\boldsymbol{k}} = -\widehat{e}\,(k)\, r_{\boldsymbol{k}} - k^2 \left\langle \gamma \right\rangle_x r_{\boldsymbol{k}} \qquad \text{and} \qquad \varphi_{\boldsymbol{k}} = \varphi_{\boldsymbol{k}}\,(0)\,. \tag{4.1.26}$$

Thus, the dynamics of the wavemodes $r_{\boldsymbol{k}}$ evolve as damped harmonic oscillators with time-dependent spring constant:

$$\varrho_m \ddot{r}_{\boldsymbol{k}} + \nu \dot{r}_{\boldsymbol{k}} = -\left(\widehat{e}\,(k) + k^2 \left\langle \gamma \right\rangle_x (t)\right) r_{\boldsymbol{k}} = -e\,(k,t)\, r_{\boldsymbol{k}} \tag{4.1.27}$$

For an initially flat membrane, all $r_{\boldsymbol{k}}$ vanish at $t = 0$, and the $r_{\boldsymbol{k}}$ increase only if the spring constant $e\,(k,t)$ is negative, consistent with the instability analysis performed in the last section. For later use, we will give the analytical solution in the limit of overdamped dynamics by dropping the inertia term:

$$\begin{aligned} \dot{r}_{\boldsymbol{k}} &= -\frac{e\,(k,t)}{\nu} r_{\boldsymbol{k}}, \\ r_{\boldsymbol{k}}(t) &= r_{\boldsymbol{k}}(0) \exp\left(-\frac{1}{\nu}\int_0^t e\,(k,\tau)\, d\tau\right) = r_{\boldsymbol{k}}(0) \exp\left(-\frac{1}{\nu}\left(\widehat{e}\,(k)\, t + k^2 \Gamma(t)\right)\right) \end{aligned} \tag{4.1.28}$$

with

$$\Gamma(t) = \int_0^t \langle \gamma \rangle_x (\tau)\, d\tau, \tag{4.1.29}$$

the cumulative integral of $\langle \gamma \rangle_x(t)$. Thus, modes are either exponentially amplified or dampened. For an infinitesimal time interval δt, the mode $r_{\boldsymbol{k}}$ evolves according to

$$\frac{r_{\boldsymbol{k}}(t+\delta t)}{r_{\boldsymbol{k}}(t)} = \exp\left(-\frac{1}{\nu}\left(\widehat{e}\,(k) + \langle \gamma \rangle_x(t)\, k^2\right) \delta t\right) = \exp\left(-\frac{e\,(k,t)}{\nu}\delta t\right). \tag{4.1.30}$$

Thus, we can apply the results of the discussion of the polynomial $e\,(k,t)$ from the last section to investigate which modes are instantaneously amplified or damped. Furthermore, by insertion of the dominant wavemode eq. (4.1.11) in eq. (4.1.30) we estimate the fastest amplitude growth timescale

$$\tau_{ampl} = \frac{4\kappa\nu}{\langle \gamma \rangle_x^2}, \tag{4.1.31}$$

for the case without elastic support. We see that the dynamics described by eqns. (4.1.28) in general do not permit non-flat stable steady states; for $r_{\boldsymbol{k}} \neq 0$ it is $\dot{r}_{\boldsymbol{k}} = 0$ if and only if

$e\left(k,t\right)=0$ for all $t>0$. Hence, $\left\langle\gamma\right\rangle_x$ has to be exactly the value which results in k being a zero crossing of $e\left(k,t\right)$.

Instead of deriving the equations of motion with the Lagrangian formalism in Fourier space, we could have also directly calculated the variation $\frac{\delta E_{tot}}{\delta h}$ of the energy eq. (4.1.6) in real space. Both approaches have advantages and disadvantages: Whereas the derivation in Fourier space allows for an easy description of the substrate energy E_{subs}, the direct variation in real space leads to membrane dynamic equations independent of an orthogonal function system. This is especially useful to derive the boundary conditions at the edges of the membrane. Without elastic substrate and for spatially constant surface tension, the membrane dynamic equations in real space read [55]

$$\varrho_m\partial_{tt}h+\nu\partial_t h=\left\langle\gamma\right\rangle_x\Delta h-\kappa\Delta\Delta h \tag{4.1.32}$$

Above equation of motion (4.1.32) remains valid if the surface tension γ depends itself on the deflection h. Note that in this case the form of the surface energy eq. (4.1.2), linear in the surface tension γ, is no longer valid. The dynamic equation (4.1.32) follows by consideration of the relation between force per volume $\boldsymbol{F}$ and the stress tensor $\overline{\boldsymbol{\sigma}}$:

$$\boldsymbol{F}=\operatorname{div}\left(\overline{\boldsymbol{\sigma}}\right). \tag{4.1.33}$$

Thus, for an isotropic surface tension γ the stress tensor reads simply

$$\overline{\boldsymbol{\sigma}}(\boldsymbol{x})=\frac{1}{d}\begin{pmatrix}\gamma(\boldsymbol{x}) & 0 & 0\\ 0 & \gamma(\boldsymbol{x}) & 0\\ 0 & 0 & 0\end{pmatrix}, \tag{4.1.34}$$

in the local basis spanned by the vectors $\{\boldsymbol{t}_1/\left|\boldsymbol{t}_1\right|,\boldsymbol{t}_2/\left|\boldsymbol{t}_2\right|,\boldsymbol{n}\}$. Transformation to Cartesian lab coordinates and evaluation of the divergence in eq. (4.1.33) yields

$$F_z d=\gamma\Delta h+\nabla\gamma\nabla h+\mathcal{O}\left(\left|\nabla h\right|^2\right)\ \text{ and }\ \left(F_x d,F_y d\right)=\nabla\gamma+\mathcal{O}\left(\left|\nabla h\right|^2\right), \tag{4.1.35}$$

with the force per area in z-direction $F_z d$ as in eq. (4.1.32) for spatially constant surface tension $\gamma\equiv\left\langle\gamma\right\rangle_x$.

4.2. Buckling with Stress-Dependent Growth

We investigate membrane buckling caused by pressure-dependent growth according to the homeostatic pressure model eq. (2.1.2). As in simulations, the membrane grows without elastic support in a dissipative medium. In the following, we construct a membrane buckling model which incorporates the homeostatic growth law, eq. (3.4.9)

$$\partial_t N=\xi\left(\gamma-\gamma_h\right)N. \tag{4.2.1}$$

Note that above equation implies a growth timescale of

$$\tau_g=\frac{1}{\xi\left|\gamma_h\right|}. \tag{4.2.2}$$

To obtain a continuum description, we want to relate the particle number N to a local particle density. For N particles in close vicinity on a tiny patch dA of the membrane, we distinguish two density measures: the *particle density* $\varrho=N/dA$ and the *projected particle density*

$\widehat{\varrho} = N/dxdy$ where $dxdy$ shall denote the projected area of dA in the xy-plane. Owing to eq. (C.3.5), both densities are related via

$$\widehat{\varrho} = \sqrt{1 + |\nabla h|^2}\varrho \approx \left(1 + \frac{1}{2}|\nabla h|^2\right)\varrho > \varrho. \tag{4.2.3}$$

For a flat membrane with $h \equiv 0$ both measures coincide. The projected density has the advantage that its reference area $dxdy$ remains constant during membrane deformation which eases the derivation of its continuity equation. It is easy to see that the projected density obeys the continuity equation

$$\frac{\partial \widehat{\varrho}}{\partial t} = \xi\left(\gamma - \gamma_h\right)\widehat{\varrho} - \nabla\left(\widehat{\boldsymbol{v}}\widehat{\varrho}\right). \tag{4.2.4}$$

with the transversal velocity $\widehat{\boldsymbol{v}} = \boldsymbol{v} - (\boldsymbol{v}\cdot\boldsymbol{e}_z)\,\boldsymbol{e}_z$. We assume that the transversal flux term is negligible compared to the growth term and neglect it for the following discussion. Next, we recast the constitutive relation, eq. (3.4.12), in terms of the projected density by virtue of eq. (4.2.3) and linearize the expression

$$\gamma - \gamma_h = \chi_a^{-1}\left(\varrho_h - \varrho\right) \approx \frac{\varrho_h}{\chi_a}\frac{1 + \frac{1}{2}|\nabla h|^2 - \frac{\widehat{\varrho}}{\varrho_h}}{1 + \frac{1}{2}|\nabla h|^2} \approx \frac{\varrho_h}{\chi_a}\left(1 + \frac{1}{2}|\nabla h|^2 - \frac{\widehat{\varrho}}{\varrho_h}\right). \tag{4.2.5}$$

The last step introduces an error of the order $\mathcal{O}\left(|\nabla h|^2\left(\varrho - \varrho_h\right)\right)$, i.e. quadratic in small quantities. Note that the constitutive relation (4.2.5) is physically sound in the sense that an area increase releases compressive stress (γ increases) whereas an increase in particle number creates compressive stress (γ decreases).

As all non-linear terms occur for spatially varying surface tension γ, we analyze the dynamics for the case of negligible deviation of γ from its spatial average, i.e. we assume

$$\gamma \approx \frac{1}{L^2}\int_U \gamma\, dxdy = \langle\gamma\rangle_x\,. \tag{4.2.6}$$

This assumption is also motivated by the spatially uniform surface tension in the initial flat state. The dynamic equation for $\langle\gamma\rangle_x$ follows by spatial averaging of eq. (4.2.5). With the total area, eq. (C.3.5),

$$A \approx \int_U 1 + \frac{1}{2}|\nabla h|^2\, dxdy = L^2 + \frac{1}{2}\sum_{\boldsymbol{k}} k^2|h_{\boldsymbol{k}}|^2, \tag{4.2.7}$$

spatial averaging of eq. (4.2.5) yields

$$\langle\gamma\rangle_x - \gamma_h = \frac{\varrho_h}{\chi_a}\left(\frac{A}{L^2} - \frac{\langle\widehat{\varrho}\rangle_x}{\varrho_h}\right). \tag{4.2.8}$$

From eq. (4.2.4) we conclude that the projected density $\widehat{\varrho}$ does neither depend on position for spatially constant γ, thus $\widehat{\varrho} = \langle\widehat{\varrho}\rangle_x$ and the density evolves according to

$$\partial_t\,\langle\widehat{\varrho}\rangle_x = \xi\left(\langle\gamma\rangle_x - \gamma_h\right)\langle\widehat{\varrho}\rangle_x. \tag{4.2.9}$$

with solution

$$\langle\widehat{\varrho}\rangle_x = \langle\widehat{\varrho}\rangle_x^0 \exp\left(\xi\left(\Gamma - \gamma_h t\right)\right), \tag{4.2.10}$$

where Γ denotes the surface tension cumulant with $\langle\gamma\rangle_x = \dot{\Gamma}$ (see eq. (4.1.29)) and $\langle\widehat{\varrho}\rangle_x^0 = \langle\widehat{\varrho}\rangle_x\,(t=0)$ the initial projected density. Equations (4.2.8), (4.2.9) together with eq. (4.1.32) from section 4.1.3 form the overdamped dynamic equations for projected density $\langle\widehat{\varrho}\rangle_x$, surface tension $\langle\gamma\rangle_x$ and membrane deflection h. As shown in section 4.1.3, the amplitudes $|h_{\boldsymbol{k}}|$ increase exponentially with time, the exponent depending on the surface tension cumulant Γ. Insertion of the solution eq. (4.1.28) for $|h_{\boldsymbol{k}}|$ into eq. (C.3.5) for the total area A yields

$$A = L^2 + \frac{1}{2}\sum_{\boldsymbol{k}} k^2 \left|h^0_{\boldsymbol{k}}\right|^2 \exp\left(\frac{2}{\nu}\left(\widehat{e}\left(k\right)t + k^2\Gamma\right)\right), \tag{4.2.11}$$

with the initial value $h^0_{\boldsymbol{k}} = h_{\boldsymbol{k}}(t=0)$ of the Fourier amplitude $h_{\boldsymbol{k}}$. With above equation for the area A and the solution (4.2.10) for $\langle\widehat{\varrho}\rangle_x$ we rewrite the relation (4.2.8) for the surface tension as a first-order differential equation in Γ:

$$\frac{d\Gamma}{dt} = \gamma_h + \frac{\varrho_h}{\chi_a}\Bigg(1 + \frac{1}{2L^2}\sum_{\boldsymbol{k}}\left\{k^2\left|h^0_{\boldsymbol{k}}\right|^2 \exp\left(\frac{2}{\nu}\left(\widehat{e}\left(k\right)t + k^2\Gamma\right)\right)\right\} - \frac{\langle\widehat{\varrho}\rangle^0_x}{\varrho_h}\exp\left(\xi\left(\Gamma - \gamma_h t\right)\right)\Bigg). \tag{4.2.12}$$

We investigate analytical properties of the buckling dynamics which result from the solution of eq. (4.2.12). In section 4.3 the results of theoretical analysis and particle-based buckling simulations are compared.

The initial configuration of the membrane shall be almost flat, with small undulations according to the thermal fluctuation spectrum

$$\left\langle\left|h_{\boldsymbol{k}}\right|^2\right\rangle = \frac{k_b T}{\kappa k^4 + \langle\gamma\rangle_x k^2 + a}, \tag{4.2.13}$$

eq. (4.2.13), see appendix E.2. The initial condition for the tension cumulant is clearly $\Gamma(t=0) = 0$ whereas the initial surface tension $\langle\gamma\rangle_x(t=0) = \langle\gamma\rangle^0_x$ depends on the initial density $\langle\widehat{\varrho}\rangle_x(t=0) = \langle\widehat{\varrho}\rangle^0_x$; as $A(t=0) = L^2$, eq. (4.2.8) yields

$$\langle\gamma\rangle^0_x = \gamma_h + \frac{\varrho_h}{\chi_a}\left(1 - \frac{\langle\widehat{\varrho}\rangle^0_x}{\varrho_h}\right). \tag{4.2.14}$$

Figure 4.4 depicts solutions of eq. (4.2.8) for initial surface tensions $\langle\gamma\rangle^0_x/\gamma_h = 0, 1/2, 1$ (color code) for the observables γ, $\sqrt{\langle h^2\rangle}$, A and $\langle\widehat{\varrho}\rangle_x$. Furthermore, the mean $\langle k\rangle$ of the wavenumber spectrum is shown to indicate the dominant wavenumber. We define the mean wavenumber $\langle k\rangle$ via

$$\langle k\rangle = \frac{\sum_k k w_k}{\sum_k w_k} \qquad \text{with} \qquad w_k = \frac{\sum_{|\boldsymbol{k}|=k}\left|h_{\boldsymbol{k}}\right|^2}{\sum_{|\boldsymbol{k}|=k} 1}. \tag{4.2.15}$$

Numerical solution of eq. (4.2.12) is performed with the `odeint()` function of the python package SciPy [87]. The buckling process can be divided into three stages, which are explained in the following: (1) build up of stress in flat state and initial out-of-plane buckling, (2) fast compressive stress relaxation owing to strong initial area growth at almost constant density, (3) slow stress relaxation and asymptotic convergence (vertical lines in fig. 4.4 indicate stages for initially stress-free membrane $\langle\gamma\rangle^0_x = 0$).

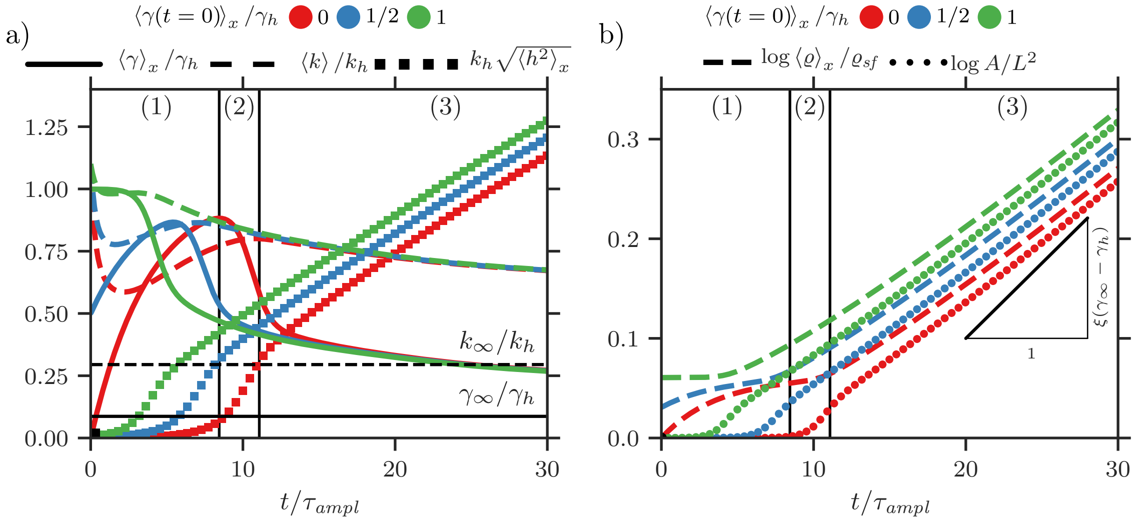

FIGURE 4.4. **a)** Numeric solution of eq. (4.2.12) for surface tension γ (solid lines), average wavenumber $\langle k\rangle$ (dashed lines) and amplitude $\sqrt{\langle h^2\rangle}$ (squares). Given in units of homeostatic stress γ_h and homeostatic wavenumber k_h, see eq. (4.2.20). Horizontal black lines depict asymptotic values for surface tension γ_∞ (solid) and average wavenumber k_∞ (dashed), see eqns. (4.2.27). Color code corresponds to initial surface tension of $\langle\gamma\rangle_x^0/\gamma_h = 0$ (red), $1/2$ (blue), 1 (green), see legend. Vertical lines indicate division into buckling stages for the data set corresponding to $\langle\gamma\rangle_x^0 = 0$ (red lines/symbols), see explanation in main text. Parameters correspond to "buckling-growth-ratios" of $\Theta' \approx 0.07$ and $\Theta'' \approx 0.004$. **b)** Logarithm of projected density $\log\left(\langle\widehat{\varrho}\rangle_x\right)$ (dashed lines) and total area $\log\left(A\right)$ (circles) corresponding to a). The density is divided by the stress-free density ϱ_{sf} at which $\gamma = 0$ in the flat state, see eq. (4.2.8). Color code corresponds to initial surface tension, as in a) (see legend). Black triangle indicates asymptotic slope $\xi\left(\gamma_\infty - \gamma_h\right)$ of both $\log A$ and $\log\widehat{\varrho}$. Vertical lines indicate buckling stages as in a). We used the method `odeint()` of the python package SciPy to obtain the solution [87].

1. Stress Build-up. The membrane starts to buckle as soon as the surface tension $\langle\gamma\rangle_x$ equals the critical value $\langle\gamma\rangle_x^c$, see eq. (4.1.10). In the flat state it is $A = L^2$, and by equating $\langle\gamma\rangle_x = \langle\gamma\rangle_x^c$ in eq. (4.2.8) we obtain the critical density

$$\langle\widehat{\varrho}\rangle_x^c = \varrho_h - \chi_a\left(\frac{4\pi^2\kappa}{L^2} - \gamma_h\right), \tag{4.2.16}$$

upon which the membrane starts to buckle. For smaller initial densities $\langle\widehat{\varrho}\rangle_x^0 < \langle\widehat{\varrho}\rangle_x^c$, we find the density dynamics by elimination of $\langle\gamma\rangle_x$ from eq. (4.2.9) with eq. (4.2.8) for $A = L^2$ which leads to

$$\partial_t\langle\widehat{\varrho}\rangle_x = \xi\frac{\varrho_h}{\chi_a}\left(1 - \frac{\langle\widehat{\varrho}\rangle_x}{\varrho_h}\right)\langle\widehat{\varrho}\rangle_x, \tag{4.2.17}$$

a logistic equation (see eq. (2.2)). The solution reads

$$\langle\widehat{\varrho}\rangle_x(t) = \frac{\varrho_h}{1+\left(\frac{\varrho_h}{\langle\widehat{\varrho}\rangle_x^0}-1\right)\exp\left(-\frac{\xi\varrho_h}{\chi_a}t\right)} \text{ for } \langle\widehat{\varrho}\rangle_x(t) < \langle\widehat{\varrho}\rangle_x^c\,. \tag{4.2.18}$$

Thus, the density increases on the timescale

$$\tau_{g,\mathit{flat}}= \frac{\chi_a}{\xi\varrho_h} < \tau_g, \tag{4.2.19}$$

in the flat state. Note that the timescale $\tau_{g,\mathit{flat}}$ determines stress relaxation towards the homeostatic pressure, whereas the timescale τ_g eq. (4.2.2) corresponds to free growth. Before the membrane buckles, the average wavenumber $\langle k\rangle$ is determined by the thermal amplitude spectrum eq. (4.2.13). As the membrane starts to buckle, compressive surface tension is relaxed as the area A increases. However, as density $\langle\widehat{\varrho}\rangle_x$ increases initially faster than the area A, the surface tension overshoots to values larger than the critical value $\langle\gamma\rangle_x > \langle\gamma\rangle_x^c$. The maximum compressive stress is reached when change rates of A/L^2 and $\langle\widehat{\varrho}\rangle_x/\varrho_h$ are equal at time t_1, which we define as the end of the first buckling phase. We estimate up to which wavenumber k modes are excited during the overshooting of the surface tension. For $\langle\widehat{\varrho}\rangle_x^0 < \varrho_h$, γ_h is clearly an upper bound for the compressive surface tension. Moreover, at $\gamma = \gamma_h$, the largest excitable wavemode is given by $k = \sqrt{|\gamma_h|/\kappa}$, whereas the dominant wavemode is (see eq. (4.1.11))

$$k_h= \sqrt{\frac{|\gamma_h|}{2\kappa}}, \tag{4.2.20}$$

which we denote as *homeostatic wavemode.* Density and surface tension continue to increase towards their homeostatic values as long as the area A is close to L^2. As the area increases with the amplitudes $|h_{\boldsymbol{k}}|$, comparison of the amplitude growth timescale τ_{ampl} eq. (4.1.31) with the density increase timescale $\tau_{g,\mathit{flat}}$ eq. (4.2.19) determines whether the area growth is slow or fast compared to the density increase. The amplitude growth is fastest for $\gamma = \gamma_h$, thus the larger the dimensionless "buckling-growth-ratio"

$$\Theta'= \frac{\kappa\nu\xi\varrho_h}{\gamma_h^2\chi_a} \propto \frac{\tau_{ampl}}{\tau_{g,\mathit{flat}}}, \tag{4.2.21}$$

the larger is the overshoot of the surface tension and the closer to the maximum wavenumber k_h we get during the initial buckling.

2. Fast Stress Relaxation. When the surface tension passes through its compressive maximum, the density increases only slowly as the growth rate $k_g \propto \langle\gamma\rangle_x - \gamma_h$ is in its minimum. Thus, as the area starts to increase, compressive surface tension relaxes very fast, see eq. (4.2.8). As the stress relaxes, density increases faster causing an inflection point at time in the surface tension at which the relaxation rate is maximal. At the inflection point the ratio γ/γ_h changes curvature from concave downward to concave upward, i.e. the first derivative increases over time. Shortly after, the second derivative passes through a maximum after which the first derivative increases much slower. We define the time t_2 of this maximum as the last timepoint of the second phase, hereby, the largest drop in compressive stress is roughly captured.

3. Asymptotic Convergence. Albeit the deflection h grows indefinitely, surface tension and the dominant wavenumber may still converge. The steady state can be identified from the surface tension dynamic eq. (4.2.8). We define γ_∞ as the constant asymptotic limit of the surface tension, insertion into eq. (4.2.8) results in

$$\langle\widehat{\varrho}\rangle_x + \chi_a\left(\gamma_\infty - \gamma_h\right) = \varrho_h \frac{A}{L^2}. \tag{4.2.22}$$

Differentiation with respect to time and division of both sides by above eq. (4.2.22) yields

$$\frac{\partial_t \langle\widehat{\varrho}\rangle_x}{\langle\widehat{\varrho}\rangle_x + \chi_a\left(\gamma_\infty - \gamma_h\right)} = \frac{\dot{A}}{A} = \frac{\sum_{\boldsymbol{k}} k^2 |h_{\boldsymbol{k}}| \partial_t |h_{\boldsymbol{k}}|}{L^2 + \frac{1}{2}\sum_{\boldsymbol{k}} k^2 |h_{\boldsymbol{k}}|^2}, \tag{4.2.23}$$

where we inserted eq. (4.2.11) for the area A. As density $\langle\widehat{\varrho}\rangle_x$ and amplitudes $|h_{\boldsymbol{k}}|$ diverge on long timescales, the constant terms in the denominators on both sides are negligible, thus, the growth rates of the logarithms of density and area converge against the same expression

$$\lim_{t\to\infty} \frac{\partial_t \langle\widehat{\varrho}\rangle_x}{\langle\widehat{\varrho}\rangle_x} = \lim_{t\to\infty} \frac{\dot{A}}{A} = 2\frac{\sum_{\boldsymbol{k}} k^2 |h_{\boldsymbol{k}}| \partial_t |h_{\boldsymbol{k}}|}{\sum_{\boldsymbol{k}} k^2 |h_{\boldsymbol{k}}|^2}. \tag{4.2.24}$$

As the amplitudes $|h_{\boldsymbol{k}}|$, eq. (4.1.28), grow exponentially, the dominant term in above sums over $\boldsymbol{k}$ corresponds to the maximal amplified wavenumber $k = \sqrt{|\gamma|/2\kappa}$, eq. (4.1.11). As the surface tension converges to γ_∞ the maximal amplified wavenumber converges against

$$k_\infty = \sqrt{\frac{|\gamma_\infty|}{2\kappa}}, \tag{4.2.25}$$

which defines the asymptotic wavenumber. Neglecting all other terms in the sums in eq. (4.2.24) and insertion of growth law (4.2.8) and amplitude evolution (4.1.28) yields

$$\frac{\partial_t \langle\widehat{\varrho}\rangle_x}{\langle\widehat{\varrho}\rangle_x} = 2\frac{\sum_{|\boldsymbol{k}|=k_\infty} |h_{\boldsymbol{k}}| \partial_t |h_{\boldsymbol{k}}|}{\sum_{|\boldsymbol{k}|=k_\infty} |h_{\boldsymbol{k}}|^2} \Rightarrow \xi\left(\gamma_\infty - \gamma_h\right) = -\frac{2}{\nu}\left(\kappa k_\infty^4 + \gamma_\infty k_\infty^2\right). \tag{4.2.26}$$

By solution of eqns. (4.2.25) and (4.2.26) we derive the asymptotic constants

$$\frac{\gamma_\infty}{\gamma_h} = \sqrt{\frac{\nu\xi\kappa}{|\gamma_h|}\left(\frac{\nu\xi\kappa}{|\gamma_h|} + 2\right)} - \frac{\nu\xi\kappa}{|\gamma_h|} \qquad \text{and} \qquad \frac{k_\infty}{k_h} = \sqrt{\frac{\gamma_\infty}{\gamma_h}}, \tag{4.2.27}$$

and area and density exhibit the same asymptotic growth rate

$$\frac{\partial_t \langle\widehat{\varrho}\rangle_x}{\langle\widehat{\varrho}\rangle_x} = \frac{\dot{A}}{A} = \xi\left(\gamma_\infty - \gamma_h\right). \tag{4.2.28}$$

The asymptotic values γ_∞ and k_∞ are drawn as horizontal lines in fig. 4.4a), a black triangle in fig. 4.4b) indicates the asymptotic slope of $\log\langle\widehat{\varrho}\rangle_x$ and $\log A$. From the expression for γ_∞, eq. (4.2.27), we see that in the limit of the growth timescale $\tau_g \propto 1/(\xi\,|\gamma_h|)$ being much smaller than the amplitude timescale $\tau_{ampl} \propto \kappa\nu/\gamma_h^2$, asymptotic surface tension and wavenumber converge against the homeostatic values (see fig. 4.5). Thus, the larger the dimensionless "second buckling-growth-ratio"

$$\Theta'' = \frac{\nu\xi\kappa}{|\gamma_h|} \propto \frac{\tau_{ampl}}{\tau_g} \tag{4.2.29}$$

the closer are asymptotic surface tension and wavenumber to the homeostatic values. Conversely, decreasing Θ'' leads to smaller asymptotic surface tension and wavenumber, until the minimum critical surface tension $\langle\gamma\rangle_x^c$ is reached at which only the system-spanning mode

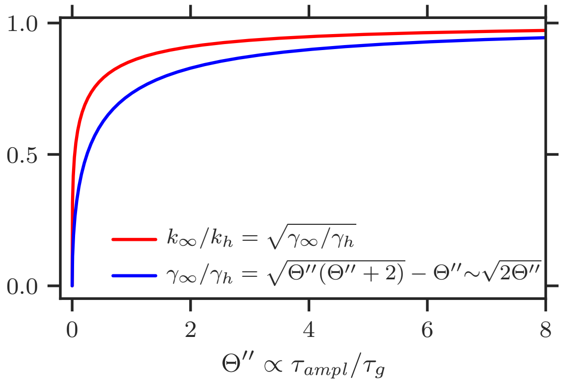

FIGURE 4.5. Asymptotic surface tension γ_∞ and wavenumber k_∞, divided by their respective homeostatic values, as a function of the dimensionless second buckling-growth-ratio Θ''. Note that both curves exhibit infinite slope for Θ'' towards zero; They scale as $\gamma_\infty/\gamma_h \sim \sqrt{2\Theta''}$ and $k_\infty/k_h \sim \sqrt[4]{2\Theta''}$.

$k = 2\pi/L$ buckles. Note, however, that this derivation has to be taken with a grain of salt as eq. (4.2.26) follows from eq. (4.2.23) only for large areas $A \gg 2L^2$ which implies $\langle|\nabla h|^2\rangle \gg 1$ which clearly violates the assumption of a nearly planar membrane (see section 4.1.3). A comparison with buckling simulations is performed in section 4.3 to judge the validity of these results.

In conclusion, the two dimensionless buckling-growth-ratios Θ' and Θ'' in eqns. (4.2.21) and (4.2.29) allow the classification of transient and asymptotic buckling behavior. Note that owing to

$$\Theta' = \frac{\varrho_h}{|\gamma_h|\,\chi_a}\Theta'', \tag{4.2.30}$$

they are not independent of each other. As $\varrho_h > |\gamma_h|\,\chi_a$ due to $\varrho_h = |\gamma_h|\,\chi_a + \varrho_{sf} > |\gamma_h|$ for the stress-free density $\varrho_{sf} > 0$ at which $\gamma = 0$, above equation implies $\Theta' > \Theta''$.

In the limit $\Theta', \Theta'' \to 0$, i.e. growth being slow compared to amplitude increase, we recover the classical buckling instability. In this situation, a flat, stress-free membrane slowly grows and builds up stress. When the stress reaches the critical stress, the membrane buckles at the largest possible wavelength $\lambda = L$, spanning the whole system. Note, however, that the slope of the γ_∞/γ_h- and k_∞/k_h-curves diverges for $\Theta'' \to 0$ (see fig. 4.5). Therefore, for large system sizes $L \gg 1/k_h$ this case may occur only for extremely small values of Θ'' (e.g. for $L = 10 \cdot 2\pi/k_h$ it is $k_\infty = 2\pi/L$ for $\Theta'' \approx 5 \cdot 10^{-5}$). Vice versa, in the limit $\Theta', \Theta'' \to \infty$, buckling occurs close to the homeostatic mode k_h. Cell growth is much faster than amplitude increase such that the density equilibrates very fast to the homeostatic value. Thus, surface tension stays close to its homeostatic value during the buckling process and the strongest amplified wavenumber is close to the homeostatic wavenumber. As the fraction k_∞/k_h as a function of Θ'' saturates quickly towards 1, we expect this case to occur for a large range of Θ'' values (it is $k_\infty/k_h \approx 0.6$ already for $\Theta'' = 0.1$). In the mixed case, $\Theta' \to \infty, \Theta'' \to 0$, initially modes close to the homeostatic mode k_h buckle, whereas the asymptotic mode is much smaller.

Our model predicts that for stress-dependent growth and without elastic substrate, buckling can occur at non-system-spanning modes $k \gg 2\pi/L$. The transition from buckling around $k = 2\pi/L$ to buckling at the homeostatic wavenumber $k_h = \sqrt{|\gamma_h|/2\kappa}$ can be tuned for a fixed value of k_h by either changing growth strength parameter ξ or the background friction strength ν. In particular, the stable wavenumber is affected by the frictional parameters of the embedding medium. Furthermore, in contrast to the differential growth hypothesis, wavenumber selection via the "buckling-growth-ratio"-mechanism does not require a gradient in growth stress along the membrane thickness. Interestingly, we obtain qualitatively very similar results if we replace the uniform background friction with a Newtonian fluid, see appendix E.3.

In the broader context, the timescales τ_{ampl} and τ_g determine whether folding dynamics are quasi-stationary or whether explicit dynamics need to be taken into account. In the limit $\tau_{ampl} \ll \tau_g$ elastic relaxation is fast compared to cell-density increase and we expect the system to evolve along minimal energy configurations. In turn, whenever $\tau_{ampl} \gtrapprox \tau_g$, folding dynamics have to be resolved explicitly. Consideration of these timescales provides insights for other types of interactions between membrane and embedding medium as well. As an example, we consider the model which we used in section 2.2 to illustrate the differential-stress hypothesis: a growing membrane subject to uniform friction with a linear elastic medium underneath. From eqns. (4.1.14) and (4.1.30) follows that, close to the flat state, the amplitude of the minimal energy wavenumber $k_{min}^{\widehat{E}}$ for $\gamma = \gamma_h$ increases exponentially with the timescale

$$\tau_{ampl}^{\widehat{E}} = \frac{\kappa\nu}{\gamma_h^2}\left(\frac{2}{3}\cos^2(\ldots) - \frac{4}{9}\cos^4(\ldots) - \sqrt{\frac{2}{3}}\sqrt{\frac{\kappa\widehat{E}^2}{|\gamma_h|^3}}\cos(\ldots)\right)^{-1} \tag{4.2.31}$$

with

$$\cos(\ldots) = \cos\left(\frac{\pi}{3} - \frac{1}{3}\arccos\left(\sqrt{\frac{27\kappa\widehat{E}^2}{8|\gamma|^3}}\right)\right). \tag{4.2.32}$$

We expect quasi-stationary dynamics to fail for $\tau_{ampl}^{\widehat{E}} \gtrapprox \tau_g$. Note that the term $\sqrt{\kappa\widehat{E}^2/|\gamma_h|^3}$, which occurs in eqns. (4.2.31) and (4.2.32), is bounded; Owing to the buckling condition $\gamma_h \geq \langle\gamma\rangle_x^{c,\widehat{E}}$, eq. (4.1.12), it is

$$0 \leq \sqrt{\frac{27\kappa\widehat{E}^2}{4|\gamma_h|^3}} \leq 1. \tag{4.2.33}$$

Within this range, a simple lower bound approximation for $\tau_{ampl}^{\widehat{E}}$ is given by

$$\frac{4\kappa\nu}{\gamma_h^2}\frac{1}{1-\sqrt{\frac{27\kappa\widehat{E}^2}{4|\gamma_h|^3}}} \leq \tau_{ampl}^{\widehat{E}}, \tag{4.2.34}$$

which eases evaluation of the condition $\tau_{ampl}^{\widehat{E}} \gtrapprox \tau_g$ in practical contexts.

4.3. Simulations of Growing Membranes

We simulate the buckling of a free membrane square subject to periodic boundary conditions at its edges and with pressure-dependent growth by means of the 2PG-method. Our goal is to investigate whether wrinkling patterns with wavenumbers larger than the system spanning mode $k > 2\pi/L$ occur without an elastic support, as predicted by the analytical theory in section 4.2. The 2PG-technique enables us to study the full membrane growth dynamics beyond the approximations made in the analytical calculations, in particular, large amplitude deformations are accessible. The analytic calculations suggest a dominant role of amplitude and growth timescales whose fraction, the "buckling-growth-ratio"

$$\frac{\tau_{ampl}}{\tau_g} \propto \Theta'' = \frac{\nu \xi \kappa}{|\gamma_h|}, \tag{4.3.1}$$

we predict to steer the dominant wavenumber in between the extremes. The limit $\Theta'' \to 0$ corresponds to growth and stress build-up being slow compared to amplitude increase and stress-relaxation; This leads to buckling close to the system spanning mode $k = 2\pi/L$ which has the smallest critical buckling stress $\gamma^c = \kappa \left(2\pi/L\right)^2$. Conversely, in the limit $\Theta'' \to \infty$, amplitude and area increase are slow compared to the build-up of growth stress and the homeostatic wavenumber $k = k_h$ is observable (see section 4.2). The control of wrinkling lengthscales via growth timescales comprises a patterning mechanism distinct from the established differential growth hypothesis (see section 2.2).

We begin with an analysis of the early small amplitude buckling where the wave pattern can be expressed in the Monge-representation. Thus, we can compare simulation results with our analytical theory. Afterwards, we take a look at the larger amplitude folding dynamics.

4.3.1. Small Amplitude Buckling. In simulations, we equilibrate a square membrane patch of size $L = 120 r_{pp}$ to its homeostatic state. Buckling during equilibration is prevented with a soft harmonic confinement as used in section 3.4.2. At $t = 0$, confinement is released and we observe the buckling in real and Fourier-space (see fig. 4.6). The FFT is performed on the same interpolated gridpoints $z_{ij} = h(id, jd)$ (with mesh size $d = r_{pp}/2$) used for the the membrane area calculation. To estimate interpolation error and the validity of the Monge-representation, we calculate for every gridpoint (i, j) the average weighted deviation from the membrane particles in range

$$\epsilon_{ij} = \sqrt{\frac{\sum_\alpha w\left(x_i - x_\alpha, y_i - y_\alpha\right)\left(z_{ij} - z_\alpha\right)^2}{\sum_\alpha w\left(x_i - x_\alpha, y_i - y_\alpha\right)}}, \tag{4.3.2}$$

with the same weight function w as used for the interpolation. For values of the maximum error around $\max_{i,j}\left(\epsilon_{ij}\right) \approx 1.3 r_{pp}$ the membrane exhibits overlapping folds shortly afterwards, such that we use this condition to separate Monge from overlapping shapes.

Simulation parameters are chosen using the parameter set of the reference system (see table I.1 in appendix I). Starred parameter values denote relative values with respect to this parameter set (e.g. $B^* = 0.6$ corresponds to 0.6 times the value in table I.1). We vary the growth strength in the range $B^* = 0.6 - 1.0$ which covers roughly one order of magnitude in the homeostatic surface tension γ_h. Around $B^* \approx 0.57$, γ_h changes its sign, i.e. the homeostatic state changes from compressive to tensile such that the flat membrane state becomes unconditionally stable. To probe the dependency of the wavepattern on the timescales τ_{ampl} and τ_g, we vary the background friction γ_b in the range $\gamma_b^* = 0.1 - 10$. We assume that the amplitude friction parameter ν is approximately $\nu \approx \varrho \gamma_b$. Furthermore, we change the intracell friction γ_c in the range $\gamma_c^* = 0.5 - 5$ while we keep the product $\gamma_c k_a = 1$ constant. In this manner, we change the timescale of cell turnover and growth for approximately constant homeostatic surface tension, thus, we change the pressure sensitivity $\xi \propto 1/\gamma_c$.

Simulation Dynamics and Theory. Examples for simulation dynamics in real and Fourier space are depicted in fig. 4.6. The FFT-spectra appear to be almost isotropic with no pronounced direction in the wavevector $\boldsymbol{k}$. Instead, the FFT-amplitudes $h_{\boldsymbol{k}}$ depend mainly on the wavenumber $k = |\boldsymbol{k}|$, with buckling occurring in a narrow strip around a mean wavenumber $\langle k \rangle$. Therefore, the membrane height profile resembles a random superposition of sinusoidal waves within a wavenumber range. Structures of this type belong to the class of so-called *Gaussian random fields* which are used, for example, to describe the structure of microemulsions [99, 100] or cosmological density fluctuations [101]. The mean wavenumber is largest shortly after out-of-plane buckling and decreases steadily afterwards. In real space, this corresponds to a coarsening of structures, as height fluctuations with small wavelength become less pronounced over time.

To understand the observed wavenumber dynamics, we compare simulations with the predictions of the theory developed in section 4.2. Figure 4.7 depicts average wavenumber $\langle k \rangle$ (see eq. (4.2.15)), surface tension $\langle \gamma \rangle_x$, area A, projected density $\langle \widehat{\varrho} \rangle_x$ and height $\sqrt{\langle h^2 \rangle_x}$ corresponding to growth strength parameter $B^* = 0.7$. The similar results for growth strengths $B^* = 0.6, 0.8, 0.9, 1.0$ are shown in appendix F. Average wavenumber $\langle k \rangle$ and surface tension $\langle \gamma \rangle_x$ exhibit the same qualitative behavior in simulation and theory. Starting from the homeostatic state $\langle \gamma \rangle_x = \gamma_h$, surface tension relaxes very fast during initial buckling and much slower on long timescales. Average wavenumber equals initially the "thermal" wavenumber k_{th} determined by the thermal amplitude distribution eq. 4.2.13. Upon buckling the average wavenumber quickly evolves towards the homeostatic wavenumber k_h and shifts to smaller values alongside the relaxation of the surface tension. As simulation and theory agree qualitatively, we deem the observed shift to smaller wavenumbers over time to be caused by the same mechanism. Buckling causes an increase in the available area per cell and therefore a relaxation of compressive stress. The smaller compressive stress favors the amplitude increase of smaller wavenumbers (see section 4.1.2) and causes the observed shift.

Simulation and theory exhibit in some cases a good quantitative agreement for surface tension $\langle \gamma \rangle_x$ and average wavenumber $\langle k \rangle$. Furthermore, in many cases with large deviations between simulation and theoretical predictions, it appears that these occur because the initial buckling dynamics in simulations and theory start at different time points. Often, the slopes of the curves agree well on long timescales. Thus, simulation and theory agree much better if theory curves are shifted along the time axis accordingly. This indicates that our theoretical predictions captures the essential dynamics also on long timescales until the membrane leaves the Monge-representation. This observation is surprising as the coarse approximations the theory relies on, spatially constant surface tension and negligible higher order curvature terms, are violated on long timescales.

In contrast, theory does not predict simulation dynamics well for area A, projected density $\langle \widehat{\varrho} \rangle$ and height $\sqrt{\langle h^2 \rangle_x}$, see fig. 4.7 c)-e). After initial buckling, these observables increase much faster in simulation than in theory. Thus, growth is much faster in simulations than in theory. Measurement of the relation between growth rate k_g and surface tension $\langle \gamma \rangle_x$ during buckling (see fig. 4.7 f)) reveals that the actual growth rates are much larger as predicted by the linear relationship $k_g = \xi \left(\gamma - \gamma_h \right)$ in eq. (4.2.4). This non-linear trend towards larger growth rates has also been observed in the ξ-measurements in section 3.4.3 for surface tensions far away from the homeostatic state $\gamma / \gamma_h < 0.8$ which are reached during buckling. Furthermore, the growth rate measurements in section 3.4.3 have been performed in the confined flat state, which may exhibits a growth behavior different from the curved buckled state. Thus, is it not surprising that the theoretical prediction with the linear growth law eq. (4.2.4) fails to reproduce the simulation dynamics. Fortunately, it is feasible to adapt our theory to a non-linear growth-surface tension relation $k_g(\langle \gamma \rangle_x) = \partial_t \langle \widehat{\varrho} \rangle / \langle \widehat{\varrho} \rangle$. Instead of

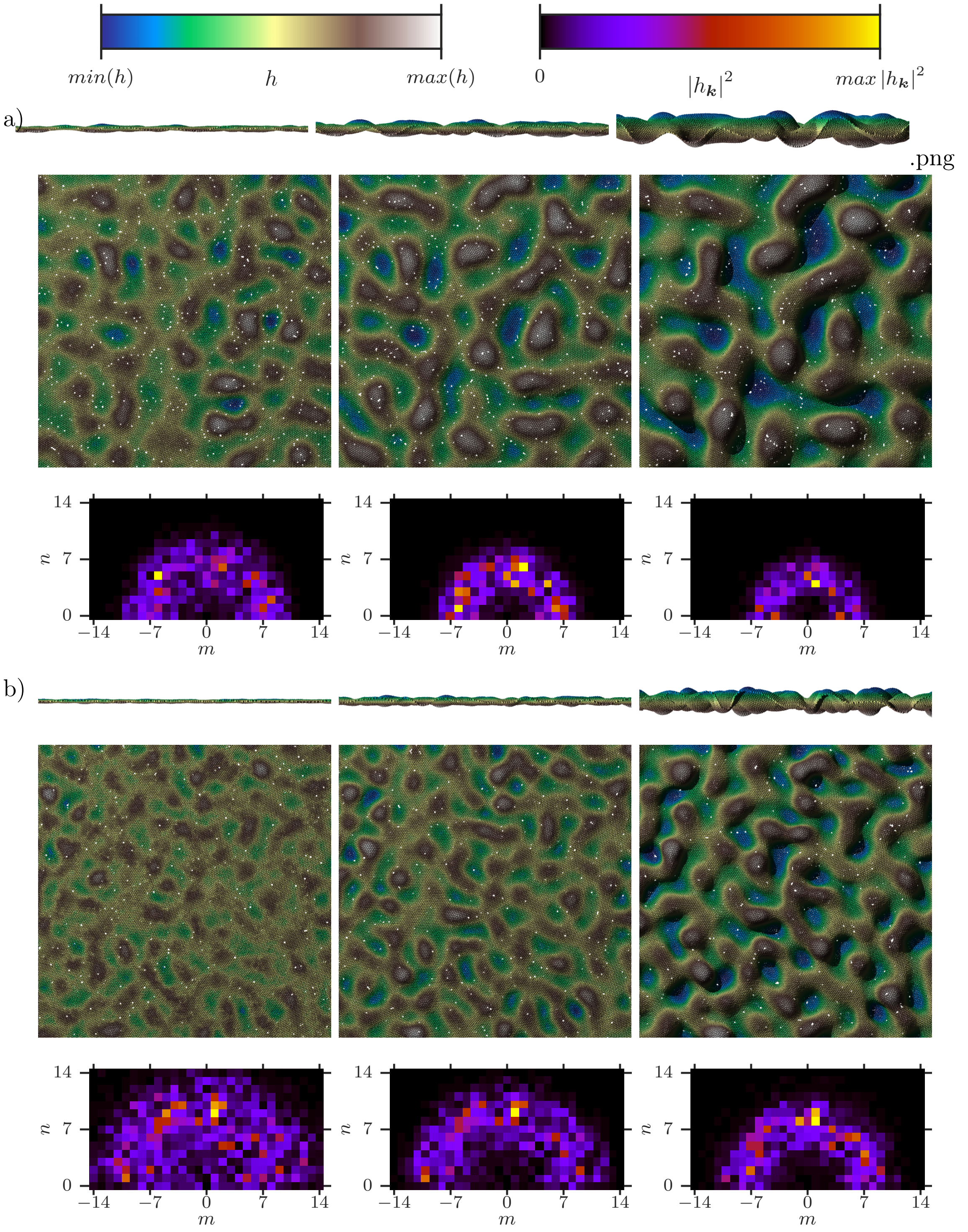

FIGURE 4.6. **a)** From top to bottom: top view, side view and FFT-spectrum of a buckling simulation with parameters $B^* = 0.8, \gamma_c^* = 1, \gamma_b^* = 1$. Time increases from left to right. FFT-spectrum depicted dependent on integer orders m, n corresponding to wavenumbers $\boldsymbol{k} = 2\pi/L\,(m, n)$. **b)** Same as a) for larger growth force strength $B^* = 1$.

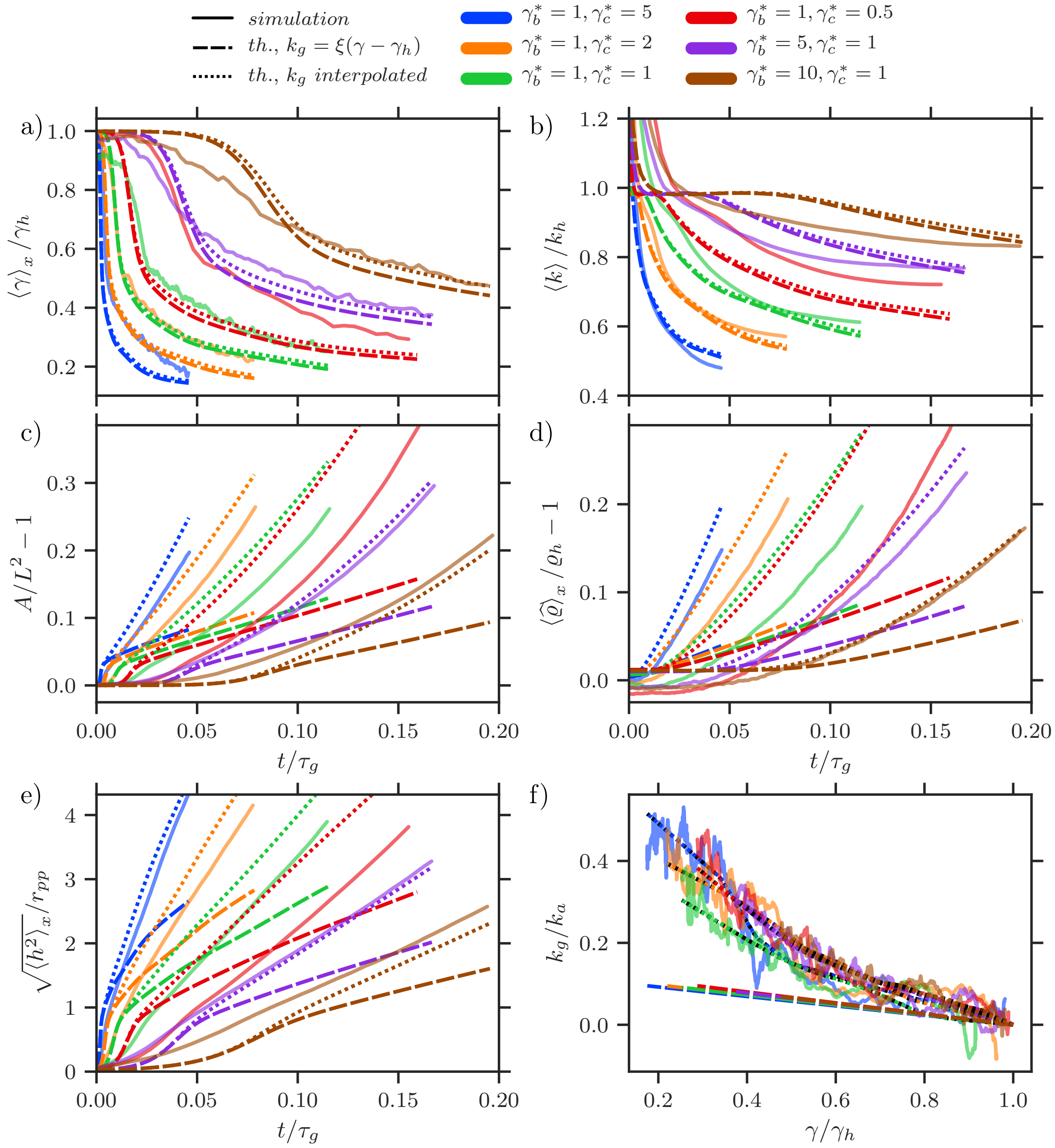

FIGURE 4.7. **a)** Surface tension $\langle\gamma\rangle_x$ as a function of time for simulations (solid lines) with growth strength parameter $B^* = 0.7$ and various values of background friction γ_b^* and intracell friction γ_c^* (see legend). Dashed lines show solution of theory with growth rate $k_g = \xi\,(\gamma - \gamma_h)$, dotted lines with piecewise linear interpolation of measured growth rate, see f). Time unit equals growth timescale τ_g. **b)-e)** As a) for average wavenumber $\langle k \rangle$, relative area increase $A/L^2 - 1$, relative density increase $\langle \widehat{\varrho} \rangle_x / \varrho_h - 1$ and square root of second height moment $\sqrt{\langle h^2 \rangle_x}$. **f)** Measured growth rate k_g during buckling versus surface tension γ in simulations (solid lines). Dashed lines depict linear growth law $k_g = \xi\,(\gamma - \gamma_h)$ from measurements in section 3.4, dotted lines with black outline depict piecewise linear interpolation used for solution of eqns. (4.3.3).

the differential equation (4.2.12) in the surface tension cumulant Γ, we express the theory dynamics in terms of the vector $(\Gamma, \langle\varrho\rangle_x)$, whose time derivative reads

$$\frac{d}{dt}\begin{pmatrix}\Gamma\\ \langle\widehat{\varrho}\rangle_x\end{pmatrix} = \begin{pmatrix}\langle\gamma\rangle_x\\ k_g(\langle\gamma\rangle_x)\,\langle\widehat{\varrho}\rangle_x\end{pmatrix} = \begin{pmatrix}\gamma_h + \frac{\varrho_h}{\chi_a}\left(\frac{A}{L^2}-\frac{\langle\widehat{\varrho}\rangle_x}{\varrho_h}\right)\\ k_g\left(\gamma_h+\frac{\varrho_h}{\chi_a}\left(\frac{A}{L^2}-\frac{\langle\widehat{\varrho}\rangle_x}{\varrho_h}\right)\right)\langle\widehat{\varrho}\rangle_x\end{pmatrix}, \tag{4.3.3}$$

by virtue of relation (4.2.8). Insertion of the area $A = A(\Gamma, t)$ from eq. (4.2.11) yields then again a first-order differential equation system of the form $y'(t) = f(y, t)$ which can be solved by standard numeric routines. To investigate how the theoretical prediction improves with a non-linear growth-surface tension relation, we solve eq. (4.3.3) with a piecewise linear approximation of $k_g(\langle\gamma\rangle_x)$, measured in simulations (see fig. 4.7 f)). As we see in fig. 4.7 c)-e), the improved theory predicts long-time behavior of A, $\langle\widehat{\varrho}\rangle$ and $\sqrt{\langle h^2\rangle_x}$ much better. Surface tension $\langle\gamma\rangle_x$ and average wavenumber $\langle k\rangle$ are slightly larger than before, as expected. In conclusion, the comparison between simulation and theory shows that the theory predicts the essential features of the simulation dynamics very well, even though the approximations made are violated during the buckling process.

Wavepattern at Transition to Overlapping Shapes. We take a look at the wavepattern close to the transition to overlapping shapes. After this transition, the description of the membrane by a projected height $h(\boldsymbol{x})$ is not possible anymore, therefore, the membrane description requires a new set of theoretical and numerical tools. We analyze in section 4.3.2 how the "last" Monge-shape is related to the dynamics of the overlapping membrane shape.

Figure 4.8 depicts an overview of average wavenumber $\langle k\rangle$ and surface tension $\langle\gamma\rangle_x$ at the last timepoint t_{lm} of the Monge-representation as a function of the "buckling-growth-ratio"

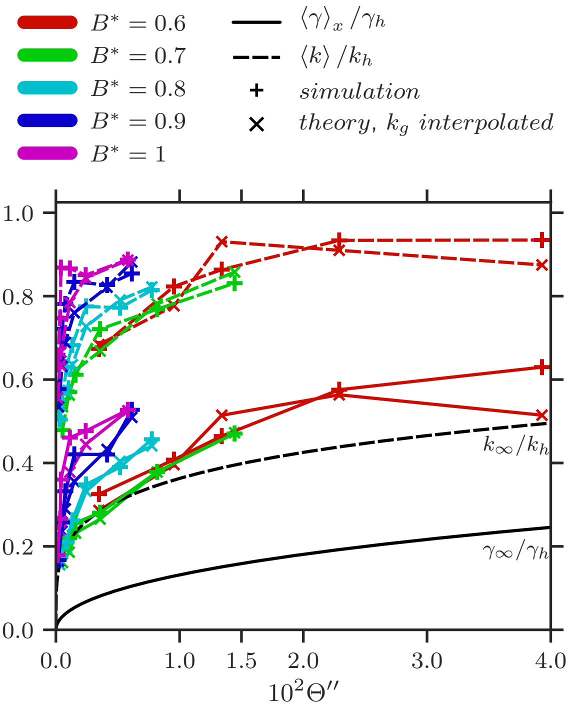

FIGURE 4.8. Surface tension ratio $\langle\gamma\rangle_x/\gamma_h$ (solid lines) and average wavenumber ratio $\langle k\rangle/k_h$ (dashed lines), measured at the transition point t_{lm} to overlapping shapes, as a function of the "second buckling-growth-ratio" $\Theta'' \propto \tau_{ampl}/\tau_g$ ("+" symbols for simulation data, "×" symbols for theory solution according to eqns. (4.3.3) with piecewise linear interpolated growth rate k_g). Note that the theory is integrated up to a timepoint t^* at which the projected density equals the value in simulations at the last point t_{lm} in Monge-representation (t^* fulfills $\langle\widehat{\varrho}\rangle_x^{theory}(t^*) = \langle\widehat{\varrho}\rangle_x^{sim}(t_{lm})$). Every color corresponds to a fixed value of the growth strength parameter B^* (see legend). Black lines depict asymptotic surface tension and wavenumber from theory with growth rate $k_g = \xi(\gamma - \gamma_h)$, see eqns (4.2.27).

$\Theta'' = \kappa\nu\xi/|\gamma_h|$. In simulations, the timepoint t_{lm} has been chosen, as in the previous section, such that the interpolation error ϵ_{ij}, eq. (4.3.2), fulfills $\max_{i,j} \epsilon_{ij} \approx 1.3 r_{pp}$. To compare the simulation with our theoretical prediction, we depict $\langle k \rangle$ and $\langle \gamma \rangle_x$ from the analytic model with piecewise linear interpolated growth rate, eqns. (4.3.3), chosen at a timepoint t^* where the theoretical projected density $\langle \widehat{\varrho} \rangle_x^{theory}$ equals the simulation projected density $\langle \widehat{\varrho} \rangle_x^{sim}$ at the last timepoint in Monge-representation; that is to say t^* fulfills $\langle \widehat{\varrho} \rangle_x^{theory}(t^*) = \langle \widehat{\varrho} \rangle_x^{sim}(t_{lm})$. To calculate Θ'', we take into account the observed larger growth rate during buckling (compared to the measurements in the flat state in section 3.4.3) by re-estimation of the growth timescale constant ξ from a fit of $k_g = \xi\,(\gamma - \gamma_h)$ to the measured growth rates $k_g(\gamma)$.

We see on fig. 4.8 that the homeostatic fractions $\langle k \rangle / k_h$ and $\langle \gamma \rangle_x / \gamma_h$ are clearly larger than the analytical asymptotic values k_∞ / k_h and γ_∞ / γ_h (see eqns. (4.2.27)). This is not surprising, as their derivation implies that asymptotic convergence occurs for areas $A \gg 2L^2$, much larger than the observed areas in the Monge-representation. Furthermore, values with similar Θ''-values but different growth strength B do not collapse onto the same data point. However, for fixed growth strength B and therefore similar homeostatic pressure γ_h, values increase with Θ'' in most cases. Thus, the asymptotic values k_∞ and γ_∞ predict the monotony in Θ'' correctly. Moreover, the solution of the model with non-linear growth rate predicts the simulation value fairly well in most cases. In conclusion, we found that for fixed homeostatic pressure, wavenumber and surface tension fraction at the transition point to overlapping shapes increase with the timescale fraction Θ''. The variation for fixed Θ'' and changing γ_h matches well with our theoretical model.

4.3.2. Shapes with Overlap. After the growing membrane left the Monge-representation, we let growth continue until the number of particles is 2-3 times the initial value in the flat state. At this point we test the elastic stability of the folded shape if growth is stopped by some external process. To do so, we replace the growth force by a harmonic spring with equilibrium length equal to the current cell axis length and disable apoptosis and division sampling. Hereby, we assume that the mechanism which stops growth conserves cell number and size. We follow the passive system over a timespan as least as long as the membrane with smallest growth strength $B^* = 0.6$ needs to leave the Monge-representation. Examples for the time-evolution of membrane folds are depicted in figs. 4.9 and 4.10.

The time evolution of height $\sqrt{\langle h^2 \rangle_x}$, projected density $\langle \widehat{\varrho} \rangle_x$ and virial stress times system volume $\overline{\boldsymbol{\sigma}} V = \overline{\boldsymbol{\sigma}} A d$ are shown in fig. 4.11. Stress measurements are difficult as they require area measurements for overlapping shapes. However, volume times stress is still accessible as only velocity and force measurements are required, see eq. (3.4.6). The quantity $\overline{\boldsymbol{\sigma}} V$ is related to the forces acting at the system boundaries, as we show in the following. With the local equation of motion $\operatorname{div} \overline{\boldsymbol{\sigma}} = \frac{d}{dt}(\varrho \boldsymbol{v})$ it is easy to verify that [55]

$$V \langle \overline{\boldsymbol{\sigma}} \rangle_x = \int_{\partial V} \boldsymbol{x} \otimes (\overline{\boldsymbol{\sigma}} \boldsymbol{n})\, dA - \int_V \boldsymbol{x} \otimes \frac{d}{dt}(\varrho \boldsymbol{v})\, dV, \tag{4.3.4}$$

where $\boldsymbol{n}$ denotes the normal vector at the volume boundaries. Note that the stress tensor on the right-hand side of eq. (4.3.4) refers to the local stress $\overline{\boldsymbol{\sigma}}(\boldsymbol{x})$ at the points on the contour; On the left-hand side appears the virial stress tensor as the spatial average of the local stress over the whole system volume. From eq. (4.3.4) follows for elastic equilibrium and vanishing

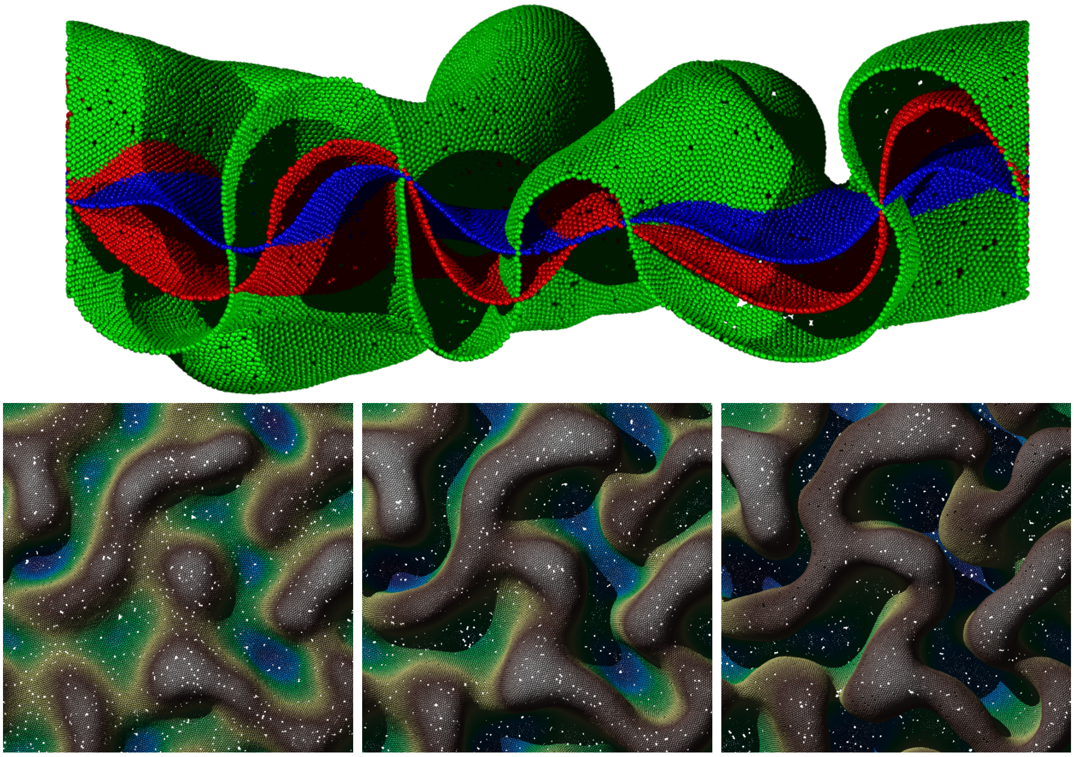

FIGURE 4.9. Top picture shows cuts along vertical direction of growing membrane with growth strength parameter $B^* = 0.7$ (all other equal standard values) at different timepoints (last Monge-frame is blue, approximately three times initial cell number is reached at green configuration, red depicts frame in the center timepoint between the latter two). Bottom row depicts corresponding top view, vertical elevation is color coded as in fig. 4.6.

in-plane shear stress $\sigma_{xy} = 0$

$$\frac{V}{L}\frac{\sigma_{xx} + \sigma_{yy}}{2} = \frac{F_x + F_y}{2} = F_{\parallel}, \tag{4.3.5}$$

where F_x, F_y denote the net forces acting at the membrane boundaries at $x, y = 0, L$ in x, y-direction and σ_{xx}, σ_{yy} components of the virial stress tensor. Shortly after overlapping shapes occur, the projected density $\langle\widehat{\varrho}\rangle_x$ increases exponentially over time, as expected for non-limited growth. As the area increases, vertical cuts through the membrane show that the initially sinusoidal wavepatterns fold inward in the horizontal direction which results in shapes similar to the letter “Ω” (see fig. 4.9). Similar shapes occur in classical elasticity theory, for example for a plane rod subject to compressive forces at its ends, see fig. 4.11. Here, the Ω-shapes result as minimal curvature energy solutions for a fixed value of projected length divided by total arc length $L_x/L \in [0, 1]$. Thus, the Ω-shapes result most likely due to local curvature energy minimization.

The lengthscale of the Ω-lobes is largely determined by the dominant wavemode at the last Monge-representable point, as almost all hills and valleys give rise to a lobe. Often, close hills either (1) develop a saddle-shaped connecting area or (2) fuse together. The first case

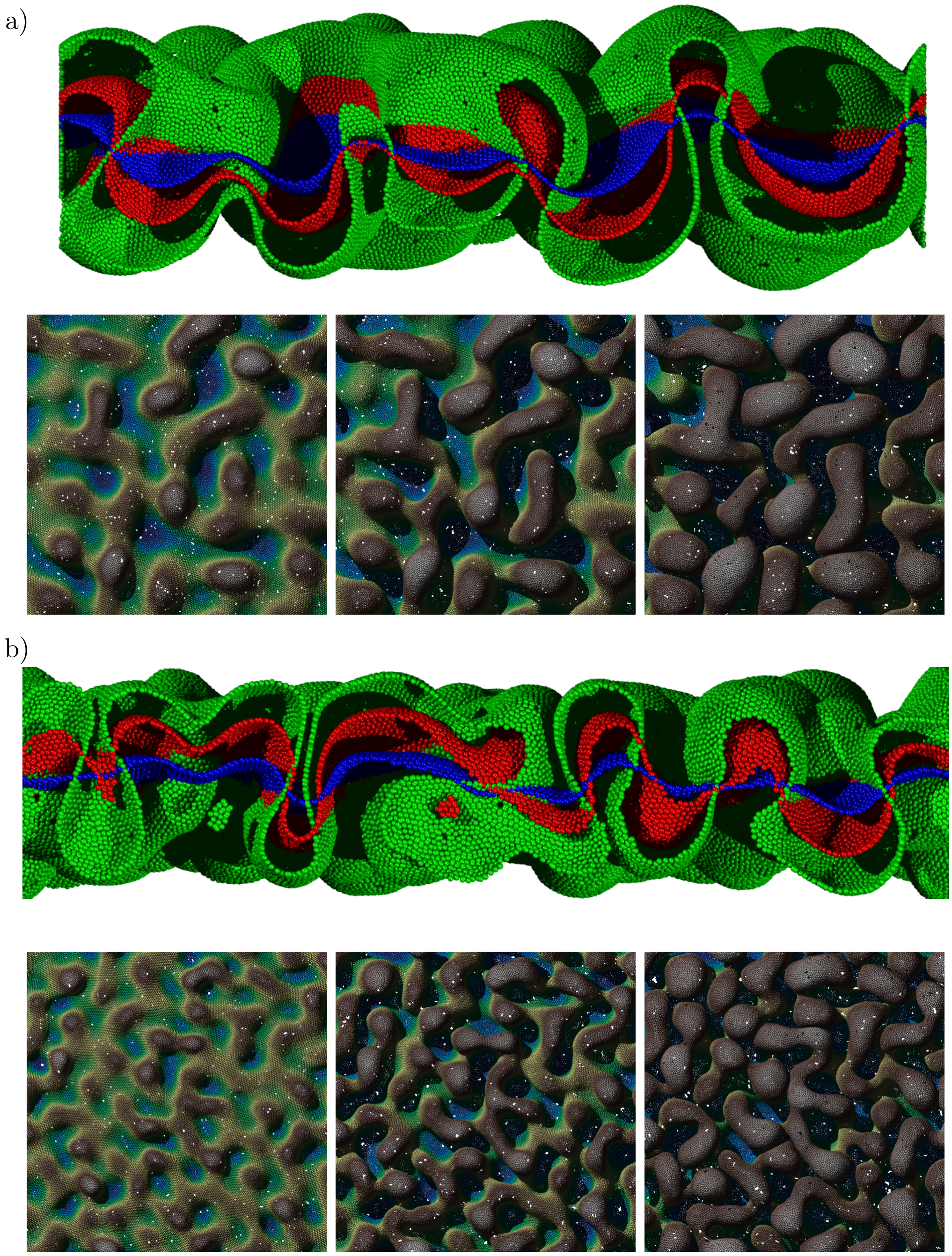

FIGURE 4.10. **a)** Top image depicts cuts along vertical direction of growing membrane with growth strength parameter $B^* = 0.8$ (all other equal standard values) at different timepoints (last Monge-frame is blue, approximately three times initial cell number is reached at green configuration, red depicts frame in the center timepoint between the latter two). Bottom image depicts corresponding top view, vertical elevation color is coded as in fig. 4.6. **b)** As a) for growth strength parameter $B^* = 1$.

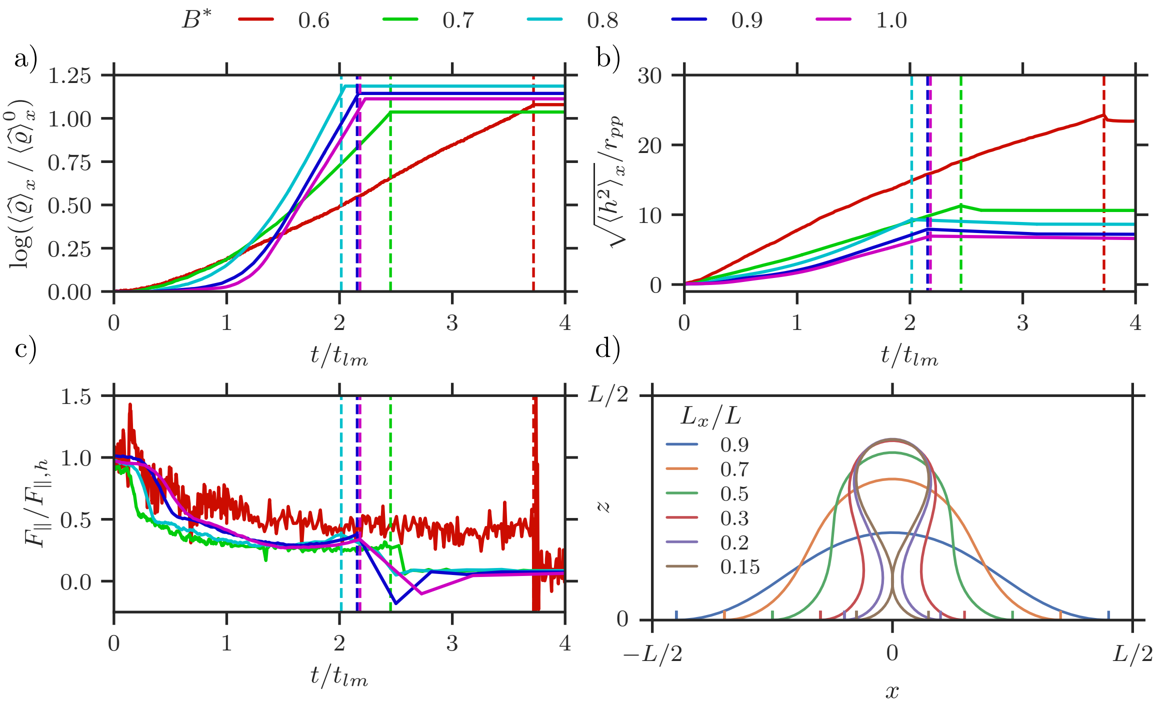

FIGURE 4.11. **a)** Logarithm of projected density over initial density as a function of time. The time axis is scaled such that the last timepoint in Monge-representation t_{lm} falls on one. Vertical dashed lines indicate when growth has been switched off. Color code corresponds to simulations for different growth strengths B^* (see legend, all other parameters equal standard values). **b)-c)** As a) for square-root of second central moment of height $\langle h^2 \rangle_x$ and in-plane boundary force divided by its homeostatic value $F_{\parallel,h} = L\gamma_h$. **d)** Shapes of minimal curvature energy for a one-dimensional rod of length L compressed in x-direction to a given value of the projected length $L_x < L$. Minimization with respect to boundary conditions $z(0) = z(L)$ and $z'(0) = 0 = z'(L)$.

occurs likely due to curvature energy reduction as saddles with opposite sign main curvatures result in smaller mean curvature H than a connection with the same elevation as both hills. The second case may occur due to the local excess area being too large to be stored in a saddle. In particular, as no new lobes occur, the length $\lambda = 2\pi/\langle k \rangle$, with $\langle k \rangle$ estimated at the last timepoint in the Monge-representation t_{lm}, yields a good lower bound estimate of the average horizontal distance between two neighboring Ω-lobes.

For simulations with large buckling wavenumber $\langle k \rangle$, we also observe folds touching each other, however, folds never mix due to short range repulsion of the MMM-potential (see section 3.3.2). In one dimension, self-intersection occurs for strong compression with L_x/L around $L_x/L \approx 0.15$. As shapes with overlaps occur, the in-plane boundary force $F_\parallel$ tends to decrease a bit and approaches a steady state for simulations without touching folds. Otherwise, $F_\parallel$ increases again as soon as folds start to touch. Furthermore, we observe little variance in the overall lobe-elevation, such that touching lobes continue to grow without one overtaking the other. In particular, we never observe that one lobe overgrows another. Overall, the height $\sqrt{\langle h^2 \rangle_x}$ increases linearly during post-Monge growth.

After stopping growth, height stays constant after a small initial drop. The initial drop appears likely due to the relaxation of compressive intracell stress, which is exactly zero in the moment when the growth potential is replaced by a harmonic spring. The drop in intracell compressive stress is visible in the boundary force $F_{||}$ which exhibits a sharp drop, sometimes large enough to even become tensile over a short period. Shortly afterwards, the boundary force relaxes to a small compressive value, which is however much smaller than the compressive forces shortly before stopping growth. Interestingly, the ratio $F_{||}/F_{||,h}$, where $F_{||,h} = L\gamma_h$ denotes the boundary force in the homeostatic state, seems to adopt the same value for all simulations.

Membrane shape undergoes only small changes during the timespan observed without growth. Small local undulations flatten out, but the overall lengthscale of larger folds remains stable. Thus, even without an elastic support underneath, the selected wavelength seems to be stable even though it is clearly not the configuration of minimal curvature energy. In one dimension and for fixed length L, curvature energy scales quadratically with the number n of bulges $E_{bend} \propto n^2$ depicted in fig. 4.11. Thus, a combination of curvature and in-plane elasticity is likely to be responsible for the stability over the observed timespan.

4.4. Summary

Overall, we deepen the understanding of the buckling behavior of a membrane with growth dependent on stress by a combination of simulations and analytic theory. In buckling simulations, we observe wavenumbers much larger than the system-spanning mode $k = 2\pi/L$ which is typically the first mode to become unstable in classical buckling theory. Furthermore, compressive surface tension relaxes over time, paralleled by a shift of the dominant wavenumber towards smaller values. The membrane leaves the Monge-representation as secondary folds in horizontal direction occur which result in shapes similar to the letter "Ω". The distance of Ω-bulbs in the xy-plane and the dominant wavelength shortly before leaving the Monge-representation are closely related as almost every sinusoidal valley or hill gives rise to a Ω-bulb. With the help of an analytical model, a combination of the homeostatic growth law $k_g \propto \gamma - \gamma_h$ with Föppl-von Kármán plate bending theory, we are able to show that the buckling pattern arises from an interplay between membrane area and cell density dynamics. In particular, the overall dynamics are well characterized by two quantities. The homeostatic wavenumber

$$k_h = \sqrt{\frac{|\gamma_h|}{2\kappa}}, \tag{4.4.1}$$

determines the upper bound of possible dominant wavemodes. Which wavenumber in the interval $2\pi/L \leq k \leq k_h$ is amplified strongest depends on the ratio of amplitude increase timescale τ_{ampl} and cell growth timescale τ_g, the "buckling-growth-ratio"

$$\Theta'' = \frac{\nu\kappa\xi}{|\gamma_h|} \propto \frac{\tau_{ampl}}{\tau_g}, \tag{4.4.2}$$

as can be understood intuitively: For $\tau_g \ll \tau_{ampl}$ equilibration towards the homeostatic state is much faster than stress relaxation via area increase such that the surface tension stays close to the homeostatic value $\gamma \approx \gamma_h$ which results in buckling close to k_h. Vice versa, for $\tau_{ampl} \ll \tau_g$, stress relaxes much faster as it can be built up due to cell growth, hence, the surface tension is close to the critical value $\gamma \approx \kappa\,(2\pi/L)^2$ which amplifies the system-spanning mode $k = 2\pi/L$. Even though our theory is only applicable in the small amplitude limit $|\nabla h|^2 \ll 1$, simulations suggest that the essential part of wavemode selection takes place in this limit, as the lengthscale carries over to post-Monge membrane dynamics. Thus, we deem k_h and τ_{ampl}/τ_g to be the key parameters which determine membrane patterns for growth in the Monge-representation and as well afterwards when overlapping shapes occur. Moreover, our findings show that explicit buckling dynamics should be taken into account if the timescales τ_g and τ_{ampl} are of comparable scale as folding dynamics do not evolve in a quasi-static manner.

CHAPTER 5

Nutrient Limited Growth of Bacterial Microcolonies

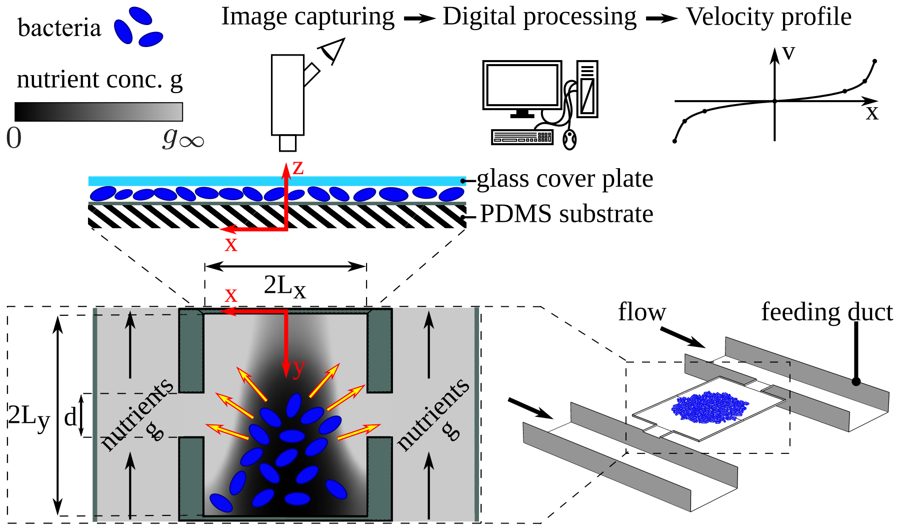

FIGURE 5.1. Schematic of microfluidic experiment in which *Corynebacterium glutamicum* are grown. The microfluidic chip consists of chambers of ≈1 µm height in between a glass cover plate and a polydimethylsiloxane (abbreviated PDMS) substrate which constrains the colony into a monolayer. Lateral chamber dimensions are in the range $60 - 120\mu m^2$, which allows for the observation of colonies up to several thousand individuals. Constant flow in the large feeding ducts provides nutrients, g_∞ denotes the feeding concentration. Inside the chamber the bacteria (blue) take up the nutrients, the local concentration g drops and nutrient gradients occur (grayscale corresponds to local concentration). The bacteria grow and a flow towards the channel outlets evolves (red-yellow arrows). Images of the bacteria are captured in fixed time intervals. Afterwards, the image stacks are digitally processed with particle image velocimetry (abbreviated PIV) to extract the flow velocity profiles. Appeared similarly in [75].

We study an example for biochemical regulation of growth similar to the systems introduced in section 2.1): the growth of colonies of bacteria of the stem *Corynebacterium glutamicum* dependent on the local nutrient availability. Our goal is a quantitative-predictive description of colony growth dynamics. In a first step, we use a microfluidic setup (see section 2.1.2) to observe the steady-state growth of a monolayered colony of bacteria dependent on the fed concentration. We choose a simple *growth channel* geometry in this first set of experiments to ease modeling, depicted in fig. 5.1 (with $d = 2L_y$) and fig. 5.2 (left image). Flow field

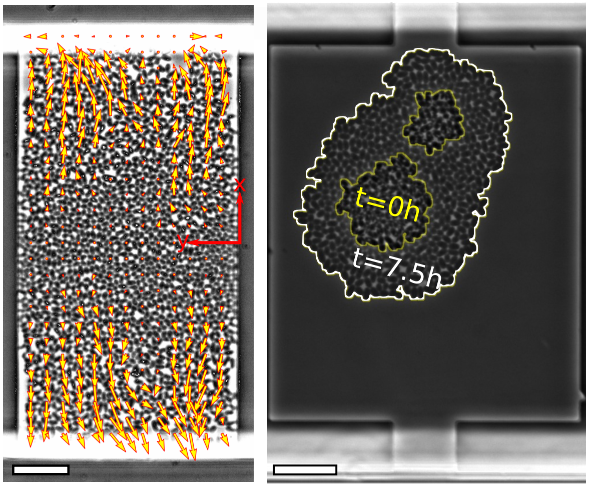

FIGURE 5.2. Left picture shows snapshot of the *growth channel* setup used to observe the steady state flow field of bacteria. Overlayed vectors depict the flow field of bacteria inside the channel, as measured by particle image velocimetry (PIV). On the right, an overlay of two snapshots at different timepoints of an experiment in a *growth chamber* is shown. The yellow and white lines depict the perimeter of the colony at different timepoints. Scale bar length corresponds to 10 µm in both pictures. Appeared similarly in [75].

measurements with particle image velocimetry (abbreviated PIV, see fig. 5.2) allow us to infer the local growth rate. We develop a minimal reaction-diffusion type model to describe nutrient transport, uptake by bacteria and the bacterial flow induced by biomass creation. A fit of our model to the measured flow profiles enables us to extract the length scale of nutrient depletion within a colony and the nutrient dependency of growth. In a second step, we extrapolate from this steady-state, quasi-one-dimensional growth channel geometry to the prediction of time-dependent growth of bacteria in a genuine two-dimensional *growth chamber*, see fig. 5.2($d < 2L_y$) and fig. 5.2 (right image). To do so, we feed the fitted parameters into the 2PG-framework, adapted to include the nutrient dynamics (see section 3.5), and compare shape and area of growing colonies over time. Hereby, we validate whether our minimal model describes bacterial growth dynamics in a more complicated setup correctly, in particular amidst its parameters having been extracted from a simple, easily reproducible setup.

We acknowledge Dr. Dietrich Kohlheyer, Dr. Alexander Grünberger and Christoph Westerwalbesloh for conducting the experiments and providing us with the data. Most of the content of this chapter has been published [75].

5.1. Bacterial Growth Model - Theory and Simulation

We construct a reaction-diffusion model for bacterial growth, similar to the models presented in sections 2.1.2-2.1.3 of the introduction. In particular, we derive a simple relationship between flow velocity and nutrient uptake which enables us to infer the nutrient uptake rate dependent on nutrient concentration. We also take a look at the pressure profile caused by the friction of bacteria with the top and bottom channel wall and the resulting channel deformation.

5.1.1. Nutrient Uptake and Biomass Conversion. An experimental study suggests that protocatechuic acid (abbreviated PCA) acts as a single limiting factor of growth for the model organism *C. glutamicum* in our experimental setup [102]. We describe the bacteria with a continuum density ϱ and the single limiting nutrient PCA with a concentration variable g. The amount of nutrients taken up depends on the concentration $g = \widehat{g}\bar{g}$ of nutrients available, where we introduced the dimensionless concentration $\widehat{g}$ and the unit conversion factor $\bar{g}$.

Furthermore, it is reasonable to assume that the nutrient uptake rate u per bacterium has an upper bound $u_\infty \bar{g}$. Hence, we write the total nutrient uptake rate per bacterium as $u_\infty \bar{g} u(\widehat{g})$, where $u(\widehat{g})$ is a dimensionless function varying between zero and unity. The nutrient concentration field $\widehat{g}$ thus obeys

$$\partial_t \widehat{g} = \nabla\left(D\nabla \widehat{g}\right) - \varrho u_\infty u(\widehat{g}) = \nabla D \cdot \nabla \widehat{g} + D\Delta \widehat{g} - \varrho u_\infty u(\widehat{g})\,, \tag{5.1.1}$$

where we assume the uptake to be linear in bacterial number density ϱ and only diffusive nutrient transport with diffusion coefficient D. In experiments, the flow of the nutrient solution is not measured, however, a simulation study of a chip design similar to ours in ref. [41] concludes that advective transport dominates in the main channel ($Pe = 10$), whereas nutrient transport inside the growth chambers is mainly diffusive ($Pe = 0.1$). Bacteria convert the absorbed nutrients into biomass with efficiency ϵ, thus, cells grow with a rate of $k_g = \epsilon u_\infty u(\widehat{g})$. Hence, the bacterial density evolves according to

$$\partial_t \varrho = -\nabla \cdot (\varrho \boldsymbol{v}) + \varrho \epsilon u_\infty u(\widehat{g})\ , \tag{5.1.2}$$

with the bacteria flow velocity $\boldsymbol{v}$. The efficiency parameter ϵ describes essentially the amount of nutrients a bacterium needs to consume in order to divide. With a growth rate directly proportional to nutrient uptake, we assume that only a negligible amount of nutrients is spent for cell maintenance (see section 2.1.3). Furthermore, we allow for different diffusion coefficients in- and outside the colony, denoted by D_{bulk} and D_{free}. This models the hindered diffusion of nutrient molecules around and through the cell membrane in a coarse-grained manner. For the growth channel experiments in section 5.2 (see fig. 5.1 with $d = 2L_y$) we assume a spatially constant diffusion constant as the whole channel is populated with bacteria in the steady state. Thus, the term $\nabla D \cdot \nabla g$ in eq. (5.1.1) vanishes in this case. For constant bacterial density and equilibration of the concentration profile via diffusion being much faster than growth activity, eqns. (5.1.1)-(5.1.2) simplify to

$$\begin{aligned} \Delta \widehat{g} &= u(\widehat{g})\,/l_g^2, \\ \nabla \cdot \boldsymbol{v} &= \epsilon u_\infty u(\widehat{g})\,, \end{aligned} \tag{5.1.3}$$

with two parameters, (1) the nutrient decay length $l_g = \sqrt{D/(\varrho u_\infty)}$ which describes the ratio of nutrient-uptake rate and diffusive nutrient flux and (2) the maximum growth rate $k_{max} = \epsilon u_\infty$. The shape of the uptake function $u(\widehat{g})$ determines at which nutrient-concentration-scale limitation of growth occurs. Under the assumption of linear uptake for small concentrations, i.e. $u \approx u'(0)\,\widehat{g}$ for $\widehat{g} \ll 1$, the nutrient concentration decays exponentially on the lengthscale $l_g/\sqrt{u'(0)}$ (see also eq. 2.1.8 in section 2.1.2). The exact uptake rate as a function of nutrient availability $u(\widehat{g})$ is generally not known; however, in one dimension, model eqns. (5.1.3) can be rearranged to read off u from a given velocity profile $v(x)$. For a quasi-one-dimensional colony of length $2L_x$, with prescribed nutrient concentration $\widehat{g}(\pm L_x) = \widehat{g}_\infty$ at the boundaries, elimination of $u(\widehat{g})$ from eqns. (5.1.3) yields

$$\widehat{g}(x) = \frac{V(x) - V_0}{k_{max} l_g^2}, \tag{5.1.4}$$

where $V(x) = \int_{x_0}^{x} v\,(x')\,dx'$ denotes the integral of v starting from the flow symmetry axis $x = x_0$ (at which $g'(x_0) = v\,(x_0) = 0$) and $V_0 = k_{max} l_g^2 \widehat{g}\,(x_0)$. Insertion of eq. (5.1.4) into eq. (5.1.3) eliminates the nutrient concentration, so that

$$\frac{dv}{dx} = k_{max} u \left(\frac{V(x) - V_0}{k_{max} l_g^2} \right) . \tag{5.1.5}$$

Thus, the shape of the uptake function $u(\widehat{g})$ as well as the scalar parameters l_g and k_{max} can be extracted from a fit of our model to experimental measurements of the velocity profile $v(x)$ for a quasi-one-dimensional growth channel. This implies that for the colony shape dynamics simulations in section 5.3, the ratio of the diffusion constants D_{bulk}/D_{free} is the sole remaining free parameter. Analytical calculations in refs. [103, 104] provide the expression $D_{bulk} = D_{free} \frac{1-\nu}{1+\nu}$ for a two-dimensional array of impermeable cylinders with packing fraction ν. The packing fraction of bacteria of $\nu \approx 0.5$ results in the estimate $D_{bulk}/D_{free} = 1/3$.

5.1.2. Pressure and Growth Channel Deformation. In the growth channel experiments the bacteria grow in a monolayer such that all bacteria are subject to friction with top and bottom chamber wall. We investigate the pressure in the bacterial colony which builds up due to this friction with the chamber. Furthermore, we calculate the resulting deformation of the top and bottom chamber wall due to the pressure profile. Thus, for known chamber deformation, the friction strength can be estimated. We assume that the friction force density of the bacteria with the channel top and bottom wall is proportional to the velocity: $\boldsymbol{f} = -c_b \boldsymbol{v}$, with a friction constant c_b. For simplicity, we assume that shear friction is negligible compared to this background friction. On long timescales, bacteria exhibit plug-flow which supports this assumption (see section 5.2). Furthermore, we assume again incompressible cells for which the continuity equation reads $\nabla \cdot \boldsymbol{v} = k_g$. Insertion into continuum momentum balance [105] yields

$$\varrho \partial_t \boldsymbol{v} + \varrho \left(\boldsymbol{v} \cdot \nabla \right) \boldsymbol{v} + \varrho \boldsymbol{v} k_g = \nabla \overline{\boldsymbol{\sigma}} - c_b \boldsymbol{v}, \tag{5.1.6}$$

from which we deduct the equation to determine the steady-state pressure profile p

$$\partial_x p = -v \left(2 \varrho k_g + c_b \right) , \tag{5.1.7}$$

in our one-dimensional growth channel model. Note that in our simulation, cell divisions generate momentum as the velocity of the mother cell is passed to the two daughter cells. This is the origin of the third term on the left-hand side of eq. (5.1.6), which leads together with the second term to the term $-2v\varrho k_g$ on the right-hand side of eq. (5.1.7). However, this term is usually negligible in our experiments and simulations, see also the discussion about eq. 3.1.10. For the one dimensional channel of length $2L_x$, it is $v\left(0\right) = 0$ due to symmetry, such that from $v' = k_g = k_{max} u(g)$ follows

$$v\left(x\right) = k_{max} \int\limits_0^x u(g\left(z\right))\, dz \, , \tag{5.1.8}$$

and hence

$$p(x) = - \int\limits_{-L_x}^{x} dx' \int\limits_0^{x'} dx \left\{ 2 \varrho k_{max}^2 u\big(g\left(x'\right)\big)\, u(g\left(x\right)) + c_b k_{max} u(g\left(x\right)) \right\} . \tag{5.1.9}$$

To get an upper bound for the pressure, we set u to its maximal value $u \equiv 1$. Calculation of the integrals results in the velocity profile

$$v\left(x\right) = k_{max} x, \tag{5.1.10}$$

and pressure profile

$$p(x) = \left(\varrho k_{max}^2 + \frac{1}{2} c_b k_{max}\right)\left(L_x^2 - x^2\right). \tag{5.1.11}$$

Top and bottom chamber wall are subject to a shear force per area unit of $p_x = c_b d_z v$ in x-direction, d_z denotes the chamber height. The pressure in eq. (5.1.11) acts as a normal pressure p_z. The maximum exerted magnitudes appear in the channel center at $x = 0$ for p_z and at the channel ends at $x = \pm L_x$ for p_x

$$p_x^{max} = c_b d_z k_{max} L_x, \qquad p_z^{max} = \left(\varrho k_{max}^2 + \frac{1}{2} c_b k_{max}\right) L_x^2. \tag{5.1.12}$$

To estimate the chamber wall deformation, we employ the Cerruti-Boussinesq-Green-tensor $\overline{\boldsymbol{G}}_{cb}$ (see appendix D) which determines the deformation vector $\boldsymbol{u}$ of an infinite, elastic half-space subject to a surface pressure $\boldsymbol{P}$ via

$$\boldsymbol{u}(x, y, z) = \int_{\mathbb{R}^2} \overline{\boldsymbol{G}}_{cb}\left(x - x', y - y', z\right) \boldsymbol{P}\left(x', y'\right) dx' dy'. \tag{5.1.13}$$

In particular, as the magnitudes of p_x and p_z are in good approximation proportional to the friction coefficient c_b, above relation implies that the deformation vector $\boldsymbol{u}$ is proportional to c_b as well. As we show in section 5.2, the observed flow patterns in growth channel experiments resemble a plug-flow with almost no dependency of the flow velocity on the y-direction. Thus, we assume the pressures p_x and p_z do not change along the y-direction and set

$$\boldsymbol{P}(x, y) = \left(p_x(x), 0, p_z(x)\right)\left(\Theta(x + L_x) - \Theta(x - L_x)\right)\left(\Theta(y + L_y) - \Theta(y - L_y)\right) \tag{5.1.14}$$

as the surface pressure, $\Theta(x)$ denotes the Heaviside-function. The resulting chamber wall deformation $\boldsymbol{u}(x, y, z = 0)$ is depicted in fig. 5.3 for a chamber aspect ratio $L_x/L_y = 2$ as in our growth channel experiments. The Poisson ratio is set to the value $\sigma = 1/2$ of the PDMS-substrate [106]. As expected, the maximum lateral deflection u_z occurs in the channel center at $x = y = 0$. The shear pressure p_x causes a shear deformation in both x- and y-direction: as the channel surface is expanded in x-direction, it shrinks along the y-direction. Along the x-direction, the deformation components rapidly decrease outside the channel, i.e. for $|x| > L_x$. Along the y-direction, the deflections decay considerably slower, e.g. for $y = 2L_y$ they are approximately $u_z/u_z^{max} \approx 1/3$ and $u_y/u_y^{max} \approx 3/4$. As the growth channels are arranged along the y-direction on the microfluidic chip, this may cause notable superposition of the deflections of neighboring channels.

5.1.3. Choice of Simulation Units and Parameters. Simulations are performed with the 2PG-model, adapted to incorporate the reaction-diffusion dynamics of the nutrient (see section 3.5). As our simulations are inherently unitless, we have to define units for length, time and concentration. The concentration unit $\bar{g}$ is fixed by a extrapolation of model fits to the growth channel experiments towards the channel inlets, as explained in sections 5.2.3 and 5.2.4.

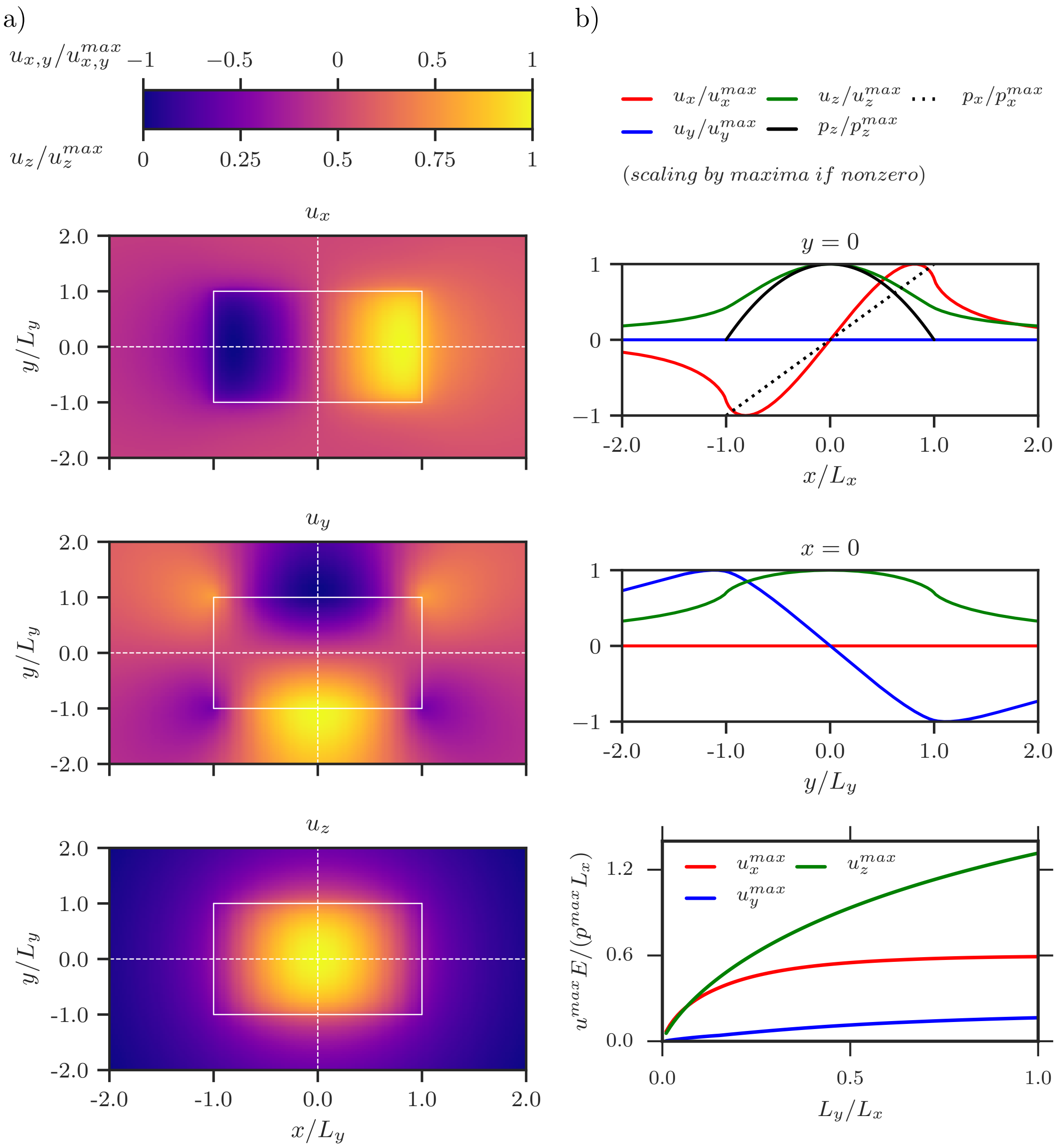

FIGURE 5.3. **a)** Components of the deformation vector $\boldsymbol{u}$ (u_x, u_y, u_z from top to bottom) at $z = 0$ for a surface pressure $\boldsymbol{P}$ as in eq. (5.1.14), channel aspect ratio $L_x/L_y = 2$ and Poisson ratio $\sigma = 1/2$. Continuous, white lines depict position of growth channel. **b)** Deformation vector components u_x, u_y, u_z along x-axis for $y = 0$ (top) and along y-axis for $x = 0$ (center). Corresponding pressure profiles $p_x(x)$ and $p_z(x)$ are depicted in top plot. Bottom plot shows maximum deflections as a function of channel aspect ratio L_y/L_x.

The diffusion constant D_{pca} of the limiting factor PCA is on the order of 100 µm^{2}s^{-1} [107]. As the bacteria grow in microfluidic domains with dimensions in the order of $L \approx$ 50µm, the concentration profile equilibrates in a timespan $\tau_{diff} = L^2/D_{pca}$ on the order of

TABLE 5.1. Standard simulation parameters for bacterial growth simulations. Forces are given relative to the background friction constant γ_b.

Parameter	Value[sim. unit]	Value[phys. unit]	Description
$\bar{t}$	1	1 h	time unit
$\bar{l}$	1	1.1 µm	length unit
$\bar{g}$	1	follows from fit, see section 5.2.3	concentration unit
dt_{dpd}	5×10^{-5}	5×10^{-5}h	DPD-integration timestep
B	follows eq. (3.5.6)		Growth force constants
r_0	1	1.1 µm	
r_{pp}	1	1.1 µm	Cutoff radius of all pair-potentials
d_c	1	1.1 µm	Size threshold for cell division
r_c	10^{-5}	1.1×10^{-5}µm	Distance at which new particles are placed after division
k_a	0	0 h^{-1}	Apoptosis rate
$\gamma_b; \gamma_t; \gamma_c$	$1; 1; 10^4$	1h^{-1}; 1h^{-1}; 10^4h^{-1}	Background/Intercell/Intracell friction constant
f_0/γ_b	460	460 µm h^{-1}	Repulsive force constant
f_1/γ_b	0	0 µm h^{-1}	Attractive force constant
dt_{fd}	10^{-5}	10^{-5}h^{-1}	finite-difference timestep
h	$0.\overline{90}$	1µm	finite-difference grid constant
D_{bulk}	2047.72(1373.31)	≈ 2478(1888)µm^2/h	Nutrient diffusion constant inside colony for Monod (Teissier)-uptake
$D_b; D_t; D_c$	10^{-3}	1.21×10^{-3}µm^2/h	Background/Intercell/Intracell noise diffusion constant of bacteria

seconds. Since bacteria move with a few µmh^{-1} and divide on a timescale of $\tau_{div} = 1/k_{max} = 3 - 4$h, the timescale of bacterial dynamics τ_{bact} is on the order of a few hours. Thus, the concentration profile equilibrates almost instantly on the timescale of bacterial dynamics. Hence, in simulations, it is not necessary to set exactly $D_{free} = D_{pca}$, any value of D_{free} large enough such that $\tau_{diff} \ll \tau_{bact}$ will result in the same bacterial dynamics (as long as u_∞ is scaled accordingly). For numerical efficiency we chose diffusion constants $D_{bulk} = 2478$ µm^2/h ($D_{bulk} = 1888$ µm^2/h for Teissier-uptake), large enough such that $\tau_{diff} \ll \tau_{bact}$.

The size threshold d_c at which a division event is sampled as well as the cutoff radius r_{pp} of the repulsive potential are set to one length unit. Cell size is therefore around one in simulations. We choose the length unit in our simulations to 1.1 µm. This choice ensures that the average number density of simulation cells roughly agrees with the density of bacteria in our growth channel experiments, manually estimated to be around $\varrho \approx 0.66$ µm^{-2}. We choose a rather small noise intensity compared to the growth force as defined by eq. 3.5.6, such that division events take place mainly deterministic. We achieve this by setting the time unit to 1 h and the effective diffusion constants $D_{b,t,c} = k_b T/\gamma_{b,t,c}$ of all particle-particle interactions to $1.21 \cdot 10^{-3}$µm^2 h^{-1}. Simulation parameters for bacterial growth simulations are summarized in table 5.1.

5.2. Growth Channel Experiments with *Corynebacterium glutamicum*

We test our growth model by quantitative comparison with microfluidic experiments with *C. glutamicum* wild type (ATCC 13032$^{\mathrm{TM}}$[108]). To limit the system to a single nutrient component, we feed modified CGXII medium [2] without glucose as growth medium. Here, protocatechuic acid (abbreviated PCA) serves as the sole carbon source and growth limiting factor [102]. Modified CGXII medium is infused at approx. $200\,\mathrm{nl\,min^{-1}}$ after cell inoculation. Steady state growth channel experiments are performed in the following manner. First, cells are cultivated at ten times the standard PCA concentration of $195\,\mu\mathrm{M}$ until chambers are filled, afterwards medium is switched to the desired concentration of PCA for steady state experiments. Microfluidic precultivation in ten times standard PCA concentration is applied to "equilibrate" cellular metabolism to the carbon source and to reduce the experimental time span for filling the microfluidic cultivation chambers. Growth channel dimensions are $2L_x = 75\,\mu\mathrm{m}, 2L_y = 40\,\mu\mathrm{m}$, see fig. 5.1. We perform growth channel experiments with four different concentrations in the feeding duct (see fig. 5.1 a)) of $g_\infty = 48.75\,\mu\mathrm{M}, 97.5\,\mu\mathrm{M}$, $390\,\mu\mathrm{M}$ and $585\,\mu\mathrm{M}$ PCA in aqueous solution. The microfluidic chip is mounted onto a motorized inverted microscope (Nikon Eclipse Ti, Nikon microscopy, Germany) equipped with an incubator to keep the temperature at 30 °C. Images of the growing microcolonies are recorded every $\Delta t = 5 - 10$min over approximately two days of microfluidic cultivation to follow the growth on different feeding levels.

Movies of growth channel experiments can be found in the supplement of ref. [75], see [109]. Starting from a few bacteria introduced into the growth channel, bacteria grow, divide and populate all available space in the growth channel. Bacteria are pushed outward at the inlets and carried away by the laminar flow in the main feeding duct. Interestingly, on short timescales, the movement of bacteria happens in an "avalanche"-like fashion: multiple layers of bacteria move abruptly in the same direction, whereas the other bacteria stand still. This indicates that a pressure has to built up before the bacteria start to move. On long timescales, a steady state with a continuous flow of bacteria evolves, with zero velocity at the center of the channel and maximal velocity at the inlets. Nutrient limitation is clearly visible for the lowest feeding concentration of $0.0975\,\mathrm{mM}$ where we observe an almost complete arrest of growth and division on a fraction of $\approx 2/3$ of the growth channel length $2L_x$. In these "dead zones" almost no activity is visible on a time scale of a day. Only directly at the channel inlets bacteria grow strong enough to push their neighbors outward the channel and to establish hereby a steady flow. The decline of growth activity down to zero growth in the middle of the channel clearly demonstrates the presence of nutrient gradients which develop on a length scale of a few cell sizes. On the contrary, for the highest feeding concentration applied $0.585\,\mathrm{mM}$, no dead zones are visible and bacterial mass production takes place along the whole channel length, paralleled by a strong flow towards the channel inlets. For the medium feeding concentration of $0.39\,\mathrm{mM}$ we observe a mixed picture: the flow is clearly much stronger than for the lowest feeding concentration, but a small fraction close to the channel mid exhibits low to no activity.

5.2.1. Selection for further Evaluation. An essential part of the evaluation of experimental results consists of careful analysis whether the conditions present during the experiment are "ideal" enough to be compared with a theory which does not take into account all the things which go wrong. We list a set of undesired events and outcomes which happen in the growth channel experiments and lead to clearly erroneous experiment data.

(1) *Stacking.* Cloudy and turbid regions appear on some frames which make it hard to track the contours of individual bacteria even for the human eye, see fig. 5.4. Sometimes, these turbid regions disappear abruptly from one frame to another. This may indicate that the bacteria are stacked to some degree on each other by lifting up the cover lid; regions become turbid because the contours of two or more bacteria are overlayed. Whenever the cover lid pushes the bacteria back into a monolayer, the cloudiness vanishes which could explain its abrupt occurrence and disappearance. Furthermore, the cloudy regions occur mostly in the center of the growth channel for higher feeding concentrations, i.e. where the pressure is highest (see section 5.1.2) and therefore a deformation of the cover lid occurs most likely. However, how many layers of bacteria are exactly stacked is difficult to measure as images are captured from the top.

(2) *Obstacles.* Obstacles occur inside the growth channel which impede the flow of bacteria and lead to an overall decrease of the flow velocity. Obstacles are often individual or small groups of bacteria which seem to be jammed. This may happen to due variations in chamber height such that the pressure exerted by the cover lid is non-homogeneous and bacteria cannot squeeze themselves through. Additionally, some bacteria exhibit filamenting, i.e. stop to divide and instead grow to large sizes up to $10 - 15\mu\text{m}$. These filamenting bacteria often move much slower than the non-filamenting surrounding bacteria.

(3) *Blockage.* Growth channels are blocked either from one or both inlets, such that bacteria cannot flow outward the chamber. This may occur due to fabrication errors during production of the microfluidic chip device.

(4) *Velocity change over time.* The flow velocity of bacteria changes over time which could be attributed to memory-effects in the biochemistry related to growth. Colonies are cultured in a PCA medium with a very high concentration of 1.95 mM (tenfold standard concentration) and may need time to adapt to the much lower concentrations present in the growth channels. This possibility is supported by the occurrence of velocity changes solely for very low feeding concentrations where the change in concentration compared to the culture medium is largest. Furthermore, the velocity is decreasing over time in these experiments, which may indicates that the bacteria first consume the reserves built up during cultivation before they adapt their growth to the much smaller concentrations present in the growth channel.

Table 5.2 shows a summary of evaluated experiments, their parameters, occurring problems during evaluation and the time interval used for PIV evaluation.

Even though events like 1-4 render the evaluation of experiments difficult, we may be able to learn something from their occurrence. In particular, the stacking of bacteria allows to estimate the order of magnitude of the friction strength c_b, if we assume that bacteria stack on each other due to the deformation of top and bottom channel walls. The Young modulus of PDMS is on the order of $E_{pdms} = 10^5 - 10^6\text{Pa}$ [106], much smaller than the modulus of glass which is on the order of $10^{10} - 10^{11}\text{Pa}$ [110]. Therefore, we assume that only the PDMS substrate is deformed. As the diameter of one bacterium is approximately $1\,\mu\text{m}$, a channel wall deformation on the order of $\approx 0.5\,\mu\text{m}$ should be sufficient to allow at least for partial stacking. With the results of section 5.1.2, we estimate the pressure to result in a maximum

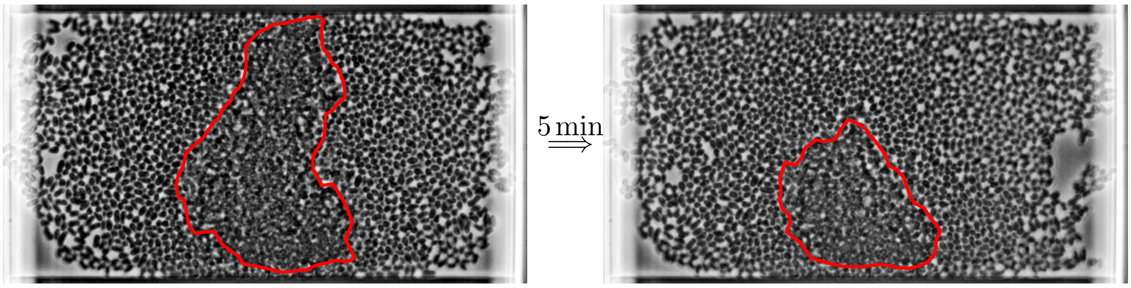

FIGURE 5.4. Example for a stacking event. The outlined area appears turbid and cloudy, individual bacteria are hardly distinguishable. On the next frame, five minutes later, a large part of the turbid area becomes abruptly clear again. This rapid de-stacking may indicate that the bacteria only partially overlap during stacking.

TABLE 5.2. Parameters of growth channel experiments and time interval used for PIV evaluation.

Experiment	Series	g_{pca}[µM]	Δt_{eval}	Problem(s)
nd004	1	97.5	100-246 = $24\frac{1}{3}$h	-
time res. 10 min/frame	2	—"—	150-246 = 16h	-
image res. 15.3846 pixel/µm	3	—"—	150-246 = 16h	-
247 frames = 41 h	4	390	177-246 = $11\frac{1}{2}$h	-
	5	—"—	200-246 = $7\frac{2}{3}$h	-
	6	—"—	200-246 = $7\frac{2}{3}$h	-
	7	585	150-246 = 16h	-
	8	—"—	150-210 = 10h	1 (frames > 210)
	9	—"—	-	1
nd112	1	48.75	-	3
time res. 5 min/frame	2	—"—	350-516 = $13\frac{5}{6}$h	4
image res. 10.9778 pixel/µm	3	—"—	350-516 = $13\frac{5}{6}$h	4
517 frames = 43 h	4	390	-	1
	5	—"—	-	1
	6	—"—	-	1
	7	585	1-200= $16\frac{2}{3}$h	1 (frames > 200)
	8	—"—	200-350= $12\frac{1}{2}$h	1 (frames < 200, > 350)
	9	—"—	-	1,2

deformation of $u_z^{max} = 0.5\,\mu\text{m}$ to

$$p_z^{max} \approx \frac{u_z^{max} E_{pdms}}{0.93 L_x} \approx 7.2 \cdot 10^2 - 7.2 \cdot 10^3\text{Pa} = 7.2 - 72\text{mbar}, \tag{5.2.1}$$

for $2L_x = 75\,\mu\text{m}$, channel aspect ratio $L_y/L_x \approx 2$ (see fig. 5.3b)) and $E_{pdms} = 10^5 - 10^6$Pa. Thus, eq. (5.1.12) for p_z^{max} results with a growth rate of $k_{max} = 0.2\,\text{h}^{-1}$ in the lower bound

$$c_b \approx 2\frac{p_z^{max}}{k_{max} L_x^2} \approx 16.5\,\text{kg}\,\mu\text{m}^{-3}\,\text{h}^{-1} = 4.6 \cdot 10^{-12}\text{kg}\,\text{m}^{-3}\,\text{s}^{-1}. \tag{5.2.2}$$

5.2.2. Measurement of Flow Fields. To quantify the observed growth, we analyze the flow patterns $\boldsymbol{v}$ with the PIV technique [111]. We explain the image processing steps which consist of preprocessing, application of the PIV-technique as well as detection and replacement of spurious flow vectors. Preprocessing steps (see fig. 5.5) are as follows: Images are cut and aligned such that only the growth channel is visible, with its x-axis parallel to the image borders. Afterwards, image stacks are stabilized, using a ImageJ-plugin [112] provided by Stefan Helfrich [113], to remove camera shaking. Then, contrast is improved via rescaling of the intensity histogram to the range between the 2nd and 98nd percentile.

We continue with a brief introduction into the PIV technique which is used to estimate the velocity field of the preprocessed image stack [111]. The technique is based on a straightforward idea: Subsequent image pairs are divided into small interrogation windows I and the image content of every window I in frame one is compared with surrounding squares within a search window S in frame two to estimate to which place the square moves. The two most important parameters of PIV are the interrogation window size s_{iw} and the search window size $s_{sw} > s_{iw}$. A match is determined by calculation of the spatial correlation function

$$C_{is}(x,y) = \sum_{i,j=0}^{s_{iw}} I(i,j)\, S(i+x, j+y) \ , \tag{5.2.3}$$

between the image intensities in interrogation square I and the search square S. The coordinates x and y denote the shift of I, relative to its original position in frame one, in the larger search square S, see fig. 5.6. Note that the coordinate system of I and S is chosen such that the centers of I and S coincide for $(x,y) = (0,0)$. A maximum of the correlation map 5.2.3 defines then the best match and the corresponding shift (x^*, y^*) the displacement

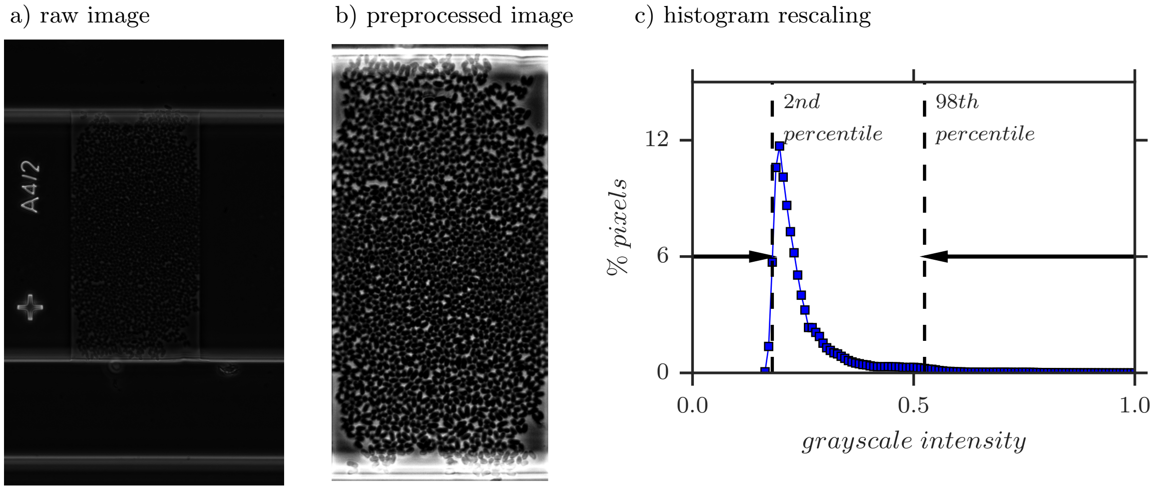

a) raw image

b) preprocessed image

c) histogram rescaling

FIGURE 5.5. **a)-b)** Before the PIV technique is applied to the image stacks of the experiments, image quality is improved by cutting, alignment and contrast enhancement. **c)** To improve contrast, intensity histograms are rescaled to the range between the 2nd and 98nd percentile (vertical lines) of the histogram for every image.

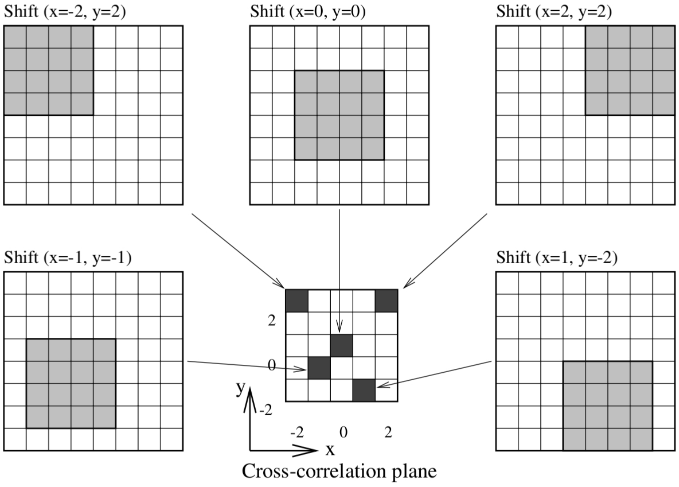

FIGURE 5.6. The interrogation window s_{iw} (gray) is moved in the larger search window s_{sw}(white) to generate a cross-correlation map of size $s_{sw} \times s_{sw}$. From [111].

of the window I between frames one and two. To obtain subpixel resolution, the maximum of the correlation map is often fitted with a rapidly decreasing function, e.g. a Gaussian. From fig. 5.6 we see that only for displacements smaller in magnitude than $d_{fo} = (s_{sw} - s_{iw})/2$ the interrogation window I has full overlap with the search window S. Thus, it is desirable to choose the window sizes such that the maximal displacement is smaller or equal to d_{fo}.

To refine the PIV-resolution, multiple passes with subsequently reduced window sizes are performed. The displacements measured in one pass are added as an offset to the interrogation window position before performing the next pass with a refined grid. This procedure has the main advantage that it increases the dynamic spatial range, i.e. the ratio of largest to smallest observable length scale. However, multipass schemes have the disadvantage that they are prone to error propagation: If in one pass the real displacement is not captured correctly, it is very likely that the successive passes cannot correct this mismatch due to the wrong offset added to their interrogation windows. Error detection and correction schemes in between passes have to be carefully chosen and tested in order to reduce this error while keeping the characteristics of the flow field.

For the task to measure the flow field of bacteria in our growth channels, we use the ImageJ PIV plugin published by Dr. Qingzong Tseng [114] which implements a multipass PIV algorithm as described above. We decide to use three passes and explain in the following how we estimate the window sizes. The choice of the window sizes is limited by several characteristics of our image data. The bacteria appear as almost featureless rods with round caps. The image information consists of contrast between areas occupied by bacteria, which occur almost black, and the brighter background. The bacteria grow from approximately 1 µm to 3 µm and their extend along the axis perpendicular to the growth axis is constant around 1 µm. Along the whole channel the bacteria are densely packed. At the contact area it is hard to tell where one bacterium ends and the other begins. The interrogation window size has to be large enough to include enough image information to correlate with the next frame. A minimal interrogation window size of around 3 µm ensures that a few bacteria and black-to-bright grayscale changes are always in the window. To avoid the aforementioned bias for displacements larger than d_{fo}, we set the search window size s_{sw} such that the maximal

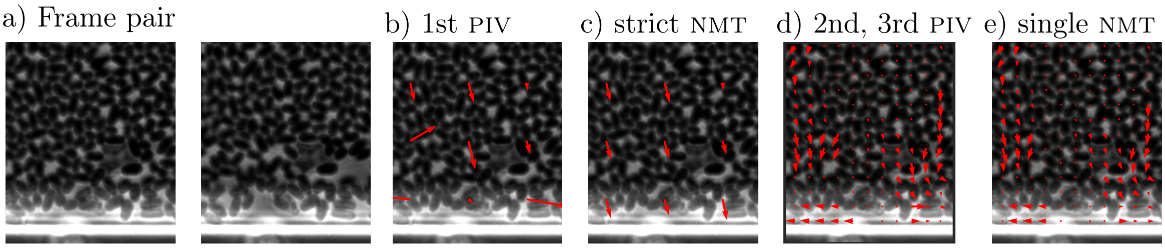

FIGURE 5.7. **a)** Example for the PIV-steps for two small cutouts of two consecutive frames. After the first, coarse PIV-pass **b)**, the NMT is applied until no spurious vector remains, **c)**. After the second and third PIV-pass with finer resolution **d)**, a single NMT-sweep yields the final flow field.

displacement d_{max} equals d_{fo}, from $d_{fo} = d_{max}$ we get

$$s_{sw} = s_{iw} + 2d_{max}. \tag{5.2.4}$$

The maximal displacement d_{max} is measured for every experiment individually by visual inspection of the fastest moving bacteria close to the channel ends. The upper limit for a suitable interrogation window size depends on the overall magnitude of the velocity gradients. Velocity changes on a length scale much smaller than the interrogation window size cannot be detected correctly. On short timescales, the movement of bacteria occurs in “avalanches” with a typical width of a few bacterial layers. This observation in mind, we chose the largest interrogation window size around 6 µm and the medium size around 4 µm. We calculate the velocity field on a square grid with lattice constants around $1-2$µm. In between the three passes we perform a *normalized median test* (abbreviated NMT) to detect spurious vectors and suppress error propagation. This test consists of the following steps to validate a velocity vector $\boldsymbol{v}$:

(1) Calculate the median vector $\boldsymbol{v}_{med}$ of the sequence of vectors consisting of $\boldsymbol{v}$ and its eight next neighbors. The median can be taken with respect to the magnitudes of the vectors or their x and y-components.

(2) Calculate the residua r_i defined as $|\boldsymbol{v}_i - \boldsymbol{v}_{med}|$ for the eight surrounding vectors $\boldsymbol{v}_i$, $i = 1, \ldots, 8$.

(3) Define r_{med} as the median of the eight residua. The vector $\boldsymbol{v}$ is considered valid if

$$\frac{|\boldsymbol{v}_{med} - \boldsymbol{v}|}{r_{med} + \epsilon_0} < \epsilon_{thres}$$

for two fixed parameters ϵ_0 and ϵ_{thres}.

The parameter ϵ_0 describes the typical noise amplitude the vectors are subject too, whereas ϵ_{thres} determines the sensitivity of the test. Commonly used values are $\epsilon_0 = 0.1 - 0.2$px and $\epsilon_{thres} = 2$ which we used as well. As detailed in ref. [111], the normalized median test provides a robust measure to find spurious vectors. We replace spurious vectors by the median vector taken over all non-spurious neighbors. This filter and replacement procedure can be repeated several times, resulting in a smoother velocity field with every repetition. Here, it is crucial no to smooth out actual features of the flow field, which may exhibit sharp gradients. For a multipass PIV scheme it is common praxis to use a strict validation and replacement scheme on the coarse first passes to suppress error propagation and less stricter ones on the finer passes. The smoothing of the coarse first pass is usually no problem since it is anyhow only a first guess for the subsequent passes.

Thus, for the first pass we use a strict validation scheme where we apply the normalized median test as many times until all vectors are considered as valid. The "avalanche"-like motion of bacteria implies that sharp velocity gradients are present. Therefore, in the second and third pass we perform only a single sweep of the normalized median test to remove single spurious vectors, but to keep these gradients. The steps of the PIV are summarized in fig. 5.7.

5.2.3. Quantitative Match between Analytic Model and Experiments. To compare the velocity profile with the one-dimensional theory from section 5.1, we define $v(x)$ as the average of v_x along the y-direction and over all steady-state timepoints. Resulting velocity profiles v for the different feeding levels are shown in fig. 5.8. For the lower feeding concentrations, intervals with zero velocity indicate zones where growth stopped. At the channel outlets, PIV underestimates the velocity due to (1) bacteria being washed out of the channel such that the correlation with the next frame often fails and (2) because velocity and frequency of division events increase, both of which raise the difficulty of a correct correlation match. Thus, the velocity decrease close to the channel outlets and the corresponding maxima are artifacts. We decide to limit our quantitative analysis to a central region of the channel, heuristically defined as the interval between the two inflection points closest to the two maxima at the channel outlets ($x_\pm$, see fig. 5.8(a)-(c), vertical dashed-dotted lines). We construct a suitable uptake function u by means of relation (5.1.5)

$$\frac{dv}{dx} = k_{max} u\left(\frac{V(x) - V_0}{k_{max} l_g^2}\right) \tag{5.2.5}$$

between velocity gradient v' and velocity cumulative integral V. Relation (5.1.5) predicts that a $v' - V$-plot of measured velocity profiles collapses onto the uptake function u if each curve is shifted along the V-axis by an offset $V_0 = k_{max} l_g^2 \widehat{g}(x_0)$ proportional to the concentration at the starting point x_0 of the integration (see fig. 5.9). An initial guess for the shifts $\left\{V_0^i\right\}$ corresponding to the different experiments is obtained easily by visual inspection, as continuity demands that data sets for $v' - V$ from different experiments have to overlap. Various common models for uptake kinetics [52, 115] agree on a set of conditions:

$$\text{– linear for small concentrations } u(\widehat{g}) \overset{\widehat{g}\to 0}{\propto} \widehat{g}, \tag{5.2.6}$$

$$\text{– saturating at high concentrations } u(\widehat{g}) \xrightarrow{\widehat{g}\to\infty} 1, \tag{5.2.7}$$

$$\text{– monotonically increasing } u' > 0 \text{ and} \tag{5.2.8}$$

$$\text{– concave everywhere, i.e. } u'' < 0. \tag{5.2.9}$$

which are also consistent with our data. We choose the unit conversion factor $\bar{g}$ such that the linear slope for small concentrations in condition (5.2.6) is equal to unity. Thus, the length scale l_g describes the exponential decay length of the nutrient concentration under limiting conditions, where $u(\widehat{g}) \approx \widehat{g}$. The conditions (5.2.6) and (5.2.7) imply a simple geometrical interpretation of the parameters k_{max} and l_g in the v'–V-plane. From eq. (5.1.5) and condition (5.2.6) it follows

$$\frac{dv}{dx} = \left(V - V_0^i\right)/l_g^2 \quad \text{for} \quad \widehat{g} \to 0, \tag{5.2.10}$$

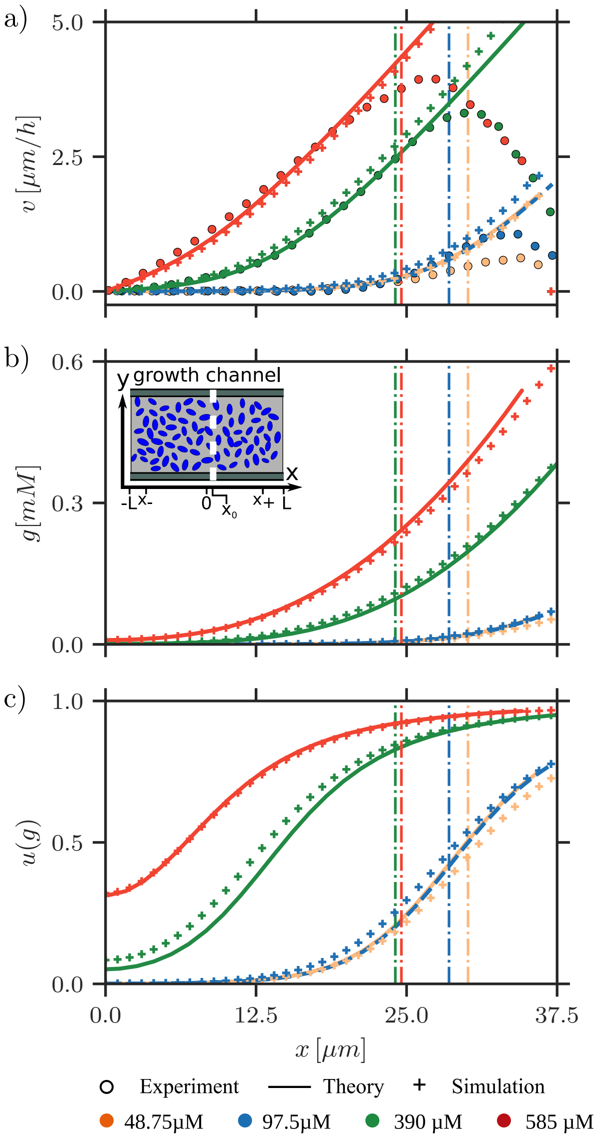

FIGURE 5.8. **a)** Velocity profiles estimated by PIV of growth channel experiments and subsequent averaging over y-direction and time (circles, see legend). One example for each feeding concentration g_∞ is shown, as indicated in legend (see appendix G for all data). Due to the symmetry of the velocity profile with respect to the channel center, the x-range from the channel center to the feeding outlets is displayed. The flow symmetry axis position x_0 is also fitted to account for small deviations from the channel center at $x = 0$. Dashed-dotted vertical lines indicate the cutoff x_+ used to constrain the data range of the fit to our analytic model eqns. (5.1.3). Continuous lines show the velocity profiles of the model fit using Monod-uptake which has been extrapolated towards the channel outlets. The line for the concentration $g_\infty = 48.75$ is dashed to increase visibility. Flow profiles of corresponding 2PG simulations are shown with "+"-symbols. Experimental and simulation data is averaged over time and y-direction. **b)-c)** g- and $u(g)$-profiles from model fit (continuous lines) and corresponding simulation results ("+"-symbols). Appeared similarly in [75].

eq. (5.1.5) and condition (5.2.7) yield

$$\frac{dv}{dx} = k_{max} \quad \text{for} \quad \widehat{g} \to \infty. \tag{5.2.11}$$

Hence, k_{max} and l_g fix the initial slope and the saturation value of the $v' - V$-curve. We use two common uptake models which comply with conditions (5.2.6)-(5.2.9), Monod-uptake $u(\widehat{g}) = \widehat{g}/(1+\widehat{g})$ [52] is explored here (see fig. 5.9), the very similar results for Teissier-uptake $u(\widehat{g}) = 1 - \exp(-\widehat{g})$ [115] can be found in appendix G. With a suitable uptake function $u(\widehat{g})$, our model, defined by eqns. (5.1.3), is complete and the theoretical predictions can be fitted to the experimental data. A direct fit of u in the $v' - V$ diagram, using eq. (5.1.5) to estimate the parameters k_{max} and l_g, provides an initial estimate. However, this approach is error-prone as it requires calculation of the derivative of noisy experimental data. Thus, we fit

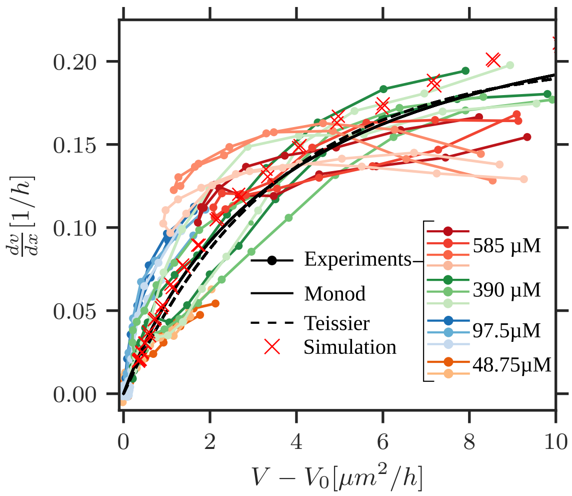

FIGURE 5.9. Velocity gradient $\frac{dv}{dx}$ versus velocity integral $V = \int_{x_0}^{x} v\,(x')\,dx'$. The integral of v starts from the flow symmetry axis at $x = x_0$. Colors correspond to different nutrient concentrations g_∞, see legend. Curves of the different experiments i are shifted by $V_0^i = k_{max} l_g^2 \widehat{g}^i(x_0)$ according to eq. (5.1.5), where the x_0^i and V_0^i are estimated by a least-square fit (details of fit described in section 5.2.4). Black lines show fits with Monod-uptake $u = \widehat{g}/(1+\widehat{g})$ (continuous) and Teissier-uptake $u = 1 - \exp(-\widehat{g})$ (dashed), the red “×”-symbols result of a corresponding particle-based simulation. Experimental and simulation data is averaged over time and the y-direction. Appeared similarly in [75].

the solution of eqns. (5.1.3) for the velocity profile $v\,(x)$ to the measured flow profiles with k_{max} and l_g as fit parameters. To account for small deviations of the velocity symmetry axis position from the channel center, we employ the concentration at the center and the center position as additional fit parameters. The technical details of the fit procedure are explained in section 5.2.4.

Note that in fig. 5.9 the experiments at $g_\infty = 390$ µM span almost the full relevant concentration range; thus, flow profiles $v\,(x)$ are fitted for this concentration and the model is then used to predict the velocity profiles at higher and lower concentrations. Model fits give good predictions of experimental data, even for extrapolations to very different concentrations (see fig. 5.8 for one example per concentration and appendix G for all data). The corresponding fitted Monod and Teissier uptake functions are depicted in fig. 5.9. For the positions x outside the interval $x_- \leq x \leq x_+$ used for the fit (see fig. 5.8, continuous model curves outside dashed-dotted lines), model predictions agree reasonably well up to the velocity maxima.

Our model also predicts the nutrient concentration profile $\widehat{g}(x)$ inside the channel (see fig. 5.8(b)-(c)); However, we emphasize that our fit procedure does not prescribe the feeding concentrations g_∞ as present in the experiments. As detailed in section 5.2.4, we estimate the unit conversion factor $\bar{g}$ by an extrapolation of the $\widehat{g}$-profile to the channel outlets and subsequent fit of the linear relation $\widehat{g}_\infty = g_\infty/\bar{g}$ between model concentration $\widehat{g}_\infty$ and actual feeding concentration g_∞. Due to the reduced bacterial density, our model is not strictly valid at the channel outlets. Thus, we expect that this approach only provides a coarse estimate of the concentration scale $\bar{g}$. Nevertheless, linear fits (see fig. 5.10) match well and estimate a conversion factor around $\bar{g} = 0.02$mM for both Monod and Teissier-uptake. In this manner, the verification of the linear relation $\widehat{g}_\infty = g_\infty/\bar{g}$ provides an additional consistency check.

In the remainder of this section, we discuss the fit results in the context of their prediction of nutrient limitations. We define the concentration scale $g_{1/2}$ as the nutrient concentration at which uptake and growth rates are half of their maximum values, thus for $\widehat{g}_{1/2}$ holds $u\big(\widehat{g}_{1/2}\big) = 1/2$. With the concentration scale $\bar{g}$, we estimate $g_{1/2}$ for Monod and Teissier uptake around

TABLE 5.3. Fit results for model parameters obtained from a least-squares minimization. Error ranges refer to the square-root of the diagonal entries of the covariance matrix, as reported by `least_squares()`, see section 5.2.4.

uptake	$k_{max}[\mathrm{h}^{-1}]$	$l_g[\mathrm{\mu m}]$	$g_{1/2}[\mathrm{\mu M}]$
Monod	0.26 ± 0.06	3.78 ± 0.17	19.9 ± 1.5
Teissier	0.20 ± 0.03	4.18 ± 0.14	13.6 ± 0.9

$g_{1/2} \approx 13 - 20\,\mathrm{\mu M}$, which is about five to ten percent of the PCA-concentration in standard CGXII medium. This estimate is much lower as the assumed value of $g_{1/2} = 100\,\mathrm{\mu M}$ for Monod kinetics in refs. [41, 102]. Our observed maximal growth rate of around $k_{max} \approx 0.2 - 0.26\,\mathrm{h}^{-1}$ agrees well with previous observations [102]. The nutrient decay length of $l_g \approx 3.8 - 4.2\,\mathrm{\mu m}$ falls in the range of $l_g \approx 2\,\mathrm{\mu m} - 5\,\mathrm{\mu m}$ which can be estimated from previous results, which are affected, however, by large uncertainties [102]. In particular, the conversion of uptake rates measured per gram cell dry weight (g_{cdw}) into uptake per single cell is prone to large errors as reported single-cell weights vary by an order of magnitude [41]. However, it is important to emphasize that the parameter estimates based on the mentioned previous studies are based on the assumption of spatial homogeneity. Our main result here is that nutrient gradients are important and have to be considered. Thus, it is no surprise that estimates differ, and we deem the approach of the present study to be more reliable (see table 5.3 for all fit results).

5.2.4. Fit Procedure. To extract values for the model parameters, maximum growth rate $k_{max} = \epsilon u_\infty$ and nutrient diffusion length scale $l_g = \sqrt{D/(\varrho u_\infty)}$, we fit the model eqns. (5.1.3) to the velocity profiles v^{exp} measured in experiments. For the uptake function, we test two different models: Monod-uptake $u(\widehat{g}) = \widehat{g}/(1+\widehat{g})$ [52] and Teissier-uptake $u(\widehat{g}) = 1 - \exp(-\widehat{g})$ [115]. In one dimension, eqns. (5.1.3) read

$$\widehat{g}'' = u(\widehat{g})\,/l_g^2, \tag{5.2.12}$$

$$v' = k_{max} u(\widehat{g})\,, \tag{5.2.13}$$

where the prime denotes spatial derivatives. Insertion of $u(\widehat{g})$ from eq. (5.2.12) into the equation for v (5.2.13) leads to

$$v' = k_{max} l_g^2 \widehat{g}''. \tag{5.2.14}$$

Due to the mirror symmetry around the channel center $x_0 = 0$ of our setup, the boundary conditions read $v(x_0) = \widehat{g}'(x_0) = 0$. Integrating once, we obtain

$$v(x) = k_{max} l_g^2 \widehat{g}'(x)\,. \tag{5.2.15}$$

We integrate eq. (5.2.12) with the `odeint()` method of the python package SciPy [87]. The corresponding velocity profile is then given according to eq. (5.2.15). We fit the model solution for the velocity profile to the velocity profiles v^{exp} measured in the experiments by means of a least-squares optimization. To avoid confusion, we enumerate quantities which belong to different experiments with a superscript i in the following, e.g. $v^{exp,i}$ denotes the velocity profile of experiment i. We define the cost function Π by the sum of the squared deviations at all points x_j^i within the fit range measured in experiments:

$$\Pi = \sum_{ij} \left[v^{exp,i}\left(x_j^i\right) - k_{max} l_g^2 \frac{d\widehat{g}^i}{dx}\left(x_j^i\right) \right]^2 . \tag{5.2.16}$$

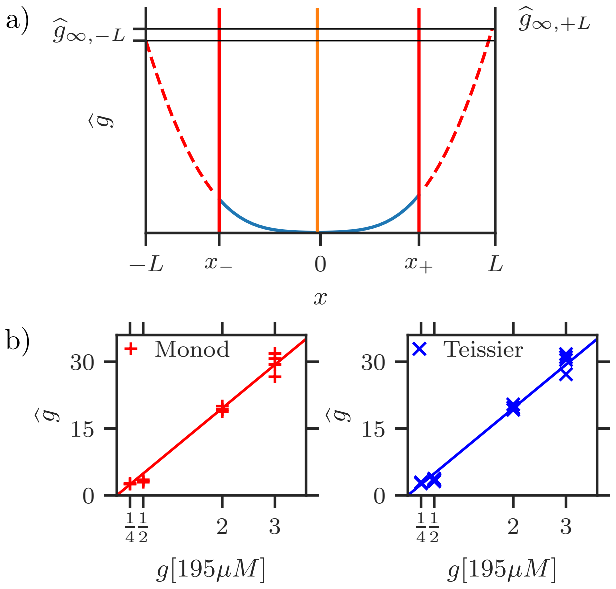

FIGURE 5.10. **a)** Due to the decreasing quality of the PIV data at the channel outlets, the model fit of the velocity profile is constrained to the data between the two points $x_\pm$ (red vertical lines). To get an estimate for $\widehat{g}_\infty$, we solve the ordinary differential equation eq. (5.2.12) for the concentration $\widehat{g}$ (blue curve) with the fitted model parameters outside the range $x_- \leq x \leq x_+$ used for the fit (dashed red lines). Due to the slight deviation of the fitted symmetry axis (green vertical) from the center $x = 0$, the estimates for $\widehat{g}_{\infty,\pm L}$ for $\widehat{g}_\infty$ differ slightly. **b)** Linear fit $\widehat{g} = g/\bar{g}$ of the concentration $\widehat{g}$ extrapolated at the channel outlets from our theory and the corresponding concentration g fed in experiment, for Monod and Teissier-uptake. Appeared similarly in [75]

To account for small deviations of the symmetry axis of the experimental flow profiles from the channel center, the positions x_0^i are also free fit parameters. Resulting symmetry axis positions x_0^i deviate only slightly from the channel center with a relative error $x_0/2L < 2.5\%$. We minimize the cost function Π with respect to the parameter l_g, the prefactor $\lambda = k_{max} l_g^2$ of g' in eq. (5.2.16), and the set of symmetry axis positions $\left\{x_0^i\right\}$ and central concentrations $\left\{\widehat{g}\left(x_0^i\right)\right\}$. Thus, for a set of N experiments the fit parameter space is of dimensionality $2 + 2N$. Minimization is performed with the `least_squares()` method of the SciPy python package[87].

As can be seen in fig. 5.9, the three independent experiments at the PCA-concentration of $g_\infty = 390\,\mu\mathrm{M}$ cover almost the complete relevant range of the uptake function. To probe the validity of our model, we estimate the model parameters l_g and k_{max} using these experiments and extrapolate to all other experiments. In the remaining experiments only the symmetry points $\left\{x_0^i\right\}$ and central concentrations $\left\{\widehat{g}\left(x_0^i\right)\right\}$ are obtained by minimization. With the optimal fit solutions for the concentrations $\widehat{g}$ at hand, we can estimate the remaining physical parameter: the concentration scale $g_{1/2}$ at which growth and uptake are at half their maximum values. To calculate nutrient concentrations in physical units, we need to estimate the concentration scale $\bar{g}$ which links between dimensionless theory concentrations $\widehat{g}$ and experimental concentrations g via $\widehat{g} = g/\bar{g}$. We estimate $\bar{g}$ by comparison of the feeding concentrations g_∞ present at the channel entries and their model prediction $\widehat{g}_\infty$. We calculate $\widehat{g}_\infty$ by extrapolation of the concentration profile g towards the channel entries at $x = \pm L$ (see fig. 5.10). We expect that this extrapolation only results in coarse estimates for the concentrations g_∞ since our model is not strictly valid at the channel entries due to reduced bacterial density. Furthermore, due to the slight deviation of the fitted symmetry axis position x_0^i from the channel center at $x = 0$, the extrapolation results in two different concentration values at the entries at $x = \pm L$. We define $\widehat{g}_\infty$ as their mean. The extrapolated concentration values $\widehat{g}_\infty$ show a good agreement with a linear fit $\widehat{g} = g/\bar{g}$ as depicted in fig. 5.10 b). Thus, the good match of experimental and theoretical concentrations provides an additional consistency check for our model.

5.2.5. Streaming Instabilities. As previously mentioned in section 5.2, the bacteria in the growth channel experiments move on short timescales in an "avalanche"-like fashion: Patches of bacteria move abruptly in the same direction, whereas bacteria around the patch stand still. Similar streaming instabilities are observed in monolayered colonies of *Escherichia Coli* [116]. There, a possible explanatory model is based on mobility changes dependent on cell-size: Larger cells experience larger drag with the substrate and move slower than smaller cells. Thus, larger cells form local, slow-moving obstacles in between smaller cells have to stream through. As cell growth and division result in a constant change of the spatial distribution of cell-sizes, number and position of streams fluctuate as well [116]. We quantify the streaming instabilities observed in the growth-channel experiments with *C. glutamicum* by analysis of spatial velocity correlations. Furthermore, we investigate the relation between cell-size and velocity to determine whether instabilities may be attributed to cell-size-dependent motility, as in ref. [116].

The "avalanche"-like motion exhibits a clear spatial correlation of velocity vectors, see fig. 5.11. Patches of correlated motion appear to be elongated in the direction where the channel is longer. Unfortunately, the time-resolution of the imaging is too low to follow the build-up of individual avalanches; In consecutive frames avalanches occur at different position in the channel. Thus, we limit the analysis to the spatial velocity correlations for a fixed time. To estimate the lengthscales of correlated motion, we calculate the two-point velocity correlation map

$$\begin{aligned} C_{vv}(x_1,y_1,x_2,y_2) &= \frac{\langle(\boldsymbol{v}(x_1,y_1)-\langle\boldsymbol{v}(x_1,y_1)\rangle)\cdot(\boldsymbol{v}(x_2,y_2)-\langle\boldsymbol{v}(x_2,y_2)\rangle)\rangle}{\sigma_v(x_1,y_1)\,\sigma_v(x_2,y_2)}, \\ \sigma_v(x,y) &= \sqrt{\left\langle(\boldsymbol{v}(x,y)-\langle\boldsymbol{v}(x,y)\rangle)^2\right\rangle}, \end{aligned} \tag{5.2.17}$$

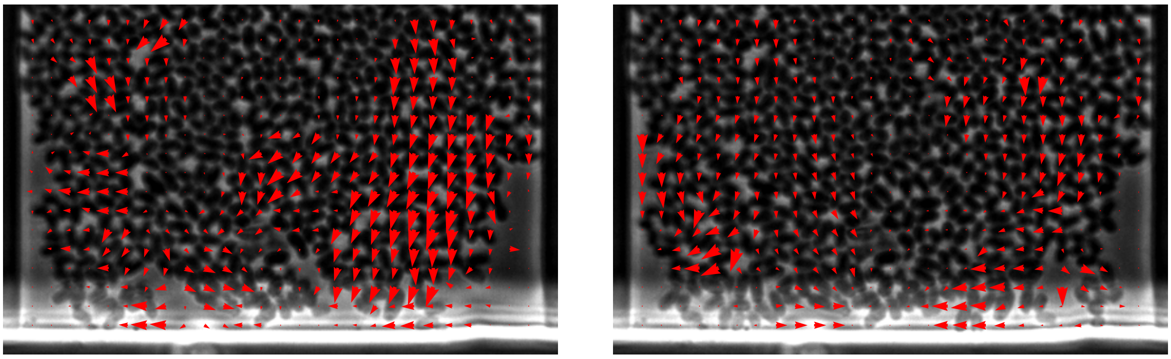

FIGURE 5.11. Examples for the "avalanche"-like motion of bacteria. Depicted is the lower third of two consecutive frames of a growth channel experiment with the PIV-velocity vectors overlayed. The overlay on the left frame corresponds to the movement in between the two frames.

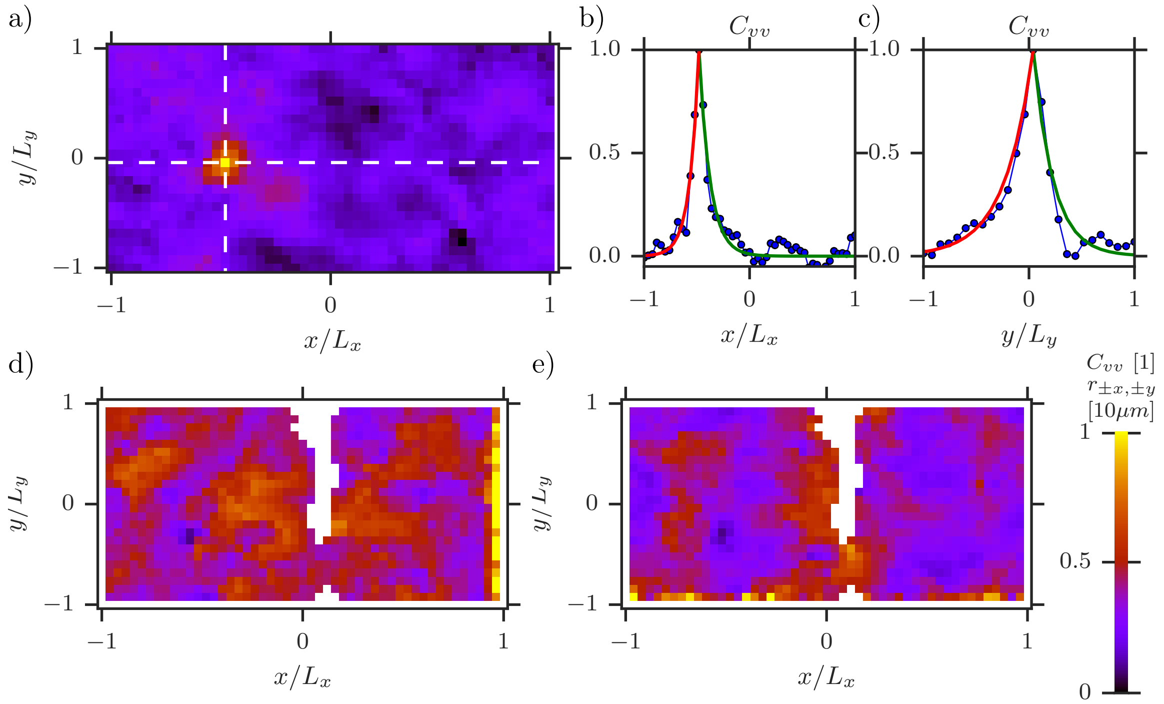

FIGURE 5.12. **a)** Example for the spatial velocity correlation map, eq. (5.2.17), with peak position $(x_p, y_p) = (L_x/4, L_y/2)$ and feeding concentration $c_{pca} = 585\,\mu\mathrm{M}$ (for color code, see legend bottom right). **b)-c)** Cuts through the peak along x- and y-direction of the correlation map of a). Red and green lines indicate exponential fits with function eq. (5.2.18). **d)** Example for decay length scale map r_{+x} dependent on peak position for the same experiment as in a). For color code, see bottom right legend. White areas have not been evaluated owing to mean velocity being smaller than $0.25\,\mu\mathrm{m\,h^{-1}}$. **e)** As d) for length scale map r_{+y}.

of the PIV velocity fields. Hereby, $\langle\cdot\rangle$ denotes a time average over the steady state frames. The correlation function C_{vv} in eq. (5.2.17) is normalized such that $C_{vv}(x, y, x, y) = 1$ and $|C_{vv}| \leq 1$. Example correlation maps are depicted in fig. 5.12. For the smaller feeding concentrations $c_{pca} = 48.75\,\mu\mathrm{M}, 97.5\,\mu\mathrm{M}$ the velocity is almost zero in a large region close to the channel center. These zero-velocity regions are obviously correlated but do not correspond to the motion patterns we want to investigate. Thus, in the following, we only evaluate the points x, y in the correlation map C_{vv} with a mean velocity larger than a threshold $|\langle \boldsymbol{v}(x, y)\rangle| \geq 0.25\,\mu\mathrm{m\,h^{-1}}$. For these points, the correlation map displays a clear peak at $(x_1, y_1) = (x_2, y_2)$ with a sharp decay around the maximum, see fig. 5.12. For large distances $|(x_1, y_1) - (x_2, y_2)|$, the correlation map fluctuates around zero. To extract the average lengthscale of correlated movement, we fit the peak with an exponentially decaying function C_{vv}^{fit}. We allow for different decay lengthscales $r_{\pm x}, r_{\pm y}$ in the four directions $\pm x, \pm y$ to account for the anisotropic shape of the avalanches:

$$C_{vv}^{fit}(x, y) = \exp\left(-\sqrt{\Theta(x)\left(\frac{x}{r_{+x}}\right)^2 + \Theta(-x)\left(\frac{x}{r_{-x}}\right)^2 + \Theta(y)\left(\frac{y}{r_{+y}}\right)^2 + \Theta(-y)\left(\frac{y}{r_{-y}}\right)^2}\right), \tag{5.2.18}$$

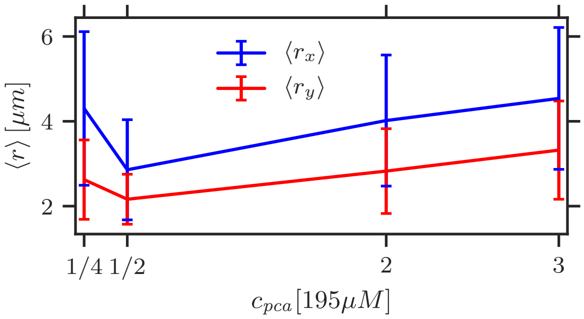

FIGURE 5.13. Decay lengthscales r_x, r_y averaged over space and all experiments of the same concentration ensemble. Error bars indicate STDEV of the average over space, time and different experiments.

where $\Theta(x)$ denotes the Heaviside function. A least-squares fit minimizing the error

$$\sum_{x,y} \left(C_{vv}(x_p, y_p, x, y) - C_{vv}^{fit}\left(x - x_p, y - y_p\right) \right)^2 \tag{5.2.19}$$

results in a map of the decay lengthscales $r_{\pm x,\pm y} = r_{\pm x,\pm y}(x_p, y_p)$ dependent on the peak position x_p, y_p, see fig. 5.12. The lengthscales $r_{\pm x}$ along the channel axis are larger than the scales $r_{\pm y}$ in the perpendicular direction, consistent with the observed elongated shape of the “avalanches”. All lengthscales appear to be more or less constant along the channel coordinates, being slightly larger in the channel center. For peak positions not too close to the channel walls, the lengthscales $r_{\pm x}$ in positive and negative x-direction agree, such that we merge them into one quantity $r_x = \left(r_{+x} + r_{-x}\right)/2$, analogous for $r_{\pm y}$. The mean values of the lengthscale maps $r_{x,y}\left(x_p, y_p\right)$ are depicted in fig. 5.13. They lie for all concentrations within a close range, $\langle r_x \rangle \approx 2 - 3$µm and $\langle r_y \rangle \approx 3 - 5$µm, such that the average “avalanche”-size does not appear to be dependent on the feeding concentration.

Next, we evaluate the relation between local cell size and velocity to investigate whether larger cells are indeed slower due to larger drag with the channel walls. To measure cell sizes, an ImageJ-plugin implemented by Stefan Helfrich is used to track the contours of the bacteria, see fig. 5.14 (the underlying segmentation algorithm is part of the open-source software *Vizardous* [113]). Unfortunately, owing to the dense packing of bacteria, the boundary between different cells is often not clearly visible. Often, only pixels in the center of the bacteria can be clearly appointed to an individual bacterium. These difficulties cause a lot of erroneous contours which we have to improve manually. As this manual inspection of contours is unfeasible to be performed for all image frames, we limited the contour analysis to five frames for each of the three feeding concentrations $c_{pca} = 98.75, 390, 585$µM. Furthermore, the estimated contours are systematically too small as a clear separation was only possible for the center pixels of bacteria, see fig. 5.14. By visual inspection we estimate that actual cell dimensions are roughly $10 - 20\%$ larger, causing a bias in the estimated cell areas of around $20 - 40\%$. However, as all cell sizes are subject to the same downward bias, we can nevertheless distinguish between small and large cells and estimate the correlation between cell size and velocity.

Figure 5.14 c) depicts profiles of cell number density ϱ, cell area a and two-dimensional packing fraction $\nu = a\varrho$ along the channel axis direction, averaged over all frames and along the perpendicular direction. In the channel center, the cell density falls in the range between $\varrho = 0.6 - 0.7$µm^{-2}, in agreement with the previously assumed constant value of $\varrho = 0.66$µm^{-2} in section 5.2.3. Apart from the lowest feeding concentration $c_{pca} = 97.5$ µM, cell density decreases slightly towards the channel entries. In contrast, the cell area a increases slightly

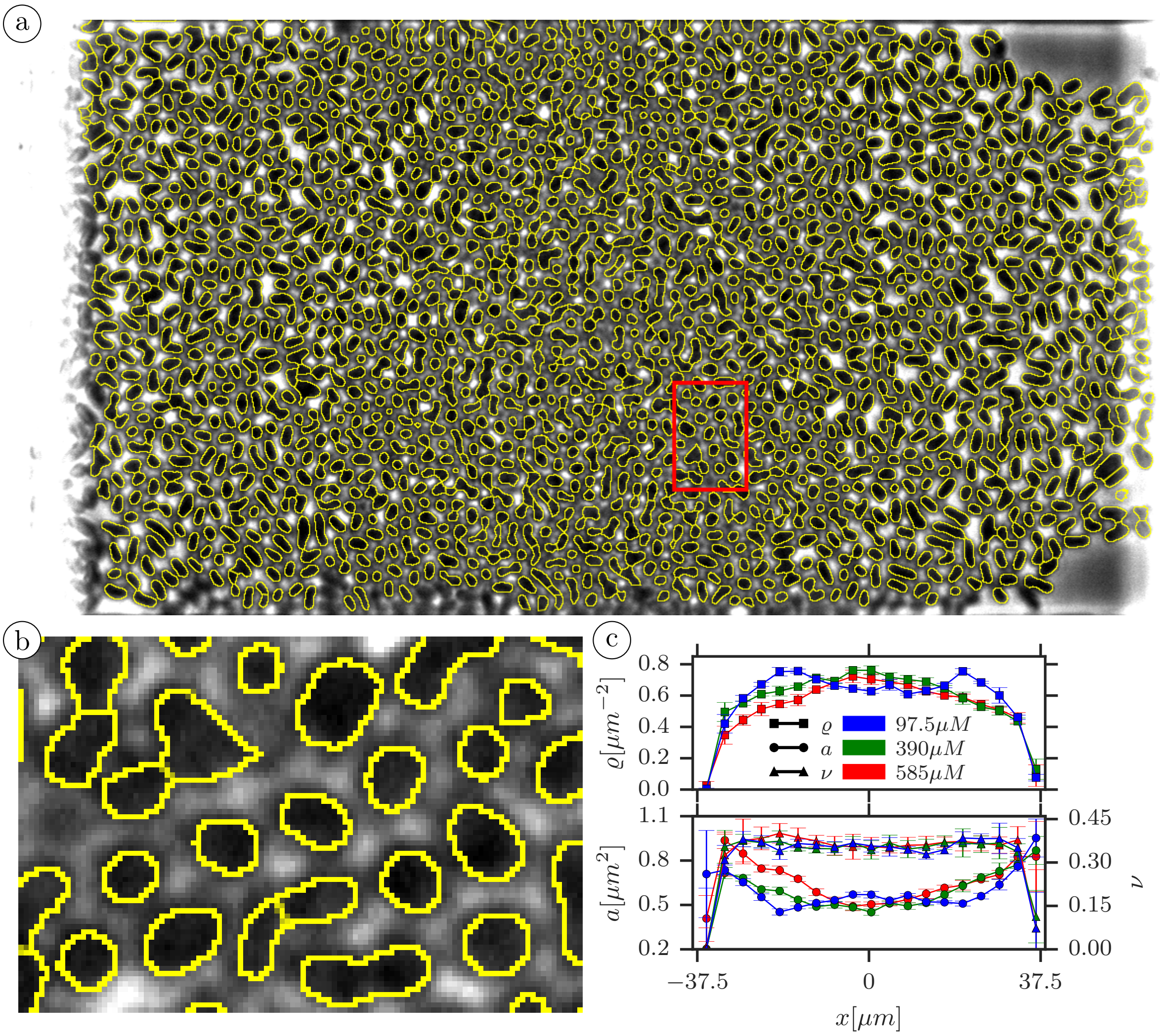

FIGURE 5.14. **a)** Example for the cell segmentation of the segmentation algorithm implemented by Stefan Helfrich [113]. Cell contours are colored in yellow. **b)** Enlarged and 90° clock-wise rotated depiction of the red square in a). Note that the contours engulf the darker inner pixels of the bacteria; It is difficult to tell to which bacterium the brighter pixels belong. **c)** Plot of cell number density ϱ (top, squares), area a (bottom, left axis, circles) and two-dimensional packing fraction $\nu = a\varrho$ (bottom, right axis, triangles) along the channel axis coordinate x for three different feeding concentrations c_{pca} (colorcode, see legend). Error bars refer to STDEV of average over y-dimension and time.

towards the channel entries. Interestingly, the overall two-dimensional packing fraction stays constant around $\nu = 0.35$ for all concentrations.

To investigate the relation between cell area a and velocity $\boldsymbol{v}$, we interpolate the PIV-velocity fields at the centroid position of the cells. Figure 5.15 depicts corresponding histograms of cell area versus velocity magnitude $v = |\boldsymbol{v}|$. Only cells with a velocity of at least $v = 1\,\mu\mathrm{m}\,\mathrm{h}^{-1}$ are counted in the histogram to exclude the non-moving cells in the

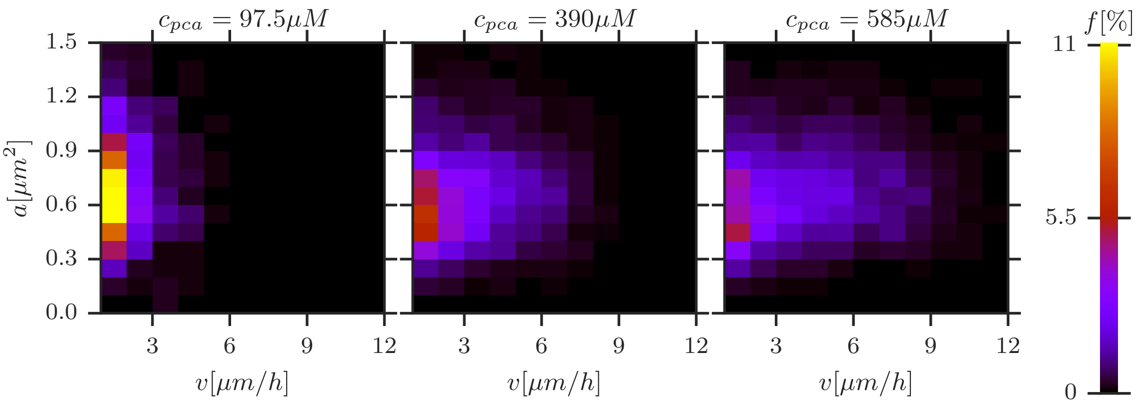

FIGURE 5.15. Histograms of cell area a versus velocity magnitude $|\boldsymbol{v}|$ for three different feeding concentrations c_{pca} (written above plot). Color code corresponds to frequency f of cells, see legend on the right.

channel center. A clear systematic relationship between area and velocity is not visible from these histograms. A quantitative evaluation of the $a-v$ correlation by means of the Pearson correlation coefficient ρ

$$\rho = \frac{\langle (a - \langle a \rangle)(v - \langle v \rangle) \rangle}{\sqrt{\left\langle (a - \langle a \rangle)^2 \right\rangle \left\langle (v - \langle v \rangle)^2 \right\rangle}}, \tag{5.2.20}$$

results in $\rho \approx 0.07, 0.12, 0.14$ for the concentrations $c_{pca} = 97.5, 390, 585\,\mu\text{M}$ which indicates a small positive correlation, i.e. larger cells being faster. However, as the estimation of area and velocity per cell is rather coarse, due to the velocity interpolation and the difficulty in the cell contour estimation, we do not deem this value to be very reliable. We interpret the very small positive correlation such, that with the current resolution and quality of velocity and contour measurement no clear correlation between cell area and velocity can be detected. In conclusion, this finding suggests that a mechanism different from cell-size dependent drag is responsible for the observed streaming instabilities.

5.3. Prediction of Colony Shape Dynamics in Two Dimensions

We simulate the time-dependent spreading of bacteria inside a rectangular *growth chamber* with two narrow feeding inlets at both sides (as in fig. 5.1 with $d < 2L_y$) and compare our predictions with experimental results. This setup allows us to test whether our model predicts successfully colony growth in a genuine two-dimensional setup, even though its parameters are measured in a much simpler, effectively one-dimensional growth channel. Furthermore, in the two-dimensional setup a new model parameter becomes accessible: the difference between diffusion constants in- and outside the colony.

In experiments, we analyze the spreading of a colony of *C. glutamicum* with prescribed feeding concentrations $g_\infty = 19.5\,\mu\text{M}$ ($n = 3$ independent experiments) and $g_\infty = 195\,\mu\text{M}$ ($n = 7$). Movies of growth chamber experiments and corresponding simulation predictions can be found in the supplement of ref. [75], see ref. [109]. A few bacteria are seeded in the growth chamber at $t = 0$, subsequent colony spreading is observed via time-lapse imaging.

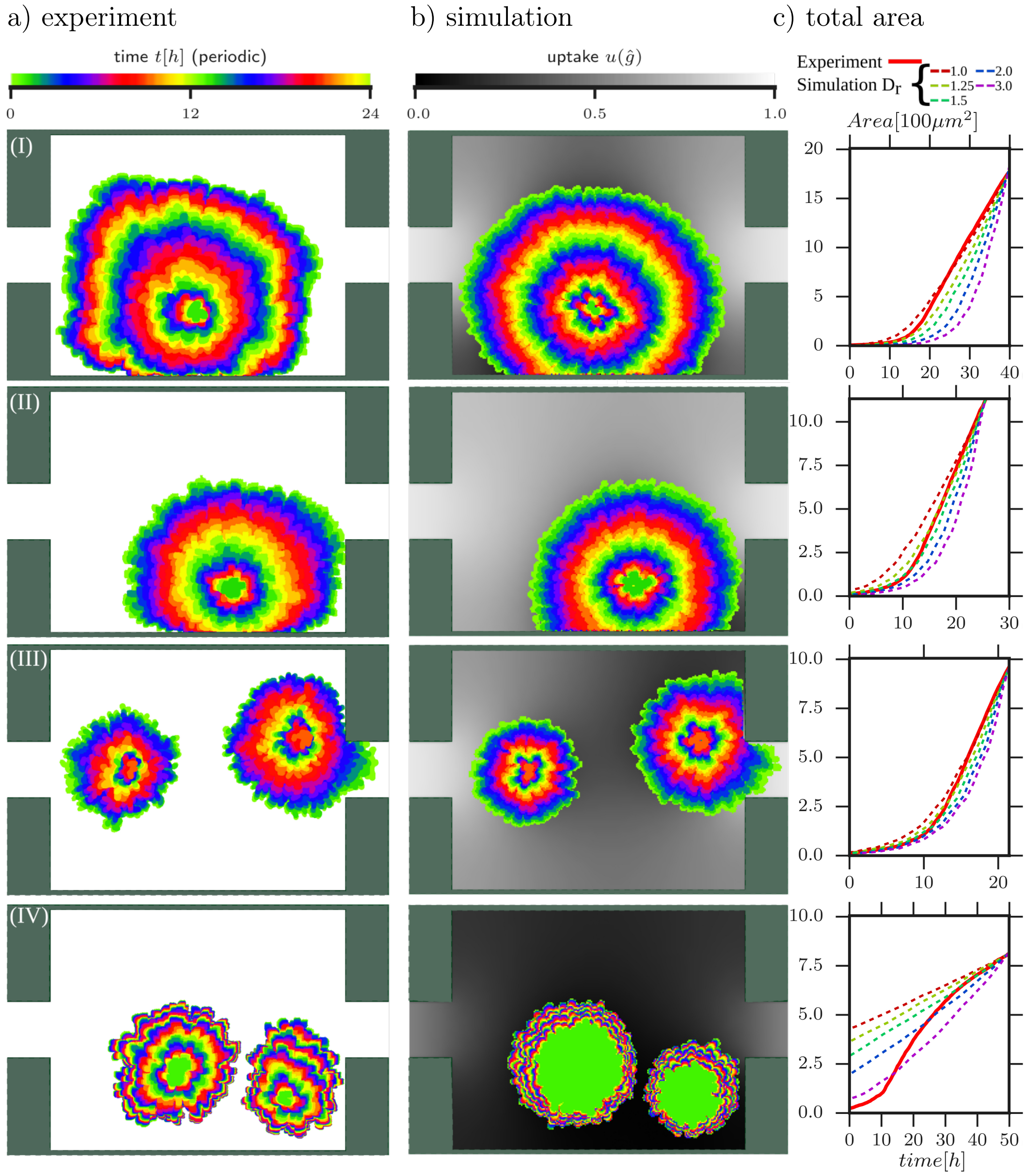

FIGURE 5.16. Four examples of colony spreading dynamics in simulation and experiment. Rows **(I)-(III)** belong to experiments with feeding concentration $g_\infty = 195\,\mu\text{M}$ while **(IV)** corresponds to $g_\infty = 19.5\,\mu\text{M}$. **a)** Depiction of the colony shape dynamics in experiments. The outlines of the colony at equidistant timepoints are shown in different colors with a periodic colorscale (legend on top), 12 hours pass between two rings with the same color. **b)** Same depiction as in left column for outlines from the corresponding simulation with $D_{free}/D_{bulk} = 1.25$ (colorscale for colony same as in left column). The area shaded in gray around the colonies shows the profile of $u(g)$ at the last timepoint (legend on top). **c)** Total colony area $A(t)$ in experiment (red line) and simulations (dashed lines) with $D_r = D_{free}/D_{bulk} = 1, 1.25, 1.5, 2, 3$ (legend on top). Simulations are shifted along the time axis such that they cross the last data point of the experiment. From [75].

The initial position of the bacteria varies among the experiment: sometimes bacteria are concentrated at one position, sometimes single bacteria give rise to separate colonies in the chamber. Clearly, the spreading dynamics is very sensitive to the initial conditions. If initially all bacteria are concentrated in one spot, a single circular colony develops, whereas if the bacteria are initially distributed over the chamber, multiple separate colonies grow and finally merge (see fig. 5.16a) and figs.H.2,H.3a) in appendix H). The simulations are initialized with the same amount of cells at identical positions as in the experiment. We convert the experimental feeding concentration g_∞ to simulation units via the previously calculated concentration scale $\bar{g}$. Visual comparison of the shape of the colony predicted by simulations and observed in experiments already shows a good agreement, with growth patterns in nice synchrony (see fig. 5.16b) and figs.H.2,H.3b)), especially for colonies larger than $A = 500\,\mu\text{m}^2$. Furthermore, the overall colony area $A(t)$ over time serves as an easily accessible quantifier for comparison (see fig. 5.16c) and figs.H.2,H.3c)). The growth of colonies which consist of only a few bacteria depends strongly on the state of the cell cycle of every individual, such that we expect a large variability in growth. Therefore, we expect that our model agrees best in the later stages of the experiment, when memory effects have worn out and the continuum description is appropriate. The simulation time axis is therefore shifted such that $A(t)$ coincides with the last data point of the experiment (see fig. H.1). For experiments with concentration $g_\infty = 195\,\mu\text{M}$ (i.e. half our "fitting concentration"), simulations agree very well with experiments even down to colonies consisting of only the few cells at the starting point of the experiment (see fig. 5.16(I)-(III)). For extrapolations to the much lower concentration $g_\infty = 19.5\,\mu\text{M}$ (see fig. 5.16(IV)) simulations still agree remarkably well for colonies larger than about $500\,\mu\text{m}^2$. In experiments with very low nutrient concentrations ($g_\infty = 19.5\,\mu\text{M}$), bacteria initially grow faster than predicted. This may be due to cell-history effects from preculture, e.g. carbon storage, or effects from the differences in population densities present in growth-channel experiments versus the smaller initial density in growth-chamber experiments. A quantitative understanding of this effect requires a more detailed study in the future.

Furthermore, our observations suggest directed growth toward the channel inlets. While, initially, colonies grow in a more or less circular shape, some elongate over time. The effect is weak, and sometimes caused by previous wall contact. However, in some cases (right colony in fig. 5.16 (IV) and fig. H.2(II) and (IV) in appendix H,) orientation toward the inlets is visible. This indicates that the nutrient gradients, as predicted by the local growth profile $u(g)$ (see fig 5.16, b)) of our model, directly affect the temporal expansion of the colony. However, these changes in shape are subtle and further quantitative analysis is required. Simulations can be improved further when hindered diffusion through bacteria is considered. In our model, this can be accounted for in a coarse-grained manner by defining two different diffusion constants, D_{bulk} and D_{free} in- and outside of the colony, respectively. The agreement with experiments is best for $D_{free}/D_{bulk} \approx 1.25$, a surprisingly small impediment if the bacteria are considered as obstacles[103, 104].

5.4. Summary

In conclusion, we achieve a mapping of the growth dynamics of the bacterium *C. glutamicum* onto a coarse-grained reaction-diffusion model. Our reaction-diffusion model describes nutrient transport, uptake, conversion into biomass and the resulting movement of bacteria through steric repulsion. In a first experiment, bacteria are cultivated in a growth channel (see fig. 5.1 with $d = 2L_y$) with an effective one-dimensional nutrient gradient. The steady state velocity profile is measured via particle image velocimetry for various concentrations g of the limiting nutrient PCA. We employ the relation

$$\frac{dv}{dx} = k_{max} u\left(\frac{\bar{g}}{k_{max} l_g^2} \int_{x_0}^{x} v\, dx - g(x_0)\right), \tag{5.4.1}$$

between steady state velocity profile v in the growth channel, concentration $g(x_0)$ in the channel center, maximal growth rate k_{max}, nutrient decay length l_g and concentration dependent uptake rate $u(g)$, $\bar{g}$ denotes a concentration unit factor. This relation enables us to construct the uptake function from the velocity data. In particular, we can infer the concentration profile inside the colony from the velocity measurements alone, avoiding elaborate concentration measurements in experiments. Our velocity data for measurements with *C. glutamicum* is consistent with a Monod-like uptake function $u(g) \propto g/\big(g_{1/2} + g\big)$ as well as a Teissier-like uptake function $u(g) \propto 1 - \exp\big(-\log(2)g/g_{1/2}\big)$, linear for small concentrations $\widehat{g} \ll g_{1/2}$ and saturating for large concentrations $g \gg g_{1/2}$. From a least-squares minimization fit of the measured velocity profiles versus the prediction of our model, we estimate maximum growth rate around $k_{max} \approx 0.2 - 0.26\text{h}^{-1}$, nutrient decay length around $l_g \approx 3.8 - 4.2\mu\text{m}$ and the concentration with half of the maximum growth rate to $g_{1/2} \approx 14 - 20\mu\text{M}$. In particular, as a single bacterium is approximately rod-shaped with dimensions $3\mu\text{m} \times 1\mu\text{m}$, l_g being only a few micrometers implies that nutrient gradients occur already for small colonies with only a few cell layers.

Furthermore, we observe that cells move in an “avalanche”-like fashion on short timescales: multiple layers of cells always move together whereas the remaining cells in the channel remain motionless. A similar streaming instability has been observed previously [116] and has been attributed to larger bacteria experiencing larger friction with the top and bottom channel walls. Therefore, bigger bacteria slow down and limit the movement of smaller bacteria which have to flow around. We analyze our velocity data to estimate the length scales of correlated movement. We find an average avalanche size of approximately $2.5\mu\text{m} \times 4\mu\text{m}$, the longer axis aligned in flow direction. Avalanche sizes exhibit only small variations along the channel. However, within the given precision of cell contour and velocity measurements, we could not detect a clear correlation between cell velocity and size. This suggests size-dependent drag is unlikely to be responsible for the observed motion pattern.

In a second experiment, a few bacteria are seeded into a □-shaped chamber with narrow feeding inlets (see fig. 5.1 with $d < 2L_y$). We follow colony growth over time and compare colony shape with 2PG-simulations, extended with the reaction-diffusion dynamics of the nutrient. With the model parameters extracted from the growth channel experiments, we find a good agreement between colony shapes in experiment and simulation for colonies larger than around $500\mu\text{m}^2$. For medium nutrient concentrations, colony shapes agree also for smaller areas $< 500\mu\text{m}^2$, whereas for low nutrient concentrations simulations deviate from experimental results. We assume these deviations occur as for a colony consisting of only a few cells, the randomness of the cell cycle causes a large variability in growth which is not captured by our deterministic model. Furthermore, as cells are precultured in a 100-fold larger nutrient concentration, memory effects may occur.

Moreover, we test the effect of hindered nutrient diffusion through bacteria in a coarse-grained manner in our simulations. We find best agreement of colony shapes for D_{free}/D_{bulk} ≈ 1.25, implying bacteria represent only a small impediment for nutrient diffusion.

CHAPTER 6

Conclusion and Outlook

We studied two examples for pattern generation in growing cell sheets: a membrane with growth dependent on pressure and a colony of bacteria with growth dependent on nutrient concentration.

To simulate membrane growth, we combined the previously established 2PG-model and the MMM-model. We performed analytic calculations which confirm that the MMM-potential (1) results in contributions to the in-plane forces quadratic in membrane thickness d, (2) yields a self-avoidant membrane, and (3) converges for curvature radii R much larger than the cutoff radius $R \gg r_{mp}$ rapidly to a curvature energy E_{bend} of the Helfrich-Canham form eq. (4.1.1). Thus, the MMM-method does hardly alter the in-plane growth dynamics and provides a bending rigidity in the usual sense.

Our simulations showed how pressure-dependent growth and a dissipative background medium yield buckling patterns with wavenumbers in the range $2\pi/L < k < \sqrt{|\gamma_h| /(2\kappa)}$, dependent on the timescales of membrane deformation τ_{ampl} and cell growth τ_g. For growth being much faster than membrane deformation, $\tau_{ampl}/\tau_g \gg 1$, wavenumbers close to the homeostatic wavenumber $k_h = \sqrt{|\gamma_h| /(2\kappa)}$ are excited, whereas the opposite limit $\tau_{ampl}/\tau_g \ll 1$ results in buckling closer to the system spanning mode $k = 2\pi/L$. Hence, our model describes a wrinkling mechanism which yields wavenumbers much larger than the system spanning mode for a monolayered membrane, without the necessity of a stress gradient along the membrane thickness. In particular, as the dominant wavenumber depends on the timescales τ_{ampl} and τ_g, it is also affected by frictional parameters of membrane and embedding medium. Moreover, our model implies that explicit wrinkling dynamics need to be taken into account if the timescale of membrane deformation is comparable or larger than the timescale of growth.

These results lay the foundation for many interesting follow-up projects. Expansion of our simulation approach to include an embedding medium with elastic response comprises a promising future prospect. This would allow us to study epithelial sheets with the supporting elastic matrix of connective tissue to investigate e.g. development of intestinal villi and crypts (in- and outward folded domains) or the folds lining the interior of the gullet. Moreover, with a solely frictional response of the embedding medium, we reached a steady state only if we disabled growth. For a growing membrane bound to an elastic medium, we expect to reach a steady state in the presence of growth, as at some point, elastic and growth stresses have to cancel.

To study bacterial growth, we mapped a coarse-grained reaction-diffusion model quantitatively onto growth patterns of *Corynebacterium glutamicum*, observed in microfluidic experiments. The concentration of the limiting nutrient protocatechuic acid (abbreviated PCA) was varied to probe the nutrient dependency of bacterial growth. Our model includes nutrient transport, uptake and conversion into biomass to describe the observed flow of bacteria as well as the nutrient concentration profile inside the chambers on the microfluidic chip. We were able to estimate the maximal growth rate $k_{max} \approx 0.2 - 0.26\,\mathrm{h}^{-1}$, the uptake rate as a function of concentration $u(g)$, which agrees with a Monod-function $u(g) \propto g/\big(g_{1/2} + g\big)$, the concentration at which the growth rate equals half its maximum $g_{1/2} \approx 14 - 20\,\mu\mathrm{M}$ and the nutrient decay length scale $l_g \approx 3.8 - 4.2\,\mu\mathrm{m}$. In particular, as the nutrient decay lengthscale corresponds to only a few layers of bacteria, we expect nutrient gradients and possible limitation effects to occur already for small colonies. Furthermore, we deem experimental protocol and subsequent data evaluation of the steady state of the quasi-one-dimensional growth channel experiments to be easy to reproduce for different bacteria or nutrient media. Thus, our work serves as a proof-of-concept study for a simple method to measure bacterial growth parameters. Furthermore, our model predicts the spatial profile of nutrient concentration inside the growth chamber, a quantity which is difficult to measure directly. Moreover, the overall good agreement of bacterial growth patterns with a coarse-grained reaction-diffusion model suggests that such a description is justified down to colony sizes of a few thousand individua.

Many interesting issues have just been touched by our investigations, leaving a lot of topics for future work. Measurements of the actual pressure inside the growth chambers are necessary to shed light on the question of the pressure-sensibility of bacterial growth. Pressure measurements with spatio-temporal resolution require elaborate techniques such as traction- or cell force microscopy [117, 118]. The good agreement of growth patterns in experiments with our reaction-diffusion model, which only takes the nutrient dependency of growth into account, suggests that pressure does not play a role for colonies of *C. glutamicum* of the observed sizes. However, pressure may have a considerable effect on larger colonies or different stems of bacteria. A systematic analysis of the role of mechanical interactions for bacterial growth would be interesting from a microbiological perspective and would also help in the design of microfluidic experiments. For example, as the maximal pressure in growth channel experiments scales quadratically with the channel length, it has to be tuned carefully if pressure-sensitive microorganisms are grown in it. Moreover, pressure measurements would also help to understand the observed turbid and cloudy frames in some of the growth channel experiments. Under the assumption that these are caused by partial overlap and stacking of bacteria, owing to a deformation of the channel walls, we estimated the pressure in the channel center to be in the 10-100 mbar range. However, as cloudy frames only occurred for a subset of the experiments, fabrication errors or heterogeneity in the stiffness of the PDMS substrate may be possible reasons as well. Furthermore, pressure measurements would also help to investigate the observed streaming instabilities, a phenomenon interesting from the perspective of granular matter physics [119, 120, 121, 122]. Additionally, a finer time resolution of the image capturing is necessary to track rise and development of single “avalanches” and therefore ease explanatory modeling. Also, the comparison of colony spreading experiments with simulations indicated that colony growth is directed towards increasing nutrient concentration, even on timescales on the order of the cell division time. However, this finding requires further experimental evaluation, as the observed growth towards larger nutrient concentrations can in some cases also be attributed to interactions between bacteria and chamber walls. The timescale on which bacterial growth adapts to the local nutrient concentration is an important input for growth models as it determines the bacterial “memory” for past concentrations. Moreover, microfluidic growth experiments appear to be a promising setup to investigate the permeability of colonies for nutrients or other diffusing agents. The colony spreading experiments indicated that the effective diffusion constant D_{bulk} of PCA inside the colony is close to the free diffusion constant D_{free}, as a ratio around $D_{free}/D_{bulk} \approx 1.25$ yielded the best match between simulations and experiments. This estimate could be improved, for example, by measuring D_{free}/D_{bulk} in a setup with a steady state flow profile which allows to perform time averages over many steady state data points.

In summary, we extended the 2PG-model with modules to simulate (1) the growth of membranes and (2) growth dependent on a diffusive factor. With these modules, we explored the basic properties of pattern formation for a wrinkling membrane and a flat colony of bacteria. It will be particularly interesting for future studies to combine these modules with other expansions of the 2PG-model. For example, a more realistic model for villi and crypt formation in the gut combines the growing membrane (epithelium) with a underlying growing bulk tissue (stroma) and regulation by diffusive growth factors.

APPENDIX A

Meshless Membrane Model - Force Calculation

To calculate the MMM-force on particle k in direction $\rho \in \{x, y, z\}$,

$$\boldsymbol{F}_k \cdot \boldsymbol{e}_\rho = -\frac{\partial}{\partial \rho_k} k_\alpha \sum_{i=1}^{N} \alpha_{pl}\Big(\boldsymbol{r}_i, \{\boldsymbol{r}_j\}_{j\neq i}\Big) , \qquad \rho \in \{x, y, z\} \tag{A.1}$$

we first note that the aplanarity in eq. (3.3.6) is a fraction of two third-order polynomials in the gyration tensor components $a_{\alpha\beta}$, thus, chain and product rule reduce the calculation of $\partial_{\rho_k}\alpha_{pl}$ ultimately to derivations of the form

$$\frac{\partial}{\partial \rho_k} a_{\alpha\beta}\Big(\boldsymbol{r}_i, \{\boldsymbol{r}_j\}_{j\neq i}\Big) . \tag{A.2}$$

To calculate $\partial_{\rho_k} a_{\alpha\beta}$, we commence with the following two identities

$$\sum_{j=1}^{N} (\alpha_j - \alpha_g)\, w\,(r_{ij}) = \sum_{j=1}^{N} \alpha_j w\,(r_{ij}) - \alpha_g \sum_{j=1}^{N} w\,(r_{ij}) = \alpha_g w_0 - \alpha_g w_0 = 0\,, \tag{A.3}$$

and

$$\begin{aligned}\frac{\partial r_{ij}}{\partial \rho_k} = \frac{1}{r_{ij}} \sum_{\eta\in x,y,z} (\eta_i - \eta_j)\, \frac{\partial}{\partial \rho_k} (\eta_i - \eta_j) &= \frac{1}{r_{ij}} \sum_{\eta\in x,y,z} (\eta_i - \eta_j)\, \delta_{\rho\eta} \,(\delta_{ik} - \delta_{jk}) \\ &= \frac{\rho_i - \rho_j}{r_{ij}} \,(\delta_{ik} - \delta_{jk})\,.\end{aligned} \tag{A.4}$$

The derivative in eq. (A.2) for $k = i$ follows then to:

$$\begin{aligned}\frac{\partial}{\partial \rho_k} a_{\alpha\beta}\Big(\boldsymbol{r}_k, \{\boldsymbol{r}_j\}_{j\neq k}\Big) &= \sum_{j=1}^{N} \left(\frac{\partial \alpha_j}{\partial \rho_k} - \frac{\partial \alpha_g}{\partial \rho_k}\right) (\beta_j - \beta_g)\, w\,(r_{kj}) \\ &+ \sum_{j=1}^{N} (\alpha_j - \alpha_g) \left(\frac{\partial \beta_j}{\partial \rho_k} - \frac{\partial \beta_g}{\partial \rho_k}\right) w\,(r_{kj}) \\ &+ \sum_{j=1}^{N} (\alpha_j - \alpha_g)\,(\beta_j - \beta_g)\, \frac{\partial w\,(r_{kj})}{\partial \rho_k}.\end{aligned} \tag{A.5}$$

For the first term on the right-hand side we get

$$\begin{aligned}\sum_{j=1}^{N} \left(\frac{\partial \alpha_j}{\partial \rho_k} - \frac{\partial \alpha_g}{\partial \rho_k}\right) (\beta_j - \beta_g)\, w\,(r_{kj}) &= \sum_{j=1}^{N} \delta_{kj}\delta_{\rho\alpha}\,(\beta_j - \beta_g)\, w\,(r_{kj}) + \frac{\partial \alpha_g}{\partial \rho_k} \sum_{j=1}^{N} (\beta_j - \beta_g)\, w\,(r_{kj}) \\ &= \delta_{\rho\alpha}\,(\beta_k - \beta_g) \cdot 1,\end{aligned} \tag{A.6}$$

due to $w\left(r_{kk}\right)=w\left(0\right)=1$ and identity (A.3). We simplify the second term on the right-hand side in the same manner, which yields the same expression as above with α and β switched. For the last summand, insertion of identity (A.4) leads to

$$\sum_{j=1}^{N}\left(\alpha_j-\alpha_g\right)\left(\beta_j-\beta_g\right)\frac{\partial w\left(r_{kj}\right)}{\partial\rho_k}=\sum_{j\neq k}\left(\alpha_j-\alpha_g\right)\left(\beta_j-\beta_g\right)\frac{w'\left(r_{kj}\right)}{r_{kj}}\left(\rho_k-\rho_j\right)\,, \tag{A.7}$$

where we abbreviated $\frac{dw}{dr}(r_{ij})=w'\left(r_{ij}\right)$. By summing up the simplified terms, we finally get

$$\begin{aligned}\frac{\partial}{\partial\rho_i}a_{\alpha\beta}\left(\boldsymbol{r}_i,\left\{\boldsymbol{r}_j\right\}_{j\neq i}\right)=&\delta_{\rho\alpha}\left(\beta_i-\beta_g\right)+\delta_{\rho\beta}\left(\alpha_i-\alpha_g\right)\\&+\sum_{j\neq i}\left(\alpha_j-\alpha_g\right)\left(\beta_j-\beta_g\right)\frac{w'\left(r_{ij}\right)}{r_{ij}}\left(\rho_i-\rho_j\right).\end{aligned} \tag{A.8}$$

Analogously, one can show for the case $k\neq i$ the result

$$\begin{aligned}\frac{\partial}{\partial\rho_k}a_{\alpha\beta}\left(\boldsymbol{r}_i,\left\{\boldsymbol{r}_j\right\}_{j\neq i}\right)=&\delta_{\rho\alpha}\left(\beta_k-\beta_g\right)w\left(r_{ki}\right)+\delta_{\rho\beta}\left(\alpha_k-\alpha_g\right)w\left(r_{ki}\right)\\&+\left(\alpha_k-\alpha_g\right)\left(\beta_k-\beta_g\right)\frac{w'\left(r_{ki}\right)}{r_{ki}}\left(\rho_k-\rho_i\right).\end{aligned} \tag{A.9}$$

With equations (A.8) and (A.9) all necessary terms to calculate the force components are determined. Note that eqns. (A.8) and (A.9) refer to different center particles and the weighted center of mass $\boldsymbol{r}_g$ has also to be calculated with respect to these.

APPENDIX B

Multibody Potentials and Stress Calculations with Spatial Resolution

We briefly recapitulate the problem of the calculation of mechanical stress with spatial resolution for a multibody potential such as the MMM-potential, introduced in section 3.3. In particular, we show that this problem is not solvable by straightforward methods as it is, in general, ambiguous. In case of the membrane system discussed in chapter 4, stress measurements with spatial resolution would allow us to spatially resolve the surface tension γ as well.

Stress measurements with spatial resolution can be performed by division of the system volume into small subvolumes and measuring the stress in each subvolume. We take a look at an arbitrary subvolume S (see fig. B.1) with volume V_S and particles at positions $\boldsymbol{r}_i$; the bond vectors $\boldsymbol{r}_{ij} = \boldsymbol{r}_j - \boldsymbol{r}_i$ may or may not cross the subvolumes surface ∂S. For pairwise interactions, the interaction potential U can be written as a function of the particle distances $U = U(\{r_{ij}\})$. Thus, we can assign every bond $\boldsymbol{r}_{ij}$ an interaction force $\boldsymbol{F}_{ij} = -\partial_{r_{ij}} U \widehat{\boldsymbol{r}}_{ij}$, where $\widehat{\boldsymbol{r}}_{ij}$ denotes the unit vector in bond direction $\widehat{\boldsymbol{r}}_{ij} = \boldsymbol{r}_{ij}/r_{ij}$. In this case, we can express the stress tensor contributions by

$$\begin{aligned} \overline{\boldsymbol{\sigma}}_{kin,S} V_S &= \sum_{\substack{\text{particles } i \\ \text{inside } S}} m \boldsymbol{v}_i \otimes \boldsymbol{v}_i \\ \overline{\boldsymbol{\sigma}}_{pot,S} V_S &= \underbrace{\sum_{\substack{\text{bonds } ij \\ \text{inside } S}} \boldsymbol{r}_{ij} \otimes \boldsymbol{F}_{ij}}_{\text{volume contributions}} + \underbrace{\sum_{\substack{\text{bonds } ij \\ \text{crossing } \partial S}} r_{ij}^S \boldsymbol{r}_{ij} \otimes \boldsymbol{F}_{ij}}_{\text{interface contributions}}, \end{aligned} \tag{B.1}$$

where $r_{ij}^S \in [0,1]$ denotes the fraction of the bond vector $\boldsymbol{r}_{ij}$ inside S (see fig. B.1) [76, 86]. In the case of S being the whole system volume V, we indeed recover eq. (3.4.6) for the virial stress, as we show in the following. For $S \equiv V$ the second term in the expression for $\overline{\boldsymbol{\sigma}}_{pot}$, the stress contribution of the interfaces between different subvolumes, vanishes. Furthermore, all bonds ij fall now in S such that we write

$$\overline{\boldsymbol{\sigma}}_{pot,S} V_S = \sum_{\text{bonds } ij} \boldsymbol{r}_{ij} \otimes \boldsymbol{F}_{ij} = \frac{1}{2} \left(\sum_{i \neq j} \boldsymbol{r}_i \otimes \boldsymbol{F}_{ij} + \sum_{i \neq j} \boldsymbol{r}_j \otimes \boldsymbol{F}_{ji} \right) = \sum_i \boldsymbol{r}_i \otimes \boldsymbol{F}_i, \tag{B.2}$$

due to $\boldsymbol{F}_{ij} = -\boldsymbol{F}_{ji}$ (actio = reactio) and with the total force $\boldsymbol{F}_i = \sum_j \boldsymbol{F}_{ij}$ on particle i. For multibody potentials, such as the MMM-potential, which cannot be expressed as a function of the particle distances $\{r_{ij}\}$, the derivative in $\boldsymbol{F}_{ij} = -\partial_{r_{ij}} U \widehat{\boldsymbol{r}}_{ij}$ cannot be calculated in a straightforward manner. Therefore, we need to find another way of properly defining the force $\boldsymbol{F}_{ij}$ in order to estimate stress with spatial resolution. The set of bond forces $\{\boldsymbol{F}_{ij}\}$

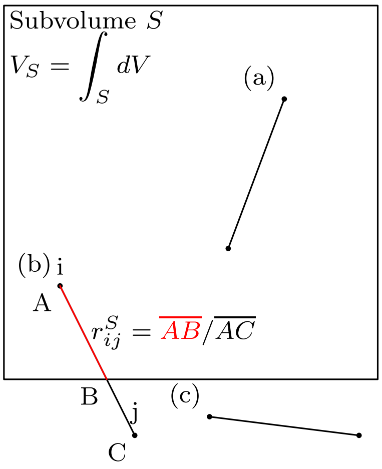

FIGURE B.1. Particle-particle bond contributions to the stress of an arbitrary subvolume S are weighted with the fraction of their total length inside S. (a) Bonds in the volume of S fully contribute to the stress, whereas (b) bonds crossing the volume are weighted with the fraction r_{ij}^S of their total length inside S (see eqns. B.1) and (c) bonds outside the subvolume do not contribute.

to a set of given particle positions $\{\boldsymbol{r}_i\}$ and total forces $\{\boldsymbol{F}_i\}$ is referred to as *central force decomposition* (abbreviated CFD). An extensive discussion in [86] shows that the problem of finding the "canonical" CFD, i.e. the CFD which accurately reflects the physics of the interactions between the particles is, in general, ambiguous. To elucidate this ambiguity, let us briefly take a look at the following three arguments:

1. In continuum mechanics, the total force density $\boldsymbol{f}$ does determine the dynamics but it does not pin-point the stress tensor: since $\boldsymbol{f} = \operatorname{div} \overline{\boldsymbol{\sigma}}$, we can add any divergence free tensor field to $\overline{\boldsymbol{\sigma}}$ to reproduce the same dynamics. Therefore, we expect that in discrete particle systems knowledge of the set of total forces $\{\boldsymbol{F}_i\}$ is neither sufficient to calculate $\overline{\boldsymbol{\sigma}}$.

2. The mathematical expression of the interaction potential $U = U(\{r_{ij}\})$ in terms of particle-particle distances $\{r_{ij}\}$ does not resolve the ambiguity. Even if we have found an expression $U = U(\{r_{ij}\})$ and try to pin-point the CFD by simply calculating $\boldsymbol{F}_{ij} = -\partial_{r_{ij}} U \widehat{\boldsymbol{r}}_{ij}$, there exists *always* a potential $\tilde{U}$ which results in the same system dynamics but $\partial_{r_{ij}} U \neq \partial_{r_{ij}} \tilde{U}$. This can be illustrated with a simple example. Imagine three particles $1, 2$ and 3 in one-dimensional space which interact with the pair potentials $U_{12}(r_{12})$, $U_{13}(r_{13})$ and $U_{23}(r_{23})$. Moreover, we define

$$\chi = (r_{12} - r_{13} - r_{23})\,(r_{23} - r_{12} - r_{13})\,(r_{13} - r_{23} - r_{12})\,(r_{12} + r_{13} + r_{23})\,. \tag{B.3}$$

It can easily be shown that $\chi \equiv 0$ due to all particles lying on a straight line; hence the interaction potentials $U = U_{12} + U_{13} + U_{23}$ and $\tilde{U} = U + \chi$ lead to the same total forces and hence the same dynamics. However, the partial derivatives $\partial_{r_{ij}} U$ and $\partial_{r_{ij}} \tilde{U}$ are *different*, leading to different CFDs using the formula $\boldsymbol{F}_{ij} = -\partial_{r_{ij}} U \widehat{\boldsymbol{r}}_{ij}$. The polynomial χ is a so-called *Cayley-Menger determinant* and it can be shown that the above example can be generalized to any number of particles and dimensions using these determinants [86]. The "correct" expression for U can only be picked if we consider additional physical arguments.

3. The numerical problem is *underdefined*. Assume we know the set of particle positions $\{\boldsymbol{r}_i\}$ and total forces $\{\boldsymbol{F}_i\}$ and want to deduce a CFD $\{\boldsymbol{F}_{ij}\}$. Obviously, the $\{\boldsymbol{F}_{ij}\}$ have to fulfill

$$\boldsymbol{F}_i = \sum_j \boldsymbol{F}_{ij} \tag{B.4}$$

by definition and

$$\boldsymbol{F}_{ij} = -\boldsymbol{F}_{ji} \tag{B.5}$$

due to momentum conservation (*actio = reactio*). Reference [86] shows that angular momentum is preserved (and hence the resulting stress tensor is symmetric) if and only if additionally

$$\boldsymbol{F}_{ij} \propto \widehat{\boldsymbol{r}}_{ij} \tag{B.6}$$

holds; bond force and bond have to be parallel. A CFD is found by solution of the system of linear equations which results from the three conditions eqns. B.4-B.6. However, one can easily show by counting the number of equations and unknowns, that, in general, the problem is underdefined, allowing for an *infinite* number of CFDs.

As the MMM-potential cannot be expressed easily in terms of pairwise interactions the question of the "correct" CFD remains unclear without further assumptions on the nature of its pairwise particle-particle interactions. We therefore constrain the analysis of the surface tension on the well-defined virial stress tensor.

APPENDIX C

Differential Geometric Framework

The membranes of importance for this work can be described as *thin* and *smooth.* To derive a mathematical description, we need to state in a mathematical precise manner what we mean by the intuitive descriptors thin and smooth. The corresponding mathematical framework belongs to the topic of *differential geometry.*

C.1. Membranes as Smooth Surfaces

Even though every physical membrane is a three-dimensional object, we assume that its thickness is of negligible extent relative to its other dimensions such that it is reasonable to represent it by a two-dimensional surface S embedded in three-dimensional space $S \subset \mathbb{R}^3$. As the surface S is two-dimensional, we may parametrize it by a vector-valued function $\boldsymbol{X}$ mapping points from a two-dimensional set $U \subset \mathbb{R}^2$ onto S:

$$\boldsymbol{X} : U \to S \text{ with } U \subset \mathbb{R}^2,\, S \subset \mathbb{R}^3. \tag{C.1.1}$$

To translate "smoothness" into the language of mathematics, we demand that the parameterizing function $\boldsymbol{X}$ is differentiable. Geometrically, differentiability implies that S can locally approximated by a tangent plane. Precisely, differentiability demands that S can locally approximated at every point $\boldsymbol{u} \in U$ by a linear function $\overline{\boldsymbol{\partial X}}_{\boldsymbol{u}}$ such that for all $\boldsymbol{\delta}$ in an open neighborhood of $\boldsymbol{u}$ holds

$$\boldsymbol{X}(\boldsymbol{u}+\boldsymbol{\delta}) - \boldsymbol{X}(\boldsymbol{u}) = \overline{\boldsymbol{\partial X}}_{\boldsymbol{u}}\boldsymbol{\delta} + O\left(\boldsymbol{\delta}^2\right). \tag{C.1.2}$$

The linear function $\overline{\boldsymbol{\partial X}}_{\boldsymbol{u}} : U \to \mathbb{R}^3$, can be represented in matrix form with the components

$$\partial X_{\boldsymbol{u},ij} = \partial_i X_j(\boldsymbol{u})\,, \tag{C.1.3}$$

and is often referred to as Jacobi matrix or Jacobian. Illustratively, the column vectors $\partial_i \boldsymbol{X}$ of the Jacobian pass S tangentially in the point S. We abbreviate these tangent vectors by

$$\boldsymbol{t}_1 = \partial_1 \boldsymbol{X}, \qquad \boldsymbol{t}_2 = \partial_2 \boldsymbol{X}, \tag{C.1.4}$$

in the following. The vectors $\boldsymbol{t}_1, \boldsymbol{t}_2$ span the tangential space T_u of S in the point u, every linear combination $\boldsymbol{t} = a\boldsymbol{t}_1 + b\boldsymbol{t}_2$ is also a tangent vector $\boldsymbol{t} \in T_u$. The requirement of differentiability avoids most "pathologies" like jumps and spikes, as in the case for a scalar function. However, it is not sufficient as illustrated by the two-dimensional example $\boldsymbol{X} : \mathbb{R} \to \mathbb{R}^2$, $u \mapsto \left(u^3, u^2\right)$, referred to as *Neile's parabola* (see fig. C.1). Neile's parabola has a cusp at $u = 0$ due to $\overline{\boldsymbol{\partial X}}_0 \equiv \boldsymbol{0}$. To avoid cusps of this kind, we have to demand that the tangent vectors $\{\partial_i \boldsymbol{X}\}$ are linear independent at every point $\boldsymbol{u} \in U$. This requirement ensures as well that we can define everywhere the surface normal

$$\boldsymbol{n} = \frac{\boldsymbol{t}_1 \times \boldsymbol{t}_2}{|\boldsymbol{t}_1 \times \boldsymbol{t}_2|}. \tag{C.1.5}$$

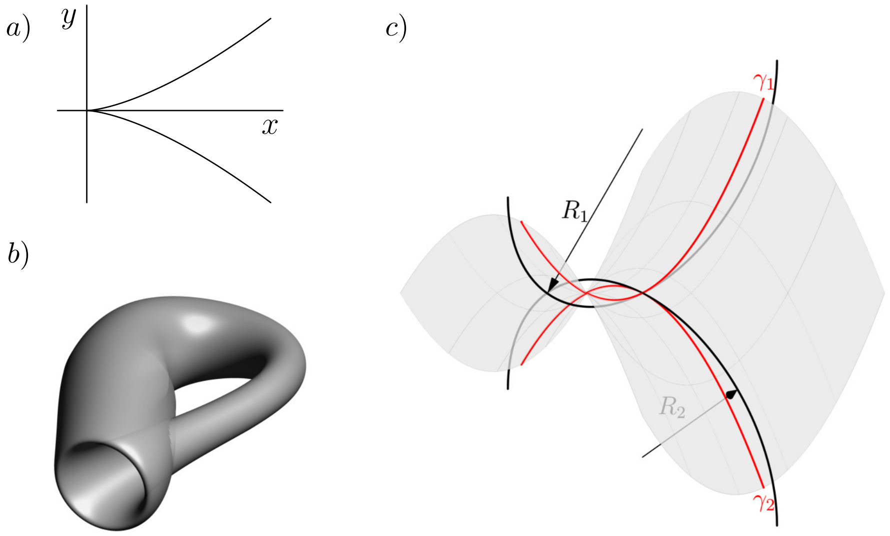

Figure C.1. **a)** Neile's parabola exhibits a cusp albeit being differentiable in its whole domain. The cusp occurs due to the vanishing tangent vector in the origin. **b)** The Klein bottle, a non-orientable surface. **c)** The curvature in a point is the inverse radius of the osculating circle. It is identical to the curvature of space curves $\boldsymbol{\gamma}$ defined as intersections with a normal plane and S.

With the surface normal definition eq. C.1.5, we can define at every point on S an orientation. For example for a sphere, the normal can either point in- or outward the sphere. In lay terms, every surface for which we clearly can define in- and outside or up- and downside is called *orientable*. The exact definition of orientability is somehow technical, the interested reader is here referred to mathematics textbooks [123]. Examples for non-orientable surfaces are the Möbius strip or the Klein bottle (see fig. C.1). Such cases are not important for this work and we demand that the surface S is orientable. Furthermore, the term “closed” for surfaces is used as well. We content ourselves with an intuitive understanding of “closeness”: S is *closed* if we dunk the impermeable surface S into a fluid and the fluid stays outside of a finite compartment.

C.2. Inner and Outer Geometry of a Surface

As we have narrowed down in mathematical terms the relevant surfaces S, we investigate how to measure properties related to area and shape of S. To measure the area A, we analyze how a tiny square $[u_1, u_1 + du_1] \times [u_2, u_2 + du_2] \subset U$ is mapped onto a tiny area dA of S by the parametrization $\boldsymbol{X}$. With the linear approximation property, eq. C.1.2, we approximate dA by a parallelogram with edge vectors $\boldsymbol{t}_1 du_1$ and $\boldsymbol{t}_2 du_2$. The area dA can then be estimated as

$$dA \approx |\boldsymbol{t}_1 du_1 \times \boldsymbol{t}_2 du_2| = \sqrt{\boldsymbol{t}_1^2 \boldsymbol{t}_2^2 - (\boldsymbol{t}_1 \boldsymbol{t}_2)^2} du_1 du_2, \qquad \text{(C.2.1)}$$

up to order $\mathcal{O}\left(du_1^2 du_2^2\right)$. Indeed, it can be shown that above approximation C.2.1 for dA is an exact area measure in the integral limit [123]. Hence, we can calculate the total area of S via integration in the parameter space U:

$$A = \int_S dA = \int_U \sqrt{\boldsymbol{t}_1^2 \boldsymbol{t}_2^2 - (\boldsymbol{t}_1 \boldsymbol{t}_2)^2} du_1 du_2. \tag{C.2.2}$$

The expression C.2.1 can be written as the determinant of a symmetric matrix $\overline{\boldsymbol{g}}$, the *first fundamental form* (or *metric tensor*):

$$\overline{\boldsymbol{g}} = (\boldsymbol{t}_i \cdot \boldsymbol{t}_j) = \begin{pmatrix} \boldsymbol{t}_1^2 & \boldsymbol{t}_1 \cdot \boldsymbol{t}_2 \\ \boldsymbol{t}_1 \cdot \boldsymbol{t}_2 & \boldsymbol{t}_2^2 \end{pmatrix}. \tag{C.2.3}$$

The metric tensor $\overline{\boldsymbol{g}}$ is a measure for all quantities related to the *inner geometry* of S such as areas, lengths and angles. For example, a tiny parallelogram spanned by vectors $\boldsymbol{u}, \boldsymbol{v} \in U$ in parameter space is mapped by $\boldsymbol{X}$ onto a tiny parallelogram on S with interior angle α with

$$\cos\alpha = \frac{\boldsymbol{u} \cdot (\overline{\boldsymbol{g}} \boldsymbol{v})}{|\boldsymbol{u}|\,|\boldsymbol{v}|}, \tag{C.2.4}$$

where $\overline{\boldsymbol{g}}$ may as well be interpreted as a bilinear form. The term *inner* geometry refers to the fact that lengths, areas and angles are measurable from *within* the surface S, i.e. from a tiny observer on S for whom the surface appears to be locally flat. In contrast, the geometry of S in the outer, embedding space is referred to as *outer geometry.* The outer geometry describes the change of tangent and normal vectors on S which leads to the concept of *curvature.* Curvature can be interpreted as a higher order approximation of the local shape of S. To first order in derivatives, S can be locally approximated by a plane whose tangent vectors are the columns of the Jacobian matrix. Illustratively, the next higher order approximates S locally by *osculating circles* (Latin circulus osculans, "kissing circle"). An osculating circle B is the circle who passes through a point P on S tangentially in direction $\boldsymbol{t}$ such that the distance of the points on S and B in normal direction decays at least in cubic order of the distance to P in direction of $\boldsymbol{t}$. In this sense, B is the circle which approaches S closest in P. The radius $R_{\boldsymbol{t}}$ of B is called the *curvature radius* of S in P in the given tangential direction, its inverse the *curvature* $C_{\boldsymbol{t}} = 1/R_{\boldsymbol{t}}$ (see fig. C.1). The curvature can also be defined by consideration of the intersection of S with a plane through P which contains the local normal vector $\boldsymbol{n}$ and a tangent vector $\boldsymbol{t}$ of S. This plane cuts out a space curve $\boldsymbol{\gamma}$ from S which has an unique arc length parametrization $\boldsymbol{\gamma}(s)$. The curvature $C_{\boldsymbol{t}}$ of S is then identical to the curvature of $\boldsymbol{\gamma}$ in P, i.e.

$$C_{\boldsymbol{t}} = \left|\frac{d^2\boldsymbol{\gamma}}{ds^2}\right|_P. \tag{C.2.5}$$

Interpreted as a space curve, the osculating circle is then the circle whose curvature coincides in P with the curvature of $\boldsymbol{\gamma}$ on S. Hence, the curvature can interpreted geometrically as rate of change of the tangent vector. In fact, the derivatives of normal and tangent vectors are closely related, as we will see in the following. We begin with the definition of the *second fundamental form* $\overline{\boldsymbol{K}} = (K_{ij})$

$$K_{ij} = \boldsymbol{n} \cdot \partial_i \boldsymbol{t}_j = \boldsymbol{n} \cdot \partial_i \partial_j \boldsymbol{X}, \tag{C.2.6}$$

which measures the change of the tangent vectors $\{\boldsymbol{t}_i\}$ in normal direction. Note that $\overline{\boldsymbol{K}}$ is symmetric $K_{ij} = K_{ji}$. Since the normal vector $\boldsymbol{n}$ determines the position of the tangent plane, and $\overline{\boldsymbol{K}}$ describes the change in the tangent vectors, we expect that $\overline{\boldsymbol{K}}$ is related to the derivatives of the normal vector $\partial_i \boldsymbol{n}$. Indeed, it is

$$\partial_i \boldsymbol{n} \cdot \boldsymbol{t}_j = -K_{ij} \text{ and } \boldsymbol{n} \cdot \partial_i \boldsymbol{n} = 0, \tag{C.2.7}$$

owing to

$$\begin{aligned} &\boldsymbol{n} \cdot \boldsymbol{t}_j = 0 \Rightarrow 0 = \partial_i \left(\boldsymbol{n} \cdot \boldsymbol{t}_j\right) = \partial_i \boldsymbol{n} \cdot \boldsymbol{t}_j + \boldsymbol{n} \cdot \partial_i \boldsymbol{t}_j = \partial_i \boldsymbol{n} \cdot \boldsymbol{t}_j + K_{ij}, \\ &\boldsymbol{n} \cdot \boldsymbol{n} = 1 \Rightarrow 0 = \partial_i \left(\boldsymbol{n} \cdot \boldsymbol{n}\right) = 2\partial_i \boldsymbol{n} \cdot \boldsymbol{n}. \end{aligned} \tag{C.2.8}$$

Hence, the components of the normal vector derivatives in the tangent space are given by the second fundamental form. Furthermore, the derivative of the normal vector is perpendicular to the normal vector itself, thus, it lies inside the tangent plane. This allows us to define the *Weingarten map* $\overline{\boldsymbol{L}}_u$ (also *shape operator*) as an endomorphism of the tangent space T_u:

$$\begin{aligned} \overline{\boldsymbol{L}}_u &: T_u \to T_u, \\ \overline{\boldsymbol{L}}_u \boldsymbol{t}_i &= -\partial_i \boldsymbol{n}. \end{aligned} \tag{C.2.9}$$

The Weingarten map is the final construct necessary to come to a mathematically closed description of curvature. With the property eq. (C.2.7), it is easy to show that

$$\overline{\boldsymbol{L}}_u \boldsymbol{t}_i \cdot \boldsymbol{t}_j = K_{ij}, \tag{C.2.10}$$

and since $K_{ij} = K_{ji}$ it follows immediately that $\overline{\boldsymbol{L}}_u$ is self-adjoint. A self-adjoint operator possesses an orthogonal basis of eigenvectors with real-valued eigenvalues. The real-valued eigenvalues C_1, C_2 of $\overline{\boldsymbol{L}}_u$ are called the *main curvatures* and the directions of the eigenvectors the *main curvature directions* of $\boldsymbol{X}$ in u. To give an easy way to calculate the main curvatures, we relate the matrix representations of $\overline{\boldsymbol{L}}, \overline{\boldsymbol{h}}$ and $\overline{\boldsymbol{g}}$ to each other. In the base $\{\boldsymbol{t}_i\}$ of T_u, the matrix of $\overline{\boldsymbol{L}} = (l_{ij})$ is defined via $\overline{\boldsymbol{L}} \boldsymbol{t}_j = \sum_i l_{ij} \boldsymbol{t}_i$ and hence

$$K_{jk} \overset{eq.\ (C.2.10)}{=} \overline{\boldsymbol{L}}_u \boldsymbol{t}_j \cdot \boldsymbol{t}_k = \sum_i l_{ij} \boldsymbol{t}_i \cdot \boldsymbol{t}_k = \sum_i l_{ij} g_{ik}, \tag{C.2.11}$$

and therefore $\overline{\boldsymbol{K}} = \overline{\boldsymbol{g}}\overline{\boldsymbol{L}}$ or

$$\overline{\boldsymbol{L}} = \overline{\boldsymbol{g}}^{-1} \overline{\boldsymbol{K}} \text{ in the basis } \{\boldsymbol{t}_i\} \text{ of } T_u. \tag{C.2.12}$$

Trace and determinant of $\overline{\boldsymbol{L}}$ are referred to as mean curvature H and Gaussian curvature G:

$$\begin{aligned} H &= \operatorname{tr} \overline{\boldsymbol{L}} = \operatorname{tr} \left(\overline{\boldsymbol{g}}^{-1} \overline{\boldsymbol{K}}\right) = C_1 + C_2, \\ G &= \det \overline{\boldsymbol{L}} = \frac{\det \overline{\boldsymbol{K}}}{\det \overline{\boldsymbol{g}}} = C_1 C_2. \end{aligned} \tag{C.2.13}$$

The hereby defined main curvatures C_1, C_2 coincide with the geometric interpretation given in fig. C.1 and eq. (C.2.5) if $\boldsymbol{t}$ if chosen as one of the eigenvectors of $\overline{\boldsymbol{L}}$. Furthermore, one can show that for arbitrary $\boldsymbol{t} \in T_u$ and $|\boldsymbol{t}| = 1$ it is

$$\overline{\boldsymbol{L}} \boldsymbol{t} \cdot \boldsymbol{t} = C_{\boldsymbol{t}}, \tag{C.2.14}$$

with $C_{\boldsymbol{t}}$ as in eq. (C.2.5) [123]. From equation (C.2.14) it is also easy to proof that the main curvatures C_1 and C_2 are *minimal* and *maximal* curvature in the given point: For any function of the form $\boldsymbol{v} \mapsto \overline{\boldsymbol{A}} \boldsymbol{v} \cdot \boldsymbol{v}$ with a real-valued, symmetric matrix $\overline{\boldsymbol{A}}$, the stationary points on the unit sphere $B_1 = \{\boldsymbol{v}; |\boldsymbol{v}| = 1\}$ are given by the eigenvectors of $\overline{\boldsymbol{A}}$. Since $\overline{\boldsymbol{L}}$ is a two-dimensional matrix, there can only be two stationary points which have to belong to minimum and maximum.

C.3. The Monge-Representation

The *Monge-representation* is a special form of the surface parameterization $\boldsymbol{X}$ which describes the surface S by an orthogonal projection onto a flat plane:

$$\boldsymbol{X} = (x, y, h(x, y)), \tag{C.3.1}$$

where $h(x, y)$ describes the elevation of S from the xy-plane at every point. It can be shown that for any differentiable, orientable surface S with linear independent tangent vectors, there exists a local Monge-representation for an open neighborhood of every point on S [123]. The differential geometric quantities take a simple form in Monge-representation, which makes it useful for applications. Furthermore, it enables the use of Fourier-transforms to treat analytical problems. We list expressions of differential geometric quantities and some lowest order approximations.

$$\boldsymbol{t}_1 = (1, 0, \partial_x h), \boldsymbol{t}_2 = (0, 1, \partial_y h), \boldsymbol{n} = \frac{(-\partial_x h, -\partial_y h, 1)}{\sqrt{1 + |\nabla h|^2}}, \tag{C.3.2}$$

$$\overline{\boldsymbol{g}} = \begin{pmatrix} 1 + (\partial_x h)^2 & \partial_x h \partial_y h \\ \partial_x h \partial_y h & 1 + (\partial_y h)^2 \end{pmatrix}, \overline{\boldsymbol{g}}^{-1} = \frac{1}{\det \overline{\boldsymbol{g}}} \begin{pmatrix} 1 + (\partial_y h)^2 & -\partial_x h \partial_y h \\ -\partial_x h \partial_y h & 1 + (\partial_x h)^2 \end{pmatrix}, \tag{C.3.3}$$

$$\det \overline{\boldsymbol{g}} = 1 + |\nabla h|^2, \tag{C.3.4}$$

$$dA = \sqrt{\det \overline{\boldsymbol{g}}} dxdy = \left(1 + \frac{1}{2} |\nabla h|^2 + \mathcal{O}\left(|\nabla h|^4\right)\right) dxdy \lessapprox \left(1 + \frac{1}{2} |\nabla h|^2\right) dxdy, \tag{C.3.5}$$

$$\overline{\boldsymbol{K}} = (K_{ij}) = \left(\frac{\partial_i \partial_j h}{1 + |\nabla h|^2}\right) = \frac{\operatorname{Hess} h}{\det \overline{\boldsymbol{g}}}, \tag{C.3.6}$$

$$H = \frac{\partial_{xx} h \left(1 + (\partial_y h)^2\right) + \partial_{yy} h \left(1 + (\partial_x h)^2\right) - 2 \partial_x h \partial_y h \partial_{xy} h}{\left(1 + |\nabla h|^2\right)^{\frac{3}{2}}} = \nabla \cdot \frac{\nabla h}{\sqrt{1 + |\nabla h|^2}}, \tag{C.3.7}$$

$$H = \Delta h + \mathcal{O}\left(|\nabla h|^2\right) \approx \Delta h, \tag{C.3.8}$$

$$G = \frac{\partial_{xx} h \partial_{yy} h - (\partial_{xy} h)^2}{\left(1 + |\nabla h|^2\right)^2} = \frac{\det \operatorname{Hess} h}{(\det \overline{\boldsymbol{g}})^2}, G = \det \operatorname{Hess} h + \mathcal{O}\left(|\nabla h|^2\right) \approx \det \operatorname{Hess} h. \tag{C.3.9}$$

Note that on the rightmost side of eq. (C.3.5), the lowest order approximation provides an upper bound of $\sqrt{\det \overline{\boldsymbol{g}}}$ due to $(1 + x)^n \leq 1 + nx$ for all $|x| < 1$. Throughout this work, the discrete Fourier-transform for a membrane with square projected area $U = [0, L]^2$ is defined with respect to the Monge-representation via

$$\begin{aligned} h(\boldsymbol{x}) &= \langle h \rangle_x + \frac{1}{L} \sum_{\boldsymbol{k} \neq \boldsymbol{0}} h_{\boldsymbol{k}} \exp(i\boldsymbol{kx}), \\ \langle h \rangle_x &= \frac{1}{L^2} \int_U h \, dxdy \\ h_{\boldsymbol{k}} &= \frac{1}{L} \int_U h \exp(-i\boldsymbol{kx}) \, dxdy, \text{ for } \boldsymbol{k} \neq \boldsymbol{0}, \end{aligned} \tag{C.3.10}$$

with $\boldsymbol{x} = (x, y) \in U$ and $\boldsymbol{k} = (k_x, k_y) \in \frac{2\pi}{L}\mathbb{Z}^2$. The brackets $\langle \cdot \rangle_x$ denote the spatial average over the projected area. Forth and back transformation follow by virtue of the orthogonality relation

$$\int_U \exp\left(i\left(\boldsymbol{k} - \boldsymbol{k'}\right)\boldsymbol{x}\right) dxdy = L^2 \delta_{\boldsymbol{k},\boldsymbol{k'}}. \tag{C.3.11}$$

Transforms of other quantities dependent on the projected coordinates x, y are defined likewise.

C.4. The Theorem of Gauss-Bonnet

The theorem of Gauss-Bonnet is a remarkable result of differential geometry which links the Gaussian curvature G with a property of the outer geometry of S, the *genus* g_S. The genus of a closed, orientable surface S is the number of cuts along disjunct closed space curves $\boldsymbol{\gamma}$ on S such that the remaining surface $\tilde{S} = S - \operatorname{Im} \boldsymbol{\gamma}$ is still connected (i.e. there is no point on $\tilde{S}$ from which one cannot reach all other points by walking on $\tilde{S}$). Illustratively, the genus is the number of "handles" of S (see fig. C.2). The theorem of Gauss-Bonnet states that for any closed, compact, orientable surface S

$$\int_S G dA = 2\pi (2 - 2g_S). \tag{C.4.1}$$

Hence, the surface integral of the Gaussian curvature can be calculated by simply counting the handles of S. Furthermore, the integral of G over S stays constant under all transformations of S which do not alter its genus, e.g. if we stretch or twist S into another shape. The quantity in parenthesis on the right-hand side of eq. C.4.1 is also referred to as the *Euler-characteristic* χ_S of S. The Euler-characteristic χ_S occurs in a variety of topological contexts and enables us to generalize the Gauss-Bonnet theorem to *non-closed* surfaces. Apart from being related with the "number of handles" g_S, the Euler-characteristic χ_S plays an important role in the classification of *triangulations* of surfaces. To avoid technical details in the definition of surface triangulations, we reside on a lay term understanding as illustrated in fig. C.2: a triangulation is a decomposition of S into triangles such that every part of S is covered by the triangles. We denote the number of faces, edges and vertices of a triangulation of S by F, E and V, one can show that [124]

$$\chi_S = V - E + F \tag{C.4.2}$$

independent of the triangulation. In particular, eq. (C.4.2) holds also for triangulations of non-closed surfaces S with a piecewise differentiable boundary curve $\boldsymbol{\gamma}_S$. The generalized

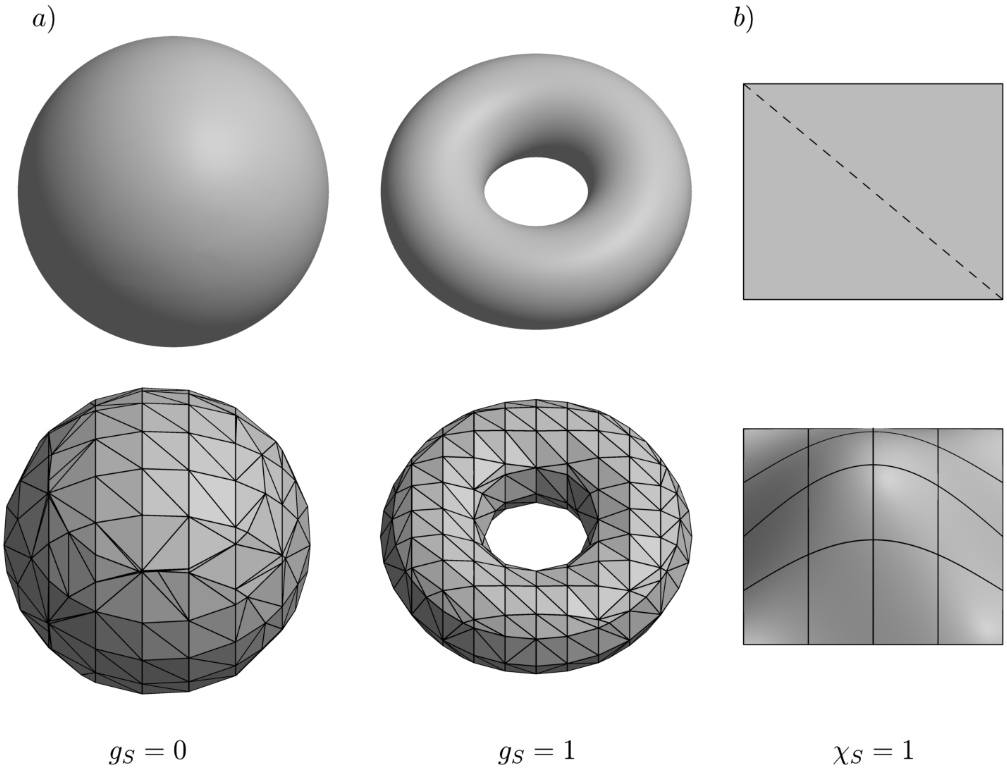

FIGURE C.2. **a)** The genus g_S of a closed, orientable surface S can be interpreted as the number of "handles" of S. Therefore, a sphere has genus zero and a torus genus one. The genus is related to the Euler-characteristic $\chi_S = 2 - 2g_S$ which, in turn, is related to a surface triangulation of S via eq. C.4.2. **b)** A square may simply be triangulated by drawing its diagonal. Hence, it has the Euler-characteristic $\chi_S = 4 - 5 + 2 = 1$. If the square is deformed, similarly to a glassblower forming a vase, the Euler-characteristic does not change.

Gauss-Bonnet theorem for non-closed surfaces reads then

$$\int_S G dA + \int_{\mathrm{Im}\,\boldsymbol{\gamma}_S} \boldsymbol{n} \cdot \left(\frac{d\boldsymbol{\gamma}_S}{ds} \times \frac{d^2\boldsymbol{\gamma}_S}{ds^2} \right) ds + \sum_i \Theta_i = 2\pi\chi_S, \tag{C.4.3}$$

where the Θ_i denote the jump angles of the tangent vectors at the non-differentiable points of $\boldsymbol{\gamma}_S$. The second term on the left-hand side is an integral over the *geodesic curvature* of $\boldsymbol{\gamma}_S$ which can be interpreted as the part of the curvature in normal direction of the surface S. The charm in the application of the Gauss-Bonnet theorem lies in the connection of the outer geometric quantity G with the topological indices g_S and χ_S which remain unchanged under

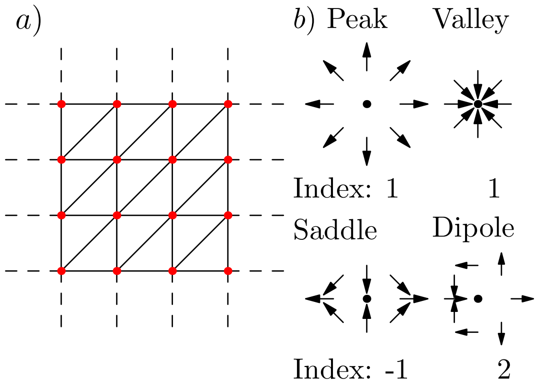

FIGURE C.3. **a)** A regular triangulation of the plane with six-fold symmetry. **b)** The index of a vector field $\boldsymbol{v}$ in a zero-crossing s_0 determines its local shape. If we interpret $\boldsymbol{v}$ as the gradient of a scalar function f, the index defines the behavior of f in its stationary points, e.g. whether s_0 is a local extremum or saddle point. An index of two corresponds to a dipole field.

deformations like stretching or twisting, as long as we do not tear S apart or glue different parts of S together.

For example, consider a simple square which we decompose into two triangles (see fig. C.2). Its Euler-characteristic is $\chi_S = 4 - 5 + 2 = 1$, consistent with eq. (C.4.3) where only the sum over the jump angles $\sum_i \Theta_i = 2\pi$ is non-zero on the left-hand side. Imagine the square is made of some plastic material and we deform it into another shape S while keeping the square boundary curve $\boldsymbol{\gamma}_S$ fixed (similar to a glassblower forming a vase from molten glass). Since χ does not change under such a deformation and the boundary curve yields the same contribution $\sum_i \Theta_i = 2\pi$ as before, we follow that $\int_S G dA$ vanishes.

Another useful application of the Gauss-Bonnet theorem arises in the analysis of *defects* of surface triangulations. Here, we consider the task of triangulating a surface with a desirably regular pattern of triangles, such that every vertex has more or less the same amount of connecting edges. For example, an infinite plane may be triangulated with a regular pattern where every vertex is connected to exactly six other vertices (see fig. C.3). Can we triangulate a sphere or a torus in the same manner? In this context, a defect is every vertex which is not sixfold connected. To investigate this question, we triangulate S by a number V_6 of six-fold connected vertices and a number V_x of vertices with unknown connectivity x such that $V = V_6 + V_x$. Since every edge is shared by two vertices, it is $2E = 6V_6 + xV_x$. Furthermore, for a closed surface without a boundary curve, every edge is exactly part of two faces such that $3F = 2E$. Insertion into the definition (C.4.2) of χ_S results in

$$\chi_S = V_x \left(1 - \frac{x}{6}\right) . \tag{C.4.4}$$

Since $V_x \in \mathbb{N}$ and $\chi_S \in \mathbb{Z}$ in above equation, it can only be fulfilled for certain numbers x and V_x. For example, for a sphere it is $\chi_S = 2$ and hence we cannot set $V_x = 0$, therefore a triangulation with only sixfold connected vertices is not possible. However, if we try $x = 4$ or $x = 5$ we conclude from equation (C.4.4) that $V_4 = 6$ four-fold connected or $V_5 = 10$ five-fold connected defects suffice for a triangulation of the sphere. We conclude this section with another interesting interpretation of the Euler-characteristic in the context of *tangential vector fields* on surfaces. A tangential vector field $\boldsymbol{v}$ is a function $\boldsymbol{v} : S \to \mathbb{R}^3$ such that at every point $s \in S$ the vector $\boldsymbol{v}(s)$ is inside the tangent space T_s of S in s. For example, we may think of $\boldsymbol{v}$ as the tangential component of a fluid flow field around S. The Euler-characteristic is closely connected to differentiable, tangential vector fields with *isolated* zero-crossings, i.e. for every zero crossing $s_0 \in S$ with $\boldsymbol{v}(s) = \boldsymbol{0}$ it is $\boldsymbol{v}(r) \neq \boldsymbol{0}$ for all r in an open neighborhood of s_0. For those, we define a quantity called the *index* of $\boldsymbol{v}$ in s_0. Consider a small disk

$D_\epsilon(s_0) \subset S$ around s_0. Since s_0 is an isolated zero crossing, the unit-vector-field $\boldsymbol{w} = \boldsymbol{v}/|\boldsymbol{v}|$ is well defined on $D_\epsilon(s_0) - s_0$ if we choose ϵ small enough. Moreover, it can be shown that every continuous unit vector field defined on the boundary ∂D_ϵ of a disk can be represented by a unique, continuous function $\varphi(t) : [0, 2\pi] \to \mathbb{R}$ such that $\boldsymbol{w} = (\cos\varphi(t), \sin\varphi(t))$ [123]. As $\boldsymbol{w}$ is continuous, it is especially $\boldsymbol{w}(0) = \boldsymbol{w}(2\pi)$ and hence

$$\varphi(2\pi) - \varphi(0) = 2\pi k \tag{C.4.5}$$

for an integer number $k \in \mathbb{Z}$, the *index* of $\boldsymbol{v}$ in s_0. The index counts how many times the vector $\boldsymbol{v}$ performs a full rotation around s_0 (see fig C.3). If we number all zero-crossings $s_{0,i}$ and their corresponding indices k_i, then it can be shown that the Euler-characteristic is identical to the sum over all k_i [123]:

$$\chi_S = \sum_i k_i. \tag{C.4.6}$$

Thus, the local behavior of $\boldsymbol{v}$ around its zero-crossings and the topology of S are deeply connected.

APPENDIX D

Deformation of Elastic Substrate

We calculate the deformation energy E_{subs} of a linear elastic, half-infinite substrate, deformed by a membrane attached to its free surface (see fig. 4.2). In particular, we derive eq. (4.1.4) for the form of the substrate energy

$$E_{subs} = \widehat{E} \sum_{\boldsymbol{k}} k \left| h_{\boldsymbol{k}} \right|^2 \tag{D.1}$$

and calculate the value of the effective elasticity modulus $\widehat{E}$. Let $U = [0, L]^2 \subset \mathbb{R}^2$ be the initial flat state of our plate in the xy-plane. We suppose the linear elastic medium extends into the half-space $(x, y, z) \in U \times \mathbb{R}^+$. Moreover, we assume (1) that the plate sticks always on top of the medium and never detaches at any point and (2) that at the boundary between plate and medium, displacements tangential to the plate are negligible such that the displacement vector of the medium at $z = 0$ reads

$$\boldsymbol{u}(x, y, z = 0) = (0, 0, h(x, y))\,. \tag{D.2}$$

An energy quadratic in the plate undulation h

$$E_{harm} = \frac{a}{2} \int_U h^2 dx dy, \tag{D.3}$$

has been suggested by Emil Winkler [125] to describe the energetic contribution of an elastic foundation. Correspondingly, an elastic foundation with a linear relation between normal pressure and undulation

$$P = ah, \tag{D.4}$$

is called a *Winkler* support. It is by far the simplest model and assumes that the medium deformation at some point of its surface is proportional to the pressure between the plate and the medium [126]. For a plate allowed to float along the tangential surface this assumption is to some extent correct, however in case of a coherent attached plate the Winkler support provides only crude results. To refine the description, it is necessary to solve the problem of the equilibrium configuration of a linear elastic medium subject to the boundary condition (D.2) at its upper surface. The solution of a kind of inverse problem, the deformation of a linear elastic substrate subject to a given *surface stress* $\boldsymbol{P}(x, y)$, can be found in ref. [55].

The solution is given by the Cerruti-Boussinesq-Greens-tensor

$$\overline{\boldsymbol{G}}_{cb}\big(x-x',y-y',z\big) = \frac{1+\sigma}{2\pi E}\begin{pmatrix} \frac{\left(z^2+2r(z+\sigma r)\right)x^2}{r^3(z+r)^2}+\frac{z+2(1-\sigma)r}{r(z+r)} & \frac{xy\left(z^2+2r(z+\sigma r)\right)}{r^3(z+r)^2} & x\left(\frac{z}{r^3}-\frac{1-2\sigma}{r(z+r)}\right) \\ \frac{xy\left(z^2+2r(z+\sigma r)\right)}{r^3(z+r)^2} & \frac{\left(z^2+2r(z+\sigma r)\right)y^2}{r^3(z+r)^2}+\frac{z+2(1-\sigma)r}{r(z+r)} & y\left(\frac{z}{r^3}-\frac{1-2\sigma}{r(z+r)}\right) \\ x\left(\frac{1-2\sigma}{r(z+r)}+\frac{z}{r^3}\right) & y\left(\frac{1-2\sigma}{r(z+r)}+\frac{z}{r^3}\right) & \frac{z^2}{r^3}+\frac{2(1-\sigma)}{r} \end{pmatrix}, \tag{D.5}$$

such that

$$\boldsymbol{u}(x,y,z) = \int_{\mathbb{R}^2} \overline{\boldsymbol{G}}_{cb}\big(x-x',y-y',z\big)\,\boldsymbol{P}\big(x',y'\big)\,dx'dy'. \tag{D.6}$$

Hence, a given surface stress determines the deformation of the medium. Note, however, that knowledge of the displacement vector $\boldsymbol{u}$ at the surface alone is not sufficient to pin-point the deformation in the medium, as we will see, further assumptions have to be made. We have to find the solution for strain tensor $\overline{\boldsymbol{u}}$ and stress tensor $\overline{\boldsymbol{\sigma}}$ for which the net force vanishes at every point, i.e.

$$\operatorname{div}\overline{\boldsymbol{\sigma}} = \boldsymbol{0}. \tag{D.7}$$

The substrate deformation energy density is then given by insertion of our solution into the general expression

$$e_{subs} = \sum_{ij}\frac{1}{2}\sigma_{ij}u_{ij} \tag{D.8}$$

For the calculation we need Hook's law for linear elastic media, given by [55]

$$\sigma_{ik} = \frac{E}{1+\sigma}\left(u_{ik}+\delta_{ik}\frac{\sigma}{1-2\sigma}\operatorname{tr}\overline{\boldsymbol{u}}\right), \tag{D.9}$$

$$u_{ik} = \frac{1}{E}\left((1+\sigma)\,\sigma_{ik}-\delta_{ik}\sigma\operatorname{tr}\overline{\boldsymbol{\sigma}}\right), \tag{D.10}$$

with

$$u_{ik} = \frac{1}{2}\left(\frac{\partial u_i}{\partial x_k}+\frac{\partial u_k}{\partial x_i}\right). \tag{D.11}$$

Insertion of eqns. (D.9)-(D.11) into eq. (D.7) leads to the equilibrium condition in terms of the deformation vector $\boldsymbol{u}$:

$$(1-2\sigma)\,\Delta\boldsymbol{u}+\operatorname{grad}\operatorname{div}\boldsymbol{u} = \boldsymbol{0}, \tag{D.12}$$

or, equivalently, expressed with stress tensor components

$$(1+\sigma)\,\Delta\sigma_{ij}+\frac{\partial^2\operatorname{tr}\overline{\boldsymbol{\sigma}}}{\partial x_i\partial x_j} = 0. \tag{D.13}$$

For the following analysis, we recall the definition of the discrete Fourier-Transform of the height h over the square $U = [0, L]^2$

$$\begin{aligned} h(\boldsymbol{x}) &= \langle h \rangle_x + \frac{1}{L} \sum_{\boldsymbol{k} \neq \boldsymbol{0}} h_{\boldsymbol{k}} \exp\left(i \boldsymbol{k} \boldsymbol{x}\right), \\ \langle h \rangle_x &= \frac{1}{L^2} \int_U h \, dxdy \\ h_{\boldsymbol{k}} &= \frac{1}{L} \int_U h \exp\left(-i \boldsymbol{k} \boldsymbol{x}\right) dxdy, \ \text{ for } \boldsymbol{k} \neq \boldsymbol{0}, \end{aligned} \tag{D.14}$$

and the corresponding orthogonality relation

$$\int_U \exp\left(i\left(\boldsymbol{k} - \boldsymbol{k'}\right) \boldsymbol{x}\right) dxdy = L^2 \delta_{\boldsymbol{k},\boldsymbol{k'}}. \tag{D.15}$$

In our coordinate system it is $\langle h \rangle_x = 0$ as we do not consider translations of the membrane as a whole.

D.1. Deformation by Single Plane Wave

We start with the investigation of the effect of a single plane wave undulation

$$\boldsymbol{u}(x, y, z = 0) = \frac{h_{\boldsymbol{k}}}{L} \exp\left(i \boldsymbol{k} \boldsymbol{x}\right) \tag{D.1.1}$$

on the medium. Afterwards, we try to find the solution for the complete set of modes by linear superposition. Note, however, that decomposition of the deflection h into periodic Fourier-modes implies that the deformation is not limited to $U = [0, L]^2$, instead it continues periodically in the xy-plane.

Let the x-axis of our coordinate system be parallel to the wavevector such that $\boldsymbol{k}\boldsymbol{x} = kx$ with $k = |\boldsymbol{k}| = \sqrt{k_x^2 + k_y^2}$. As the equilibrium equations (D.12) for the three unknowns u_x, u_y, u_z are of second order, we see that we need $2 \cdot 3 = 6$ boundary conditions in order to completely define the problem. Apart from the three boundary conditions at the surface, eq. (D.2), it is intuitive to demand that the shear deformations u_{xy} and u_{zy} vanish, as the imposed plane wave undulation has no y-component. From $u_{xy} = 0 = u_{zy}$ and eq. (D.9) follows that the corresponding shear stress components vanish as well $\sigma_{xy} = 0 = \sigma_{zy}$. As a last boundary condition we can demand that either the strain u_{yy} or the stress σ_{yy} perpendicular to the wavevector $\boldsymbol{k}$ vanish, but not both at once. Both assumptions lead to very similar results such that we deem the question which one to use of lesser importance [127]. We set in the following $u_{yy} = 0$, the calculation for $\sigma_{yy} = 0$ can be found in ref. [128]. The resulting problem belongs to the category of *plane deformations* as all non-vanishing strain components are in the xz-plane. Particularly suited for this kind of problems is the approach via a scalar *stress function* χ which has to satisfy [55]

$$\Delta \Delta \chi = 0, \tag{D.1.2}$$

and is connected with the remaining stress components via

$$\sigma_{xx} = \frac{\partial^2 \chi}{\partial z^2}, \, \sigma_{xz} = -\frac{\partial^2 \chi}{\partial x \partial z}, \, \sigma_{zz} = \frac{\partial^2 \chi}{\partial x^2}, \, \sigma_{yy} = \sigma \left(\frac{\partial^2 \chi}{\partial z^2} + \frac{\partial^2 \chi}{\partial x^2} \right) = \sigma \left(\sigma_{xx} + \sigma_{zz} \right). \tag{D.1.3}$$

The equilibrium equation in terms of χ, eq. (D.1.2), can be solved in Cartesian coordinates by a separation approach of the form $\chi = X(x)Z(z)$. We skip this calculation here and state directly the solution [127]:

$$\chi = A\left(1/k - Bz\right)\frac{h_{\boldsymbol{k}}}{L}\exp\left(ikx - kz\right), \tag{D.1.4}$$

with

$$A = \frac{-2E\left(1-\sigma\right)}{\left(1+\sigma\right)\left(4\sigma-3\right)},\; B = -\frac{1}{1-\sigma}. \tag{D.1.5}$$

To avoid later confusion, we denote the stress tensor of this single-wavevector undulation by $\overline{\boldsymbol{\varsigma}} = (\varsigma_{ij})$, a different typeset of the Greek letter σ. The stress components follow according to eqns. (D.1.3) to

$$\begin{aligned}
\varsigma_{xx}(x,z,k) &= Ak\left(1+2B-Bkz\right)\frac{h_{\boldsymbol{k}}}{L}\exp\left(ikx-kz\right) &&= q_{xx}(z,k)\,\frac{h_{\boldsymbol{k}}}{L}\exp\left(ikx\right),\\
\varsigma_{xz}(x,z,k) &= iAk\left(1+B-Bkz\right)\frac{h_{\boldsymbol{k}}}{L}\exp\left(ikx-kz\right) &&= q_{xz}(z,k)\,\frac{h_{\boldsymbol{k}}}{L}\exp\left(ikx\right),\\
\varsigma_{zz}(x,z,k) &= -Ak\left(1-Bkz\right)\frac{h_{\boldsymbol{k}}}{L}\exp\left(ikx-kz\right) &&= q_{zz}(z,k)\,\frac{h_{\boldsymbol{k}}}{L}\exp\left(ikx\right),\\
\varsigma_{yy}(x,z,k) &= 2AB\sigma k\frac{h_{\boldsymbol{k}}}{L}\exp\left(ikx-kz\right) &&= q_{yy}(z,k)\,\frac{h_{\boldsymbol{k}}}{L}\exp\left(ikx\right),
\end{aligned} \tag{D.1.6}$$

where we defined the prefactors q_{xx}, q_{xz}, q_{zz} and q_{yy} to abbreviate the expressions. In particular, the plate needs to exert the lateral stress $\varsigma_{zz}(z=0)$ onto the medium in order to sustain the deformation. Note that the stress tensor is directly proportional to the specified undulation $\overline{\boldsymbol{\varsigma}} \propto u_z(z=0)$. If we interpret the factors q_{ij} as the non-vanishing components of a symmetric matrix $\overline{\boldsymbol{q}}$, we can write

$$\overline{\boldsymbol{\varsigma}} = \overline{\boldsymbol{q}}\; u_z(z=0)\,. \tag{D.1.7}$$

We conclude this section with an outline of the derivation of the deformation vector $\boldsymbol{u}$. With the solution for the stress components σ_{ij}, the corresponding strains u_{ij} follow directly from Hook's law. To calculate the deformation vector $\boldsymbol{u}$, we make use of the relations eqns. D.11, starting with the calculation of u_z via

$$u_z(x,y,z) = u_z(x,y,z=0) + \int_0^z \frac{\partial u_z}{\partial z}(x,y,z')\,dz' = u_z(x,y,z=0) + \int_0^z u_{zz}(x,y,z')\,dz', \tag{D.1.8}$$

the remaining components follow likewise.

D.2. Deformation by Arbitrary Wavepattern

We turn to the solution of the problem for a general form of the plate, i.e. we impose

$$\boldsymbol{u}(x,y,z=0) = (0,0,\frac{1}{L}\sum_{\boldsymbol{k}\neq\boldsymbol{0}} h_{\boldsymbol{k}}\exp\left(i\boldsymbol{k}\boldsymbol{x}\right)). \tag{D.2.1}$$

We start with the observation that we can solve the problem separately for every wavevector $\boldsymbol{k}$ if we change the coordinate system by rotation around the z-axis such that the new x'-axis is again parallel to $\boldsymbol{k}$, i.e. $\boldsymbol{e}_{x'} \parallel \boldsymbol{k}$. In the coordinates (x',y',z') the problem reduces again to a plane deformation with the solution for the stresses $\sigma_{x'x'}, \sigma_{x'z'} \ldots$ etc. given by eqns. (D.1.6). As all equations are linear we can use the principle of superposition: we solve the plane deformation problem like this separately for every wavevector $\boldsymbol{k}$ and sum up all solutions at the end to get the solution for the problem with all wavevectors. However, as the coordinate system (x', y', z') in which we can re-use our obtained plane deformation solution is different for every wavevector, care has to be taken on how we transform the solutions for the stress tensor back from the (x', y', z') coordinate systems to our lab coordinate system (x, y, z). The rotation angle α to rotate the lab coordinates into the (x', y', z') coordinates and the wavevector $\boldsymbol{k}$ are connected via

$$\begin{aligned} c_\alpha &= \cos\alpha = \frac{k_x}{k}, \\ s_\alpha &= \sin\alpha = \frac{k_y}{k}, \end{aligned} \tag{D.2.2}$$

and the coordinate system base vectors are related by

$$\begin{aligned} \boldsymbol{e}_{x'} &= c_\alpha \boldsymbol{e}_x + s_\alpha \boldsymbol{e}_y & \boldsymbol{e}_x &= c_\alpha \boldsymbol{e}_{x'} - s_\alpha \boldsymbol{e}_{y'} \\ \boldsymbol{e}_{y'} &= -s_\alpha \boldsymbol{e}_x + c_\alpha \boldsymbol{e}_y & \boldsymbol{e}_y &= s_\alpha \boldsymbol{e}_{x'} + c_\alpha \boldsymbol{e}_{y'}. \\ \boldsymbol{e}_{z'} &= \boldsymbol{e}_z, \end{aligned} \tag{D.2.3}$$

For the product $\boldsymbol{kx}$ holds $\boldsymbol{kx} = k_x x + k_y y = kx' = \boldsymbol{k}'\boldsymbol{x}'$. The correct transformation of the stress tensor is intuitively derived with the general definition of the tensor component σ_{ij}

$$\sigma_{ij} = \boldsymbol{e}_i \cdot (\overline{\boldsymbol{\sigma}} \boldsymbol{e}_j), \tag{D.2.4}$$

which is valid for any orthonormal basis $\{\boldsymbol{e}_i\}$. For example for the component σ_{xx}:

$$\begin{aligned} \sigma_{xx} = (\overline{\boldsymbol{\sigma}} \boldsymbol{e}_x) \cdot \boldsymbol{e}_x &= \big(\overline{\boldsymbol{\sigma}} \cdot \big(c_\alpha \boldsymbol{e}_{x'} - s_\alpha \boldsymbol{e}_{y'}\big)\big) \cdot \big(c_\alpha \boldsymbol{e}_{x'} - s_\alpha \boldsymbol{e}_{y'}\big) \\ &= c_\alpha^2 \sigma_{x'x'} - \cancel{2 s_\alpha c_\alpha \sigma_{x'y'}} + s_\alpha^2 \sigma_{y'y'} \\ &= c_\alpha^2 \sigma_{x'x'} + s_\alpha^2 \sigma_{y'y'}, \end{aligned} \tag{D.2.5}$$

where we used in the second row that the shear stress $\sigma_{x'y'}$ vanishes. Analogously follow the transformations for the remaining components to

$$\begin{aligned} \sigma_{yy} &= s_\alpha^2 \sigma_{x'x'} + c_\alpha^2 \sigma_{y'y'} & \sigma_{xy} &= s_\alpha c_\alpha \left(\sigma_{x'x'} - \sigma_{y'y'}\right) \\ \sigma_{zz} &= \sigma_{z'z'} & \sigma_{xz} &= c_\alpha \sigma_{x'z'} \\ & & \sigma_{yz} &= s_\alpha \sigma_{x'z'}. \end{aligned} \tag{D.2.6}$$

We can now write down the solution for an arbitrary boundary condition of the form eq. (D.2.1) by summation over all single-wavevector contributions given by eqns. (D.1.6):

$$\begin{aligned}
\sigma_{xx} &= \sum_{\boldsymbol{k}} \frac{1}{k^2}\left(k_x^2 \varsigma_{xx}(x', z, k) + k_y^2 \varsigma_{yy}(x', z, k)\right), \\
\sigma_{xy} &= \sum_{\boldsymbol{k}} \frac{k_x k_y}{k^2}\left(\varsigma_{xx}(x', z, k) - \varsigma_{yy}(x', z, k)\right) \\
\sigma_{yy} &= \sum_{\boldsymbol{k}} \frac{1}{k^2}\left(k_y^2 \varsigma_{xx}(x', z, k) + k_x^2 \varsigma_{yy}(x', z, k)\right), \\
\sigma_{xz} &= \sum_{\boldsymbol{k}} \frac{k_x}{k} \varsigma_{xz}(x', z, k), \\
\sigma_{zz} &= \sum_{\boldsymbol{k}} \varsigma_{zz}(x', z, k), \\
\sigma_{yz} &= \sum_{\boldsymbol{k}} \frac{k_y}{k} \varsigma_{xz}(x', z, k).
\end{aligned} \tag{D.2.7}$$

Note that the single-wavevector solutions have to be taken at $x' = (k_x x + k_y y)/k$. From eqns. (D.2.7) and eq. D.1.7 we see that the stress tensor $\overline{\boldsymbol{\sigma}}$ can be written as a convolution over the discrete set of wavevectors:

$$\overline{\boldsymbol{\sigma}} = \frac{1}{L} \sum_{\boldsymbol{k} \neq \boldsymbol{0}} \overline{\boldsymbol{Q}}(z, \boldsymbol{k})\, h_{\boldsymbol{k}} \exp(i \boldsymbol{k x}), \tag{D.2.8}$$

with

$$\overline{\boldsymbol{Q}} = \begin{pmatrix} \frac{1}{k^2}\left(k_x^2 q_{xx} + k_y^2 q_{yy}\right) & \frac{k_x k_y}{k^2}\left(q_{xx} - q_{yy}\right) & \frac{k_x}{k} q_{xz} \\ \frac{k_x k_y}{k^2}\left(q_{xx} - q_{yy}\right) & \frac{1}{k^2}\left(k_y^2 q_{xx} + k_x^2 q_{yy}\right) & \frac{k_y}{k} q_{xz} \\ \frac{k_x}{k} q_{xz} & \frac{k_y}{k} q_{xz} & q_{zz} \end{pmatrix}, \tag{D.2.9}$$

and the q_{ij} evaluated at (z, k).

D.3. Energy of Deformed Support

We express the substrate energy density e_{subs}, given by eq. (D.8), as a function of the stress components σ_{ij} by insertion of Hook's law eq. (D.9):

$$e_{subs} = \sum_{ij} \frac{\sigma_{ij}}{2} \frac{1}{E}\left((1+\sigma)\sigma_{ij} - \delta_{ij} \sigma \operatorname{tr} \overline{\boldsymbol{\sigma}}\right) = \frac{1+\sigma}{2E}\left(\sum_{ij} \sigma_{ij}\sigma_{ij}\right) - \frac{\sigma}{2E} \operatorname{tr}(\overline{\boldsymbol{\sigma}})^2. \tag{D.3.1}$$

To analyze the net deformation energy, we assume that the deformation D.2.1 only contains functions of periodicity L and integrate the energy density e_{subs} over an in z-direction infinite column with square cross section of length L,

$$E_{subs} = \int_0^\infty dz \int_0^L dx \int_0^L dy \left\{ \frac{1+\sigma}{2E}\left(\sum_{ij} \sigma_{ij}\sigma_{ij}\right) - \frac{\sigma}{2E} \operatorname{tr}(\overline{\boldsymbol{\sigma}})^2 \right\}. \tag{D.3.2}$$

By rewriting the energy density contributions with the form eq. D.2.8 of the stress tensor

$$\sigma_{ij}\sigma_{mn} = \frac{1}{L^2} \sum_{\boldsymbol{k},\boldsymbol{k}' \neq \boldsymbol{0}} Q_{ij}(z,\boldsymbol{k})\, Q_{mn}\big(z,\boldsymbol{k}'\big)\, h_{\boldsymbol{k}} h_{\boldsymbol{k}'} \exp\big(i\left(\boldsymbol{k}+\boldsymbol{k}'\right)\boldsymbol{x}\big)\,, \tag{D.3.3}$$

we see that the orthogonal undulation modes decouple in the deformation energy. Hence, it is sufficient to calculate the energy contribution of a single wave undulation and summing over all wavemodes. This results in the net free energy

$$E_{subs} = \widehat{E} \sum_{\boldsymbol{k}} k \left|h_{\boldsymbol{k}}\right|^2, \tag{D.3.4}$$

with

$$\widehat{E} = E \frac{2\sigma^2 - 10\sigma + 5}{2\left(4\sigma - 3\right)^2\left(\sigma + 1\right)}. \tag{D.3.5}$$

APPENDIX E

Buckling Dynamics in Small Angle Limit

Phase Angle Dynamics - Fluctuation Spectra - Hydrodynamic Interactions

We broaden the discussion of buckling instabilities in sections 4.1.3-4.2 by (1) inclusion of the phase angle $\varphi_{\boldsymbol{k}}$ dynamics for non-vanishing spontaneous curvature C_0, (2) derivation of relations between amplitude fluctuations and bending rigidity as well as phase angle fluctuations and spontaneous curvature and (3) investigation of the effect of hydrodynamic interactions on the buckling behavior of a membrane embedded in a Newtonian fluid.

E.1. Phase Angle Dynamics and Spontaneous Curvature

For a non-vanishing spontaneous curvature $C_0 = C_0(\boldsymbol{x}) \neq 0$, we recall its Fourier transform

$$\begin{aligned} C_0(\boldsymbol{x}) &= \langle C_0 \rangle_x + \frac{1}{L} \sum_{\boldsymbol{k} \neq \boldsymbol{0}} C_{0,\boldsymbol{k}} \exp\left(i\boldsymbol{k}\boldsymbol{x}\right), \\ \langle C_0 \rangle_x &= \frac{1}{L^2} \int_U C_0 dxdy \\ C_{0,\boldsymbol{k}} &= \frac{1}{L} \int_U C_0 \exp\left(-i\boldsymbol{k}\boldsymbol{x}\right) dxdy = \lambda_{\boldsymbol{k}} \exp\left(i\theta_{\boldsymbol{k}}\right), \text{ for } \boldsymbol{k} \neq \boldsymbol{0}. \end{aligned} \tag{E.1.1}$$

For spatially constant surface tension, the total energy in eq. (4.1.7) becomes

$$\mathcal{V} = \sum_{\boldsymbol{k} \in \text{⬒}} \left(\kappa k^4 + \langle \gamma \rangle_x k^2 + \widehat{E} k \right) r_{\boldsymbol{k}}^2 + 2\kappa k^2 \lambda_{\boldsymbol{k}} r_{\boldsymbol{k}} \cos\left(\varphi_{\boldsymbol{k}} - \theta_{\boldsymbol{k}}\right). \tag{E.1.2}$$

Together with the kinetic energy from eq. (4.1.24) follow the Lagrangian equations of motion (4.1.19) to

$$\begin{aligned} 0 &= \varrho_m \ddot{r}_{\boldsymbol{k}} - \varrho_m r_{\boldsymbol{k}} \dot{\varphi}_{\boldsymbol{k}}^2 + \left(\kappa k^4 + \langle \gamma \rangle_x k^2 + \widehat{E} k \right) r_{\boldsymbol{k}} + \kappa k^2 \lambda_{\boldsymbol{k}} \cos\left(\varphi_{\boldsymbol{k}} - \theta_{\boldsymbol{k}}\right) + \nu \dot{r}_{\boldsymbol{k}}, \\ 0 &= \varrho_m r_{\boldsymbol{k}}^2 \ddot{\varphi}_{\boldsymbol{k}} + 2\varrho_m r_{\boldsymbol{k}} \dot{r}_{\boldsymbol{k}} \dot{\varphi}_{\boldsymbol{k}} - \kappa k^2 \lambda_{\boldsymbol{k}} r_{\boldsymbol{k}} \sin\left(\varphi_{\boldsymbol{k}} - \theta_{\boldsymbol{k}}\right) + \nu r_{\boldsymbol{k}}^2 \dot{\varphi}_{\boldsymbol{k}}. \end{aligned} \tag{E.1.3}$$

From eqns. (E.1.3) we see that the spontaneous curvature term proportional to $\lambda_{\boldsymbol{k}}$ leads to coupling of amplitudes $r_{\boldsymbol{k}}$ and moduli $\varphi_{\boldsymbol{k}}$. To analyze the role of spontaneous curvature for the $\varphi_{\boldsymbol{k}}$-dynamics, we recall the definition of the generalized momenta conjugated to $\varphi_{\boldsymbol{k}}$

$$p_{\boldsymbol{k}}^{\varphi} = \frac{\partial \mathcal{L}}{\partial \dot{\varphi}_{\boldsymbol{k}}} = 2\varrho_m r_{\boldsymbol{k}}^2 \dot{\varphi}_{\boldsymbol{k}}, \tag{E.1.4}$$

which we use to rewrite the second equation of eqns. (E.1.3) as

$$\frac{d}{dt} p_{\boldsymbol{k}}^{\varphi} = 2\kappa k^2 \lambda_{\boldsymbol{k}} r_{\boldsymbol{k}} \sin\left(\pi + \theta_{\boldsymbol{k}} - \varphi_{\boldsymbol{k}}\right) - \frac{\nu}{\varrho_m} p_{\boldsymbol{k}}^{\varphi}. \tag{E.1.5}$$

Thus, $p^{\varphi}_{\boldsymbol{k}}$ can be interpreted as the angular momentum related to rotate the wavemode $h_{\boldsymbol{k}}$ in complex space. Amplitude $r_{\boldsymbol{k}}$ and modulus $\varphi_{\boldsymbol{k}}$ are then length and angle coordinate of the "leaver" along the mode $h_{\boldsymbol{k}}$ is rotated. In this sense, the term

$$M_{\boldsymbol{k}} = 2\kappa k^2 \lambda_{\boldsymbol{k}} r_{\boldsymbol{k}} \sin\left(\pi + \theta_{\boldsymbol{k}} - \varphi_{\boldsymbol{k}}\right), \tag{E.1.6}$$

corresponds to a generalized torque with a constant force of magnitude $2\kappa k^2 \lambda_{\boldsymbol{k}}$, the phase angle $\theta_{\boldsymbol{k}} + \pi$ determines the direction of the force. The torque $M_{\boldsymbol{k}}$ vanishes as soon as $\varphi_{\boldsymbol{k}} = \theta_{\boldsymbol{k}} + \pi$, i.e. leaver and force are parallel. In this sense, the spontaneous curvature term yields a torque rotating the moduli $\varphi_{\boldsymbol{k}}$ until they are antiparallel to $\theta_{\boldsymbol{k}}$.

We conclude this section with a note about the corresponding real space dynamics. Without elastic substrate, the membrane dynamic equations in real space read [55]

$$\varrho_m \partial_{tt} h + \nu \partial_t h = \langle \gamma \rangle_x \Delta h - \kappa \Delta\Delta h + \kappa \Delta C_0. \tag{E.1.7}$$

We see that the spontaneous curvature acts effectively as a lateral pressure $P = \kappa \Delta C_0$ on the membrane. Note, however, that even for $\Delta C_0 = 0$ the spontaneous curvature may still enter in the boundary conditions if $C_0 \neq 0$, whereas only a lateral pressure $P \neq 0$ can enter the boundary conditions.

E.2. Amplitude and Phase Angle Fluctuations in the Planar State

To investigate thermal fluctuations of amplitudes $\{r_{\boldsymbol{k}}\}$ and phase angles $\{\varphi_{\boldsymbol{k}}\}$, we recall the equipartition theorem

$$\left\langle x_i \frac{\partial \mathcal{H}}{\partial x_j} \right\rangle = k_b T \delta_{ij}, \tag{E.2.1}$$

where the $x_i \in \{q_i, p_i\}$ denote the generalized coordinates and momenta, $\mathcal{H}\left(\{q_i\}, \{p_i\}\right) = \mathcal{T} + \mathcal{V}$ denotes the Hamiltonian of the system [129]. The generalized momenta are given by

$$p^{\varphi}_{\boldsymbol{k},} = \frac{\partial \mathcal{L}}{\partial \dot{\varphi}_{\boldsymbol{k}}} = 2\varrho_m r^2_{\boldsymbol{k}} \dot{\varphi}_{\boldsymbol{k}} \qquad \text{and} \qquad p^{r}_{\boldsymbol{k}} = \frac{\partial \mathcal{L}}{\partial \dot{r}_{\boldsymbol{k}}} = 2\varrho_m \dot{r}_{\boldsymbol{k}} \tag{E.2.2}$$

and the kinetic energy $\mathcal{T}$ in terms of the momenta reads

$$\mathcal{T} = \frac{1}{4\varrho_m} \sum_{\boldsymbol{k} \in ⬒} \left(p^{r}_{\boldsymbol{k}}\right)^2 + \frac{\left(p^{\varphi}_{\boldsymbol{k}}\right)^2}{r^2_{\boldsymbol{k}}}. \tag{E.2.3}$$

We assume that the surface tension equilibrates to a spatial constant value $\langle \gamma \rangle_x$. The moduli $\varphi_{\boldsymbol{k}}$ fluctuate then around the equilibrium values

$$\langle \varphi_{\boldsymbol{k}} \rangle = \theta_{\boldsymbol{k}} + \pi. \tag{E.2.4}$$

With eqns. (E.2.3) and (E.1.2), the partial derivatives $\frac{\partial \mathcal{H}}{\partial x_i}$ follow to

$$\begin{aligned}
\frac{\partial \mathcal{H}}{\partial r_{\boldsymbol{k}}} &= 2e(k)\, r_{\boldsymbol{k}} + 2\kappa k^2 \lambda_{\boldsymbol{k}} \cos\left(\varphi_{\boldsymbol{k}} - \theta_{\boldsymbol{k}}\right) - \frac{\left(p^{\varphi}_{\boldsymbol{k}}\right)^2}{2\varrho r^3_{\boldsymbol{k}}} \\
&= 2e(k)\, r_{\boldsymbol{k}} + 2\kappa k^2 \lambda_{\boldsymbol{k}} \cos\left(\varphi_{\boldsymbol{k}} - \theta_{\boldsymbol{k}}\right) - 2\varrho r_{\boldsymbol{k}} \dot{\varphi}^2_{\boldsymbol{k}}, \\
\frac{\partial \mathcal{H}}{\partial \varphi_{\boldsymbol{k}}} &= -2\kappa k^2 \lambda_{\boldsymbol{k}} r_{\boldsymbol{k}} \sin\left(\varphi_{\boldsymbol{k}} - \theta_{\boldsymbol{k}}\right), \\
\frac{\partial \mathcal{H}}{\partial p^r_{\boldsymbol{k}}} &= \frac{p^r_{\boldsymbol{k}}}{2\varrho} = \dot{r}_{\boldsymbol{k}}, \\
\frac{\partial \mathcal{H}}{\partial p^{\varphi}_{\boldsymbol{k}}} &= \frac{p^{\varphi}_{\boldsymbol{k}}}{2\varrho r^2_{\boldsymbol{k}}} = \dot{\varphi}_{\boldsymbol{k}}.
\end{aligned} \tag{E.2.5}$$

Thus,

$$\begin{aligned}
\left\langle p^{\varphi}_{\boldsymbol{k}} \frac{\partial \mathcal{H}}{\partial p^{\varphi}_{\boldsymbol{k}}} \right\rangle &= \left\langle 2\varrho r^2_{\boldsymbol{k}} \dot{\varphi}^2_{\boldsymbol{k}} \right\rangle = k_b T, \\
\left\langle p^{r}_{\boldsymbol{k}} \frac{\partial \mathcal{H}}{\partial p^{r}_{\boldsymbol{k}}} \right\rangle &= \left\langle 2\varrho \dot{r}^2_{\boldsymbol{k}} \right\rangle = k_b T, \\
\left\langle \varphi_{\boldsymbol{k}} \frac{\partial \mathcal{H}}{\partial \varphi_{\boldsymbol{k}}} \right\rangle &= -\left\langle 2\kappa k^2 \lambda_{\boldsymbol{k}} r_{\boldsymbol{k}} \varphi_{\boldsymbol{k}} \sin\left(\varphi_{\boldsymbol{k}} - \theta_{\boldsymbol{k}}\right) \right\rangle = k_b T, \\
\left\langle r_{\boldsymbol{k}} \frac{\partial \mathcal{H}}{\partial r_{\boldsymbol{k}}} \right\rangle &= \left\langle 2\left(\kappa k^4 + \langle \gamma \rangle_x k^2 + \widehat{E} k\right) r^2_{\boldsymbol{k}} + 2\kappa k^2 \lambda_{\boldsymbol{k}} r_{\boldsymbol{k}} \cos\left(\varphi_{\boldsymbol{k}} - \theta_{\boldsymbol{k}}\right) - 2\varrho r^2_{\boldsymbol{k}} \dot{\varphi}^2_{\boldsymbol{k}} \right\rangle = k_b T,
\end{aligned} \tag{E.2.6}$$

and by insertion of the first into the last equation, the amplitude fluctuations become

$$\left\langle r^2_{\boldsymbol{k}} \right\rangle = \frac{k_b T - \kappa k^2 \lambda_{\boldsymbol{k}} \left\langle r_{\boldsymbol{k}} \cos\left(\varphi_{\boldsymbol{k}} - \theta_{\boldsymbol{k}}\right) \right\rangle}{\kappa k^4 + \langle \gamma \rangle_x k^2 + \widehat{E} k}. \tag{E.2.7}$$

In the case of vanishing spontaneous curvature, the second term in the numerator disappears and the amplitude fluctuation spectrum depends solely on the wavenumber k, the membrane parameters $\kappa, \langle \gamma \rangle_x, \widehat{E}$ and temperature. In particular, measurement of the fluctuation spectrum $\left\langle r^2_{\boldsymbol{k}} \right\rangle$ is a common practice to estimate the bending rigidity, see section 3.4.5. Note that in case of the surface tension being larger than the critical buckling tension, the system is not in equilibrium and the equipartition theorem does not apply. However, in simulations, we can always enforce a stable flat state by adding a harmonic potential

$$\mathcal{V}_{harm} = \frac{a}{2} \int_U h^2 dA, \tag{E.2.8}$$

to the potential energy $\mathcal{V}$. This leads to an additional term a in the denominator of eq. E.2.7 which reads then $\kappa k^4 + \langle \gamma \rangle_x k^2 + \widehat{E} k + a$.

The average $\left\langle r_{\boldsymbol{k}} \cos\left(\varphi_{\boldsymbol{k}} - \theta_{\boldsymbol{k}}\right) \right\rangle = -\left\langle r_{\boldsymbol{k}} \cos\left(\pi + \theta_{\boldsymbol{k}} - \varphi_{\boldsymbol{k}}\right) \right\rangle$ is negative for small phase angle fluctuations $\left|\pi + \theta_{\boldsymbol{k}} - \varphi_{\boldsymbol{k}}\right| \leq \pi/2$, thus, the spontaneous curvature increases amplitude fluctuations $\left\langle r^2_{\boldsymbol{k}} \right\rangle$. To investigate the phase angle fluctuations, we approximate

$$\sin\left(\varphi_{\boldsymbol{k}} - \theta_{\boldsymbol{k}}\right) = \sin\left(\pi + \theta_{\boldsymbol{k}} - \varphi_{\boldsymbol{k}}\right) \approx \pi + \theta_{\boldsymbol{k}} - \varphi_{\boldsymbol{k}} \tag{E.2.9}$$

for $|\pi + \theta_{\boldsymbol{k}} - \varphi_{\boldsymbol{k}}| \ll 1$ in the third equation of eqns. (E.2.6), in order to obtain

$$\frac{k_b T}{2\kappa k^2 \lambda_{\boldsymbol{k}}} = \langle r_{\boldsymbol{k}} \varphi_{\boldsymbol{k}} \sin(\varphi_{\boldsymbol{k}} - \theta_{\boldsymbol{k}}) \rangle \approx \langle r_{\boldsymbol{k}} \varphi_{\boldsymbol{k}} (\pi + \theta_{\boldsymbol{k}} - \varphi_{\boldsymbol{k}}) \rangle . \tag{E.2.10}$$

Above equation enables us estimate the Fourier components of the spontaneous curvature by measurement of phase angle fluctuations. Thus, by measurement of both amplitude and phase fluctuations in the flat state, except for the saddle-splay modulus, all membrane parameters may be estimated.

E.3. Growing Membrane with Hydrodynamic Interactions at Low Reynolds Numbers

So far, we have assumed for simplicity that the interactions of the membrane with the dissipative background medium result in a friction force density $\boldsymbol{F}_\nu$ proportional to the lateral membrane velocity

$$\boldsymbol{F}_\nu = \nu \partial_t h \boldsymbol{e}_z. \tag{E.3.1}$$

Here, we improve this description and assume the membrane is embedded in an incompressible Newtonian fluid with viscosity η. We assume that the Reynolds number of the fluid flow generated by the membrane movement is small enough such that a description by the linear Stokes equation is sufficient. This assumption is justified by the long timescales of weeks and months on which growth processes typically happen. We estimate the Reynolds number of the flow via

$$Re = \frac{\varrho v_z L}{\eta}, \tag{E.3.2}$$

with ϱ the fluid mass density, L the membrane size and v_z a typical velocity of the lateral membrane deflection. For a total deflection on the scale Δz during the time Δt we see that the requirement $Re \ll 1$ is equivalent to

$$\frac{\varrho \Delta z L}{\eta} \ll \Delta t, \tag{E.3.3}$$

which we assume to be fulfilled. Moreover, we suppose the membrane is partially permeable for the embedding fluid with a permeability constant λ_p in units of velocity per pressure. The linearized equations of motion for membrane deflection $h(\boldsymbol{x}, t) = h(x, y, t)$ and fluid flow velocity $\boldsymbol{v} = (v_x, v_y, v_z)$ read then [98]

$$\partial_t h(\boldsymbol{x}, t) - v_z(\boldsymbol{x}, z = 0, t) = \lambda_p \left(\langle \gamma \rangle_x \Delta h - \kappa \Delta\Delta h \right), \tag{E.3.4}$$

$$\eta \Delta \boldsymbol{v}(\boldsymbol{x}, z, t) = \nabla p(\boldsymbol{x}, z, t) + (\kappa \Delta\Delta h - \gamma \Delta h)\, \delta(z)\, \boldsymbol{e}_z, \tag{E.3.5}$$

$$\nabla \cdot \boldsymbol{v}(\boldsymbol{x}, z, t) = 0. \tag{E.3.6}$$

Equation (E.3.4) states the so-called Darcy's law: the flow velocity through a permeable medium is proportional to the pressure gradient along the medium. The limit $\lambda_p \to 0$ corresponds to an impermeable membrane. We see that in this case the velocities of the membrane and of the fluid at the membrane, approximately at $z = 0$, have to be the same as no flow through the membrane is possible. The second equation (E.3.5) is the Stokes equation for the fluid flow, hereby, the last term on the right-hand side corresponds to the forces exerted on the fluid by the membrane. The third equation (E.3.6) corresponds to the common incompressibility condition. Fourier transformation of eqns. (E.3.4)-(E.3.6) and elimination of the flow field yields the following dynamic equation for the membrane Fourier modes [98]

$$\partial_t h_{\boldsymbol{k}} = -\left(\lambda_p + \frac{1}{4\eta k}\right)\left(\kappa k^4 + \langle\gamma\rangle_x k^2\right) h_{\boldsymbol{k}} \tag{E.3.7}$$

The term $1/(4\eta k)$ occurs due to interactions of distant membrane parts which are mediated through the flow of the embedding fluid. Interactions of this type are called *hydrodynamic interactions*. We see that in the limit of large permeability $\lambda_p \gg 1/(4\eta k)$ we recover the dynamic equation with uniform friction, eq. (4.1.28), if we set $\nu = \lambda_p^{-1}$. Note that the small wavenumbers are most critical for this limit as for these the term $1/(4\eta k)$ is largest. For a membrane of size L, the smallest wavenumber is $k = 2\pi/L$, hence, the limit of large permeability is for sure valid if

$$\lambda_p \gg \frac{L}{8\pi\eta}. \tag{E.3.8}$$

In the opposite limit of low permeability, the term $1/(4\eta k)$ dominates in the first parenthesis in eq. (E.3.7) and we obtain the dynamic equation

$$\partial_t h_{\boldsymbol{k}} = -\frac{1}{4\eta}\left(\kappa k^3 + \gamma k\right) h_{\boldsymbol{k}}, \tag{E.3.9}$$

with solution

$$h_{\boldsymbol{k}} = h_{\boldsymbol{k}}(t=0)\exp\left(-\frac{1}{4\eta}\left(\kappa t k^3 + \Gamma(t) k\right)\right) \tag{E.3.10}$$

where Γ denotes the cumulative integral $\Gamma(t) = \int_0^t \langle\gamma\rangle_x(\tau)\, d\tau$. Thus, the amplitudes grow exponentially as in the dynamics with uniform friction, eq. (4.1.28), however, other wavemodes are amplified as the polynomial in k in the exponent is different. We investigate how hydrodynamic interactions affect the asymptotic behavior of the growing membrane. Quantities which refer to this case are denoted with a η, either in exponent or subscript, to distinguish them from the corresponding variables without hydrodynamic interactions (see section 4.2), e.g. we write k^η_{min} for the minimal energy wavenumber with hydrodynamic interactions. We begin with the observation that for a given compressive surface tension $\langle\gamma\rangle_x = \text{const.} < 0$, the strongest amplified wavemode k^η_{min} is given by the minimum of the polynomial $\kappa k^3 + \langle\gamma\rangle_x k$. This minimum has to fulfill the condition

$$\left.\frac{d}{dk}\left(\kappa k^3 + \langle\gamma\rangle_x k\right)\right|_{k=k_{min}} = 0, \tag{E.3.11}$$

which yields

$$k^\eta_{min} = \sqrt{\frac{|\langle\gamma\rangle_x|}{3\kappa}}. \tag{E.3.12}$$

Thus, for a membrane in the homeostatic state with $\langle\gamma\rangle_x = \gamma_h$, the corresponding homeostatic wavenumber k^η_h reads

$$k^\eta_h = \sqrt{\frac{|\gamma_h|}{3\kappa}}, \tag{E.3.13}$$

which is ≈20% smaller than the corresponding value $k_h = \sqrt{|\gamma_h|/(2\kappa)}$, eq. (4.2.20), without hydrodynamic interactions. We assume the membrane is initially in its homeostatic state, the homeostatic surface tension represents then an upper bound for the compressive surface tension during buckling. Hence, a lower bound τ^{η}_{ampl} for the timescale on which buckling amplitudes increase exponentially is given by

$$\tau^{\eta}_{ampl} = \left.\frac{-4\eta}{\kappa k^3 + \gamma_h k}\right|_{k=k^{\eta}_h} = 6\sqrt{3}\eta\sqrt{\frac{\kappa}{|\gamma_h|^3}}. \tag{E.3.14}$$

Compared to the value $\tau_{ampl} = 4\kappa\nu/|\gamma_h|$ without hydrodynamic interactions, eq. (4.1.31), τ^{η}_{ampl} scales with a smaller exponent in the bending rigidity κ but a larger exponent in the homeostatic surface tension γ_h. For the analysis of the asymptotic behavior of the growing membrane, we assume the same homeostatic growth law, eq. (4.2.9), and the same elastic relation between projected density and surface tension, eq. (4.2.8), as in the case without hydrodynamic interactions. This implies that the timescale of growth is on the same order of magnitude as before, i.e. $\tau_g = 1/(\xi\,|\gamma_h|)$. Moreover, the derivation of asymptotically stable wavenumber k^{η}_{∞} and surface tension γ^{η}_{∞} stays largely the same as in section 4.2, we only have to replace $h_{\boldsymbol{k}}$ and $\partial_t h_{\boldsymbol{k}}$ with the corresponding expressions E.3.10 and E.3.9. The analogous equations to eqns. (4.2.25) and (4.2.26) to determine k^{η}_{∞} and γ^{η}_{∞} read then

$$k^{\eta}_{\infty} = \sqrt{\frac{|\gamma^{\eta}_{\infty}|}{3\kappa}}, \tag{E.3.15}$$

$$\xi\left(\gamma^{\eta}_{\infty} - \gamma_h\right) = -\frac{1}{2\eta}\left(\kappa\left(k^{\eta}_{\infty}\right)^3 + \gamma^{\eta}_{\infty}k^{\eta}_{\infty}\right). \tag{E.3.16}$$

The solutions can be expressed as a function of the timescale ratio $\tau^{\eta}_{ampl}/\tau_g$, similarly as in section (4.2), we define the analogous "second growth-buckling-ratio" via

$$\Theta''_{\eta} = \eta\xi\sqrt{\frac{\kappa}{|\gamma_h|}} \propto \frac{\tau^{\eta}_{ampl}}{\tau_g}. \tag{E.3.17}$$

We give the solutions for k^{η}_{∞} and γ^{η}_{∞} relative to the respective homeostatic values:

$$\begin{aligned}
\frac{k^{\eta}_{\infty}}{k^{\eta}_h} &= \begin{cases} \sqrt{3}\Theta''_{\eta}\left[2\cosh\left(\frac{1}{3}\operatorname{arccosh}\left(\frac{1}{2}\left(\Theta''_{\eta}\right)^{-2} - 1\right)\right) - 1\right], & \text{for } 0 < \Theta''_{\eta} \leq \frac{1}{2} \\ \sqrt{3}\Theta''_{\eta}\left[2\cos\left(\frac{1}{3}\arccos\left(\frac{1}{2}\left(\Theta''_{\eta}\right)^{-2} - 1\right)\right) - 1\right], & \text{for } \frac{1}{2} < \Theta''_{\eta} \leq \frac{1}{\sqrt{2}} \\ \sqrt{3}\Theta''_{\eta}\left[2\cos\left(\frac{\pi}{3} - \frac{1}{3}\arccos\left(1 - \frac{1}{2}\left(\Theta''_{\eta}\right)^{-2}\right)\right) - 1\right], & \text{for } \frac{1}{\sqrt{2}} < \Theta''_{\eta} \end{cases} \\
\frac{\gamma^{\eta}_{\infty}}{\gamma_h} &= \left(\frac{k^{\eta}_{\infty}}{k^{\eta}_h}\right)^2
\end{aligned} \tag{E.3.18}$$

Figure E.1 a) shows a comparison of k^{η}_{∞} and γ^{η}_{∞} with the corresponding results $k_{\infty}, \gamma_{\infty}$ without hydrodynamic interactions (see section 4.2). Both are plotted as functions of their respective "buckling-growth-ratio", i.e. $k^{\eta}_{\infty}, \gamma^{\eta}_{\infty}$ as functions of Θ''_{η} and $k_{\infty}, \gamma_{\infty}$ as functions of Θ''. As expected, k^{η}_{∞} and γ^{η}_{∞} converge against their respective homeostatic values in the limit of growth being much faster than membrane deformation, i.e. $\Theta''_{\eta} \to \infty$. However, in the opposite limit of slow growth, $\Theta''_{\eta} \to 0$, $k^{\eta}_{\infty}/k^{\eta}_h$ and $\gamma^{\eta}_{\infty}/\gamma_h$ scale with slightly larger

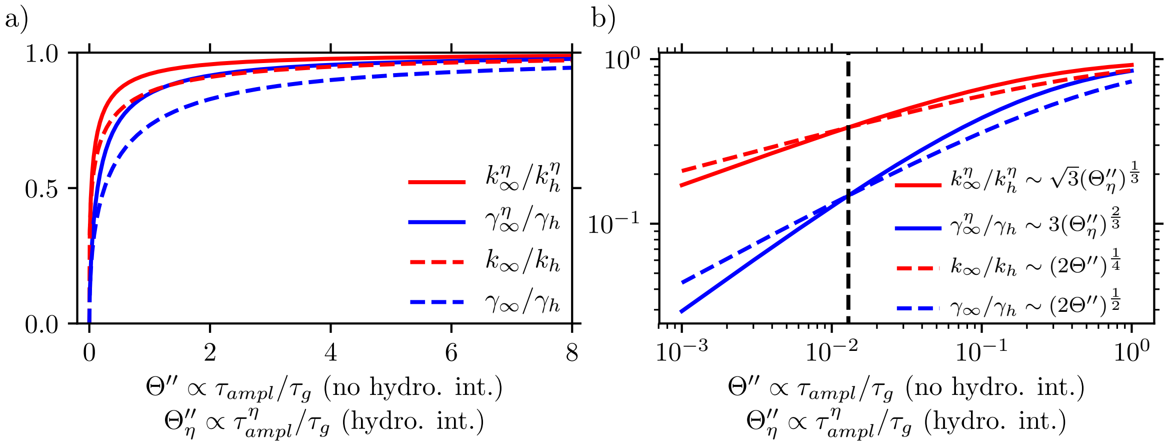

FIGURE E.1. **a)** Asymptotic wavenumber k_∞^η and surface tension γ_∞^η, divided by their respective homeostatic values, as a function of the "buckling-growth-ratio" Θ''_η. Solid lines depict the results with hydrodynamic interactions, eqns. (E.3.18), dashed lines the corresponding results of section 4.2, eqns. (4.2.27), with uniform background friction (without hydrodynamic interactions). **b)** As a) but with logarithmic scale on both axes. The crossover at $\Theta'' = \Theta''_\eta \approx 0.013$ is indicated with a vertical dashed line. Legend states scaling behavior in the limit of slow growth, $\Theta''_\eta, \Theta'' \to 0$.

exponents than their counterparts without hydrodynamic interactions:

$$\begin{aligned} \frac{k_\infty^\eta}{k_h^\eta} &\sim \sqrt{3}\left(\Theta''_\eta\right)^{\frac{1}{3}} \qquad & \frac{k_\infty}{k_h} &\sim \left(2\Theta''\right)^{\frac{1}{4}} \\ \frac{\gamma_\infty^\eta}{\gamma_h} &\sim 3\left(\Theta''_\eta\right)^{\frac{2}{3}} \qquad & \frac{\gamma_\infty}{\gamma_h} &\sim \left(2\Theta''\right)^{\frac{1}{2}} \end{aligned} \tag{E.3.19}$$

Thus, in the limit $\Theta''_\eta \to 0$ the ratios without hydrodynamic interactions k_∞/k_h and γ_∞/γ_h become larger than the respective ratios with hydrodynamic interactions; without hydrodynamic interactions, wavemode and surface tension are closer to their homeostatic values. Interestingly, the curves exhibit a crossover at around $\Theta'' = \Theta''_\eta \approx 0.013$, see fig. E.1 b). Hence, in the presence of hydrodynamic interactions, wavemode and surface tension converge in the limit of fast growth, $\Theta''_\eta \to \infty$, faster against their homeostatic values. Table E.1 summarizes the main differences in the buckling parameters between the models with and without hydrodynamic interactions.

In conclusion, our analysis predicts that inclusion of hydrodynamic interactions results in qualitatively similar asymptotic behavior of dominant wavenumber and surface tension as in the case of a simple uniform background friction. In particular, the ratio of membrane deformation timescale τ^η_{ampl} and growth timescale τ_g, the "growth-buckling-ratio" $\Theta''_\eta \propto \tau^\eta_{ampl}/\tau_g$, remains the crucial parameter which determines whether buckling occurs close to system-spanning modes $k = 2\pi/L$ (in the limit $\Theta''_\eta \to 0$) or close to the homeostatic wavenumber $k_h = \sqrt{|\gamma_h|/(3\kappa)}$ (in the limit $\Theta''_\eta \to \infty$).

Table E.1. Summary of buckling parameters for the models with hydrodynamic interactions (and an impermeable membrane) and without hydrodynamic interactions.

Parameter	No hydro. int.	With hydro. int.	Description
$\partial_t \log h_{\boldsymbol{k}} =$	$-\lambda_p \left(\kappa k^4 + \langle\gamma\rangle_x k^2\right)$	$-\frac{1}{4\eta}\left(\kappa k^3 + \langle\gamma\rangle_x k\right)$	Deflection dynamic eq.
τ_g	$\dfrac{1}{\xi \lvert\gamma_h\rvert}$	$\dfrac{1}{\xi \lvert\gamma_h\rvert}$	Growth timescale
τ_{ampl}	$\dfrac{4\kappa\nu}{\lvert\gamma_h\rvert^2}$	$6\sqrt{3}\eta\sqrt{\dfrac{\kappa}{\lvert\gamma_h\rvert^3}}$	Membr. def. timescale
$\Theta'' \propto \dfrac{\tau_{ampl}}{\tau_g}$	$\dfrac{\nu\xi\kappa}{\lvert\gamma_h\rvert}$	$\eta\xi\sqrt{\dfrac{\kappa}{\lvert\gamma_h\rvert}}$	"Second growth-buckling-ratio"
k_h	$\sqrt{\dfrac{\lvert\gamma_h\rvert}{2\kappa}}$	$\sqrt{\dfrac{\lvert\gamma_h\rvert}{3\kappa}}$	Homeostatic wavenumber
$\lim\limits_{\Theta''\to 0} \dfrac{\gamma_\infty}{\gamma_h}$	$\sim (2\Theta'')^{\frac{1}{2}}$	$\sim 3(\Theta'')^{\frac{2}{3}}$	Surf. tension, slow growth limit
$\lim\limits_{\Theta''\to 0} \dfrac{k_\infty}{k_h}$	$\sim (2\Theta'')^{\frac{1}{4}}$	$\sim \sqrt{3}(\Theta'')^{\frac{1}{3}}$	Wavenumber, slow growth limit

APPENDIX F

Simulations of Growing Membranes

All Simulation and Theory Data

We compare growing membrane simulations with theoretical results with (1) a growth rate linear in surface tension $k_g = \xi\,(\gamma - \gamma_h)$ and (2) an improved theory with piecewise linear interpolation of the growth rate $k_g = k_g(\gamma)$ measured during simulations. Figure 4.7 in section 4.3.1 depicts results for growth strength parameter $B^* = 0.7$, here, we show the results for all remaining growth strengths.

Often, the initial buckling happens at different times in theory and simulation. This may be caused by the strong sensitivity of the exponentially increasing amplitudes $\{h_{\boldsymbol{k}}\}$ to the initial conditions $h_{\boldsymbol{k}}(t = 0)$. Therefore, we shift the theory curves corresponding to the piecewise linear interpolated growth rate along the time axis onto simulation data such that at the last data point in the Monge-representation, projected densities $\langle \widehat{\varrho} \rangle_x$ coincide. The curves for the linear growth rate $k_g = \xi\,(\gamma - \gamma_h)$ theory are plotted using the same time shift to allow for easy comparison of the two theoretical approaches.

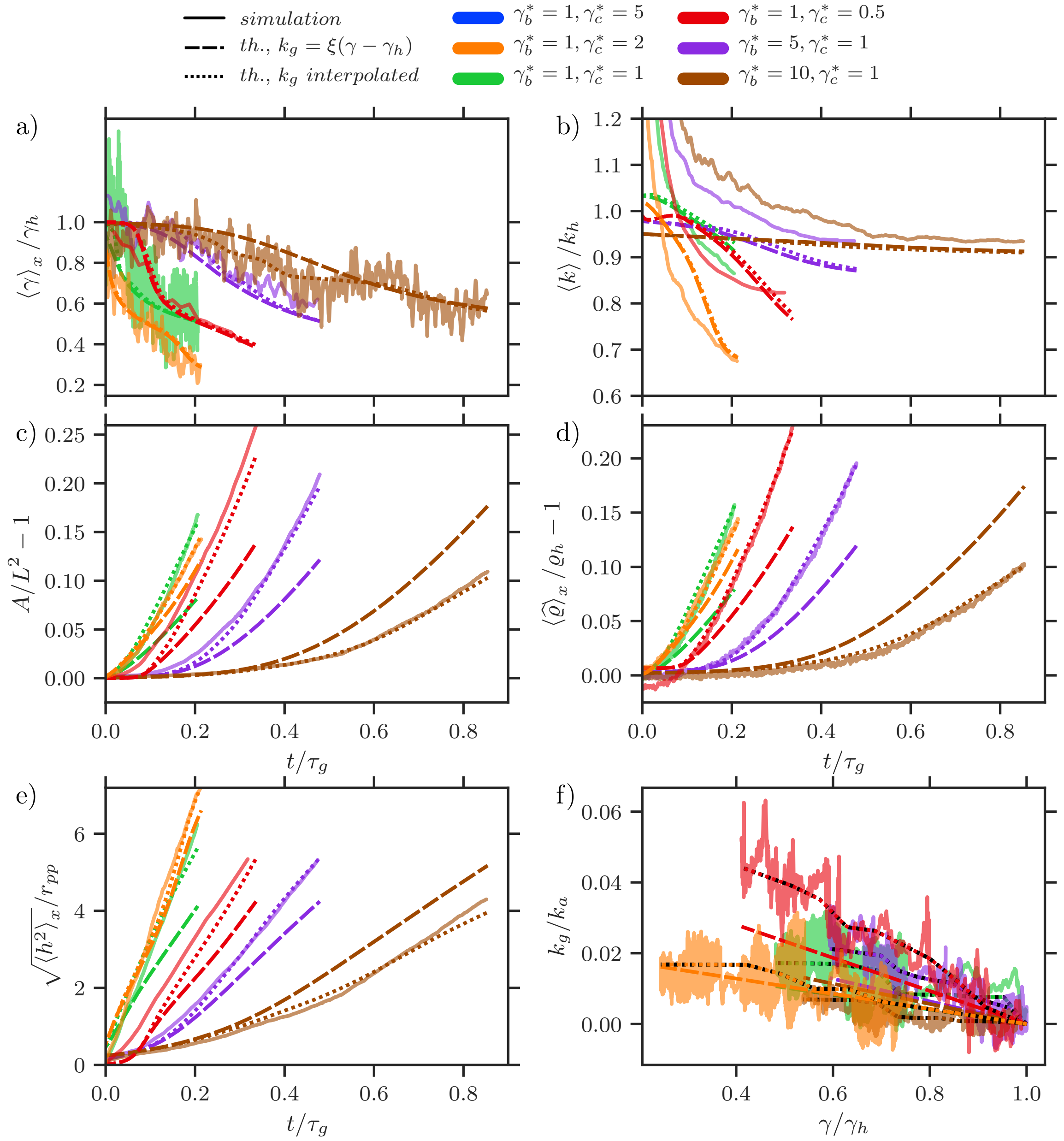

FIGURE F.1. **a)** Surface tension $\langle\gamma\rangle_x$ as a function of time for simulations (solid lines) with growth strength parameter $B^* = 0.6$ and various values of background friction γ_b^* and intracell friction γ_c^* (see legend). Dashed lines show solution of theory with growth rate $k_g = \xi(\gamma - \gamma_h)$, dotted lines with piecewise linear interpolation of measured growth rate, see f). Time unit equals growth timescale τ_g. **b)-e)** As a) for average wavenumber $\langle k\rangle$, relative area increase $A/L^2 - 1$, relative density increase $\langle\hat{\varrho}\rangle_x / \varrho_h - 1$ and square root of second height moment $\sqrt{\langle h^2\rangle_x}$. **f)** Measured growth rate k_g during buckling versus surface tension γ in simulations (solid lines). Dashed lines depict linear growth law $k_g = \xi(\gamma - \gamma_h)$ from measurements in section 3.4, dotted lines with black outline depict piecewise linear interpolation used for solution of eqns. (4.3.3).

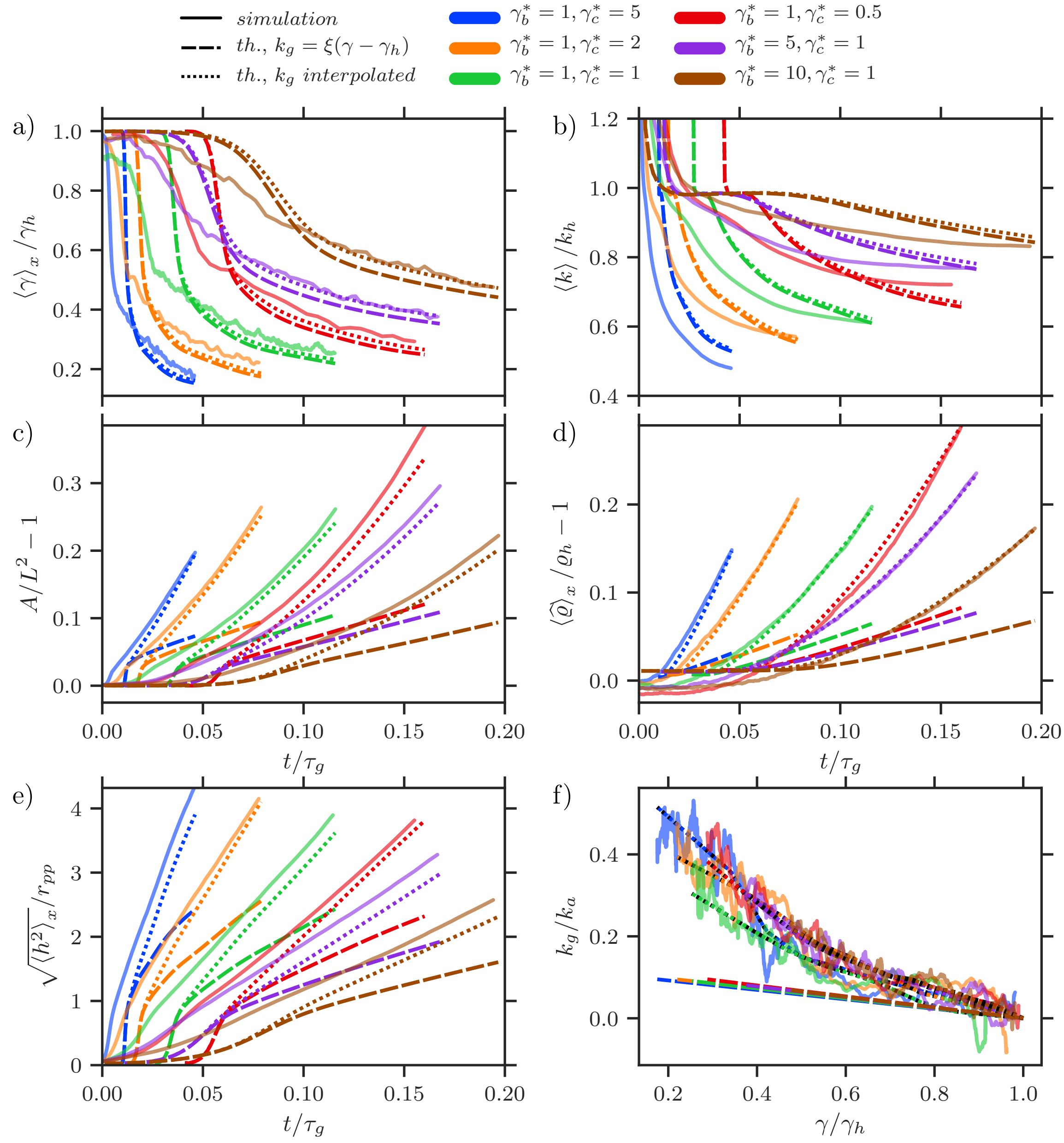

FIGURE F.2. As fig. F.1 for growth strength $B^* = 0.7$.

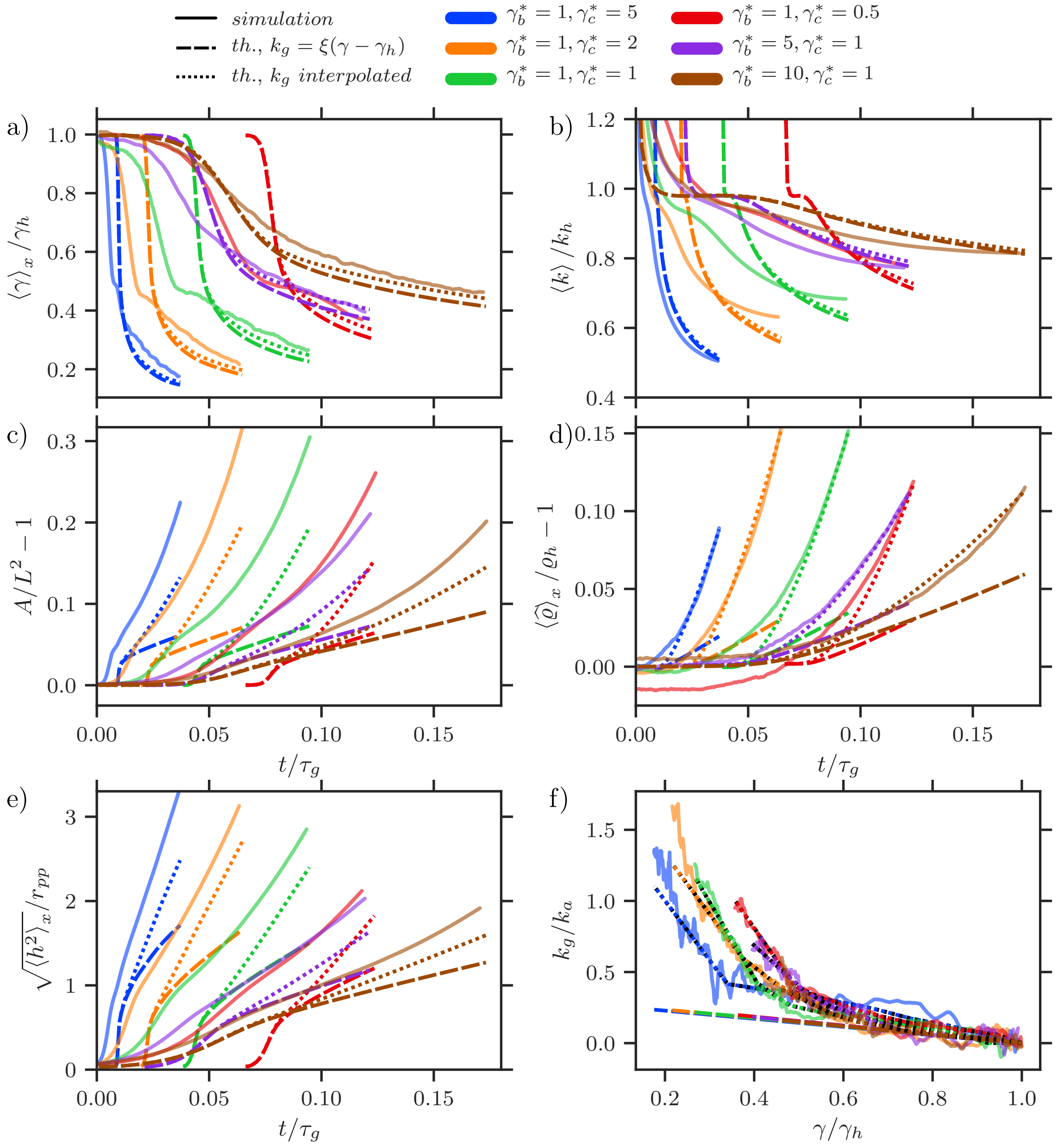

FIGURE F.3. As fig. F.1 for growth strength $B^* = 0.8$.

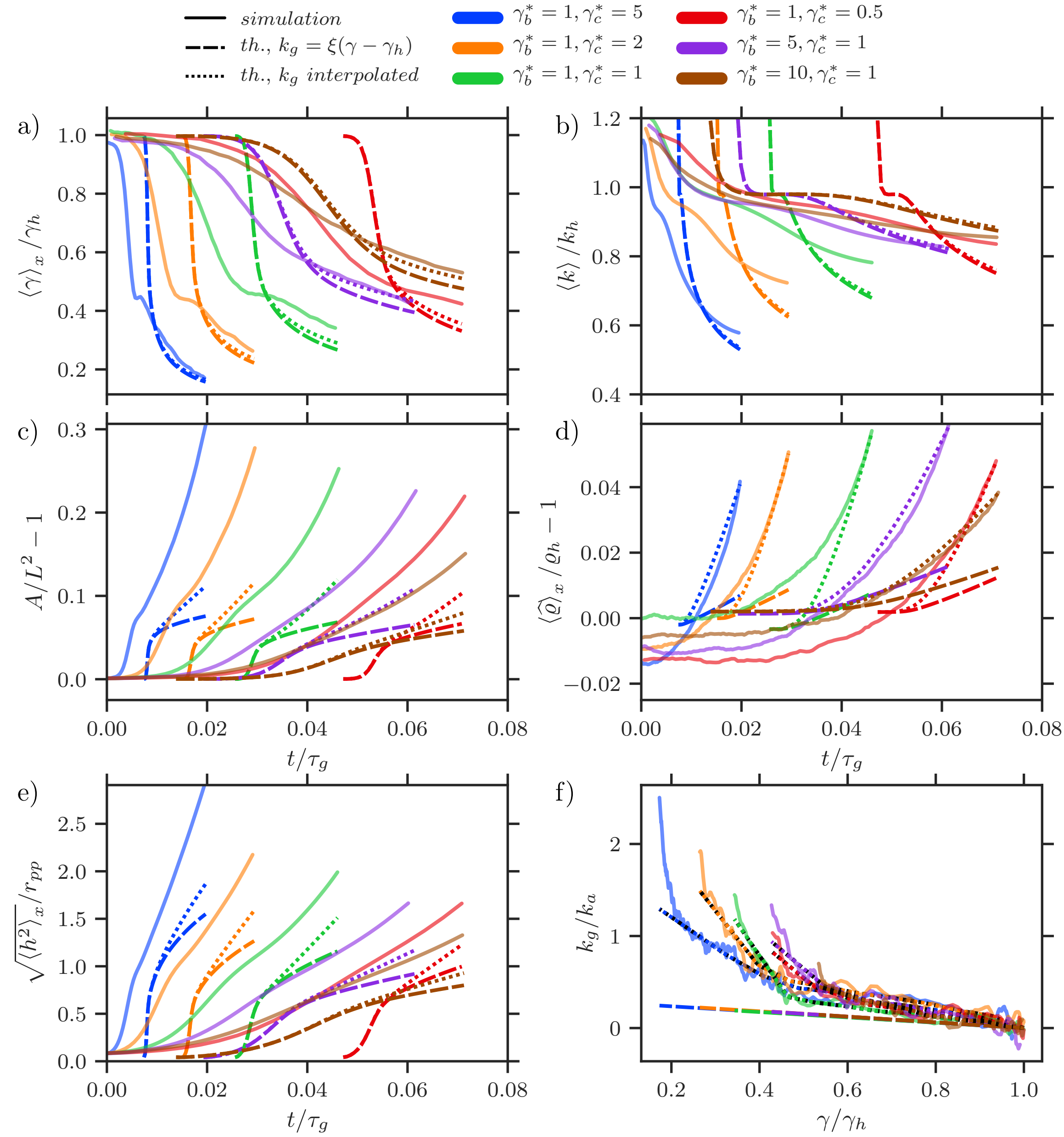

FIGURE F.4. As fig. F.1 for growth strength $B^* = 0.9$.

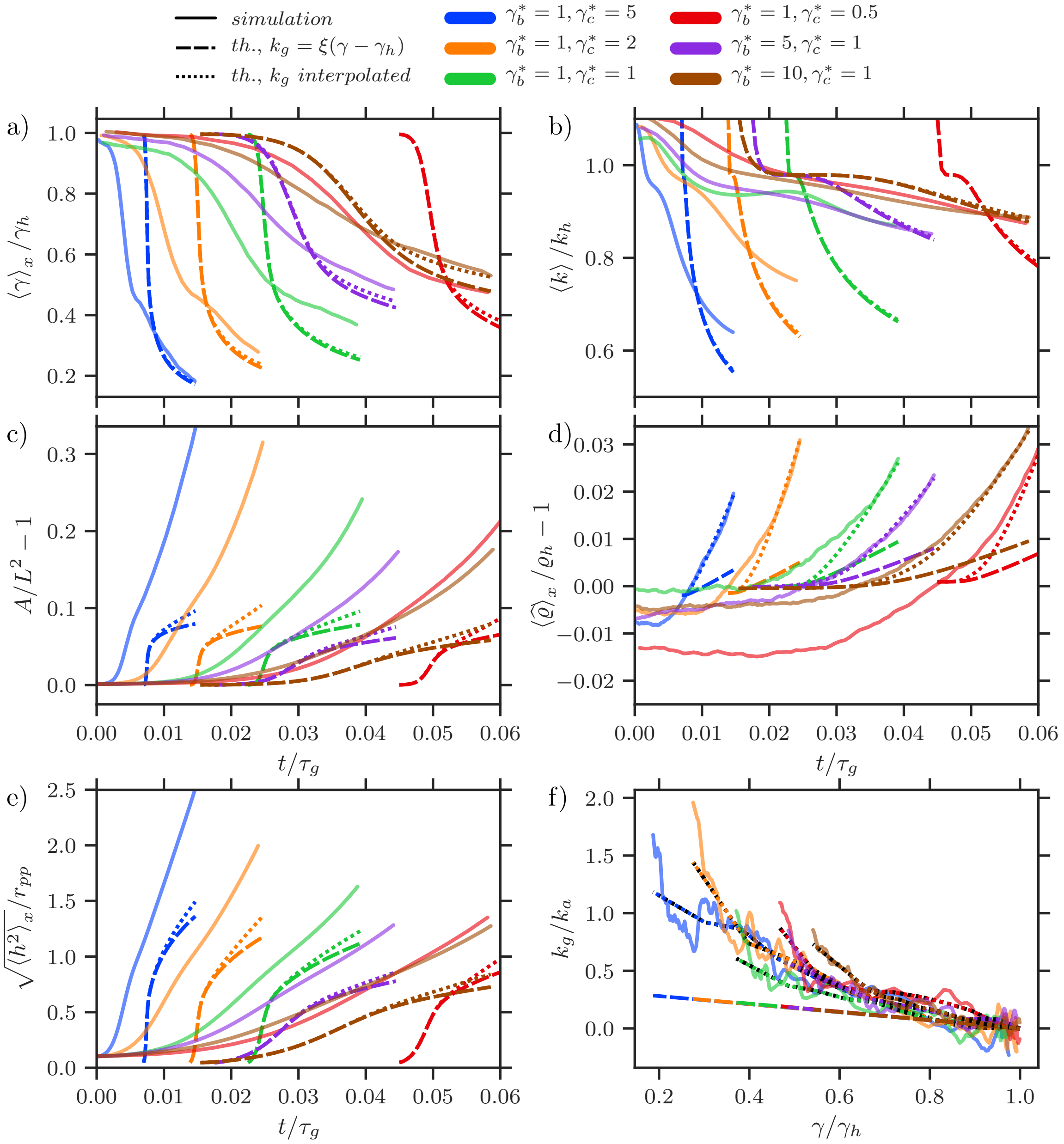

FIGURE F.5. As fig. F.1 for growth strength $B^* = 1.0$.

APPENDIX G

Growth Channel Experiments

All Velocity Profile Data

The results of the fit of model eqns. (5.1.3) to all twelve growth channel experiments are shown (see section 5.2). Figures G.1-G.4 depict model fits with the Monod-uptake function

$$u(\widehat{g}) = \frac{\widehat{g}}{1+\widehat{g}}, \tag{G.1}$$

in the dimensionless concentration variable $\widehat{g}$, figs. G.5-G.8 show fits with the Teissier-uptake function

$$u(\widehat{g}) = 1 - \exp\left(-\widehat{g}\right). \tag{G.2}$$

Similar figures depicting the same data appeared in ref. [75].

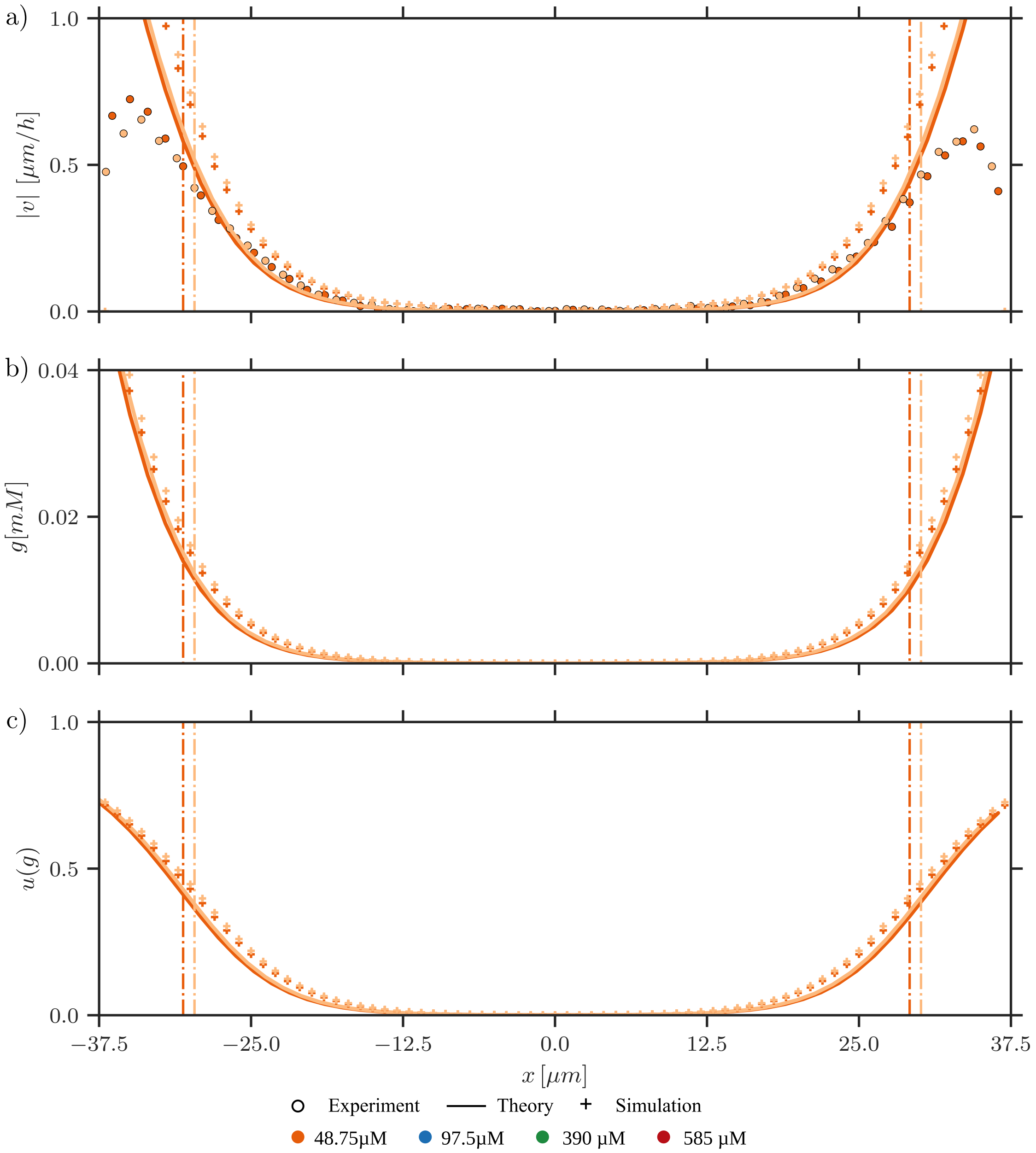

Figure G.1. **a)** Velocity profiles of growth channel experiments (circles, see legend). Depicted are two experiments at PCA-concentration 48.75 µM (different color shades). Due to the symmetry of the velocity profile with respect to the channel center, the absolute value of the velocity is shown. Dashed-dotted vertical lines indicate the cutoff x_+ used to constrain the data range used for the fit to the analytic model eqns. (5.1.3), assuming Monod-uptake. Continuous lines show the velocity profiles of the model fit. Flow profiles of corresponding 2PG simulations are shown with “+”-symbols. Experimental and simulation data has been averaged over time and y-direction. **b)-c)** g- and $u(g)$-profiles from model fit (continuous lines) and corresponding particle simulation results (“+”-symbols).

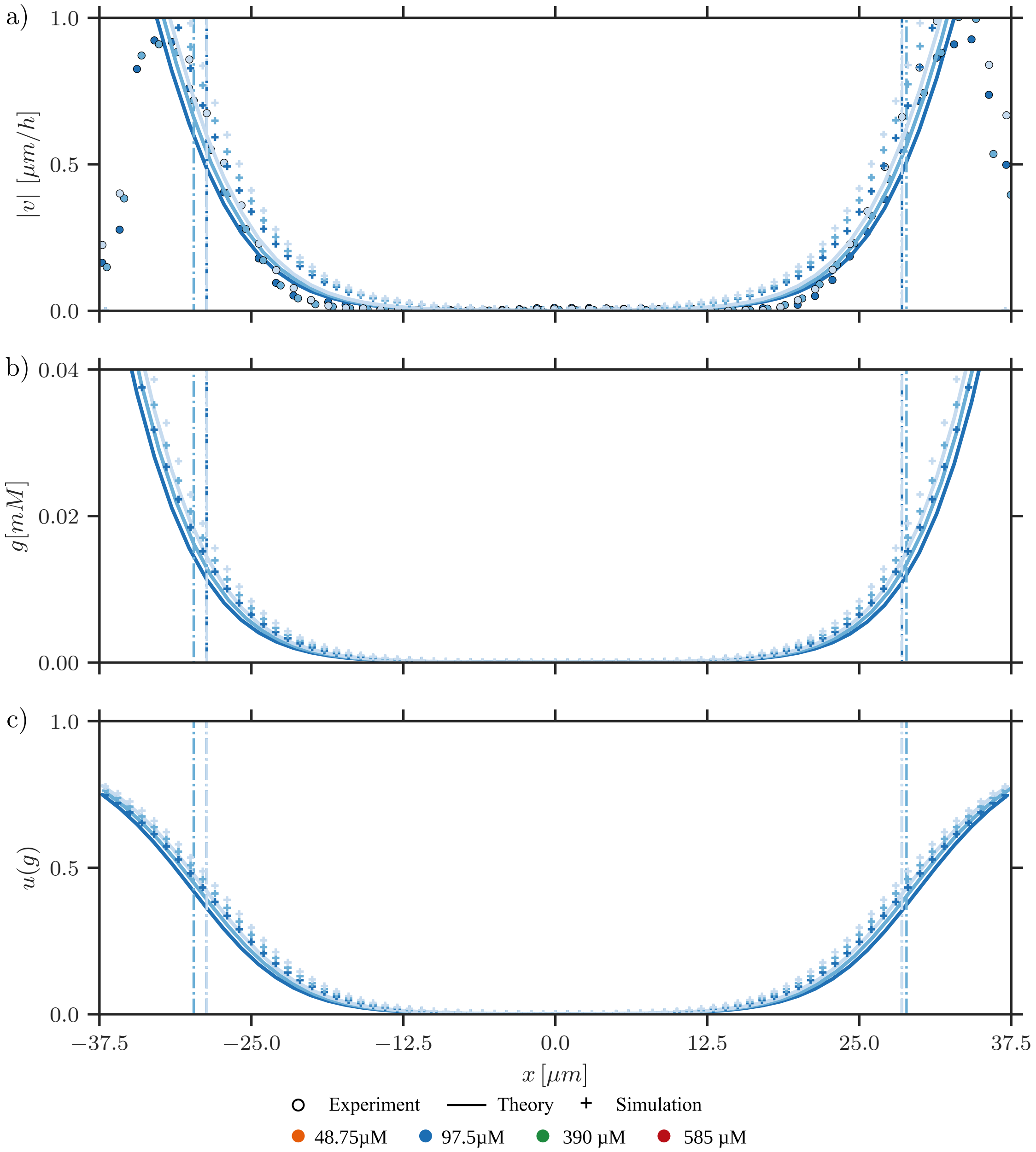

Figure G.2. As fig. G.1 for three experiments with PCA-concentration 97.5 µM and Monod-uptake for model fit.

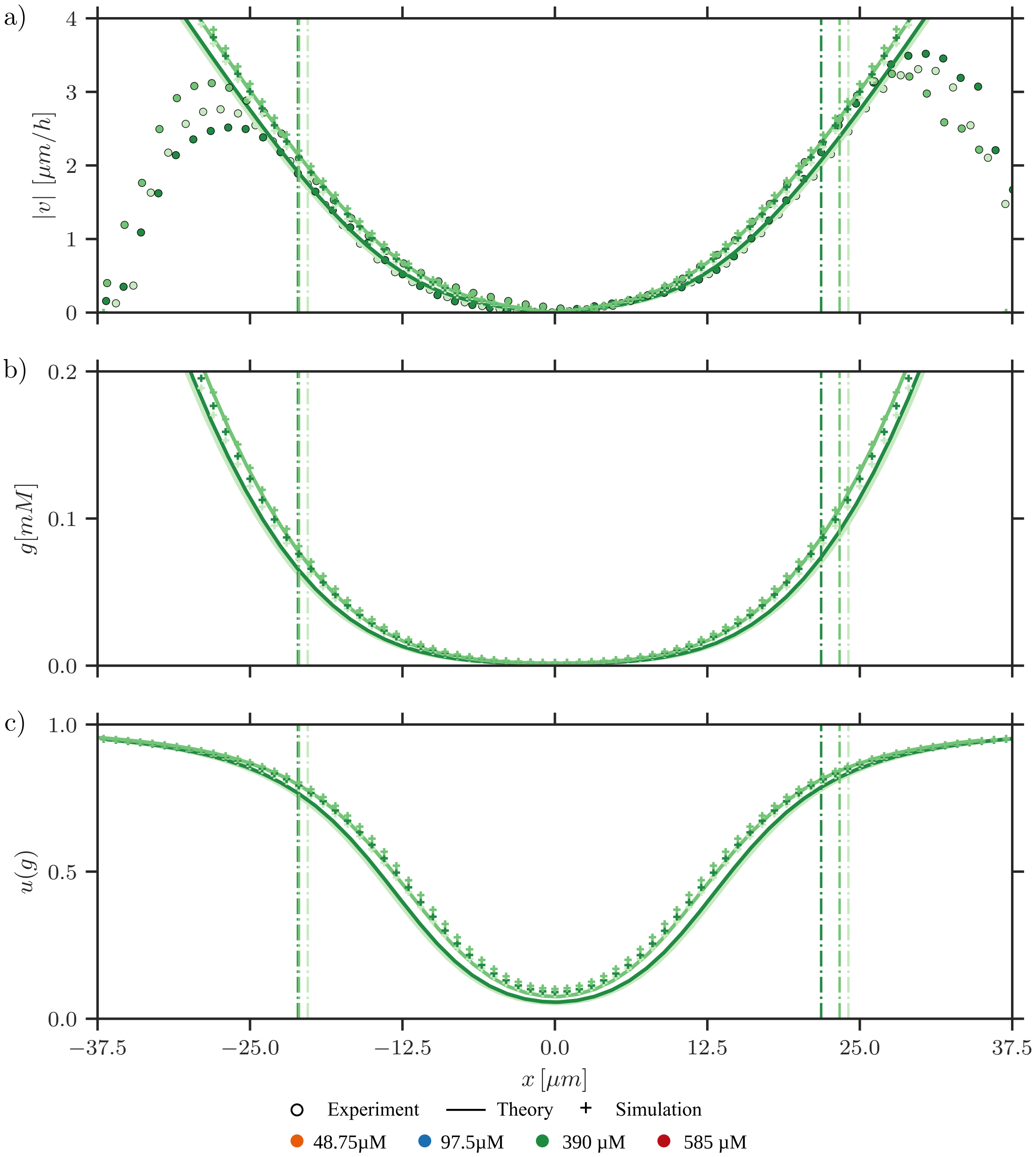

Figure G.3. As fig. G.1 for three experiments with PCA-concentration 390 μM and Monod-uptake for model fit.

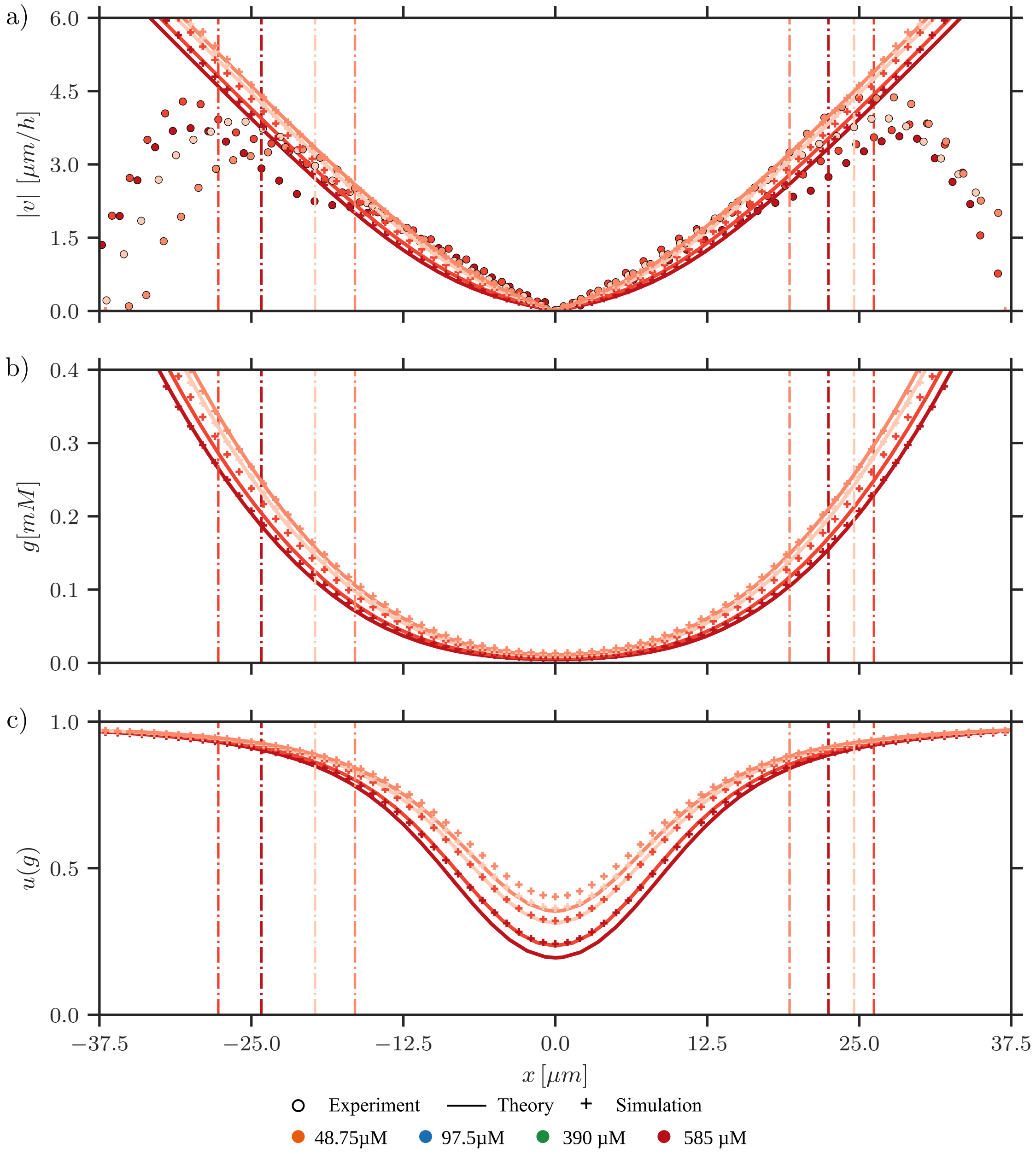

FIGURE G.4. As fig. G.1 for four experiments with PCA-concentration 585 µM and Monod-uptake for model fit.

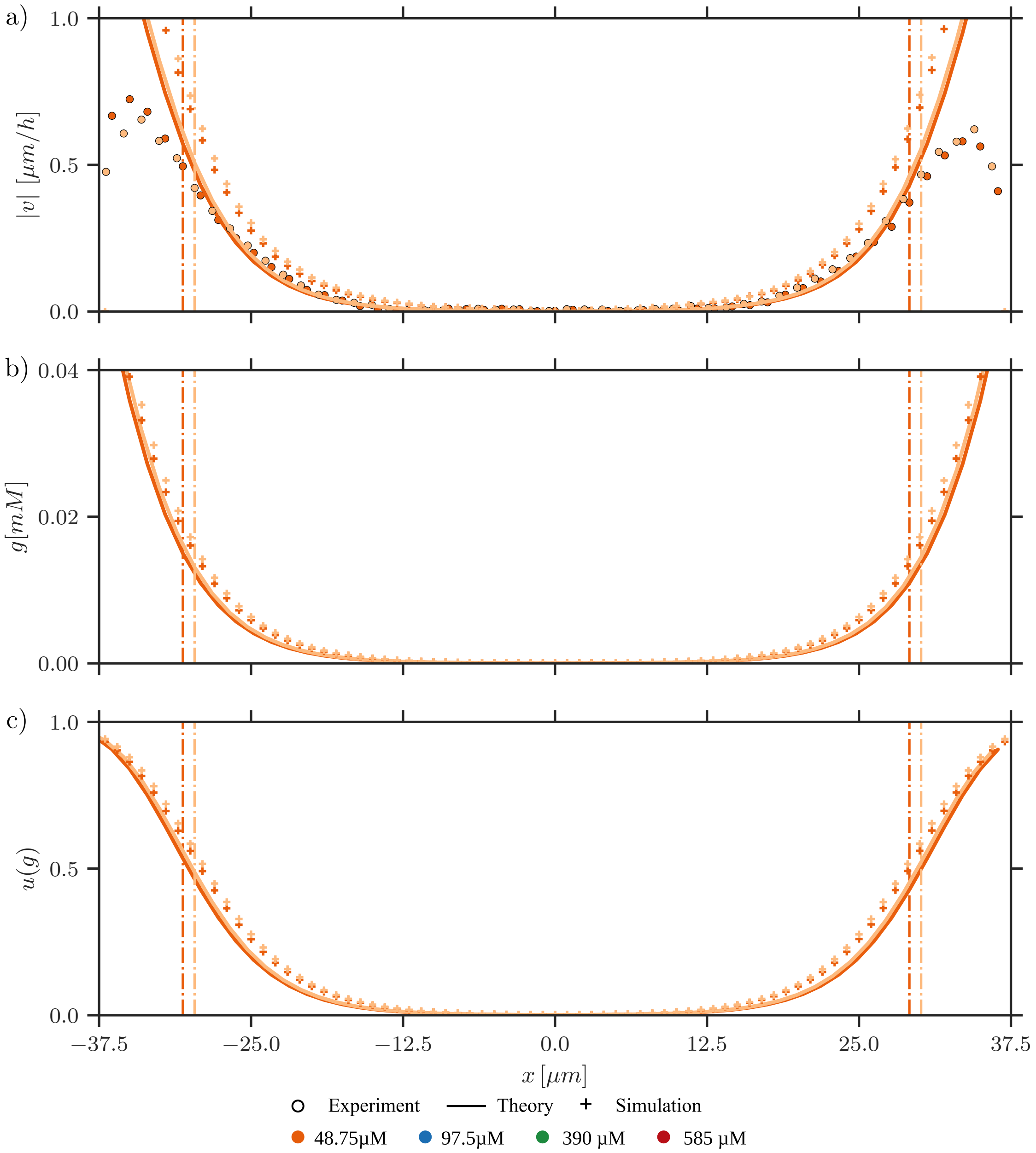

FIGURE G.5. As fig. G.1, with Teissier-uptake for model fit.

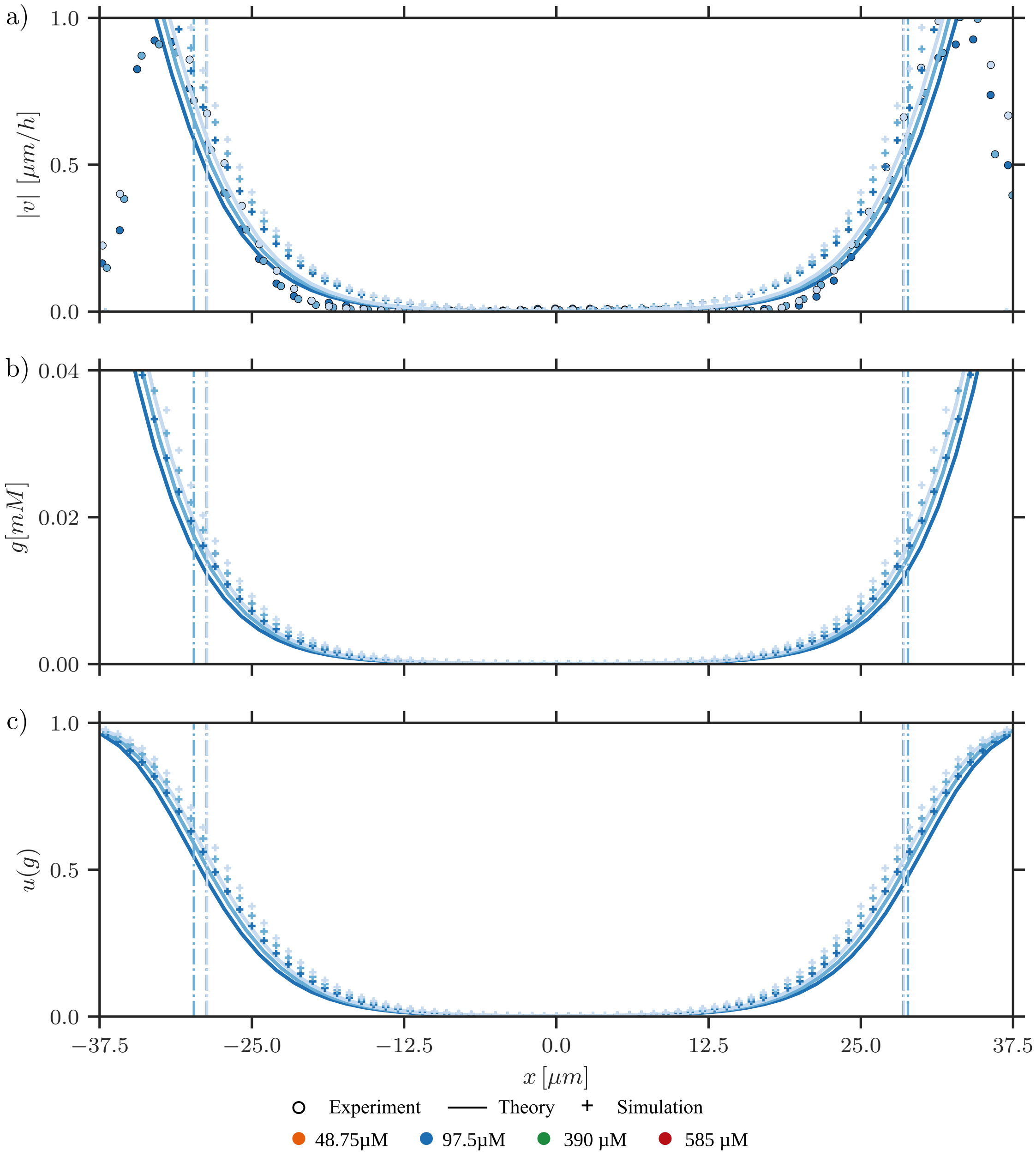

FIGURE G.6. As fig. G.1 for three experiments with PCA-concentration 97.5 µM and Teissier-uptake for model fit.

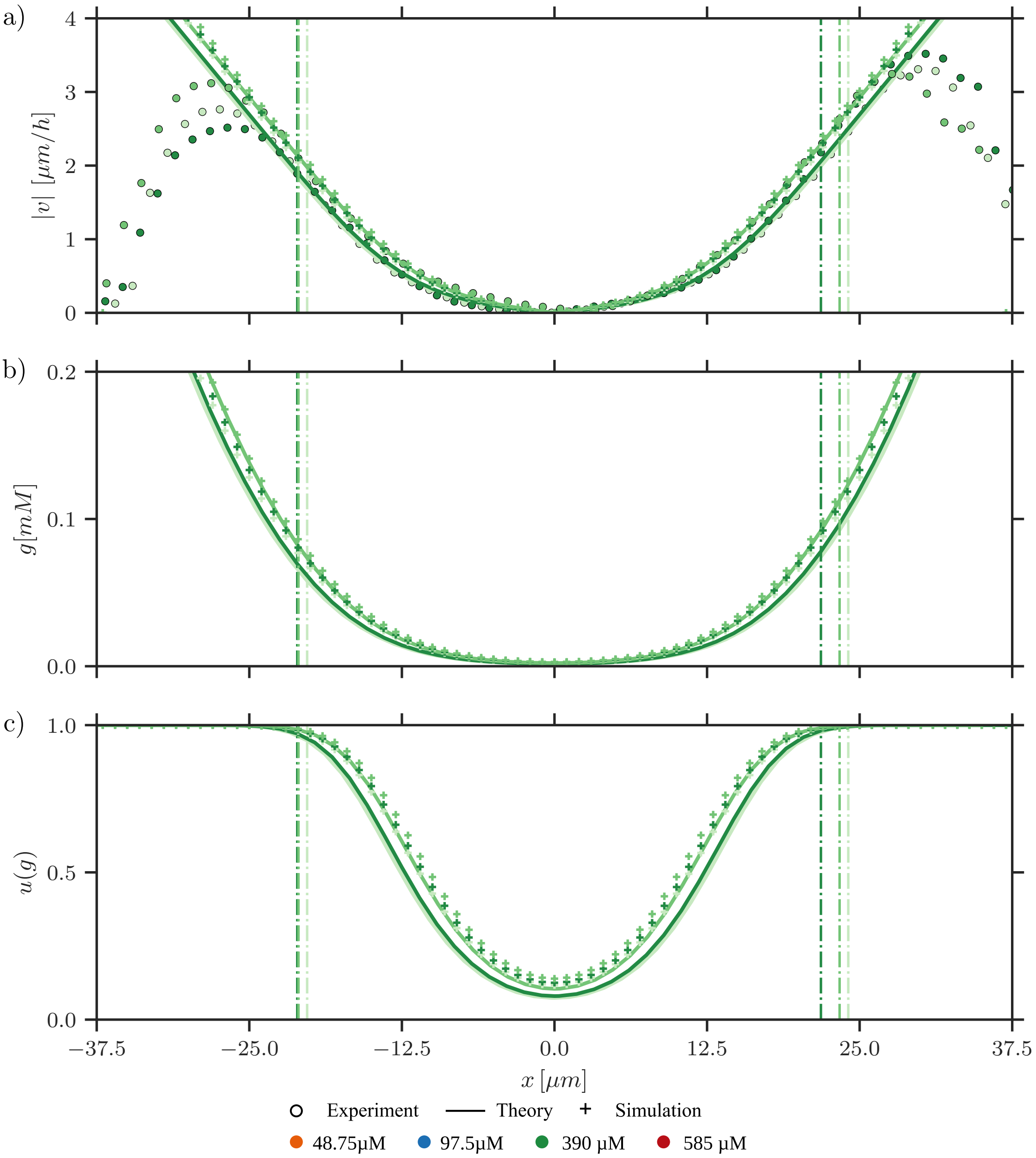

FIGURE G.7. As fig. G.1 for three experiments with PCA-concentration 390 µM and Teissier-uptake for model fit.

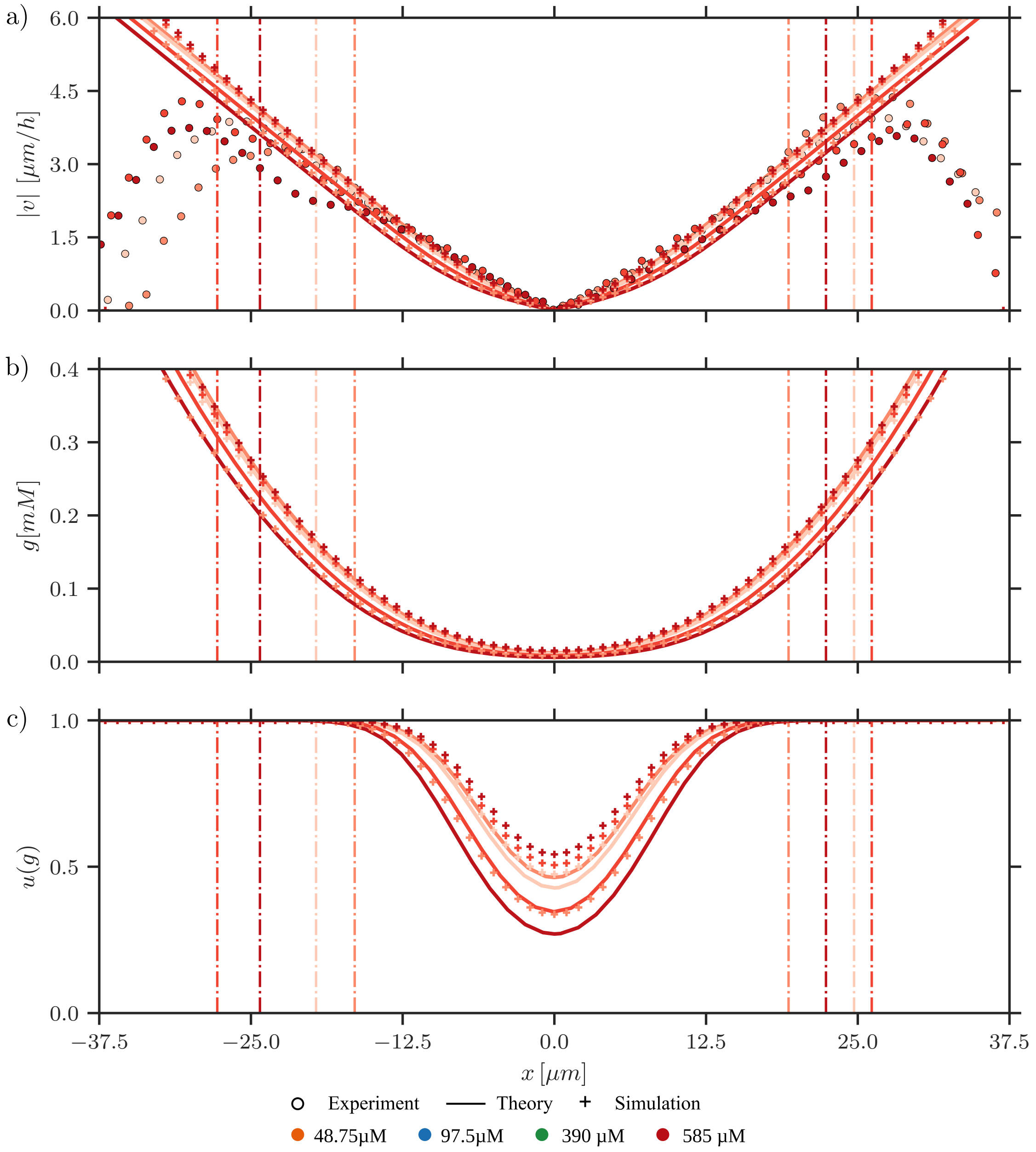

FIGURE G.8. As fig. G.1 for four experiments with PCA-concentration 585 µM and Teissier-uptake for model fit.

APPENDIX H

Growth Chamber Experiments

All Colony Spreading Data

We show additional colony spreading experiments, similar to the experiments shown in (fig. 5.16), for feeding concentrations $g_\infty = 195\,\mu\text{M}$ (fig. H.2) and $g_\infty = 19.5\,\mu\text{M}$ (fig. H.3). Figure H.1 explains how simulation data has been shifted along the time-axis to match with experiment data.

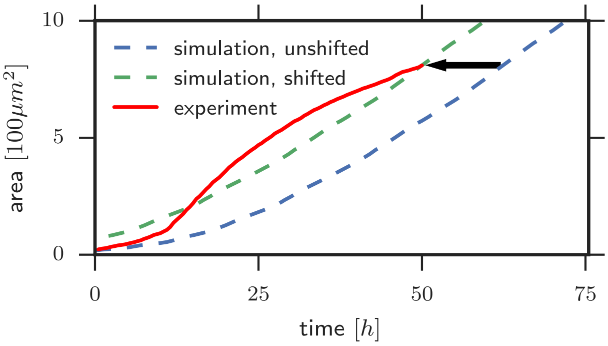

FIGURE H.1. In experiments, we expect a large variability in growth for small colonies due to the different state of the cell cycle in every individual. Therefore, we suppose that our simulation results for the colony spreading dynamics agree better with later stages of the experiment (red line), when memory effects have worn out. We shift every simulation area curve (dashed lines) such that the last recorded data point of the experiment coincides with a simulation data point (black arrow). The same shift along the time axis is also applied to compare colony shapes over time in simulation and experiment. From [109].

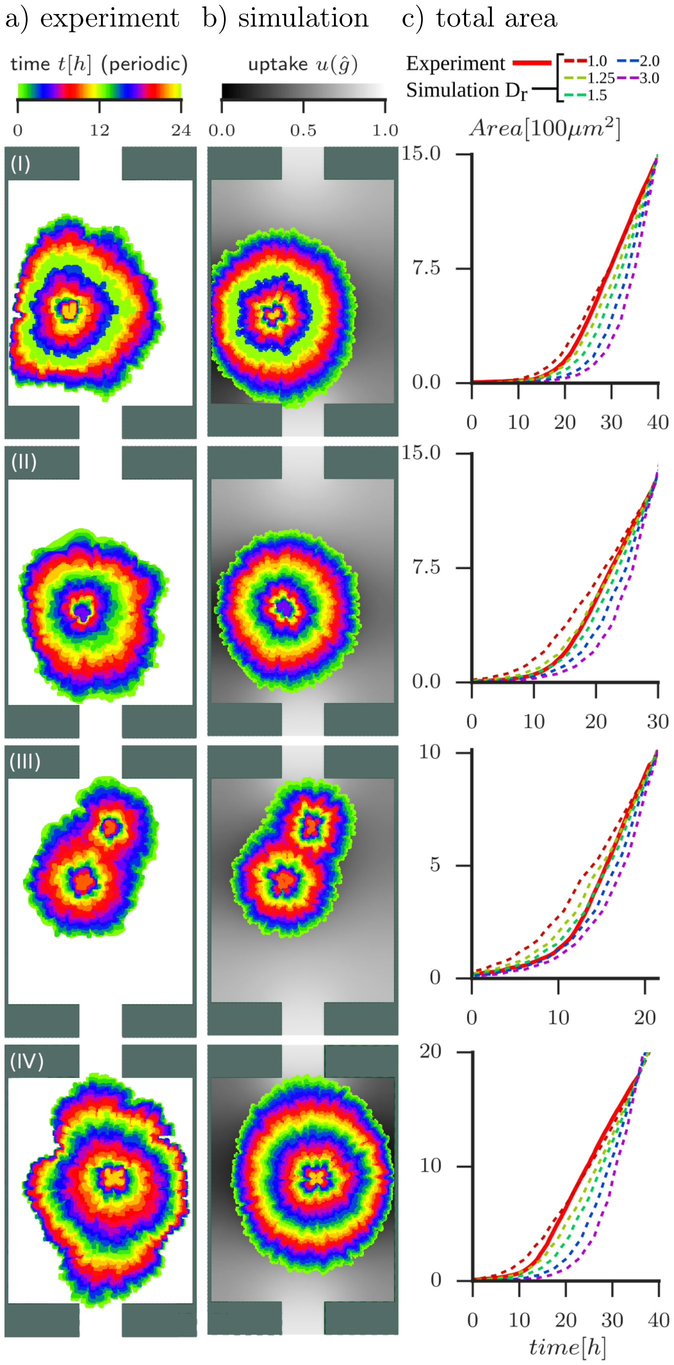

FIGURE H.2. Four examples of colony spreading dynamics in simulation and experiment. All rows **(I)-(IV)** belong to experiments with feeding concentration $g_\infty = 195\,\mu\text{M}$. **a)** Depiction of the colony shape dynamics in experiments. The outlines of the colony at equidistant timepoints are shown in different colors with a periodic colorscale (legend on top), 12 hours have passed between two rings with the same color. **b)** Same depiction as in left column for outlines from the corresponding simulation with $D_{free}/D_{bulk} = 1.25$ (colorscale for colony same as in left column). The area shaded in gray around the colonies shows the profile of $u(g)$ at the last timepoint, (legend on top). **c)** Total colony area $A(t)$ in experiment (red line) and simulations (dashed lines) with $D_r = D_{free}/D_{bulk} = 1, 1.25, 1.5, 2, 3$. Simulations have been shifted along the time axis such that they cross the last data point of the experiment. From [109].

FIGURE H.3. As fig. H.2 for two experiments with feeding concentration $g_\infty = 19.5\,\mu\text{M}$. From [109].

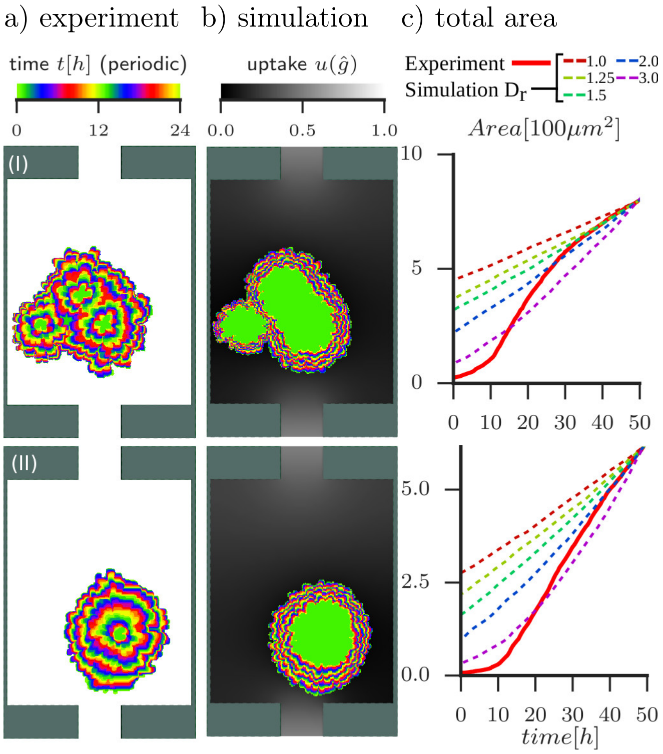

APPENDIX I

Standard Simulation Parameters

Starred parameters refer to relative values with respect to the parameters in table I.1, e.g. $B^* = 0.6$ corresponds to $B = 0.6 \cdot 50 = 30$.

Table I.1. Standard simulation parameters for growing membrane simulations.

Parameter	Value [sim. units]	Description
dt_{dpd}	10^{-3}	DPD-integration timestep
h	0.5	Grid constant for area- and FFT-calculation
dt_{fft}	10^{-2}	Timestep for area- and FFT-calculation
B	50	Growth force constants
r_0	1	
$r_{pp}; r_{mp}$	1;1.5	Cutoff radius of pair/MMM-potential(s)
d_c	0.8	Size threshold for cell division
r_c	10^{-5}	Distance at which new particles are placed after division
k_bT	0.1	Noise temperature (both DPD- and BD-noise)
$\gamma_b; \gamma_t; \gamma_c$	$0.1; 50; 100$	Background/Intercell/Intracell friction constant
$f_0; f_1$	$2.39566; 7.5$	Repulsive/Attractive force constant
k_α	10	MMM-potential strength

Table I.2. Results of membrane parameter measurements for different growth strength parameters B^*, other parameters as in standard set. Uncertainty estimates show square root of covariance matrix of corresponding least-squares minimization fit (for κ) or standard deviation of data set (all others). All values are rounded to two digits after comma.

B^*	0.60	0.65	0.70	0.80	0.90	1.00	Description
$-\gamma_h$	0.52	2.54	4.53	8.25	10.99	14.37	Homeostatic surface tension
$\Delta\gamma_h$	0.16	0.14	0.10	0.14	0.31	0.19	
$10^4\xi$	3.97	3.61	2.69	3.59	2.63	2.50	Growth rate pressure sensitivity
$10^4\Delta\xi$	0.25	0.45	0.27	0.61	0.14	0.06	
ϱ_h	3.55	3.64	3.71	3.83	3.99	4.13	Homeostatic particle density
$10^3\Delta\varrho_h$	0.31	3.72	5.04	30.12	24.92	34.24	
$10^2\chi_a$	3.79	3.60	4.41	2.08	2.59	2.40	Area compressibility
$10^2\Delta\chi_a$	0.17	0.19	0.14	0.37	0.21	0.23	
κ	22.65	23.49	24.10	25.03	25.25	25.42	Bending rigidity
$\Delta\kappa$	0.08	0.07	0.06	0.04	0.06	0.05	

TABLE I.3. Homeostatic surface tension measurements for varying growth strengths B^*, background friction constants γ_b^* and intracellular friction constants γ_c^*. For changing γ_c^*, the apoptosis rate k_a is adjusted such that $k_a \gamma_c = 1$, as in the standard parameter set. Uncertainty estimates show standard deviation of data set.

	B^*	0.60	0.70	0.80	0.90	1.00
γ_b^*	γ_c^*					
5	1	0.80±0.11	4.79±0.11	8.47±0.07	11.72±0.09	14.36±0.06
10	1	0.72±0.11	4.87±0.09	8.32±0.10	11.82±0.08	14.30±0.08
1	0.5	1.18±0.10	4.96±0.09	8.64±0.08	11.80±0.08	14.54±0.10
1	2	0.54±0.10	4.51±0.10	8.20±0.08	11.51±0.10	14.13±0.11
1	5	0.32±0.12	4.28±0.10	7.95±0.07	11.21±0.12	14.05±0.09

TABLE I.4. Standard simulation parameters for bacterial growth simulations. Forces are given relative to the background friction constant γ_b.

Parameter	Value[sim. unit]	Value[phys. unit]	Description
$\bar{t}$	1	1 h	Time unit
$\bar{l}$	1	1.1 µm	Length unit
$\bar{g}$	1	follows from fit, see section 5.2.3	Concentration unit
dt_{dpd}	5×10^{-5}	5×10^{-5}h	DPD-integration timestep
B	follows eq. (3.5.6)		Growth force constants
r_0	1	1.1 µm	
r_{pp}	1	1.1 µm	Cutoff radius of all pair-potentials
d_c	1	1.1 µm	Size threshold for cell division
r_c	10^{-5}	1.1×10^{-5}µm	Distance at which new particles are placed after division
k_a	0	0 h^{-1}	Apoptosis rate
$\gamma_b; \gamma_t; \gamma_c$	$1; 1; 10^4$	$1\mathrm{h}^{-1}; 1\mathrm{h}^{-1}; 10^4\mathrm{h}^{-1}$	Background/Intercell/Intracell friction constant
f_0/γ_b	460	460 µm h^{-1}	Repulsive force constant
f_1/γ_b	0	0 µm h^{-1}	Attractive force constant
dt_{fd}	10^{-5}	$10^{-5}\mathrm{h}^{-1}$	Finite-difference timestep
h	$0.\overline{90}$	1µm	Finite-difference grid constant
D_{bulk}	2047.72(1373.31)	≈ 2478(1888)$\mu\mathrm{m}^2$/h	Nutrient diffusion constant inside colony for Monod (Teissier)-uptake
$D_b; D_t; D_c$	10^{-3}	$1.21 \times 10^{-3}\mu\mathrm{m}^2$/h	Background/Intercell/Intracell noise diffusion constant of bacteria

Bibliography

[1] Frigo M, Johnson SG, 2005 The Design and Implementation of FFTW3. *Proceedings of the IEEE* 93, 216–231. Special issue on "Program Generation, Optimization, and Platform Adaptation" (Cited on pages 14 and 68.)

[2] Keilhauer C, Eggeling L, Sahm H, 1993 Isoleucine Synthesis in Corynebacterium glutamicum: Molecular Analysis of the ilvB-ilvN-ilvC Operon. *Journal of Bacteriology* 175, 5595–5603 (Cited on pages 14 and 108.)

[3] Koshland DE, 2002 The Seven Pillars of Life. *Science* 295, 2215–2216 (Cited on page 17.)

[4] 2018 Definition of "Life" in Merriam-Webster Dictionary, accessed on 15 Feb. 2018. URL `https://www.merriam-webster.com/dictionary/life` (Cited on page 17.)

[5] Aristotelis, Drossaart Lulofs HJ, 1965 De Generatione Animalium. Oxford University Press., Oxford (Cited on page 17.)

[6] Grüntzig JW, Mehlhorn H, 2010 Robert Koch: Seuchenjäger und Nobelpreisträger. Spektrum Akademischer Verlag (Cited on page 17.)

[7] Fleming A, 1922 On a remarkable bacteriolytic element found in tissues and secretions. *Proceedings of the Royal Society of London. Series B, Containing Papers of a Biological Character* 93, 306–317 (Cited on page 17.)

[8] Thompson DW, 1917 On Growth and Form. Cambridge University Press (Cited on page 17.)

[9] Tallinen T, Chung JY, Rousseau F, Girard N, Lefèvre J, Mahadevan L, 2016 On the growth and form of cortical convolutions. *Nature Physics* 12, 588–593 (Cited on pages 17, 19, and 35.)

[10] Glover JD, Wells KL, Matthäus F, Painter KJ, Ho W, Riddell J, Johansson JA, Ford MJ, Jahoda CAB, Klika V, Mort RL, Headon DJ, 2017 Hierarchical patterning modes orchestrate hair follicle morphogenesis. *PLOS Biology* 15, 1–31 (Cited on page 17.)

[11] Schwarcz D, Levine H, Ben-Jacob E, Ariel G, 2016 Uniform modeling of bacterial colony patterns with varying nutrient and substrate. *Physica D: Nonlinear Phenomena* 318–319, 91–99. Nonlinear Models in Molecular and Cell Biology (Cited on page 17.)

[12] Farrell FDC, Hallatschek O, Marenduzzo D, Waclaw B, 2013 Mechanically Driven Growth of Quasi-Two-Dimensional Microbial Colonies. *Physical Review Letters* 111, 168101 (Cited on pages 17, 29, and 30.)

[13] Rose M, 1938 Mózg Józefa Piłsudskiego (fr. Le cerveau de Joseph Pilsudski), volume 1. Wilno (Cited on page 19.)

[14] 2017 Feather follice formation. URL `https://www.ed.ac.uk/roslin/chicken-embryology/images`. Photo courtesy of The Roslin Institute Chicken Embryology group (RICE), The Roslin Institute, The University of Edinburgh. Accessed on 22.01.2019. (Cited on page 19.)

[15] Wetzel B, Schaefer H, 1980 Breast cancer cell. URL `https://visualsonline.cancer.gov/`. Image released to public domain by the National Cancer Institute, US Department of Health and Human Services (ID: AV-8000-0302-B). (Cited on page 19.)

[16] Fox C, 1987 Breast cancer cells. URL `https://visualsonline.cancer.gov/`. Image released to public domain by the National Cancer Institute, US Department of Health and Human Services (ID: AV-8708-3073). (Cited on page 19.)

[17] Ben-Jacob E, 2011 From left to right: Two colonies generated by the branching (tipe splitting) morphotype bacteria of *Paenibacillus dendritiformis*, a colony generated by *Paenibacillus vortex* sp. bacteria and a colony generated by the chiral morphotype bacteria of *P. dendritiformis*. Published under license CC BY-SA 3.0 `https://creativecommons.org/licenses/by-sa/3.0`. URL `https://commons.wikimedia.org/wiki/File:Paenibacillus_dendritiformis_colony.jpg`, `https://commons.wikimedia.org/wiki/File:Paenibacillus_dendritiformis_colony.png`, `https://commons.wikimedia.org/wiki/File:Paenibacillus_vortex_colony.jpg`, `https://commons.wikimedia.org/wiki/File:Paenibacillus_dendritiformis_colony_(Chiral_morphotype).jpg` (Cited on page 19.)

[18] Nelson CM, Jean RP, Tan JL, Liu WF, Sniadecki NJ, Spector AA, Chen CS, 2005 Emergent patterns of growth controlled by multicellular form and mechanics. *Proceedings of the National Academy of Sciences of the United States of America* 102, 11594–11599 (Cited on page 19.)

[19] Montel F, Delarue M, Elgeti J, Malaquin L, Basan M, Risler T, Cabane B, Vignjevic D, Prost J, Cappello G, Joanny JF, 2011 Stress Clamp Experiments on Multicellular Tumor Spheroids. *Physical Review Letters* 107, 188102 (Cited on pages 19, 23, and 37.)

[20] Frisch SM, Screaton RA, 2001 Anoikis mechanisms. *Current Opinion in Cell Biology* 13, 555 – 562 (Cited on page 19.)

[21] Hannezo E, Prost J, Joanny JF, 2014 Theory of epithelial sheet morphology in three dimensions. *Proceedings of the National Academy of Sciences* 111, 27–32 (Cited on pages 19 and 36.)

[22] Hoson T, 2014 Plant Growth and Morphogenesis under Different Gravity Conditions: Relevance to Plant Life in Space. *Life* 4, 205–216 (Cited on page 19.)

[23] Lonsdale D, 1999 Principles of tree hazard assessment and management. Stationery Office Ltd, Publications Centre, London, UK (Cited on page 19.)

[24] Shraiman BI, 2005 Mechanical feedback as a possible regulator of tissue growth. *Proceedings of the National Academy of Sciences of the United States of America* 102, 3318–3323 (Cited on page 19.)

[25] Widmann TJ, Dahmann C, 2009 Dpp signaling promotes the cuboidal-to-columnar shape transition of Drosophila wing disc epithelia by regulating Rho1. *Journal of Cell Science* 122, 1362–1373 (Cited on pages 19, 35, and 36.)

[26] Hannezo E, Prost J, Joanny JF, 2011 Instabilities of Monolayered Epithelia: Shape and Structure of Villi and Crypts. *Physical Review Letters* 107, 078104 (Cited on pages 19, 35, and 78.)

[27] Shyer AE, Tallinen T, Nerurkar NL, Wei Z, Gil ES, Kaplan DL, Tabin CJ, Mahadevan L, 2013 Villification: How the Gut Gets Its Villi. *Science* 342, 212–218 (Cited on pages 19 and 35.)

[28] Basan M, Risler T, Joanny JF, Sastre-Garau X, Prost J, 2009 Homeostatic competition drives tumor growth and metastasis nucleation. *HFSP Journal* 3, 265–272 (Cited on

pages 19, 22, 23, and 37.)

[29] Gause GF, 1932 Experimental Studies on the Struggle for Existence. *Journal of Experimental Biology* 9, 389–402 (Cited on page 22.)

[30] Morgan BJT, 1976 Stochastic models of grouping changes. *Advances in Applied Probability* 8, 30–57 (Cited on page 22.)

[31] Krebs CJ, 1972 The experimental analysis of distribution and abundance. Ecology. New York: Harper and Row (Cited on page 22.)

[32] Tsoularis A, Wallace J, 2002 Analysis of logistic growth models. *Mathematical Biosciences* 179, 21–55 (Cited on page 22.)

[33] Waters CM, Bassler BL, 2005 Quorum Sensing: Cell-to-Cell Communication in Bacteria. *Annual Review of Cell and Developmental Biology* 21, 319–346 (Cited on page 22.)

[34] Schwartz MA, 2009 The Force Is with Us. *Science* 323, 588–589 (Cited on page 22.)

[35] Wozniak MA, Chen CS, 2009 Mechanotransduction in development: a growing role for contractility. *Nature Reviews. Molecular Cell Biology* 10, 34–43 (Cited on page 22.)

[36] Molski M, Konarski J, 2003 Coherent states of Gompertzian growth. *Physical Review E* 68, 021916 (Cited on page 23.)

[37] Basan M, Prost J, Joanny JF, Elgeti J, 2011 Dissipative particle dynamics simulations for biological tissues: rheology and competition. *Physical Biology* 8, 026014 (Cited on pages 23 and 37.)

[38] Podewitz N, Delarue M, Elgeti J, 2015 Tissue homeostasis: A tensile state. *EPL (Europhysics Letters)* 109, 58005 (Cited on pages 24, 37, and 60.)

[39] Haidvogel DB, Beckmann A, 1999 Numerical Ocean Circulation Modeling. Imperial College Press (Cited on page 24.)

[40] Chandran KB, Rittgers SE, Yoganathan AP, 2006 Biofluid Mechanics: The Human Circulation. CRC press, Boca Raton (Cited on page 24.)

[41] Westerwalbesloh C, Grünberger A, Stute B, Weber S, Wiechert W, Kohlheyer D, von Lieres E, 2015 Modeling and CFD simulation of nutrient distribution in picoliter bioreactors for bacterial growth studies on single-cell level. *Lab on a Chip* 15, 4177–4186 (Cited on pages 24, 26, 103, and 117.)

[42] Westerwalbesloh C, Grünberger A, Wiechert W, Kohlheyer D, Lieres E, 2017 Coarse-graining bacteria colonies for modelling critical solute distributions in picolitre bioreactors for bacterial studies on single-cell level. *Microbial Biotechnology* 10, 845–857 (Cited on page 24.)

[43] Folkman J, D'Amore PA, 1996 Blood Vessel Formation: What Is Its Molecular Basis? *Cell* 87, 1153–1155 (Cited on page 25.)

[44] Weinberg R, 2013 The biology of cancer. Garland Science, New York (Cited on page 25.)

[45] Grünberger A, Wiechert W, Kohlheyer D, 2014 Single-cell microfluidics: opportunity for bioprocess development. *Current Opinion in Biotechnology* 29, 15 – 23. Cell and Pathway Engineering (Cited on page 25.)

[46] Long Z, Nugent E, Javer A, Cicuta P, Sclavi B, Lagomarsino MC, Dorfman KD, 2013 Microfluidic chemostat for measuring single cell dynamics in bacteria. *Lab on a Chip* 13, 947–954 (Cited on page 25.)

[47] Grünberger A, Probst C, Heyer A, Wiechert W, Frunzke J, Kohlheyer D, 2013 Microfluidic picoliter bioreactor for microbial single-cell analysis: fabrication, system setup, and operation. *Journal of Visualized Experiments* 82, e50560 (Cited on page 25.)

[48] Short MB, Solari CA, Ganguly S, Powers TR, Kessler JO, Goldstein RE, 2006 Flows driven by flagella of multicellular organisms enhance long-range molecular transport. *Proceedings of the National Academy of Sciences* 103, 8315–8319 (Cited on page 26.)

[49] Marieb EN, Hoehn K, 2007 Human Anatomy & Physiology. Pearson Education, San Francisco (Cited on page 26.)

[50] Hermanowicz SW, 2001 A simple 2D biofilm model yields a variety of morphological features. *Mathematical Biosciences* 169, 1–14 (Cited on pages 26 and 27.)

[51] Kawasaki K, Mochizuki A, Matsushita M, Umeda T, Shigesada N, 1997 Modeling Spatio-Temporal Patterns Generated by Bacillus subtilis. *Journal of Theoretical Biology* 188, 177–185 (Cited on pages 27 and 28.)

[52] Monod J, 1949 The Growth of Bacterial Cultures. *Annual Review of Microbiology* 3, 371–394 (Cited on pages 29, 114, 115, and 117.)

[53] Pirt S, 1965 The Maintenance Energy of Bacteria in Growing Cultures. *Proceedings of the Royal Society of London B: Biological Sciences* 163, 224–231 (Cited on page 29.)

[54] Wang Q, Zhang T, 2010 Review of mathematical models for biofilms. *Solid State Communications* 150, 1009–1022. Nanoscale Interfacial Phenomena in Complex Fluids (Cited on page 29.)

[55] Landau LD, Lifshitz EM, Kosevich AM, Pitaevski LP, 1986 Theory of Elasticity - Course of Theoretical Physics Volume 7. Butterworth-Heinemann, Oxford, third edition (Cited on pages 29, 75, 76, 81, 94, 149, 150, 151, and 158.)

[56] World Health Organisation, 2014 Antimicrobial Resistance: Global Report on Surveillance. ISBN: 978 92 4 156474 8 (Cited on page 30.)

[57] Greulich P, Scott M, Evans MR, Allen RJ, 2015 Growth-dependent bacterial susceptibility to ribosome-targeting antibiotics. *Molecular Systems Biology* 11, 796 (Cited on pages 30 and 31.)

[58] Greulich P, Waclaw B, Allen RJ, 2012 Mutational Pathway Determines Whether Drug Gradients Accelerate Evolution of Drug-Resistant Cells. *Physical Review Letters* 109, 088101 (Cited on pages 31 and 32.)

[59] Finberg RW, Moellering RC, Tally FP, Craig WA, Pankey GA, Dellinger EP, West MA, Joshi M, Linden PK, Rolston KV, Rotschafer JC, Rybak MJ, 2004 The Importance of Bactericidal Drugs: Future Directions in Infectious Disease. *Clinical Infectious Diseases* 39, 1314–1320 (Cited on page 31.)

[60] Bremer H, Dennis PP, 1996 E. coli and S. Typhimurium: Cellular and Molecular Biology, chapter: Modulation of Chemical Composition and Other Parameters of the Cell by Growth Rate, 1553–1569. ASM Press Washington, DC (Cited on page 31.)

[61] Hiscock TW, Megason SG, 2015 Orientation of Turing-like Patterns by Morphogen Gradients and Tissue Anisotropies. *Cell Systems* 1, 408–416 (Cited on pages 32, 33, and 34.)

[62] Turing AM, 1952 The chemical basis of morphogenesis. *Philosophical Transactions of the Royal Society of London. Series B, Biological Sciences* 237, 37–72 (Cited on page 33.)

[63] Cross MC, Hohenberg PC, 1993 Pattern formation outside of equilibrium. *Reviews of Modern Physics* 65, 851–1112 (Cited on page 33.)

[64] Mukherjee R, Sharma A, Steiner U, 2011 Generating Micro- and Nanopatterns on Polymeric Materials, chapter 11: Surface Instability and Pattern Formation in thin Polymer Films, 217–265. John Wiley & Sons, Ltd (Cited on page 34.)

[65] Wang Q, Zhao X, 2015 A three-dimensional phase diagram of growth-induced surface instabilities. *Scientific Reports* 5, 8887 (Cited on page 34.)

[66] Chirat R, Moulton DE, Goriely A, 2013 Mechanical basis of morphogenesis and convergent evolution of spiny seashells. *Proceedings of the National Academy of Sciences* 110, 6015–6020 (Cited on page 36.)

[67] Drasdo D, Loeffler M, 2001 Individual-based models to growth and folding in one-layered tissues: Intestinal crypts and early development. *Nonlinear Analysis: Theory, Methods & Applications* 47, 245 – 256. Proceedings of the Third World Congress of Nonlinear Analysts (Cited on page 36.)

[68] Podewitz N, 2015 Growing tissues: A simulation study. Ph.D. thesis, Universität zu Köln (Cited on pages 37, 39, 57, 60, and 62.)

[69] Frenkel D, Smit B, 2001 Understanding Molecular Simulation: From Algorithms to Applications. Academic press, London, 2nd edition (Cited on pages 37 and 40.)

[70] Ranft J, Basan M, Elgeti J, Joanny JF, Prost J, Jülicher F, 2010 Fluidization of tissues by cell division and apoptosis. *Proceedings of the National academy of Sciences of the United States of America* 107, 20863–20868 (Cited on pages 37, 40, and 66.)

[71] Basan M, Elgeti J, Hannezo E, Rappel WJ, Levine H, 2013 Alignment of cellular motility forces with tissue flow as a mechanism for efficient wound healing. *Proceedings of the National Academy of Sciences* 110, 2452–2459 (Cited on page 37.)

[72] Marel AK, Podewitz N, Zorn M, Rädler JO, Elgeti J, 2014 Alignment of cell division axes in directed epithelial cell migration. *New Journal of Physics* 16, 115005 (Cited on page 37.)

[73] Noguchi H, Gompper G, 2006 Meshless membrane model based on the moving least-squares method. *Physical Review E* 73, 021903 (Cited on pages 37, 42, and 68.)

[74] Shiba H, Noguchi H, 2011 Estimation of the bending rigidity and spontaneous curvature of fluid membranes in simulations. *Physical Review E* 84, 031926 (Cited on pages 37, 42, and 68.)

[75] Hornung R, Grünberger A, Westerwalbesloh C, Kohlheyer D, Gompper G, Elgeti J, 2018 Quantitative modelling of nutrient-limited growth of bacterial colonies in microfluidic cultivation. *Journal of The Royal Society Interface* 15, 20170713 (Cited on pages 38, 101, 102, 108, 115, 116, 118, 123, 124, and 171.)

[76] Allen MP, Tildesley DJ, 1989 Computer Simulation of Liquids. Oxford University Press, Oxford (Cited on pages 38, 40, 55, 57, 60, and 135.)

[77] Español P, Warren P, 1995 Statistical Mechanics of Dissipative Particle Dynamics. *EPL (Europhysics Letters)* 30, 191 (Cited on page 38.)

[78] Pagonabarraga I, Hagen MHJ, Frenkel D, 1998 Self-consistent dissipative particle dynamics algorithm. *EPL (Europhysics Letters)* 42, 377 (Cited on page 41.)

[79] Nikunen P, Karttunen M, Vattulainen I, 2003 How would you integrate the equations of motion in dissipative particle dynamics simulations? *Computer Physics Communications* 153, 407 – 423 (Cited on page 41.)

[80] Nelson D, Piran T, Weinberg S, eds., 2004 Statistical Mechanics of Membranes and Surfaces. World Scientific, Singapore (Cited on page 42.)

[81] Noguchi H, 2011 Solvent-free coarse-grained lipid model for large-scale simulations. *Journal of Chemical Physics* 134, 055101 (Cited on page 42.)

[82] Drouffe JM, Maggs AC, Leibler S, 1991 Computer simulations of self-assembled membranes. *Science* 254, 1353–1356 (Cited on page 42.)

[83] Wolfram Research, Incorporation, 2016 Mathematica, Version 11.0.1.0. Champaign, IL (Cited on page 55.)

[84] Thompson AP, Plimpton SJ, Mattson W, 2009 General formulation of pressure and stress tensor for arbitrary many-body interaction potentials under periodic boundary conditions. *The Journal of Chemical Physics* 131, 154107 (Cited on page 57.)

[85] Rowlinson JS, Widom B, 2013 Molecular Theory of Capillarity. Dover Publications, Mineola, New York (Cited on pages 59 and 75.)

[86] Admal NC, Tadmor EB, 2010 A unified interpretation of stress in molecular systems. *Journal of Elasticity* 100, 63–143 (Cited on pages 60, 135, 136, and 137.)

[87] Oliphant TE, 2007 Python for Scientific Computing. *Computing in Science & Engineering* 9, 10–20 (Cited on pages 63, 65, 68, 83, 84, 117, and 118.)

[88] Berendsen HJC, Postma JPM, van Gunsteren WF, DiNola A, Haak JR, 1984 Molecular dynamics with coupling to an external bath. *The Journal of Chemical Physics* 81, 3684–3690 (Cited on page 63.)

[89] Helfrich W, 1985 Effect of thermal undulations on the rigidity of fluid membranes and interfaces. *Journal de Physique* 46, 1263–1268 (Cited on page 66.)

[90] Peliti L, Leibler S, 1985 Effects of Thermal Fluctuations on Systems with Small Surface Tension. *Physical Review Letters* 54, 1690–1693 (Cited on page 66.)

[91] Pinnow HA, Helfrich W, 2000 Effect of thermal undulations on the bending elasticity and spontaneous curvature of fluid membranes. *The European Physical Journal E* 3, 149–157 (Cited on page 66.)

[92] Risler T, Peilloux A, Prost J, 2015 Homeostatic Fluctuations of a Tissue Surface. *Physical Review Letters* 115, 258104 (Cited on pages 66 and 80.)

[93] Salbreux G, Jülicher F, 2017 Mechanics of active surfaces. *Physical Review E* 96, 032404 (Cited on page 66.)

[94] Strikwerda JC, 2004 Finite Difference Schemes and Partial Differential Equations. SIAM, Philadelphia (Cited on page 70.)

[95] Helfrich W, 1973 Elastic Properties of Lipid Bilayers: Theory and Possible Experiments. *Zeitschrift für Naturforschung C* 28, 693–703 (Cited on page 74.)

[96] Canham P, 1970 The Minimum Energy of Bending as a Possible Explanation of the Biconcave Shape of the Human Red Blood Cell. *Journal of Theoretical Biology* 26, 61–81 (Cited on page 74.)

[97] Goldstein H, Poole Jr CP, Safko Sr JL, 2012 Klassische Mechanik. John Wiley & Sons (Cited on page 79.)

[98] Prost J, Manneville JB, Bruinsma R, 1998 Fluctuation-magnification of non-equilibrium membranes near a wall. *The European Physical Journal B - Condensed Matter and Complex Systems* 1, 465–480 (Cited on pages 80, 160, and 161.)

[99] Jinnai H, Hashimoto T, Lee D, Chen SH, 1997 Morphological Characterization of Bicontinuous Phase-Separated Polymer Blends and One-Phase Microemulsions. *Macromolecules* 30, 130–136 (Cited on page 90.)

[100] Teubner M, 1991 Level Surfaces of Gaussian Random Fields and Microemulsions. *EPL (Europhysics Letters)* 14, 403–408 (Cited on page 90.)

[101] Bardeen JM, Bond JR, Kaiser N, Szalay AS, 1985 The Statistics of Peaks of Gaussian Random Fields. *The Astrophysical Journal* 304, 15–61 (Cited on page 90.)

[102] Unthan S, Grünberger A, van Ooyen J, Gätgens J, Heinrich J, Paczia N, Wiechert W, Kohlheyer D, Noack S, 2014 Beyond Growth Rate 0.6: What Drives Corynebacterium glutamicum to Higher Growth Rates in Defined Medium. *Biotechnology and Bioengineering* 111, 359–371 (Cited on pages 102, 108, and 117.)

[103] Ochoa-Tapia JA, Stroeve P, Whitaker S, 1994 Diffusive Transport in Two-Phase Media: Spatially Periodic Models and Maxwell's theory for Isotropic and Anisotropic Systems. *Chemical Engineering Science* 49, 709–726 (Cited on pages 104 and 125.)

[104] Wood BD, Quintard M, Whitaker S, 2002 Calculation of Effective Diffusivities for Biofilms and Tissues. *Biotechnology and Bioengineering* 77, 495–516 (Cited on pages 104 and 125.)

[105] Happel J, Brenner H, 1983 Low Reynolds number hydrodynamics: with special applications to particulate media. Martinus Nijhoff Publishers, The Hague (Cited on page 104.)

[106] Mark JE, 1999 Polymer Data Handbook. Oxford University Press, Oxford (Cited on pages 105 and 109.)

[107] Srinivas K, King JW, Howard LR, Monrad JK, 2011 Binary diffusion coefficients of phenolic compounds in subcritical water using a chromatographic peak broadening technique. *Fluid Phase Equilibria* 301, 234–243 (Cited on page 106.)

[108] American Type Culture Collection Corynebacterium glutamicum, ATCC® 13032™. URL `http://www.lgcstandards-atcc.org/products/all/13032.aspx` (Cited on page 108.)

[109] Hornung R, Grünberger A, Westerwalbesloh C, Kohlheyer D, Gompper G, Elgeti J, 2018 Supplementary material from "Quantitative modelling of nutrient-limited growth of bacterial colonies in microfluidic cultivation". doi:10.6084/m9.figshare.c.3991626.v2. URL `https://figshare.com/collections/Supplementary_material_from_Quantitative_modelling_of_nutrient-limited_growth_of_bacterial_colonies_in_microfluidic_cultivation_/3991626/2` (Cited on pages 108, 123, 181, 182, and 183.)

[110] Kuchling H, 2011 Taschenbuch der Physik. Carl Hanser (Cited on page 109.)

[111] Raffel M, Willert CE, Wereley S, Kompenhans J, 2013 Particle Image Velocimetry: A Practical Guide. Springer (Cited on pages 111, 112, and 113.)

[112] Schneider CA, Rasband WS, Eliceiri KW, 2012 NIH Image to ImageJ: 25 years of image analysis. *Nature methods* 9, 671–675 (Cited on page 111.)

[113] Helfrich S, Azzouzi CE, Probst C, Seiffarth J, Grünberger A, Wiechert W, Kohlheyer D, Nöh K, 2015 Vizardous: interactive analysis of microbial populations with single cell resolution. *Bioinformatics* 31, 3875–3877 (Cited on pages 111, 121, and 122.)

[114] Tseng Q, Duchemin-Pelletier E, Deshiere A, Balland M, Guillou H, Filhol O, Théry M, 2012 Spatial organization of the extracellular matrix regulates cell–cell junction positioning. *Proceedings of the National Academy of Sciences* 109, 1506–1511 (Cited on page 112.)

[115] Teissier G, 1937 Les Lois Quantitatives de la Croissance. Number 455 in Actualités Scientifiques et Industrielles: Exposés de Biométrie et de Statistique Biologique. Hermann & Cie, Paris (Cited on pages 114, 115, and 117.)

[116] Mather W, Mondragón-Palomino O, Danino T, Hasty J, Tsimring LS, 2010 Streaming Instability in Growing Cell Populations. *Physical Review Letters* 104, 208101 (Cited on pages 119 and 126.)

[117] Merkel R, Kirchgeßner N, Cesa CM, Hoffmann B, 2007 Cell Force Microscopy on Elastic Layers of Finite Thickness. *Biophysical Journal* 93, 3314–3323 (Cited on page 130.)

[118] Schwarz US, Soiné JRD, 2015 Traction force microscopy on soft elastic substrates: A guide to recent computational advances. *Biochimica et Biophysica Acta (BBA) - Molecular Cell Research* 1853, 3095 – 3104. Mechanobiology (Cited on page 130.)

[119] Gniewek P, Hallatschek O, 2019 Fluid flow through packings of elastic shells. *Physical Review E* 99, 023103 (Cited on page 130.)

[120] Delarue M, Hartung J, Schreck C, Gniewek P, Hu L, Herminghaus S, Hallatschek O, 2016 Self-driven jamming in growing microbial populations. *Nature Physics* 12, 762–766 (Cited on page 130.)

[121] Aranson IS, Tsimring LS, 2001 Continuum description of avalanches in granular media. *Physical Review E* 64, 020301 (Cited on page 130.)

[122] Denisov DV, Lörincz KA, Uhl JT, Dahmen KA, Schall P, 2016 Universality of slip avalanches in flowing granular matter. *Nature communications* 7, 10641 (Cited on page 130.)

[123] Eschenburg JH, Jost J, 2007 Differentialgeometrie und Minimalflächen. Springer-Verlag, Berlin (Cited on pages 140, 141, 142, 143, and 147.)

[124] Do Carmo MP, 2016 Differential Geometry of Curves and Surfaces: Revised and Updated Second Edition. Courier Dover Publications (Cited on page 144.)

[125] Winkler E, 1867 Die Lehre von der Elastizität und Festigkeit mit besonderer Rücksicht auf ihre Anwendung in der Technik. Dominicius, Prague (Cited on page 149.)

[126] Ventsel E, Krauthammer T, 2001 Thin Plates and Shells: Theory, Analysis, and Applications. CRC Press, Boca Raton (Cited on page 149.)

[127] Groenewold J, 2001 Wrinkling of plates coupled with soft elastic media. *Physica A: Statistical Mechanics and its Applications* 298, 32–45 (Cited on pages 151 and 152.)

[128] Allen HG, 1969 Analysis and Design of Structural Sandwich Panels. Pergamon Press, Oxford (Cited on page 151.)

[129] Schwabl F, 2006 Statistische Mechanik. Springer, Berlin (Cited on page 158.)

List of Figures

1.1 Examples for morphogenesis, regulation of growth: horns of sheep, goats, antelopes; spiral seashells; brain folds; feather follicle formation; bacteria grown on agar plates. Misregulation of growth leads to cancer. 19

2.1 Competition simulation of two tissues with different homeostatic pressure, the tissue with larger homeostatic pressure takes over the compartment. 23

2.2 Images of microfluidic experiments, microorganisms grow in chambers which are provided by feeding ducts with a constant stream of growth medium to maintain a constant chemical environment. 25

2.3 Biofilm growth in a cellular automata model yields various morphologies: from densely populated to different degrees of branched shapes. 27

2.4 Comparision of densely branched morphology in an experiment with *Bacillus subtillis* grown on agarose with a reaction-diffusion simulation. 28

2.5 An IBM which includes elastic interactions between rod-shaped bacteria to investigate the effect of steric interactions on the branching transition. 30

2.6 **a)** Growth rate of *Escherichia Coli* in presence of various concentration levels of four different ribosome-targeting antibiotics, relative to drug-free growth rate. Reversibly binding ribosome-targeting antibiotics suppress fast-growing infections better, irreversibly binding antibiotics slow-growing infections. **b)** In presence of a spatial drug gradient, the mutational pathway which leads to increasing antibiotic resistance has an effect on the mean time necessary to reach the maximal resistant mutation. The mean time is shorter for monotonic increasing resistance versus a pathway with a fitness valley. 31

2.7 Turing patterns generated with the Swift-Hohenberg model. The isotropic model results in labyrinthine patterns, oriented stripe patterns occur if the symmetry is broken, e.g. by anisotropic diffusion. 33

2.8 Examples for pattern generation through elastic instabilities (differential growth hypothesis) or spatial change of elastic parameters: chicken gut, simulation and experiment; *Drosophila melanogaster* wing disc; human brain folding. 35

3.1 Cell division in the 2PG-model: cell consists of two point particles; they repell each other with a defined force; at a size threshold a new cell is inserted. 38

3.2 Interaction of a single particle with a flat plane in the MMM-model. 45

3.3 2PG-potential energy for a single particle interacting with a flat membrane. Harmonic confinement if particle is close to membrane; repulsion if intrudes from far away; both limits are separated by a potential hill with finite binding energy. 47

3.4 **Inset**: A small membrane patch at the pole of a spherical surface interacts via the MMM-potential with all particles in the spherical cap cut out by the cutoff radius. **Graph**: The MMM-potential energy of a sphere converges against the corresponding Helfrich-Canham curvature energy for sphere radii much larger than the cutoff radius. 49

3.5 A small membrane patch on a cylindric surface interacts via the MMM-potential with all particles inside the cylindrical cap cut out by the cutoff radius. Geometric derivation of the azimuthal angles which correspond to the cylindrical cap, dependent on the cylinder axis coordinate. 50

3.6 Intermediate results in the approximative calculation of the MMM bending rigidity for non-uniform weight function. Relative deviation of final approximation from results at intermediate approximation steps. 54

3.7 Homeostatic surface tension measurement for different growth strengths, dependent on the applied harmonic confinement strength. For increasing confinement strength, surface tension becomes more compressive, total potential energy stored in confinement increases, height fluctuations decrease. Optimal confinement strength chosen as trade-off between stored confinement potential energy and height fluctuations. 61

3.8 Surface tension measurements with optimal confinement strength dependent on growth strength, background friction and intracell friction. 62

3.9 Growth rate as a function of surface tension for various growth strength parameters. A linear fit of growth rate versus surface tension, close to the homeostatic state, estimates the growth pressure sensitivity ξ. 63

3.10 Surface tension versus particle density for various growth strengths. Linear fit of growth rate versus density, close to the homeostatic state, estimates the area compressibility χ_a. 65

3.11 Area compressibility and homeostatic density dependent on growth strength. 65

3.12 Inverse height fluctuation spectra for various growth strengths. Fits to the thermal fluctuation spectrum exhibit increasing residual with increasing wavenumber cutoff. Resulting bending rigidity from fit exhibits larger uncertainty for decreasing wavenumber cutoff. Optimal wavenumber cutoff chosen as tread-off between residual and uncertainty. 67

3.13 Estimation of effective temperature corresponding to height fluctuations suggest that effective temperature is slightly larger than the preset value. With this correction, bending rigidity measurements in simulations yield approximately 20% smaller values than the analytical result. 69

4.1 Examples for simulations of temporal evolution of wrinkling patterns of a growing, square membrane. 73

4.2 Degrees of freedom of a membrane on top of an elastic substrate are membrane bending, membrane stretching and substrate deformation. 74

4.3 The sign of the polynomial $e(k) = \kappa k^4 + \langle\gamma\rangle_x k^2 + \widehat{E}k$ determines the unstable buckling modes for spatially constant surface tension and vanishing spontaneous curvature. Without elastic substrate, the unstable modes lie between the two zero-crossings $k = 0$ and $k = \sqrt{-\langle\gamma\rangle_x/\kappa}$ of $e(k)$. With elastic substrate, the linear term $\widehat{E}k$ increases the energy contribution of all modes k which contracts the interval of unstable modes. 77

4.4 Numeric solution of model eq. (4.2.12) for surface tension, average wavenumber, amplitude, projected density and area. 84

4.5 Asymptotic surface tension γ_∞ and wavenumber k_∞ as a function of the dimensionless second buckling-growth-ratio Θ''. Surface tension and wavenumber converge against their homeostatic values in the limit $\Theta'' \to \infty$ and converge against zero in the opposite limit $\Theta'' \to 0$. 87

4.6 Top view, side view and FFT-spectrum of a buckling simulation at three different points in time. 91

4.7 Surface tension, average wavenumber, area, density and average height as a function of time, in simulations and theory, with various values of background friction and intracell friction. In simulations, growth rate as a function of surface tension is much larger than previous measurements. A piecewise linear interpolation of the actual growth rate in simulations is performed. The analytical model is adapted accordingly which improves its predictions for area, density and average height. 92

4.8 Surface tension and average wavenumber, at the transition point to overlapping shapes, as a function of the "second buckling-growth-ratio" $\Theta'' \propto \tau_{ampl}/\tau_g$. The analytical model, integrated up to a timepoint at which the projected density equals the value in simulations at the last point in Monge-representation, predicts the simulations fairly well. 93

4.9 Cuts along vertical direction of growing membrane at different time points to show the evolution of overlapping shapes. 95

4.10 As fig. 4.9 for stronger growth. 96

4.11 Temporal evolution of projected density, average height and in-plane boundary force for an initially flat membrane which grows and develops overlapping shapes. As growth is deactivated, the membrane remains stable and does not fold into the configuration of minimal curvature energy on the observed timescales. 97

5.1 Schematic depiction of microfluidic experiment setup in which *Corynebacterium glutamicum* grow, dependent on the local nutrient concentration, and flow towards the channel outlets. Flow profile measurements with the PIV technique allow to estimate the local growth rate and comparison with a theoretical model. 101

5.2 Microscopic images of (1) the quasi-one-dimensional growth channel geometry used to observe the steady state flow field of bacteria and (2) a genuine two-dimensional growth chamber setup with which we test the predictions of our simulation model. 102

5.3 Deformation of a linear elastic halfspace subject to a surface pressure as in eq. (5.1.14) which may arise due to friction of the flowing bacteria with top and bottom chamber wall. 106

5.4 Image of a growth channel experiment where a part of the channel appears turbid and cloudy, individual bacteria are hardly distinguishable. This may occur due to a large pressure inside the chamber such that top and bottom wall deform and bacteria stack on each other. 110

5.5 Example for the preprocessing steps of the growth channel image data: cutting, alignment and contrast enhancement. 111

5.6 Working principle of PIV: The interrogation window from frame oneis moved in the larger search window in frame two in order to generate a cross-correlation map. 112

5.7 Example for the PIV-steps for two small cutouts of two consecutive frames. 113

5.8 Velocity profiles $v\left(x\right)$, estimated by PIV of growth channel experiments and subsequent averaging over y-direction and steady state frames. Analytical model predictions of local nutrient concentration and uptake in the channel. 115

5.9 Velocity gradient v' versus velocity integral $V = \int_{x_0}^{x} v\left(x'\right) dx'$ for velocity profiles of growth channel experiments. According to model eq. (5.1.5), $v'-V$-plots should collapse onto the uptake function u. 116

5.10 Schematic depiction of the extrapolation of the predicted concentration profile $\widehat{g}$ towards the channel inlets. Comparison of predicted concentration with actually fed concentration allows to estimate the unit conversion factor between dimensionless concentration in analytical model and real concentration. 118

5.11 Examples for the "avalanche"-like motion of bacteria. 119

5.12 Spatial velocity correlation function of growth channel experiments in order to estimate the lengthscale of coordinated motion during the "avalanche"-like movement of bacteria. 120

5.13 Decay lengthscales of spatial velocity correlation function of growth channel experiments. 121

5.14 Example for cell segmentation of a single snapshot of a growth channel experiment. Segmentation allows measurement of cell density, area per cell and two-dimensional packing fraction. 122

5.15 Histograms of cell area versus velocity magnitude to estimate whether larger cells move slower. 123

5.16 Examples of colony spreading dynamics in the growth chamber geometry, in simulation and experiment, for two different feeding concentrations. For medium feeding concentration, simulation and experiment agree, whereas for low feeding concentrations, deviations occur for small colony sizes. 124

B.1 Illustriation how different kinds of particle-particle bonds contribute to the local mechanical stress in a subvolume of a system. 136

C.1 Neile's parabola as an example for a differentiable curve with vanishing tangent vector. The Klein bottle as an example for a non-orientable surface. Curvature as the inverse radius of the osculating circle. 140

C.2 Illustration of the genus of a closed, orientable surface, which can be interpreted as the number of "handles". The genus is also related in a simple manner to the Euler-characteristic of a surface triangulation. 145

C.3 Regular triangulation with six-fold symmetry. Index of an continious vector field in an isolated zero crossing corresponds to the number of rotations the vector performs on the boundary of a small disc centered in the zero crossing. 146

E.1 Asymptotic wavenumber and surface tension for the growing membrane model with Newtonian fluid as embedding medium, in the limit of low Reynolds numbers. 163

F.1 Surface tension, average wavenumber, area, density and average height as a function of time, in simulations and theory, for growth strength parameter $B^* = 0.6$ and with various values of background friction and intracell friction. In simulations, growth rate as a function of surface tension is much larger than previous measurements. A piecewise linear interpolation of the actual growth rate in simulations is performed. The analytical model is adapted accordingly which improves its predictions for area, density and average height. 166

F.2 As fig. F.1 for growth strength $B^* = 0.7$. 167

F.3 As fig. F.1 for growth strength $B^* = 0.8$. 168

F.4 As fig. F.1 for growth strength $B^* = 0.9$. 169

F.5 As fig. F.1 for growth strength $B^* = 1.0$. 170

G.1 Velocity profiles $v(x)$ estimated by PIV of growth channel experiments and subsequent averaging over y-direction and steady state frames. Analytical model predictions of local nutrient concentration and uptake in the channel. Two experiments with PCA-concentration of 48.75 µM, Monod-uptake used for model fit. 172

G.2 As fig. G.1 for three experiments with PCA-concentration 97.5 µM and Monod-uptake for model fit. 173

G.3 As fig. G.1 for three experiments with PCA-concentration 390 µM and Monod-uptake for model fit. 174

G.4 As fig. G.1 for four experiments with PCA-concentration 585 µM and Monod-uptake for model fit. 175

G.5 As fig. G.1, with Teissier-uptake for model fit. 176

G.6 As fig. G.1 for three experiments with PCA-concentration 97.5 µM and Teissier-uptake for model fit. 177

G.7 As fig. G.1 for three experiments with PCA-concentration 390 µM and Teissier-uptake for model fit. 178

G.8 As fig. G.1 for four experiments with PCA-concentration 585 µM and Teissier-uptake for model fit. 179

H.1 Illustration how simulation data for colony spreading experiments is shifted along time axis to compare with experimental data. 181

H.2 Examples of colony spreading dynamics in the growth chamber geometry, in simulation and experiment, for feeding concentration of 195 µM. 182

H.3 As fig. H.2 for experiments with feeding concentration 19.5 µM. 183

List of Tables

3.1 Standard simulation parameters for the 2PG model. 39
3.2 Iteration steps of VV-algorithm and DPD-VV-algorithm. 41

5.1 Standard simulation parameters for bacterial growth simulations. 107
5.2 Parameters of growth channel experiments and time interval used for PIV evaluation. 110
5.3 Fit results for parameters of reaction-diffusion model of bacterial growth. 117

E.1 Summary of buckling parameters for the models with hydrodynamic interactions (and an impermeable membrane) and without hydrodynamic interactions. 164

I.1 Standard simulation parameters for growing membrane simulations. 185
I.2 Results of membrane parameter measurements for different growth strength parameters B^*, other parameters as in standard set. 185
I.3 Homeostatic surface tension measurements for varying growth strengths B^*, background friction constants γ_b^* and intracellular friction constants γ_c^*. 186
I.4 Standard simulation parameters for bacterial growth simulations. 186

Erklärung der Selbständigkeit

Ich versichere, dass ich die von mir vorgelegte Dissertation selbständig angefertigt, die benutzten Quellen und Hilfsmittel vollständig angegeben und die Stellen der Arbeit – einschließlich Tabellen, Karten und Abbildungen – , die anderen Werken im Wortlaut oder dem Sinn nach entnommen sind, in jedem Einzelfall als Entlehnung kenntlich gemacht habe; dass diese Dissertation noch keiner anderen Fakultät oder Universität zur Prüfung vorgelegen hat; dass sie – abgesehen von unten angegebenen Teilpublikationen – noch nicht veröffentlicht worden ist, sowie, dass ich eine solche Veröffentlichung vor Abschluss des Promotionsverfahrens nicht vornehmen werde. Die Bestimmungen der Promotionsordnung sind mir bekannt. Die von mir vorgelegte Dissertation ist von Dr. habil. Jens Elgeti betreut worden.

Teilpublikation:
Hornung R, Grünberger A, Westerwalbesloh C, Kohlheyer D, Gompper G, Elgeti J, 2018 Quantitative modelling of nutrient-limited growth of bacterial colonies in microfuidic cultivation. *Journal of The Royal Society Interface* 15, 20170713. (doi:10.1098/rsif.2017.0713)

Jülich, den 4. November 2019

Raphael Hornung

Lebenslauf

Name	Hornung	Geburtsdatum	03.05.1989
Vorname	Raphael	Geburtsort	Zweibrücken
Staatsangehörigkeit	Deutsch		

Seit SS 2015 Universität zu Köln	Promotionsstudent im Fach Physik
Seit März 2015 Forschungszentrum Jülich GmbH Jülich, Nordrhein-Westfalen	Mitglied der Graduiertenschule IHRS BioSoft Organisator: Dr. Thorsten Auth
Seit März 2014 Forschungszentrum Jülich GmbH Jülich, Nordrhein-Westfalen	Doktorand im Institute of Complex Systems (ICS-2):Theorie der Weichen Materie und Biophysik, Betreuer: Prof. Dr. Gerhard Gompper und Dr. habil. Jens Elgeti
Okt. 2011 - Nov. 2013 Universität des Saarlandes Saarbrücken	Masterstudium der Physik mit Nebenfach Mathematik, Masterarbeit: “Calcium-induzierte Selbstorganisation der Mitochondrien-Relokation bei T-Zell-Aktivierung”, Betreuer: Prof. Dr. Heiko Rieger Abschluss mit Master of Science (M.Sc.)
Okt. 2008 - Juli 2011 Universität des Saarlandes Saarbrücken	Bachelorstudium der Physik mit Nebenfach Mathematik, Bachelorarbeit: “Theoretische Modellierung von Calcium-Dynamik bei T-Zellen-Aktivierung”, Betreuer: Prof. Dr. Heiko Rieger Abschluss mit Bachelor of Science (B.Sc.)
Aug. 1999 - Juni 2008 Von-der-Leyen Gymnasium Blieskastel, Saarland	Abitur und Erwerb der allgemeinen Hochschulreife

Jülich, den 11. November 2019

Raphael Hornung